JOURNAL OF SCIENCE
SAKARYA UNIVERSITY

Sakarya University Journal of Science



SAKARYA UNIVERSITY
e-issn: 2147-835X

VOLUME: 24
ISSUE: 3
JUNE 2020

Sakarya University Journal of Science
Volume: 24 Issue: 3 June 2020

Editorial Boards

Editor-in-Chief

Editors

Editorial Board

Guest Editorial Board

SAKARYA UNIVERSITY JOURNAL OF SCIENCE
CONTENTS
Volume: 24 - Issue: 3 (JUNE 2020)

RESEARCH ARTICLES

Sakarya University Journal of Science

ISSN 1301-4048 | e-ISSN 2147-835X | Period Bimonthly | Founded: 1997 | Publisher Sakarya University | http://www.saujs.sakarya.edu.tr/en/

Title: Sex Prediction Using Finger, Hand and Foot Measurements for Forensic Identification in a Nigerian Population

Authors: O. Ogbonnaya IROANYA, T. Frank EGWUATU, O. Temitope TALABI, I. Stella OGUNLEYE
Recieved: 2019-05-16 13:45:06

Accepted: 2019-12-30 17:03:08

Article Type: Research Article
Volume: 24
Issue: 3
Month: June
Year: 2020
Pages: 432-445

How to cite
O. Ogbonnaya IROANYA, T. Frank EGWUATU, O. Temitope TALABI, I. Stella OGUNLEYE; (2020), Sex Prediction Using Finger, Hand and Foot Measurements for Forensic Identification in a Nigerian Population. Sakarya University Journal of Science, 24(3), 432-445, DOI: https://doi.org/10.16984/saufenbilder.566377
Access link
http://www.saujs.sakarya.edu.tr/en/issue/52472/566377

Sakarya University Journal of Science 24(3), 432-445, 2020

Sex Prediction Using Finger, Hand and Foot Measurements for Forensic Identification in a Nigerian Population

O. Ogbonnaya IROANYA[*1], T. Frank EGWUATU[1], O. Temitope TALABI[1], I. Stella OGUNLEYE[1]

Abstract

In forensics, the identification of recovered human remains is important and of great significance. Sex determination is the most important primary parameter in human identification. We investigated the predictive role of the anthropometric measurements of hand, finger and foot dimensions in sex determination. The main objective was to correlate sexual dimorphism with hand, finger and foot dimensions and determine their sectioning point(s) and also ascertain the variables which can better predict sex. A cross sectional study was carried out using 200 students from Faculty of Science, University of Lagos, Nigeria aged 16-30years. The collected data was analyzed using IBM SPSS version 23. The average hand length, breadth and index were found to be 17.44mm, 8.09mm and 0.3781mm greater in male compared to the female subjects respectively, with no significant ($p<0.05$) difference between the right and left hand in the same sex. The resultant hand index suggests the females have higher dolichocheir morphology compared to males and no hyperbrachycheir morphology. The cutoff point index for the right (≤43.41mm) and left (≤42.90mm) hand is suggestive of female, but is suggestive of male if the right hand is >43.41mm and left hand is >42.90mm. A foot index section points for the right (347.9mm) and left (349.4mm) foot was taken for male and female foot identification. A cut of point of 348.7mm was obtained to define sexual dimorphism of the foot index. There was strong correlation between foot dimensions of both feet for the same sex ($p<0.01$) while the foot dimensions of the male and the female were significantly ($p<0.05$) different. The hand (length and breadth), index/ring fingers ratio, foot (length and breadth) and ankle breadth are therefore important indices and forensic identification tool for predicting sexual dimorphism and identifying human remains for medicolegal examinations.

Keywords: sexual dimorphism, index/ring fingers ratio, hand and foot dimensions, dolichocheir, medicolegal examinations

[*]Corresponding Author: oiroanya@unilag.edu.ng

[1]University of Lagos, Department of Cell Biology and Genetics, Akoka Yaba, Lagos Nigeria, ORCID: 0000-0002-5122-1466; 0000-0002-6083-4133; 0000-0003-2667-1251; 0000-0001-8464-0336

1. INTRODUCTION

Precise identification is the most important step in forensic and medicolegal practices [1]. The establishment of the identity of the deceased in cases of disaster is of the greatest importance to the forensic scientists [2]. Identification of victims using dismembered human remains has constantly been a challenge in medico-legal investigations [3]. Anthropometry involves the technique of measuring the shape of the human body quantitatively. In Forensics, anthropometry can assist in the identification of mutilated, decomposed and or skeletal unidentified remains so as to determine the sex, age, stature and or race. It can also help to estimate how long a corpse has been decomposing, determine possible cause of death e.g. fractured skull and some inimitable feature(s) of an individual like some medical procedures.

Sex determination using anthropometric parameters is currently covered in many studies [1,4 - 6]. When they are available, the pelvic and cranial features were the most accurate and commonly used features to determine sex. Some researchers have used the measurements of other parts of the body to estimate sex [1, 4 - 11].

In this study we were able to, predict the sex of individuals using morphometric measurements of finger, hand and foot, decipher the variables that are independents sex predictors and also estimate the sectioning point for determining sex using foot, hand and finger dimensions of some students in the Faculty of Science, University of Lagos, Nigeria via the use of statistical analysis. Based on the results of this research, the anthropometric dimensions of the finger, hand and foot can be used to predict gender. The data presented in this study will aid detectives and other researchers especially forensic scientists, determine sex from the foot, finger and hand dimensions. To the best of our knowledge, this is the first study that determined sex of students from the Faculty of Science, University of Lagos, Nigeria using anthropometric dimensions of the finger, hand and foot.

2. MATERIAL AND METHODS

Study Design

This study was conducted using two hundred students (100 male and 100 female) between the age of 16 and 30 years from the Faculty of Science, University of Lagos, Nigeria. During the preliminary study, all measurements for 10 participants were taken by one of the researchers so as to assess intra-observer error. The next day, all measurements for the 10 participants were taken independently by two researchers and the measurements were assessed for inter-observer error. For this study, all measurements were taken for all the 200 participants by two researchers in duplicate so as to avoid observer bias and the mean values used. The subjects with any disease, deformity, injury, fracture, amputation or history of any surgical procedures of the feet were excluded from the study.

Methods

The technique used for measuring the parameters was according to the methods described by Phang *et al.* (2017) [12]. The hand measurements were taken in millimetre (mm) using a tape rule and Vernier Calipers of KTC (KYOTO TOOL) while foot measurements, weight and height were taken in millimetre (mm) using a Stadiometer (RGZ-160) and sliding calliper.

Hand Dimension Measurements

The hand measurements taken were hand length and breadth, arm length, forearm length, wrist width, individual phalange length of each finger for the right and left hands. Arm length was measured as a straight distance from the uppermost edge of the posterior border of the acromion process of the scapula, to mark the beginning of the shoulders using a tape rule,

to the tip of the middle finger. Using a tape rule, other arm measurements were taken e.g. the distances between shoulder to elbow, elbow to wrist and the wrist breadth (i.e. the circumference of the wrist). Hand length and breadth were measured as a straight distance from the midpoint of a line joining the styloid process of the radius and ulna bone of the forearm, to the tip of the middle finger, and as a straight distance from the most laterally set point on the head of the second metacarpal bone to the most medially set point on the head of the fifth metacarpal bone using a Vernier caliper respectively [13]. Phalange length of each finger was also measured, this is the straight distance from the metacarpophalangeal crease of each digit to the tip of the finger.
The hand and finger indices were calculated as:
To calculate IFL/RFL ratio, the index finger length was divided by ring finger length of the same hand.
Hand Index was analyzed and classified based on the standard range described by Martin and Saller (1957) [14] in which five range of hand indices were introduced.

$$\text{Hand index} = \frac{\text{Hand breadth}}{\text{Hand length}} \times 100$$

Five standard range of Hand indices described by Martin & Saller

Variations	Range
Hyperdolichocheir	X – 40.9
Dolichocheir	41.0 – 43.9
Mesocheir	44.0 – 46.9
Brachycheir	47.0 – 49.9
Hyperbrachycheir	50.0 – X

Foot Dimension Measurements

The foot measurements taken were the right foot left (RFL), right foot breadth (RFB), right ankle breadth (RAB), left foot length (LFL), left foot breadth (LFB) left ankle breadth (LAB). Foot length (FL) and breadth (FB) were measured as the direct maximum distance from the most posteriorly projecting point on the heel (pternion) to the anterior tip of whichever toe yields the longest measurement, and the distance from the medial margin of the head of the first metatarsal bone (metatarsal tibiale) to the lateral margin of the head of the fifth metatarsal bone (metatarsal fibulare) respectively. Ankle breadth (AB) was measured as the distance between the points that protrude most laterally. RFL/RFB, LFL/LFB ratios and foot index were estimated.

$$\text{Foot index} = \frac{\text{foot breadth}}{\text{foot length}} \times 100$$

Data Analysis

The data obtained was analysed statistically using IBM SPSS (SPSS; Statistical program for Social Sciences, Inc., Chicago, IL, USA) version 23.0 computer software. Mean, standard error of mean (SEM) for the parameters examined were calculated and *p*-value <0.05 was considered as significant. Average of mean foot index, RFL/RFB and LFL/LFB ratio of both sexes were used for sex determination of the subjects, which is termed as ‘‘sectioning point’’ [2]. A dividing line (cut-off point) for foot index between the two sexes will be based on sectioning point analysis.

$$\text{Sectioning point} = \frac{\text{mean male value} + \text{mean female value}}{2}$$

3. RESULTS

Measurements of the Hand and finger Dimensions

The descriptive statistics of hand and finger measurements in male and females are shown in table 1. The males showed higher

mean values in all the parameters measured compared to the females.

Table 1
Descriptive statistics for the hand and finger dimension measurements (mm) of the male and female subjects

Parameter (mm)	Males			Females		
	Minimum	Maximum	Mean±S.E	Minimum	Maximum	Mean±S.E
Right hand length	159	225	194.2±1.16	158	200	177.1±1.35
Right hand breadth	76	95	84.4±0.52	70	85	76.5±0.56
Left hand length	164	230	196.1±1.79	160	199	177.7±1.36
Left hand breadth	75	92	84.1±0.51	70	85	75.9±0.59
Right thumb	58	77	65±0.59	51	68	59±0.48
Right index finger	60	80	71.5±0.55	53	77	66.2±0.66
Right middle finger	70	92	81±0.64	65	84	74.8±0.65
Right ring finger	63	85	73.7±0.73	59	78	67.7±0.62
Right little finger	49	70	59.1±0.58	42	64	52.1±0.68
Left thumb	59	75	65.8±0.61	54	69	59.7±0.45
Left index finger	63	83	72.8±0.66	56	79	67±0.65
Left middle finger	69	93	81.7±0.67	65	86	75±0.67
Left ring finger	64	86	75.6±0.65	56	80	68.5±0.67
Left little finger	48	68	59.9±0.65	44	63	52.3±0.69
Right shoulder to middle finger	740	950	842.7±5.46	715	920	779.3±5.58
Right shoulder to elbow	380	465	422.1±2.61	340	450	392.6±3.27
Right elbow to wrist	265	355	301.7±2.27	245	320	277.2±27
Right wrist's width	150	185	169.1±1.14	140	185	159.3±1.43
Left shoulder to middle finger	750	940	837.5±5.41	720	912	775±5.38
Left shoulder to elbow	345	455	418.3±3.20	345	455	390.3±3.10
Left elbow to wrist	245	350	296.7±2.46	235	315	271.9±2.17
Left wrist's width	155	185	168.6±1.10	155	185	160.1±1.41

Measurements of the Foot Dimensions of the Male and female

The measurements of the foot dimensions of the male and females are shown in table 2. The stature of the males was high compared to the females, though the mean BMI value of the females was higher than the mean BMI values of the male. The males showed higher values in the foot parameters measured compared to the females

Table 2

Descriptive statistics of the age, height, weight, BMI and foot dimension measurements of the male and females

Parameters	Females			Males		
	Minimum	Maximum	Mean±SE	Minimum	Maximum	Mean±S.E
Age (years)	17	37	21.3±0.35	18	32	21.4±0.39
Height (mm)	1545	1840	1639.6±7.38	1590	1905	1752.9±7.97
Weight (kg)	45	130	66.1±2.10	50	87	68.2±19
BMI (kg/m^2)	17.7	38.4	24.45±0.66	17.7	31.1	22.2±0.36
Right Foot Length (mm)	230	300	268±0.27	250	335	293.7±2.32
Right Foot Breadth (mm)	84	104	93.8±0.79	87	114	101±0.88
Right Ankle Breadth (mm)	220	315	247.1±2.40	215	300	255.2±2.63
Left Foot length (mm)	175	310	265.4±3.10	250	330	292.6±2.25
Left Foot Breadth (mm)	80	105	93.2±0.78	86	119	101.1±0.89
Left Ankle Breadth (mm)	225	315	249.3±2.37	215	300	256.1±2. 46

Prediction of Sex using both of Hand and Foot Indices

Table 3 shows the individual variation and percentage in hand indices of the males and females based on standard range described by Martin and Saller (1957) [14]. The females showed more dolichocheir and mesocheir morphology compared to males though no female showed hyperbrachycheir morphology.

Table 3
The individual variation in hand indices of the males and females based on standard range described by Martin and Saller

Variation	Male		Female	
	Right hand Index	Left hand Index	Right hand Index	Left hand Index
Hyperdolichocheir	10 (10 %)	18 (18 %)	14 (14 %)	12 (12 %)
Dolichocheir	52 (52 %)	52 (52 %)	48(48 %)	62 (62 %)
Mesocheir	30 (30 %)	24 (24 %)	36 (36 %)	24 (24 %)
Brachycheir	4 (4 %)	6 (6 %)	2 (2 %)	2 (2 %)
Hyperbrachycheir	4 (4 %)	0 (0 %)	0 (0 %)	0 (0 %)

Prediction of sex using hand and foot dimensions and index

The sectioning points for RHI, LHI, RFI and LFI in both sexes are 43.33, 42.8, 34.7 and 34.84 respectively as shown in table 4. The cut-off points for hand indices, foot indices and LIFL/LRFL and RIFL/RRFL in both male and female subjects are 43.07, 34.77 and 0.97 respectively and they define sexual dimorphism among the subjects that participated in this study. The RFI, LFI, RIFL/RRFL ratio and LIFL/LRFL ratio values of the females are high compared to the males.

Table 4

Mean values of hand and foot indices for sex prediction in both male and female subjects

	RHI	LHI	RFI	LFI	RIFL/RRFL	LIFL/LRFL
Male	43.46	42.89	34.39	34.55	0.9699	0.9627
Female	43.2	42.71	35.00	35.12	0.9781	0.9769
Sectioning Point	43.33	42.8	34.7	34.84	0.974	0.9698
Cut Off Point	43.07		34.77		0.9719	

Key:
RHI=Right hand index **LHI=Left hand index**
RFI=Right foot index **RRFL=Right ring finger length** **LIFL=Left index finger length**
LFI=Left foot index **RIFL=Right index finger length** **LRFL= Left ring finger length**

Pearson correlation analyses for the male and female subjects using Foot, Hand, Finger and Hand dimension measurements

In both sexes, height and weight significantly correlated with right foot breadth, right ankle breadth, left foot length, left foot breadth and left ankle breadth ($p \leq 0.05$) as shown in table 5. However, there was no correlation between age and all foot parameters studied in both sexes.

Table 5

Correlation between age, height, weight, BMI and foot dimension measurements in both sexes

	Age (yrs)	Height (mm)	Weight (kg)	BMI (kg/m^2)	RFL (mm)	RFB (mm)	RAB (mm)	LFL (mm)	LFB (mm)	LAB (mm)
Age (yrs)	1	0.02	0.02	0.04	-0.01	-0.00	-0.06	0.04	0.04	0.07
Height (mm)	0.02	1	0.34**	-0.19	0.16	0.56**	0.43**	0.65**	0.63**	0.41**
Weight (kg)	0.02	0.34**	1	0.85**	0.15	0.45**	0.59**	0.44**	0.41**	0.65**
BMI (kg/m^2)	0.04	-0.19	0.85**	1	0.07	0.19	0.37**	0.11	0.09	0.45**
RFL (mm)	-0.01	0.16	0.15	0.07	1	0.27**	0.19	0.3**	0.26**	0.17
RFB (mm)	-0.00	0.56**	0.47**	0.19	0.27**	1	0.65**	0.56**	0.89**	0.63**
RAB (mm)	-0.06	0.43**	0.59**	0.37**	0.19	0.65**	1	0.48**	0.57**	0.92**
LFL (mm)	0.04	0.65**	0.44**	0.11	0.3**	0.56**	0.48**	1	0.6**	0.45**
LFB (mm)	0.04	0.63**	0.41**	0.09	0.26**	0.89**	0.57**	0.6**	1	0.57**
LAB (mm)	0.07	0.41**	0.65**	0.45**	0.17	0.63**	0.92**	0.45**	0.57**	1

*. Correlation is significant at the 0.05 level (2-tailed).

**. Correlation is significant at the 0.01 level (2-tailed).

Key:
LFL = Left Foot length
BMI=Body Mass Index
RFL = Right Foot Length
RFB = Right Foot Breadth
RAB = Right Ankle Breadth
LFB = Left Foot Breadth
LAB = Left Ankle Breadth

In both sexes, height and weight significantly correlated with right hand length, right hand breadth, left hand length and left hand breadth ($p \leq 0.05$) as shown in table 6. However, there was no correlation between age and all hand parameters studied in both sexes.

Table 6
Correlation between age, height, weight and hand dimension measurements in both sexes

	Age (yrs)	Height (mm)	Weight (kg)	BMI (kg/m^2)	Right Hand Length(mm)	Right Hand Breadth(mm)	Left Hand Length(mm)	Left Hand Breadth(mm)
Age(yrs)	1	0.02	0.02	0.08	-0.03	0.1	-0.04	0.15
Height (mm)	0.02	1	0.34**	-0.13	0.8**	0.76**	0.81**	0.74**
Weight (kg)	0.02	0.34**	1	0.69**	0.39**	0.42**	0.38**	0.45**
BMI(kg/m^2)	0.08	-0.13	0.69**	1	0.04	0.01	-0.00	0.05
Right Hand Length (mm)	-0.03	0.8**	0.39**	0.03	1	0.77**	0.96**	0.78**

Right Hand Breadth(mm)	0.1	0.76**	0.42**	0.01	0.77**	1	0.77**	0.94**
Left Hand Length (mm)	-0.04	0.81**	0.38**	-0.00	0.96**	0.77**	1	0.78**
Left Hand Breadth(mm)	0.15	0.74**	0.45**	0.05	0.78**	0.94**	0.78**	1

*. Correlation is significant at the 0.05 level (2-tailed). **. Correlation is significant at the 0.01 level (2-tailed).

In both sexes, height and weight significantly correlated with right index finger, right middle finger, right ring finger, right little finger, left thumb, left index finger, left middle finger, left ring finger and left little finger ($p \leq 0.05$) as shown in table 7. However, there was no correlation between age and all finger parameters studied in both sexes.

Table 7:
Correlation between age, height, weight and finger dimension measurements in both sexes

	Age (yrs)	Height (mm)	Weight (mm)	BMI (kg/m^2)	RT (mm)	RI (mm)	RM (mm)	RR (mm)	RL (mm)	LT (mm)	LI (mm)	LM (mm)	LR (mm)	LL (mm)
Age (yrs)	1	0.02	0.02	0.08	0.03	-0.04	-0.09	-0.11	-0.06	-0.02	-0.01	-0.07	-0.06	0.01
Height (mm)	0.03	1	0.34**	-0.13	0.73**	0.68**	0.75**	0.73**	0.72**	0.67**	0.72**	0.75**	0.77**	0.71**
Weight (kg)	0.02	0.34**	1	0.69**	0.29**	0.49**	0.45**	0.4**	0.38**	0.23*	0.44**	0.38**	0.43**	0.37**
BMI (kg/m^2)	0.08	0.13	0.69**	1	-0.12	0.08	0.02	-0.03	-0.04	-0.13	0.05	-0.02	0.01	-0.02
RT (mm)	0.03	0.73**	0.29**	-0.12	1	0.72**	0.7**	0.72**	0.74**	0.82**	0.75**	0.74**	0.76**	0.75**
RI (mm)	-0.04	0.68**	0.49**	0.08	0.72**	1	0.92**	0.85**	0.79**	0.64**	0.93**	0.89**	0.88**	0.81**
RM (mm)	-0.09	0.75**	0.45**	0.02	0.7**	0.92**	1	0.91**	0.79**	0.64**	0.88**	0.89**	0.88**	0.8**
RR (mm)	-0.11	0.73**	0.4**	-0.03	0.72**	0.85**	0.91**	1	0.81**	0.65**	0.86**	0.91**	0.92**	0.81**
RL (mm)	-0.06	0.72**	0.38**	-0.04	0.74**	0.79**	0.79**	0.81**	1	0.71**	0.79**	0.81**	0.83**	0.91**
LT (mm)	-0.02	0.67**	0.23*	-0.13	0.82**	0.64**	0.64**	0.65**	0.71**	1	0.74**	0.68**	0.68**	0.7**
LI (mm)	-0.01	0.72**	0.44**	0.05	0.76**	0.93**	0.88**	0.86**	0.79**	0.74**	1	0.9**	0.89**	0.81**
LM (mm)	-0.07	0.75**	0.38**	-0.02	0.74**	0.89**	0.89**	0.91**	0.81**	0.68**	0.9**	1	0.93**	0.84**

LR (mm)	-0.06	0.77**	0.43**	0.01	0.76**	0.88**	0.88**	0.92**	0.83**	0.68**	0.89**	0.93**	1	0.87**
LL (mm)	0.01	0.71**	0.37**	-0.02	0.75**	0.81**	0.8**	0.81**	0.91**	0.7**	0.81**	0.84**	0.87**	1

*. Correlation is significant at the 0.05 level (2-tailed). **. Correlation is significant at the 0.01 level (2-tailed).

Key:
Right Thumb = RT
Right Index = RI
Right Middle = RM
Right Ring = RR
Right Little = RL
Left Thumb = LT
Left Index = LI
Left Middle = LM
Left Ring = LR
Left Little = LL

In both sexes, height and weight significantly correlated with right shoulder to finger length, right shoulder to elbow length, right elbow to wrist length, right wrist width, left shoulder to finger length, left shoulder to elbow length, left elbow to wrist length and left wrist width ($p \leq 0.05$) as shown in table 8. There was no correlation between age and all finger parameters studied in both sexes.

Table 8:
Correlation between age, height, weight and hand dimension measurements in both sexes

	Age (yrs)	Height (mm)	Weight (kg)	BMI (kg/m^2)	RSF (mm)	RSE (mm)	REW (mm)	RWW (mm)	LSF (mm)	LSE (mm)	LEW (mm)	LWW (mm)
Age (yrs)	1	0.02	0.02	0.08	0.02	0-.09	0.09	0.1	0.02	0-.02	0.09	0.18
Height (mm)	0.02	1	0.34**	-0.13	0.84**	0.72**	0.79**	0.57**	0.83**	0.72**	0.74**	0.54**
Weight (kg)	0.02	0.34**	1	0.69**	0.44**	0.34**	0.41**	0.69**	0.43**	0.37**	0.39**	0.67**
BMI (kg/m^2)	0.08	-0.13	0.69**	1	-0.00	-0.04	-0.01	0.31**	0.01	.008	-0.03	0.31**
RSF (mm)	0.02	0.84**	0.44**	-0.00	1	0.84**	0.82**	0.64**	0.98**	0.84**	0.79**	0.63**
RSE (mm)	-0.09	0.72**	0.34**	-0.04	0.84**	1	0.67**	0.49**	0.83**	0.86**	0.62**	0.48**
REW (mm)	0.09	0.79**	0.41**	-0.01	0.82**	0.67**	1	0.61**	0.82**	0.65**	0.88**	0.58**
RWW (mm)	0.1	0.57**	0.69**	0.31**	0.64**	0.49**	0.61**	1	0.62**	0.52**	0.58**	0.92**
LSF (mm)	0.02	0.83**	0.43**	0.01	0.97**	0.83**	0.82**	0.62**	1	0.89**	0.8**	0.62**
LSE (mm)	-.015	0.72**	0.37**	0.01	0.84**	0.86**	0.65**	0.52**	0.88**	1	0.64**	0.5**
LEW (mm)	0.09	0.74**	0.39**	-0.03	0.79**	0.62**	0.88**	0.58**	0..8**	0.64**	1	0.56**
LWW (mm)	0.18	0.54**	0.66**	0.31**	0.63**	0.48**	0.58**	0.92**	0.62**	0.5**	0.56**	1

*. Correlation is significant at the 0.05 level (2-tailed). **. Correlation is significant at the 0.01 level (2-tailed).

Key:
RSF = Right Shoulder to Finger
RSE = Right Shoulder to Elbow
REW = Right Elbow to Wrist
RWW = Right Wrist Width
LSF = Left Shoulder to Finger
LSE = Left Shoulder to Elbow
LEW= Left Elbow to Wrist
LWW = Left Wrist Width

4. DISCUSSION

The identification of a human using skeletal remnants and or dismembered body parts is one of the most important tasks to be achieved by the forensic scientists especially when information vis-à-vis the deceased is unavailable. Sex determination becomes the first priority in the process of identification of a person by a forensic investigator in the case of mishaps, chemical and nuclear bomb explosions, natural disasters, crime investigations, and ethnic studies [15]. Consequently, this study was carried out to ascertain if hand, finger, foot dimensions and their indices can be used to determine sexual dimorphism using some undergraduate students from Faculty of Science, University of Lagos Nigeria.

The results of this study show that the mean value of hand and finger measurements in all the parameters investigated was higher in males compared to females. This is in accordance with the findings in earlier studies whereby female hand dimensions were consistently smaller compared to the male in different human populations [4-6, 8, 16]. This suggests that there is morphological gender difference in the length of the hands and fingers. A key point is that these measurements should be done separately in each population, because the racial and ethnic differences are effective on these measures and reduce the possibility of generalizing [17]. The hand length and breadth observed within the sampled population was found to be greater than that reported by Rastogi *et al* (2008) [18] in a population from North and South India, also in a population from Mauritius and in a population from Upper Egypt [19] and these differences can be explained by racial and population variations.

The right and left index and ring finger ratio (RIFL/RRFL and LIFL/LRFL ratio) was found to be higher in females (0.9781 and 0.9769) compared to males (0.9699 and 0.9627). This is in accordance with the studies by different researchers whereby the index and ring finger ratio in females is higher compared to the males [5, 20]. In this study, index and ring finger ratio $\leqslant$0.9699 for the right hand and $\leqslant$0.9627 for the left hand are suggestive of male while index and ring finger ratio <0.9781 for the right hand and <0.9759 for the left hand is suggestive of female. In a study to determine sex from hand and index/ring finger length ratio in North Saudi population, the index and ring finger ratio $\leqslant$0.920 for the right hand and $\leqslant$0.913 for the left hand is suggestive of male while Index and ring finger ratio <0.920 for the right hand and <0.913 for the left hand is suggestive of female [5]. In an Egyptian population, the index and ring finger ratio $\leqslant$0.976 is suggestive of males, and ratio >0.976 is suggestive of females [19].
In this study, a hand index $\leqslant$43.07 is suggestive of females and is suggestive of males when it is >43.07, while in an Egyptian population some researchers reported that hand index $\leqslant$40.55 is suggestive of females and >40.55 is suggestive of males [19]. However, the average hand index in this study is smaller than that recorded in a Mauritius population [21]. The cut-off points estimated for hand index in this study was found to be ≤43.33 for the right hand and ≤42.80 for the left hand as indicative of a female, while a cut-off point greater than (>) 43.33 for the right hand and greater than (>) 42.80 for the left hand was indicative of a male. This hand index cut-off point is greater than that reported by Rastogi *et al* (2008) [18].

From this study, there are comparatively larger variations in the ring finger length between male and female than in the index finger lengths. These results are in agreement with previous studies using Upper Egyptians and North Saudi population [5, 19] In this current study, the female subjects were reported to have a significantly higher IFL/RFL ratio than the male in both hands. These findings are consistent with the work of McFadden *et al* (2002) [22] where higher digit ratios are

usually an indication of 'femininity' and lower digit ratios indicative of 'masculinity', thus making the IFL/RFL ratios a potentially beneficial parameter for the determination of sex. The cut-off point for the IFL/RFL ratio obtained for sex differentiation in this research were 0.9757 and 0.9702 for the right and left hand respectively. This means that for the right and left hand, ≥0.9757 and ≥0.9702 respectively are predictive of the female sex while lower values predict male. This data is similar to that found in the study of the Upper Egyptian population in which the cut-off point derived for sex differentiation was 0.976 [19] and in the South Indian adult and adolescent population the cut-off point was (0.970) [23]. The IFL/RFL ratio is a statistically significant marker for sex determination in this study and this is in accordance with the works of Kanchan *et al* (2008) [23]. However, Voracek *et al* (2009) [24], performed a comparative analysis and concluded that the IFL/RFL ratio is of modest benefit for the determination of sex, restricting its use in forensic lawsuits. This contrariety may be attributed to the remarkable influence of ethnic and population variability on this ratio, due to the dimensional diversity of the human body, anthropometric measurements of an individual are not constantly credible tools for the determination of sex but still remains assertive for the prediction of sexual dimorphism.

Morphology and morphometry of human feet is greatly affected by the combined effects of heredity and living style of man and that determines the size and shape of the feet or footprints and makes them unique parameter to establish human identity [25, 26]. The study also revealed that sexual dimorphism in the foot length and breadth was larger in the male subjects than in the female subjects. This finding agrees with the reports in some earlier studies [6, 21, 27]. Studies showed that there was a consistent difference in the range of foot index between male and female subjects across ages 18 – 22 and above [28, 29]. This study revealed the foot index of 34.77 cm as the cutoff point therefore a foot index ⩽34.77 is suggestive of males and is suggestive of females when it is >34.77. this showed a similar pattern compared to Agnihotri *et al* 2006 [28] that concluded that a foot index >37 is suggestive of female and ≤37 is that of male. The foot indices in this study showed a dissimilar pattern compared to, the study on randomly selected students of the Ahmadu Bello University, Zaria, Nigeria whereby they stated that foot indices >38 will certainly denote a male Nigerian [30], a study at IDST College, Modinagar, Uttar Pradesh, India whereby all the cases with cutoff point index of ≤37.60 were suggestive of females and ≥37.60 were indicative of males for both the feet [20], and on students from Sri Siddhartha university, Tumkur, Karnataka that states that the average foot index in males and females were 44.91 and 42.63 respectively [27]. The relationship between foot dimensions for the same sex is strongly significant. The correlation values of the foot dimensions between same sex and differences in the male and the female subjects showed that foot is a good determining factor for sex determination. This study revealed that there was a clear difference in the measurement of the foot dimensions of both the male and female subjects, and thus suggests that male's foot dimensions are generally larger than that of the female subjects. This finding is in agreement with reports of Montrakis *et al* (2010) [9].

5. CONCLUSION

The determination of sex in a medical and/or legal examination of a severed hand and foot can be accurately and practically achieved by simply obtaining anthropometric measurements of the hand, fingers and foot. This study showed that hand (length, breadth, wrist width, elbow to wrist length, shoulder to finger length and

shoulder to elbow length), finger (index, middle, ring and little) and foot (breath and ankle breadth) measurements yielded important predictive information about human sexual dimorphism. Foot indices, hand indices and index finger length and ring finger length ratios are good predictors of sex.

Further researches using larger sample sizes and various populations across Nigeria are essential to validate the use of hand, finger and foot indices in the identification of sex for forensic investigations.

REFERENCES

[1] O. O. Iroanya, T. F. Egwuatu, A. O. Sonaike, and N. D. Uwaezuoke, "Sex estimation using foot measurements, stature and body mass index (BMI) in a Nigerian population", Acta Scientifica Naturalis, 5, 2, 32 - 37, 2018. DOI: 10.2478/asn-2018-0018.

[2] K. Burns, "*Forensic anthropology training manual",* Upper Saddle River Publisher, New Jersey, United State of America, 45-53, 2007.

[3] N. Jeyaseelan, P. Ravindran, U. Pitadeniya, V. Baskaran, S. Mostofa, and S. Putraperaman, "Estimation of hand index and sex variations among the University students of Malaysia –an Anthropometric study", *IOSR Journal of Human Social Science*. 21(1). 17-23, 2016.

[4] M. K. Bindurani, A. N. Kavyashree, and L. P. Subhash, "Sexual dimorphism on metric valuation of hand dimensions", International Journal of Anatomy and Research, 4, 2, 2212 – 2215, 2016. DOI: http://dx.doi.org/10.16965/ijar.2016.180

[5] M. A. B. Ibrahim, A. M. Khalifa, A. M. Hagras, and N. I. Alwakid, "Sex determination from hand dimensions and index/ring finger length ratio in North Saudi population: Medico-legal view", Egyptian Journal of Forensic Sciences, 6, 4, 435-444, 2016, https://doi.org/10.1016/j.ejfs.2016.11.002

[6] P. Agarwal, A. Singh, and R. Gupta, "Estimation of human stature by measurements of foot", National Journal of Integrated Research in Medicine,9, 5, 38-43, 2018

[7] R. A. Lippa, "Are 2D:4D Finger-Length Ratios Related to Sexual Orientation? Yes for Men, No for Women", Journal of Personality and Social Psychology, 85, 1, 179–188, 2003, DOI: 10.1037/0022-3514.85.1.179.

[8] T. Kanchan, K. Krishan, A. Sharma, and R. G. Menezes, "A study of correlation of hand & foot dimensions for personal identification in mass disasters" Forensic Science International, 199,1-3,112, e1-6, 2010. doi: 10.1016/j.forsciint.2010.03.002

[9] C. Mountrakis, C. Eliopoulos, C. G. Koilias, and S. K. Manolis, "Sex determination using metatarsal osteometrics from the Athens collection" Forensic Science International, 200, 1, 178-184, 2010.

[10] S.R. Habib, and N.N. Kamal, "Stature estimation from hand and phalanges lengths of Egyptians" Journal of Forensic Legal Medicine, 17, 3, 156–60, 2010.

[11] M. Akhlaghi, B. Moradi, and M. Hajibeygi, "Sex determination using anthropometric dimensions of the clavicle in Iranian population" Journal of Forensic and Legal Medicine, 19, 7, 381-385, 2012, doi.org/10.1016/j.jflm.2012.02.016

[12] S. F. Phang, A. I. Normaizatul, and P. S. Lai, "Stature and sex estimation using foot measurements" Journal of Forensic Science & Criminology, 5, 1, 105-110, 2017.

[13] I. P. Singh, and M. K. Bhasin, "A Manual of Biological Anthropology" New Delhi: Kamla Raj Enterprises, 2004.

[14] R. Martin, and K. Saller, "Lehrbuch der Anthropologie", Dritte Auflage, Stuttgart, Gustav Fischer Verlag, II, 1957.

[15] S. P. Nagare, R. S. Chaudhari, R. S. Birangane, and P. C. Parkarwar, "Sex determination in forensic identification, a review" Journal of Forensic Dental Sciences, 10, 2, 61–66, 2018. doi: 10.4103/jfo.jfds_55_17

[16] S. Dey, and A. K. Kapoor, "Sex determination from hand dimensions for forensic identification" International Journal of Research in Medical Sciences, 3, 6, 1466-1472, 2015

[17] A. Memarian, S. Soltani, and K. Aghakani, "Estimation of Body Height by Measuring Foot Dimensions: A Survey on Iranian Adult People" Journal of Medical Toxicology and Clinical Forensic Medicine, 3, 1-16, 2017

[18] P. Rastogi, K. R. Nagesh, and K. Yoganarasimha, "Estimation of stature from hand dimensions of north and south Indians" Legal Medicine, 10, 4, 185–189, 2008.

[19] K. E. Aboul-Hagag, S. A. Mohamed, M. A. Hilal, and E. A. Mohamed, "Determination of sex from hand dimensions and index/ring finger length ratio in Upper Egyptians", Egypt Journal of Forensic Science, 1, 2, 80–86, 2011.

[20] S. Gupta, V. Gupta, N. Tyagi, Ettishree, S. Bhagat, M. Dadu, N. Anthwal, and T. Ashraf. "Index/Ring Finger Ratio, Hand and Foot Index: Gender Estimation Tools", Journal of Clinical and Diagnostic Research, 11, 6, ZC73-ZC77, 2017 doi: 10.7860/JCDR/2017/25807.10084

[21] A. K. Agnihotri, B. Purwar, N. Jeebun, and S. Agnihotri, "Determination of sex by hand dimensions", International Journal of Forensic Science, 1, 2, 12–24, 2006.

[22] D. McFadden, E. Shubel, "Relative lengths of fingers and toes in human males and females", Hormonal Behaviors, 42, 4, 492–500, 2002.

[23] T. Kanchan, R. G. Menezes, R. Moudgil, R. Kaur, M. S. Kotian, and R. K. Garg, "Stature estimation from foot dimensions", Forensic Science International, 179, 241, e1-e5, 2008.

[24] M. Voracek, and L. M. Loibl, "Scientometric analysis and bibliography of digit ratio (2D: 4D) research, 1998–2008 1, 2", Psychological Report, 104, 3, 922–956, 2009.

[25] V. V. Pillay, "Textbook of Forensic Medicine and Toxicology", Paras Publishing, Hyderabad, India, 2004.

[26] T. A. Philip, "Formulae for establishing stature from foot size by regression method", Journal of Indian Academy of Forensic Medicine, 12, 57-62, 1990.

[27] M. K. Bindurani, A. N. Kavyashree, K. R. Asha, and L. Subhash, "Determination of sex from foot dimensions", International Journal of Anatomy and Research, 5, 4.3, 4702-4706, 2017. DOI: https://dx.doi.org/10.16965/ijar.2017.450

[28] A. K. Agnihotri, S. Shukla, and B. Purwar, "Determination of sex from the foot measurements", International Journal of Forensic Science, 2, 1, 1-4, 2007.

[29] A. K. Tyagi, M. Rani, and A. Kohli, "Sexing by foot index (2000 – 2001)", Forensic Medical Toxicology, 21, 10-11, 2004.

[30] B. Danborno, and A. Elukpo, "Sexual dimorphism in hand and foot length, indices, stature-ratio and relationship to height in Nigerians", International Journal of Forensic Science, 3, 1, 379–383, 2008.

Sakarya University Journal of Science

ISSN 1301-4048 | e-ISSN 2147-835X | Period Bimonthly | Founded: 1997 | Publisher Sakarya University | http://www.saujs.sakarya.edu.tr/en/

Title: Optimization of Axial Misalignment due to Glass Drilling by Statistical Methods

Authors: Faruk HARMANCI, Sabri ÖZTÜRK
Recieved: 2019-11-13 10:00:41

Accepted: 2020-01-16 09:52:13

Article Type: Research Article
Volume: 24
Issue: 3
Month: June
Year: 2020
Pages: 446-454

How to cite
Faruk HARMANCI, Sabri ÖZTÜRK; (2020), Optimization of Axial Misalignment due to Glass Drilling by Statistical Methods. Sakarya University Journal of Science, 24(3), 446-454, DOI: https://doi.org/10.16984/saufenbilder.646183
Access link
http://www.saujs.sakarya.edu.tr/en/issue/52472/646183

Sakarya University Journal of Science 24(3), 446-454, 2020

Optimization of Axial Misalignment due to Glass Drilling by Statistical Methods

Faruk HARMANCI[1] , Sabri ÖZTÜRK[*2]

Abstract

Flat glass has a significant utilization in the domestic appliances sector. Drilling of glass is frequently used in the white goods sector. In this research, the glass drilling method is explained in detail, the determined axial misalignment values using the tool rotation speed and the feed rate were investigated. The drilling operation with its parameters must be optimized precisely, in order to have good control over the productivity, quality, and cost aspect of the application. Using the Ø18.3 mm drill tool, drilling process was performed with different rotation speeds (rpm) and feed rates (mm/sec). The impressions of drilling parameter on output variable were investigated using Analysis of Variance (ANOVA). Probabilistic uncertainty analysis based on Monte Carlo simulation was carried out. According to the results, the suggested model and optimization method could be used for estimating axial misalignment and this investigation is reliable and proper for figuring out the problems met in machining operations. Furthermore, Monte Carlo simulations were obtained quite effective for identification of the uncertainties in axial misalignment that could not be possible to be caught by deterministic ways. The optimum axial misalignment value was found to be 0.11823 mm.

Keywords: Flat Glass, Drilling, Axial Misalignment, Analysis of Variance (ANOVA), Monte Carlo Simulation

[1] Bolu Abant İzzet Baysal University, harmancifaruk@gmail.com, ORCID ID: 0000-0002-2892-7436
[*] Corresponding Author
[2] Bolu Abant İzzet Baysal University, sabriozturk@ibu.edu.tr, ORCID ID: 0000-0002-1377-9338

1. INTRODUCTION

The glass material is known as one of the amorphous materials that are cooled down from the molten state without showing crystallization. The glass is resistant to chemical interactions, easy to recycle, no chemical leakage as in plastic materials and can also withstand extreme cold and temperature [2].

Glass is a kind of inorganic brittle structure. It has many excellent properties such as hardness, transparency, good temperature stability, homogeneity and corrosion resistance. Such features are widely used in the glass optics industry, the semiconductor industry, the military industry, and many similar places. Glass material plays an important role in the biomedical industry [3].

Glass, first softens and then becomes fluent. If sufficient heat is applied, the glass material flows like water. Glass material is defined as a mine. However, there is a significant change when compared to other mines. This change is not the melting point, the softening point. Glass is a mixture formed with together of silicon dioxide (SiO2) and mineral oxides. It is an interesting condition in the structure of the atom, which feature gains real meaning to glass.

Because of these interesting features of glass material, neither exactly is a liquid nor is it like a true solid with a crystal structure. It has an important place between these two situations. The arrangement of atoms in the glass material is random as in a liquid material. As a result, glass is not affected by gravity due to these reasons and it has the feature of protecting the shape [4].

According to myths, the people's comments about the glass are related to the fact that a Phoenician sailor flows from the sands under a pot where he cooks on the beach for dinner. This showed us the source of the glass. However, according to archaeological evidence, the construction of the first glass was made in Eastern Mesopotamia and Egypt [5-6].

In next to the production of glass materials, the processing of glass has an important place. It is a material with a crystal-free (amorphous) structure and exhibiting glass transition when heated from a liquid state, covering each solid [1].

According to the information we have investigated, the basic processes applied to the glass material are as follows; glass material production, cutting process, edge processing, grinding process, hole drilling, printing process, annealing and tempering processes.

First of all for glass drilling process, the glass should be drill to certain dimensions. Previous research, shear strength, tooling features and by working on processing temperatures has investigated that costs can be reduced. Most features must be taken into account when glass cutting process was applied [7].

The adequate selection of cutting tool affects the success of drilling process. Obviously the effective of the machining operation depends on the features of drilling tools, obtained the quality of workpiece layer surface in interaction with the operation conditions and workpiece materials. Glass drilling is carried out with two drills of the same diameter. Hole drilling process is done with drills in the upper and lower section. When we look at the machining, the surfaces processed using the manufacturing processes are affected by the cutting parameters. Incorrectly selected machining parameters result in rapid wear and break of the cutting tools. Therefore, it causes economic losses due to the deterioration of work piece and surface quality [8].

In recent years, the use of soda-lime glass, which is an organic material in many engineering fields, is superior in comparison to other materials with hardness, low density, low heat and electrical conductivity [9-12].

Cutting parameters are very important in drilling operations. During the drilling operations, many undesirable situations were occurred such as excessive surface roughness, axial misalignment, burr formation, tool wear and circularity.

Many analysis methods have been used for the optimization of the parameters used for glass

machining and for the design of the experiment. Also, the experimental design of Taguchi method is used for planning of experiments [13-17].

For drilling of glass, drill performance needs to be critically evaluated in their economic and commercial impact. In this case, tests are conducted in order to analyze the axial misalignment due to glass drilling under different cutting speed and feed rates.

First, ANOVA is used for data analysis to determine the degree of importance of the drilling factors. Then, the axial misalignment as a response variable of the drilling operation is measured and correlated with different drilling parameters. Mathematical models based on multi non-linear regression analysis have been described and the stochastic prediction of axial misalignment of drilling with probabilistic uncertainty analysis has been determined by the Monte Carlo simulation.

Therefore, it is ensured that efficiency and sensitivity are increased by a good determination of the optimum cutting parameters [18]. A vertical type Coordinate Measuring Machine (CMM) was used to determine the axial misalignment during drilling.

2. MATERIAL and METHODS

Drilling process is employed with glass drilling tolls. The drills are composed of two parts, the metal body and the diamond-binder mixture in the cutter. As a comparison between different types of diamonds, hardness and abrasion resistance is one of the most important features of diamond. In the literature, diamond hardness measurement was reported [19].

The diamonds used in the cutting tools are coated with nickel or titanium in order to better cut them and to keep the diamond grains of the binders well. The coating extends the life of a material and provides strength. Soft binders are used in drills. The binder and abrasive parts of the drilling tools are approximately 8 to 10 mm in length.

As an experiment sample, bronze reflective glass was used in Figure 1. Different input variables were chosen throughout the experiments. Moreover, each drilling test was repeated three times to abstain experimental errors.

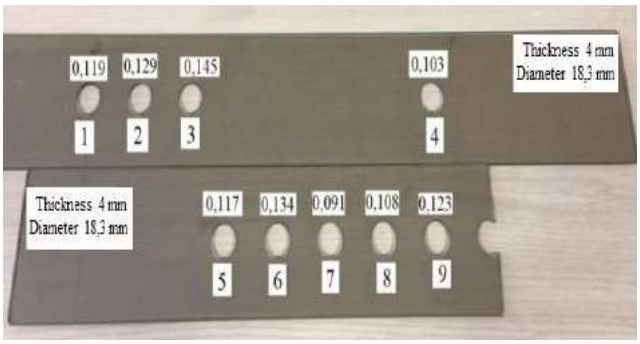

Figure 1. Test samples

As shown in Figure 2, axial misalignment resulting from the hole drilling was measured by CMM (Coordinate Measuring Machine). Vertical type CMM device is used. The measurement is realized at the end of the machine probe tip. The device moves in X, Y and Z axes. To tell you where to use the CMM devices; it is used to check whether the parts to be measured are within the geometric tolerances.

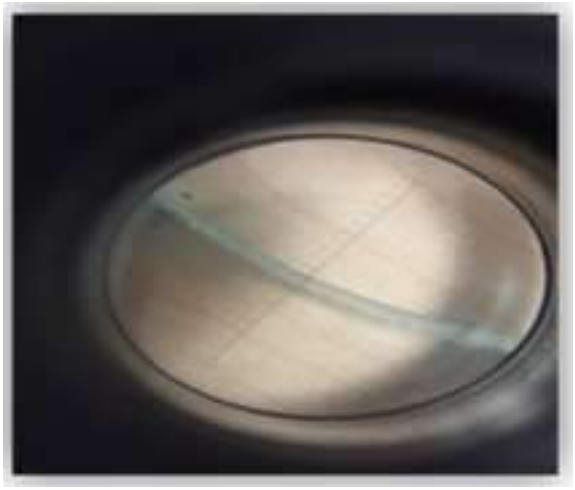

Figure 2. Measuring axial misalignment

Coordinate Measuring Machines (CMM) are reliable tools in validation rooms or laboratories. It is based on more data processing capabilities including the ability to measure complex parts, change the geometry with its powerful service point, coordinate subtraction and the ability to adjust point coordinates [20].

The controlled ambient temperature is 20±2 °C. It is a basic parameter that the machine performs a methodologically accurate measurement at such a stable ambient temperature. For this reason, temperature compensated CMM's have been developed in recent years [21].

How the data obtained by variance analysis (ANOVA) interact in themselves and to investigate the effects of emerging interactions on dependent variables. It is used to determine the variability between the groups to be compared with this analysis method [22].

Another method of analysis is the regression analysis method, which enables us to analyze the functional relations between dependent and independent variables by mathematical modeling with systematically and comprehensively [23].

An uncertainty analysis has to be applied to define the unexpressed part of the suggested MNLR model. One of the main novel part of the current investigation was achieved as probabilistic uncertainty analysis based on the Monte Carlo simulation.

Monte Carlo method is a numerical method that can solve math problems by using random samples. This method is very useful in real solutions. It is a method based on probability theory [24].

Monte Carlo technique is known as a technique, which aims to achieve the result by selecting randomly from a plurality of probability distributions in an experiment or a simulation study [25, 26].

3. EXPERIMENTAL RESULTS

Statistical analysis and optimization were employed by obtaining the experimental data in the current study. Table 1 shows the revolutions, feed rate and axial misalignment values used in the experiments. The sample glass thickness is 4 mm.

Firstly, it is examined how the independent variables have an interaction with variance analysis. Variance analysis method is preferred when the number of independent variables is high. To predict the axial misalignment of the drilling application, an MNLR model achieved with the high coefficient number of adjusted and predicted regression.

Table 1. Experimental design and results

Drill Diameter = Ø 18.3 mm		
Rotation Speed (rpm)	**Feed Rate (mm/sec)**	**Axial Misalignment (mm)**
3200	2.5	0.119
3200	2.75	0.129
3200	3	0.145
3450	2.5	0.103
3450	2.75	0.117
3450	3	0.134
3700	2.5	0.091
3700	2.75	0.108
3700	3	0.123

Another important outcome is also unexpressed part of the variability in response variable could not be described by suggested best-fit MNLR model. Thereby, an uncertainty analysis has to be applied to explain the unexplained part of the suggested MNLR model. One of the main new breakthroughs of this research is the probability uncertainty analysis based on the Monte Carlo simulation has been successfully achieved.

Table 2. Variance analysis for Ø18.3 mm drill tool

	Coefficient		**Standard**	**95% CI**	**95% CI**	
Factor	Estimate	df	Error	Low	High	VIF
Intercept	0.12	1	6.003E-004	0.11	0.12	
A-Rotation Speed	-0.012					1.00
B-Feed Rate	0.015					1.00

AB	1.500E-003	1.00
A^2	1.672E-003	1.17
B^2	1.672E-003	1.17

Table 2 shows variability of the tool rotation speed and the feed rate. Although, these statistical coefficients characterized the strong part of the suggested MNLR model was found significant, they were not adequate to describe the obtained MNLR model completely. Therefore, some extra statistical coefficients should be calculated for the further identification of the obtained MNLR model.

Variation inflation number (VIF) can be identified as fundamental points that indicated the multicollinearity, in order to meet the criteria that underlie the assumption in the design of the MNLR model. VIF factor should be between from 0 to 10.

As it can be showed in Table 2, VIF value was calculated lower than 10.

All parametrical data in the distribution of variance are calculated by dividing the results by the arithmetic mean and the result is divided by the number of data. When we take the square of the standard deviation, it gives us the variance.

$$\text{Axial misalignment mathematical model} = 0.86507 - 2.97968E - 004\,x\,A - 0.17064\,xB + 2.40000E - 005\,x\,A\,x\,B + 2.67586E - 008\,x\,A^2 + 0.026759\,x\,B^2 \quad (1)$$

Using the data obtained from the experiments was used in the mathematical model. This model is the equation of the curve obtained from the graph in Figure 6.

Table 3. Quadratic model ANOVA analysis of response surface for Ø18.3 mm drill tools

	Sum of		**Mean**	**F**	**P-value**	
Source	Square	df	Square	Value	Prob > F	
Model	2.194E-003	5	4.389E-004	209.95	< 0.0001	significant
A-Tool Rotation Speed	8.402E-004	1	8.402E-004	401.93	< 0.0001	
B-Progress Amount	1.320E-003	1	1.320E-003	631.56	< 0.0001	
AB	9.000E-006	1	9.000E-006	4.31	0.0767	
A^2	7.725E-006	1	7.725E-006	3.70	0.0960	
B^2	7.725E-006	1	7.725E-006	3.70	0.0960	
Residual	1.463E-005	7	2.090E-006			
Lack of Fit	7.832E-006	3	2.611E-006	1.54	0.3354	Not significant
Pure Error	6.800E,006	4	1.700E-006			
Cor. Total	2.209E-003	12				

Since F value is 209.95, it expresses the importance of the model (Table 3). We create our model according to the experimental data obtained. The terms A and B, where probabilistic values (p) are less than 0.05, are important for the model. It is desirable that the lack of fit is high. In the analysis, the low mismatch value of 1.54 indicates that the model cannot be used for a study conducted in this way.

Table 4. Analysis values for Ø18.3 mm drill tools

Standart Deviation	1.446E-003	R-Square	0.9934
Mean	0.12	Adj R-Squared	0.9886
C.V.%	1.23	Pred R-Squared	0.9612
PRESS	8.575E-00E	Adeq Precision	54.299
-2 Log Likelihood	-141.17	BIC	-125.78
		AICc	-115.17

The mean value of the axial misalignment was found 0.12 mm. The percentage value of R squared variation may be valid by 0.9934 (Table 4). The R squared value assumes that each argument in the model describes the dependent variables.

The estimated R squared value was found 0.9612. It is seen that there is a difference of 4% compared to the actual values. That is, it shows the difference between the data obtained from the experiments and the data obtained from our model.

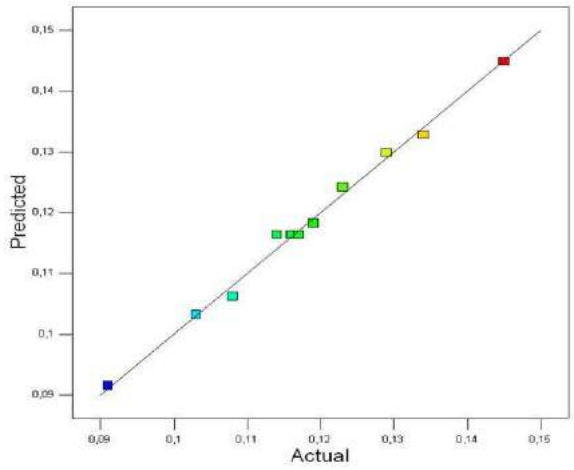

Figure 3. Plot of predicted versus actual results

The data obtained from the experiments and the data obtained from the mathematical model were found to be close to each other as can be seen in Figure 3.

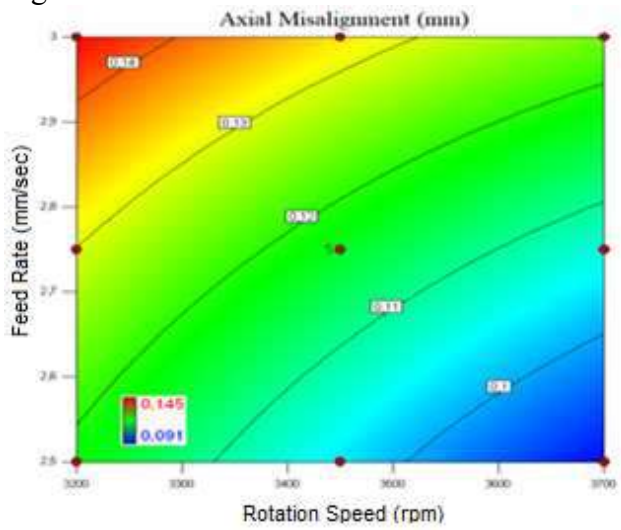

Figure 4. Dual interaction effects of input variables on axial misalignment

Difference in the tool rotation speed and the feed rate, in terms of axial misalignment can be observed in Figure 4. According to the graph, the lowest axial misalignment value was found 0.091 mm and the highest axial misalignment value was found 0.145 mm.

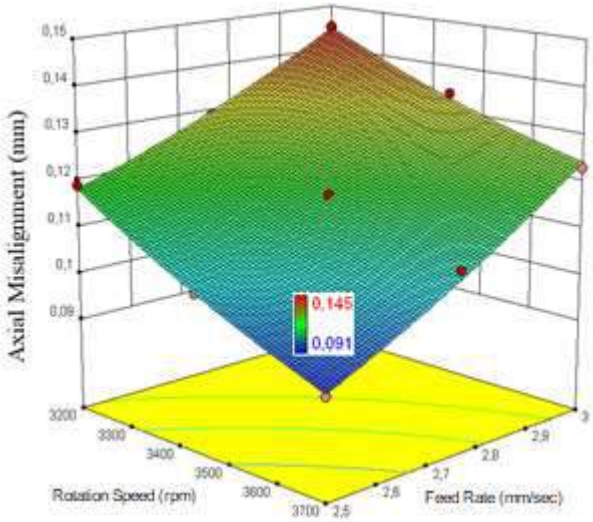

Figure 5. Three-dimensional response graph for the rotation speed and feed rate as compared to the axial misalignment value

As the amount of progression in Figure 5 increases, the value of the axial misalignment also increases. The tool rotation speed also has an effect on axial misalignment. In the three dimensional graph, the lowest axial misalignment value was found 0.091 mm and the highest axial offset value was found 0.145 mm.

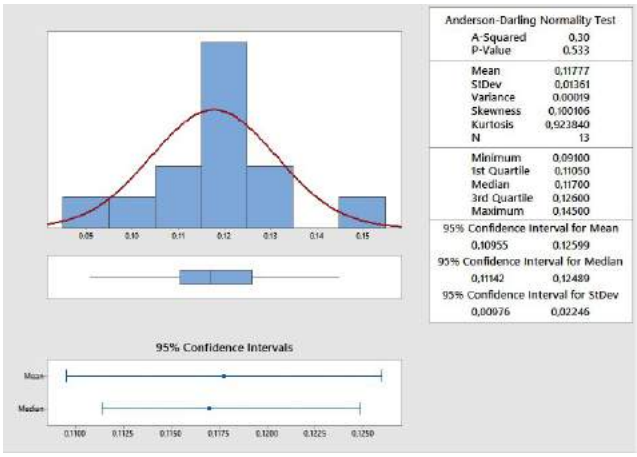

Figure 6. Conclusion with descriptive statistics of experimental drilling results for all the input variables

The histogram distribution of the response variable obtained from experiments can be seen in Figure 6. This model produced with very low values found in P values suggests that it is logical and meaningful.

Less experimentation is required with ease of experimental design. It is saving time as a positive situation. According to the results of our 13 tests and at the same time, the average axial misalignment value in the 95% confidence interval was found 0.11777 mm.

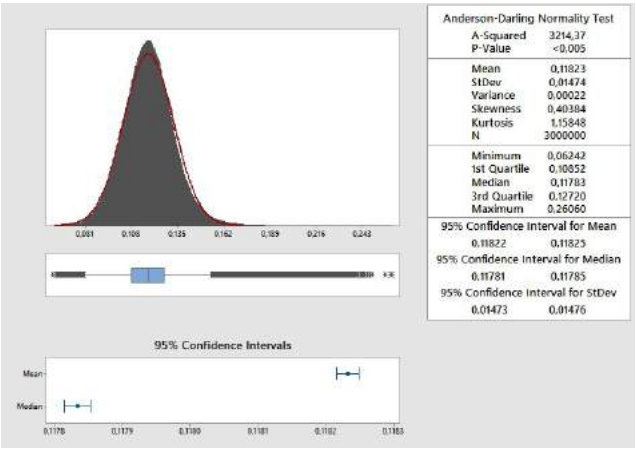

Figure 7. The result of Monte Carlo simulation

For the unpredictable ratio, Monte Carlo method produced 100 thousand random data for explanatory variables and 30 repetitions were made. Our explanatory variables are the tool rotation speed and the feed rate. As can be observed in Figure 7, the range of mean values of the Monte Carlo simulation was determined. According to the Figure 7, the mean value was quite closely with the mean value obtained from experimental results. This is the distribution of the produced data. Then, this data are produced in the generated mathematical model and axial misalignment values are generated.

It was observed that the graph obtained by experimental data and the standard deviation and average of the data produced by Monte Carlo method were close to each other. According to the results of three billion experiments, the mean value of the axial misalignment was found to be 0.11823 mm when we consider the 95% confidence interval [27].

4. CONCLUSION

In this work, the drilling characteristics and effect of the drilling parameters on the axial misalignment are studied for optimizing the drilling operations. Drilling parameters are statistically significant in controlling average axial misalignment value in flat glass machining. ANOVA analysis method was used to understand the accuracy of the model. Conclusions demonstrated that input variables are influential on the drilling operation. It is seen in our practice that there is no uncertainty as it is seen that the standard deviation of these data, which is derived by the experimental data. By incorporating Monte Carlo uncertainty analysis, not only the suggested model depends on MNLR has been made more realistic, but also to predict the surface roughness more accurately.

With the mathematical model produced, it is possible to select the cutting parameters with the optimization method for the axial misalignment value.

The axial misalignment results of the drilling parameters used in the glass drilling were optimized with statistical methods. The result of optimization the most ideal values were determined by statistical method.

From experimental results, the drilling application that optimized is considered proper for manufacturing processes. It can be applied if it provides the desired axial misalignment for industrial applications.

REFERENCES

[1] E.D. Zanotto and J.C. Mauro, “The Glassy State of Matter: Its Definition and Ultimate Fate,” Journal of Non-Crystalline Solids, vol. 471, pp. 490-495, 2017.

[2] M. Sayuti, A.D. Sarhan Ahmed, and M. Hamdi, “Optimizing the Machining Parameters in Glass Grinding Operation on the CNC Milling Machine for Best Surface Roughness,” Advanced Materials Research, vol. 154-155, pp. 721-726, 2011.

[3] J. Cheng, C. Wang, X. Wen, and Y. Gong, "Modeling and Experimental Study on Micro-fracture Behavior and Restraining Technology in Micro-grinding of glass," International Journal of Machine Tools and Manufacture, vol. 85, pp. 36-48, 2014.

[4] Ö. Küçükerman, "Glass Art and Examples from Traditional Turkish Glassware," Turkey Isbank Culture Publications, vol. 271, Art Series: 39, 1985.

[5] E. Axinte, "Glasses as Engineering Materials: A review," Materials and Design, vol. 32, pp. 1717-1732, 2011.

[6] B. Karasu, O. Bereket, E. Biryan, and D. Sanoğlu, "The Latest Developments in Glass Science and Technology," El-Cezerî Journal of Science and Engineering, vol. 4, no 2, pp. 209-233, 2017.

[7] S. Öztürk, "Microstructural Analysis of Metal-bond Diamond Tools in Grinding of Flat Glass, Material," Wissen Schaft Und Werkstoff Technik/Materials Science And Engineering Technology, vol. 45, no. 3, pp. 187-191, 2014.

[8] K. Habalı, H. Gökkaya, and H. Sert, "Experimental Investigation of the Effects of Cutting Tool Coating Materials on Surface Roughness in Machining of AISI 1040 Steel," Journal of Polytechnic, vol. 9, no. 1, 35-38, 2006.

[9] S. Ozturk, "Grinding of flat glass with Fe- and Cu-based diamond tools." Proceedings of the Institution of Mechanical Engineers, Part B: Journal of Engineering Manufacture, vol. 232, no. 9 pp. 1561-1568 2018.

[10] M. F. Kahraman, and S. Öztürk, "Experimental study of newly structural design grinding wheel considering response surface optimization and Monte Carlo simulation." Measurement, vol. 147, arcticle num. 106825, 2019.

[11] S. Öztürk, and M. F. Kahraman, "Modeling and optimization of machining parameters during grinding of flat glass using response surface methodology and probabilistic uncertainty analysis based on Monte Carlo simulation," Measurement, vol. 145, pp. 274-291, 2019.

[12] M. F. Kahraman, H. Bilge, and S. Öztürk, "Uncertainty analysis of milling parameters using Monte Carlo simulation, the Taguchi optimization method and data-driven modeling," Materials Testing, vol. 61, no. 5, pp. 477-483, 2019.

[13] S. Ozturk, "Application of the Taguchi method for surface roughness predictions in the turning process," Materials Testing, vol. 58, no. 9, pp. 782-787, 2016.

[14] S. Ozturk, "Application of ANOVA and Taguchi Methods for Evaluation of the Surface Roughness of Stellite-6 Coating Material," Materials Testing, vol. 56, no. 11-12, pp. 1015-1020, 2014.

[15] E. Kuram, and B. Ozcelik, "Multi-objective optimization using Taguchi based grey relational analysis for micro-milling of Al 7075 material with ball nose end mill," Measurement, vol. 46, no. 6, pp. 1849-1864, 2013.

[16] S. Ozturk, "Machinability of stellite-6 coatings with ceramic inserts and tungsten carbide tools," Arabian Journal of Science and Engineering, vol. 39, no. 10, pp. 7375-7383, 2014.

[17] M. F. Kahraman, H. Bilge, and S. Öztürk, "Uncertainty analysis of milling parameters using Monte Carlo simulation, the Taguchi optimization method and data-driven modeling," Materials Testing, vol. 61, no. 5, pp. 477-483, 2019.

[18] Ş. Bayraktar, Y. Siyambaş, and Y. Turgut, "Drilling Process: A Review," Sakarya University Journal of the Institute of Science and Technology, vol. 21, no. 2, pp. 120-130, 2017.

[19] V. Blank, M. Popov, G. Pivovarov, N. Lvova, and S. Terentev, "Mechanical Properties of Different Types of Diamond," Diamond and Related Materials, vol. 8, pp. 1531-1535, 1999.

[20] R. Calvo, R. D'Amato, E. Gómez, and R. Domingo, "A Comparative Experimental Study of an Alternative CMM Error Model Under Least-squares and Minimum Zone Fittings for İndustrial Measuring," Procedia Engineering, vol. 132, pp. 780-787, 2015.

[21] D. Kubátová, M. Melichar, and J. Kutlwašer, "Evaluation of Repeatability and Reproducibility of CMM Equipment," Procedia Manufacturing, vol. 13, pp. 558-564, 2017.

[22] M. Kayri, "The Multiple Comparison (Post-Hoc) Techniques to Determine the Difference Between Groups in Researches," Fırat University Journal of Social Science, vol. 19, no. 1, pp. 51-64 2009.

[23] Y. Dursun, and E. Kocagöz, "Structural Equation Modeling and Regression: A Comparative Analysis," Erciyes University Faculty of Economics and Administrative Sciences Journal, vol. 35, pp. 1-17, 2010.

[24] T.F. Çavuş, and E. Yanıkoğlu, "Reliability Analysis of Complex Systems with Monte Carlo Method," Sakarya University Journal of the Institute of Science and Technology, vol. 7, no. 3, pp. 99-102, 2003.

[25] A. Hançerlioğulları, "Monte Carlo Simulation Method and Mcnp Code System," Kastamonu Education Journal, vol. 14, no. 2, pp. 545-556, 2006.

[26] M. F., Kahraman, and S Öztürk, "Uncertainty analysis of cutting parameters during grinding based on RSM optimization and Monte Carlo simulation," Materials Testing, vol. 61 no. 12, pp. 1215-1219, 2019.

[27] F. Harmancı, "Optimization of Cutting Parameters During Drilling of Glass with Using Statistical Methods," Msc Thesis, Abant Izzet Baysal University Graduate School of Natural and Applied Sciences, Bolu, 2018.

JOURNAL OF SCIENCE
SAKARYA UNIVERSITY

Sakarya University Journal of Science

ISSN 1301-4048 | e-ISSN 2147-835X | Period Bimonthly | Founded: 1997 | Publisher Sakarya University | http://www.saujs.sakarya.edu.tr/en/

Title: Synthesis and Dielectric Properties of Magnesium Silicate Hydrate Deposited With SnO2

Authors: Yüksel AKINAY
Recieved: 2019-12-16 13:35:20

Accepted: 2020-02-22 17:23:25

Article Type: Research Article
Volume: 24
Issue: 3
Month: June
Year: 2020
Pages: 455-459

How to cite
Yüksel AKINAY; (2020), Synthesis and Dielectric Properties of Magnesium Silicate Hydrate Deposited With SnO2. Sakarya University Journal of Science, 24(3), 455-459, DOI: https://doi.org/10.16984/saufenbilder.659958
Access link
http://www.saujs.sakarya.edu.tr/en/issue/52472/659958

Sakarya University Journal of Science 24(3), 455-459, 2020

Synthesis and Dielectric Properties of Magnesium Silicate Hydrate Deposited With SnO_2

Yüksel AKINAY*[1]

Abstract

In this study, the dielectric properties of SnO_2 coated Magnesium Silicate Hydrate (MSH) pigments were evaluated. The SnO_2 coated MSH pigments were obtained by chemical reduction method with the 3:7 SnO_2/MSH ratio by weight. The structural and dielectric properties of this pigment and MSH were investigated. The surface morphology and phase types were determined by scanning electron microscope (SEM) and x-ray diffraction (XRD). The bond types were characterized by Fourier Transform Infrared Spectrophotometer (FT-IR). The surface of MSH was uniformly coated with SnO_2 as accepted in the SEM images. The existence of XRD peaks for SnO_2 nanoparticles proves the presence of SnO_2 coating. The dielectric properties of prepared pigments were measured via vector network analyzer (VNA) in the frequency range of 8.2–12.4 GHz (X-Band). The dielectric properties of SnO_2 deposited MSH pigments were obtained to be about almost 3-4 times than MSH in the 8-12 GHz frequency range. This study is the first report for the dielectric properties of SnO_2 deposited MSH pigments.

Keywords: Magnesium silicate hydrate, SnO_2, permittivity, pearlescent pigments

1. INTRODUCTION

Pearlescent pigments found naturally and synthetically show outstanding color properties based on optical thin layers. The inorganic pearlescent pigments are obtained by coating a low refractive substrate with high refractive metal oxides. Furthermore, these pigments have superior performance such as thermal and UV stability [1-3]. Inorganic pigments have been widely used in industrial fields such as enamel, ink, plastics, cosmetics and printed products. In recent years, solar reflective and thermal coatings have attracted great attention because they can reduce solar heat in the building and improve indoor thermal conditions, reducing demand for air-conditioning buildings [4,5]. However, there is increasing requests for dielectric properties in the civil and military application such as electromagnetic wave absorber or shielding. Because the high dielectric loss tangent provides

* Correspondin Author: yukselakinay@yyu.edu.tr
[1] Van Yüzüncü Yıl University, Mining Engineering, Van, Turkey. ORCID ID: 0000-0002-6171-6307

high microwave absorption performance for the defense and civil industries. [6].

Magnesium silicate hydrate (MSH) is a typical mineral that composed the MgO-SiO_2-H_2O system and forms in a short time at room temperature when $MgO/Mg(OH)_2$ containing silicate layer contact with water [7]. The chemical reactions M-S-H gel at room temperature is shown in Eq. (1) [8].

$$3Mg^{2+} + 6OH^- + 4SiO_2 \rightarrow Mg_3Si_4O_{10}(OH)_2 + 2H_2O \quad (1)$$

MSH (Talc) improves the fracture properties of the surface by converting adhesion fractures into cohesion fractures. It has a high resistance to heat, electricity, and acid due to its flake structure. Talc is widely used as a functional pigment such as paints, ceramics, and cosmetics due to its high mechanical strength, chip resistance, color effects, insoluble in water, and corrosion resistance [9,10]. Lefebvre et al. have modified the surface of Talc layers by dry coating method with different level of hydrophobic Silica. They have controlled the wettability and dispersity of particles in aqueous solutions with modifying the surface of Talc particles. [10]. Du et al. (2008) prepared the three and four-layer structure pigment systems by the conventional wet chemical method. These functional pigments were prepared by precipitating different metal oxide ions [11].

Recently, many studies have reported the syntheses of pearlescent pigments and characterized their optic properties [12-14]. But there is a lack of studies on dielectric properties of special pigments. In this study, a novel approach for applications of MSH pigments was discussed due to their high dielectric properties. The SnO_2 deposited MSH pigments were synthesized by the chemical reduction method. The dielectric properties of these pigments were investigated in the frequency range of 8-12 GHz.

2. MATERILAS AND METHODS

The MSH (Talc) flakes with the particle size ranging 10-50 μm was provided by ISIK Madencilik in Turkey. These MSH flakes were milled and then passed through a 25 μm sieve for uniform and smaller size distribution. SnO_2 and $NaBH_4$ nanoparticles were purchased from Sigma Aldrich supplier.

The SnO_2 nanoparticles with 20-50 nm were deposited on MSH flakes via chemical reduction method. The SnO_2 ratio to MSH is 3:7 by weight. Firstly, MSH particles were mixed in pure water under magnetic stirring for 2h. Secondly, SnO_2 particles were added to the MSH solution and keep stirring 2 h. 93 mg $NaBH_4$ was dissolved in 3 ml pure water mechanically. Finally, $NaBH_4$ solution was added to the MSH solution and stirred 24 h. The solution was centrifuged and dried at 80°C. The MSH/SnO_2 and pure MSH were labeled as T1 and T2 respectively. The surface structure of obtained pigments was obtained by using field-emission scanning electron microscope (FESEM) and phases properties of pigments were determined by Rigagu ULTRA IV x-ray diffraction (XRD). The bond type of particles was characterized by Bruker ALPHA Fouirer Transform Infrared Spectrophotometer (FTIR) spectrometer. For dielectric properties, the obtained particles were added to epoxy with 3:7 mass ratio and dielectric properties were determined by using a two-port waveguide technique with a vector network analyzer.

3. RESULTS AND DISCUSIONS

The SEM images of MSH (T2) and SnO_2 (T1) deposited MSH pigments are given in figure 1. The surface of talc flakes detected as a smooth lamella-shaped with 2-10 μm sizes. The surface of MSH pigments was coated uniformly with SnO_2 nanoparticles. It was proved that the chemical reduction is a suitable method for doped SnO_2 on MSH flakes.

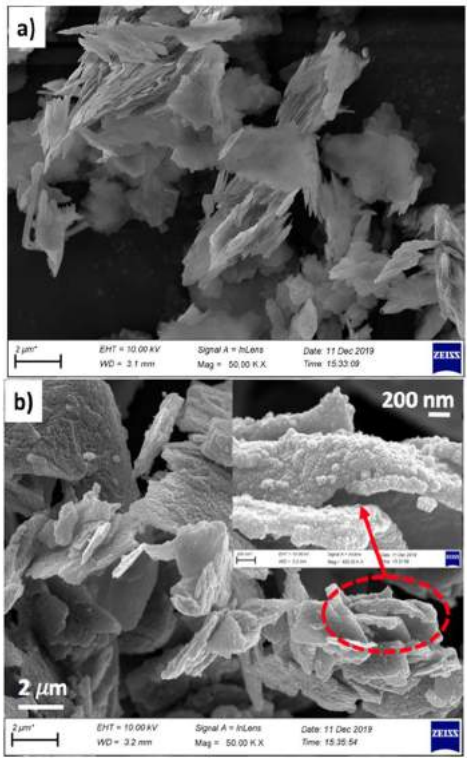

Figure 1. SEM images of MSH (a) and SnO_2 deposited MSH

Figure 2 shows the FT-IR spectra of T1 and T2 pigments. The typical peaks at 668 cm^{-1} correspond to the stretching of Si–O–Si bending. Another peak that appears around 1013 cm^{-1} was assigned to Si-O vibration. Nied et al. have reported that the intensity of the 1013 cm^{-1} peak depends on the Mg/Si ratio [15]. They have obtained that the peak intensity has increased with an increase of Mg/Si ratio. The OH peak from brucite (MgOH) was characterized by the sharp band at 3675 cm^{-1} [7,15].

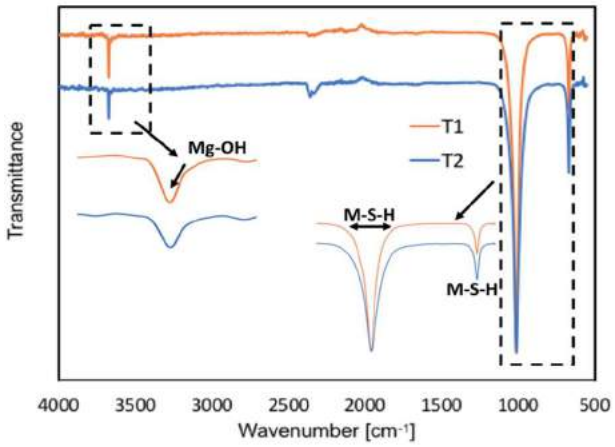

Figure 2. FT-IR spectra of T1 and T2

XRD result of MSH (3*a*) and MSH/SnO_2 (3*b*) presented in Fig. 3. The peaks at 9,5, 19, 29, 37, 49, 61° 2θ is peaks of Talc ($Mg_3Si_4O_{10}(OH)_2$). SiO_2 peaks which are another compound of MSH are detected at 27 and 32° [16]. The intensity of peaks obtained at 9,5 and 29 decreased after SnO_2 deposition on MSH. The tetragonal SnO_2 reflections were obtained at peaks (110), (101), (211), (211), (220) and (002) in 28.7, 52.3, 55,4 and 58,7º respectively [6].

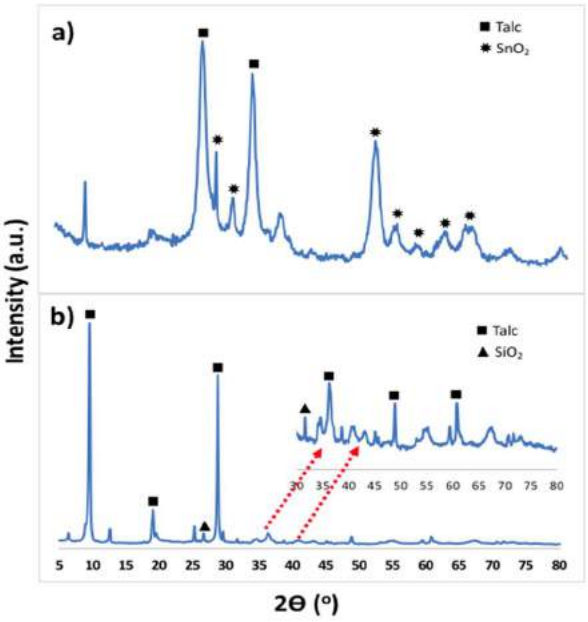

Figure 3. XRD patterns of T1 and T2

The dielectric constants of the T1 and T2 (reel (ε') and imaginary (ε'') part of permittivity) are given in Figure 4*a,b*. For T1, two decreasing peaks have appeared from ε' while two increasing peaks obtained from ε'' at the same frequency range. As seen in figure 4a and 4b, the dielectric constants (reel and imaginary) of T2 (MSH) are relatively stable but dielectric properties of T2 (SnO_2 deposited MSH) was obtained to be about almost 3-4 times than those of obtained from T1 in the 8-12 GHz frequency range. These are can be attributed to interfacial polarization [17-19]. Zhu et al. have attributed this to the existence of dipoles moments resulting from the natural physical properties of the shell. [20]. It was clearly seen that the deposition of SnO_2 has increased the dielectric constant of MSH.

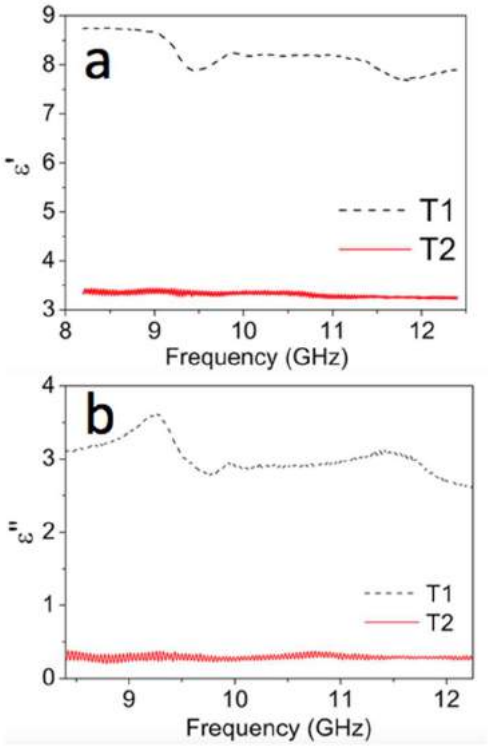

Figure 4. Frequency dependence of dielectric properties of T1 and T2, real permittivity **a**, and imaginary permittivity **b**.

The dielectric loss tangent (tan $\delta\varepsilon = \varepsilon''/\varepsilon'$) of T1 and T2 were calculated to evaluate microwave attenuate performance and given in Fig. 5. It can be clearly seen that SnO_2 deposited MSH pigment (T1) provided higher dielectric loss tangent values. The dielectric loss tangent value of T1 reached a peak value of 0.45 between 9-10 GHz. It was concluded that the deposition of SnO_2 to talc flake gained high dielectric loss and microwave attenuate performance.

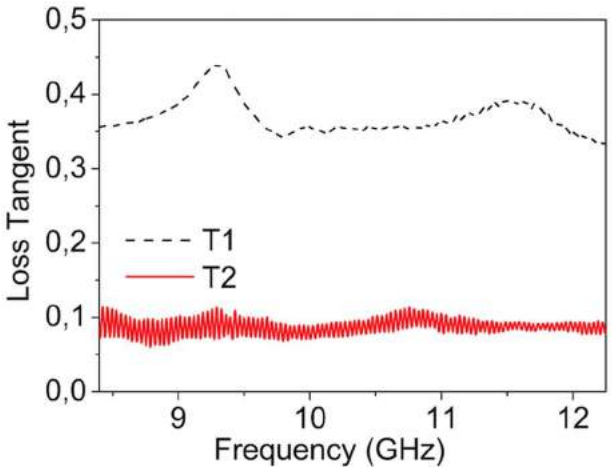

Figure 5. Dielectric loss tangent of T1 and T2

4. CONCLUSION

The MSH/SnO_2 pigments were synthesized by chemical reduction method. The structural and dielectric characterizations were carried out. The existence of SnO_2 on MSH flakes was proved by SEM and XRD results. The SEM images showed that SnO_2 nanoparticles were deposited on surface of MSH continuously. The existence of SnO_2 increased the reel (ε') and imaginary (ε'') part of dielectric values. In addition, the higher dielectric loss tangent values were obtained with SnO_2 coated. This study presents a novel approach for applications of MSH pigments due to their high dielectric and loss properties.

Acknowledgments

This study is supported by Van YYU University Scientific Research Projects Coordination Unit. Project Number: FBA-2019-7959.

REFERENCES

[1] A. R. Mirhabibi, "Ceramic Coatings for Pigments," Ceramic Coatings - Applications in Engineering, vol. 24, pp. 1-286, 2012.

[2] B. B. Topuz, G. Gündüz, B. Mavis, and Ü. Çolak, "The effect of tin dioxide (SnO_2) on the anatase-rutile phase transformation of titania (TiO_2) in mica-titania pigments and their use in paint," Dyes and Pigments, vol. 90 (2), pp. 123-128, 2011.

[3] Q. Gao, X. Wu, Y. Fan, and X. Zhou, "Low temperature synthesis and characterization of rutile TiO_2-coated mica–titania pigments," Dyes and Pigments, vol. 95(3), pp. 534-539, 2012.

[4] L. Xiaojuan, X. Haiquan, C. Jing, C. Juncai, Y. Yuxiang, and L. Xiangnong, "Research of Mica/Fe_3O_4 Pearlescent Pigment by Co-Precipitation," Glass Physics and Chemistry, vol. 37, pp. 330–342, 2011.

[5] Q. Gaoa, X. Wua, Y. Fana and X. Zhoua, "Low temperature synthesis and characterization of rutile TiO_2-coated micaetitania pigments," Dyes and Pigments, vol. 95, pp. 534-539, 2012.

[6] W. Chen, Q. Zhou, F. Wan and T. Gao, "Gas sensing properties and mechanism of nano-SnO_2-based sensor for hydrogen and carbon monoxide," Journal of Nanomaterials, vol. 2012, pp. 1, 2012.

[7] F. Jin and A. Al-Tabbaa, "Strength and hydration products of reactive MgO–silica pastes," Cement and Concrete Composites, vol. 52, pp. 27-33, 2014.

[8] H. M. Tran and A. Scott, "Strength and workability of magnesium silicate hydrate binder systems," Construction and Building Materials, vol. 131, pp. 526-535, 2017.

[9] B. Kaur and S. N. Bhattachary, "Automotive dyes and pigments. In: Handbook of Textile and Industrial Dyeing," Woodhead Publishing, p. 231-251, 2011.

[10] G. Lefebvre, L. Galet, and A. Chamayou, "Dry coating of talc particles with fumed silica: Influence of the silica concentration on the wettability and dispersibility of the composite particles," Powder Technology, vol. 208(2), pp. 372-377, 2011.

[11] J. Du, X. Li, S. Wang, Y. Wu, X. Hao, C. Xu, C. and X. Zhao, "Microwave-assisted synthesis of highly luminescent glutathione-capped $Zn_{1-x}Cd_xTe$ alloyed quantum dots with excellent biocompatibility," Journal of Materials Chemistry, vol. 22, pp. 11390–11395, 2012.

[12] T. Junru, H. Yunfang, H. Wenxiang, C. Xiuzeng and F. Xiansong, "The preparation and characteristics of cobalt blue mica coated titania pearlescent pigment," Dyes and Pigments, vol. 52(3), pp. 215-222, 2002.

[13] J. Tan, L. Shen, X. Fu, W. Hou and X. Chen, "Preparation and conductive mechanism of mica titania conductive pigment," Dyes and pigments, vol. 62(2), pp. 107-114, 2004.

[14] Q. Gao, X. Wu, Y. Fan, and Q. Meng, "Color performance and near infrared reflectance property of novel yellow pigment based on Fe_2TiO_5 nanorods decorated mica composites," Dyes and Pigments, vol. 146, pp. 537-542, 2017.

[15] D. Nied, K. Enemark-Rasmussen, E. L'Hopital, J. Skibsted, and B. Lothenbach, "Properties of magnesium silicate hydrates (MSH)," Cement and Concrete Research, vol. 79, pp. 323-332, 2016.

[16] W. Qin, T. Xia, Y. Ye, and P. P. Zhang, "Fabrication and electromagnetic performance of talc/$NiTiO_3$ composite," Royal Society open science, vol. 5(2), 171083, 2018.

[17] T. Xia, C. Zhang, N. A. Oyler, and X. Chen, "Hydrogenated TiO_2 nanocrystals: a novel microwave absorbing material," Advanced Materials, vol. 25(47), pp. 6905-6910, 2012.

[18] Q. Liu, Q. Cao, H. Bi, C. Liang, K. Yuan, W. She and R. Che, "CoNi@ SiO2@ TiO2 and CoNi@ Air@ TiO2 microspheres with strong wideband microwave absorption," Advanced Materials, vol. 28(3), pp. 486-490, 2016.

[19] Y. Akinay, F. Hayat and B. Çolak, "Absorbing properties and structural design of PVB/Fe_3O_4 nanocomposite," Materials Chemistry and Physics, vol. 229, pp. 460-466, 2019.

[20] C. L. Zhu, M. L. Zhang, Y. J. Qiao, G. Xiao, F. Zhang, and Y. J. Chen, "Fe_3O_4/TiO_2 core/shell nanotubes: synthesis and magnetic and electromagnetic wave absorption characteristics," The Journal of Physical Chemistry C, vol. 114(39), pp. 16229-16235, 2010.

JOURNAL OF SCIENCE
SAKARYA UNIVERSITY

Sakarya University Journal of Science

ISSN 1301-4048 | e-ISSN 2147-835X | Period Bimonthly | Founded: 1997 | Publisher Sakarya University | http://www.saujs.sakarya.edu.tr/en/

Title: Artic Determination of Dynamic Characteristics the Structure with ARX and ARMAX Estimation Methods

Authors: Hidayet UYAR, Elif AĞCAKOCA
Recieved: 2019-08-29 14:24:30

Accepted: 2020-02-24 09:15:55

Article Type: Research Article
Volume: 24
Issue: 3
Month: June
Year: 2020
Pages: 460-471

How to cite
Hidayet UYAR, Elif AĞCAKOCA; (2020), Artic Determination of Dynamic Characteristics the Structure with ARX and ARMAX Estimation Methods. Sakarya University Journal of Science, 24(3), 460-471, DOI: https://doi.org/10.16984/saufenbilder.612826
Access link
http://www.saujs.sakarya.edu.tr/en/issue/52472/612826

Sakarya University Journal of Science 24(3), 460-471, 2020

Artic Determination of Dynamic Characteristics the Structure with ARX and ARMAX Estimation Methods

Hidayet UYAR[1], Elif AĞCAKOCA[2*]

Abstract

In this study, the dynamic behavior of a single-span four-storey steel model structure is tried to determine by using 2 different methods. Connections between beams and columns are produced as rigid and the structure is connected to the shake table by a fixed support. In order to measure the forced vibration values applied to the model structure with the help of the shaking table, the smartphone was placed on the shaking table base and the top of the steel model structure and acceleration records were taken. After the records have been processed, structural algorithm is created using MATLAB autoregressive ARX and autoregressive moving average ARMAX models. Smartphone records from the shake table are defined as inputs and smartphone from the top of the structure are defined as outputs in MATLAB autoregressive ARX and autoregressive moving average ARMAX models. By doing this, structure's dynamic behavior is to be obtained by MATLAB autoregressive ARX and autoregressive moving average ARMAX models when only vibrating table acceleration record is inputted. Dynamic characteristics obtained by ARX and ARMAX were tried to be confirmed by finite element method using Sap2000 software. In order to determine the dynamic characteristics of the building, the earthquake records of Kobe, Sakarya, Loma-Priate and El-Centro were used as forced vibration. At the end of the study, dynamic properties obtained by numeric models (ARX and ARMAX) using input acceleration record are compared to the dynamic properties obtained by Sap2000 analysis. By doing this it was determined whether dynamic properties can be reliably obtained using autoregressive ARX and autoregressive moving average ARMAX models. Advantages and disadvantages of using this method to define structural behavior are discussed.

Keywords: Shaking table, ARX and ARMAX, Smartphone

[1] Sakarya University, Civil Engineeringt, Sakarya, Turkey. ORCID ID:0000 0002 8514 3398
[2] Sakarya University, Civil Engineeringt, Sakarya, Turkey. ORCID ID:0000 0001 8228 0592
[*] Corresponding Author: elifd@sakarya.edu.tr

1. INTRODUCTION

Since the beginning of the 20th century, steel started to be used for structure, one of the most basic needs of humans. Nowadays, structural steel is widely used especially in high rise building construction because of the development of the modern steel construction technics, high strength of the material and easiness of construction. High strength of the material used in the structure reduces the loss of life and property caused by natural disasters such as earthquakes. From structural aspect, in order to maximally decrease financial losses and casualties, it is important to evaluate and establish properties of the material under dynamic loading. The studies performed in structural dynamics field play important role in establishing dynamic properties of structures and designing earthquake resistant structures. In our country (Turkey) earthquake resistant design principles are specified in Turkey Building Earthquake Code (Türkiye Bina Deprem Yönetmeliği).

There are many methods for determining the dynamic behavior of structures numerically. However, the uncertainty of the boundary conditions of building elements, the material behavior can not be fully modeled and the earthquake movement varies with time. Therefore, it requires experimental studies to determine the structure behavior.

Since shaking table tests constitute a widespread experimental method, there are numerous studies on this topic in the literature. Durgun, successfully obtained the natural frequencies, mode shapes and peak displacements data of the undamaged structure model in the laboratory [1]. Özcelik, explores the change between parameters caused by the change of story stiffness of the model fixed to the electro-dynamic shaker and also the interaction between the model and the shaker [2]. Türker explores the effect of the P-Δ effects of different type of structure models on their periods [3]. Aydın observed improved behavior of models with mass tuned dumpers under harmonic excitation [4]. Birdal calibrated the results of structural analyses using results from different analytical methods for analysis [5]. Qui, the behavior of the steel structure connection points under the influence of earthquake was controlled with the help of shaking table [6]. With developing technologies, smart phones started to take their place in experimental studies. Among the studies within the literature that use smartphones, Yan Yu [7] showed that by using an application called Mobile-SHM smartphones can be used as a part of system for structural health monitoring. Also, Zhao et al [8] used 4 smartphones in dynamic experiment and they gave results which agreed with results acquired by other independent sensors. Mari [9] is attempting to prove the functionality of "ishake" smartphone system by performing field table shaking tests with 30 users. Qingkai [10] argues that smartphones can be used to detect traditional network earthquake data that they can be used to record earthquakes of magnitude of 5 from 10km or less of distance and filter them from non-earthquake motion. In addition, the effect of reinforced column-beam connections on modal parameters was investigated [11]. In addition, the effect of damage in the column-beam region on the dynamic behavior of the element was also investigated [12].

In the method used in this study, structural dynamic properties of a model steel structure are determined by autoregresive ARX and autoregresive moving average ARMAX models. Autoregresive moving average ARMAX models are known as Box-Jenkins model "time series prodiction" method in statistics and is applied to time series with equal time increments. In ARMAX model is used to understand and predict next increment values in a time series of X(t) form. While creating ARMAX model, model is established in 2 stages. Firstly, autoregresive AR part, then the moving average parts (MA) are created. In ARMAX Model, p and q indeces is defined as autoregresive and moving average part degrees respectively and model is shown as ARMA (p,q).

2. EXPERIMENTAL SETUP

The shaking table used in the study is 1x1m size. It has 1250kN load capacity and is shown in Figure 1. The table is designed to have maximum

movement capacity of 92.5mm, maximum horizontal force capacity of 2500N, maximum acceleration capacity of 2g and maximum velocity of 500mm/s. Thanks to load control algorithm table can reproduce the motion of many different earthquake records such as Kobe (1995), Sakarya (1999), etc.

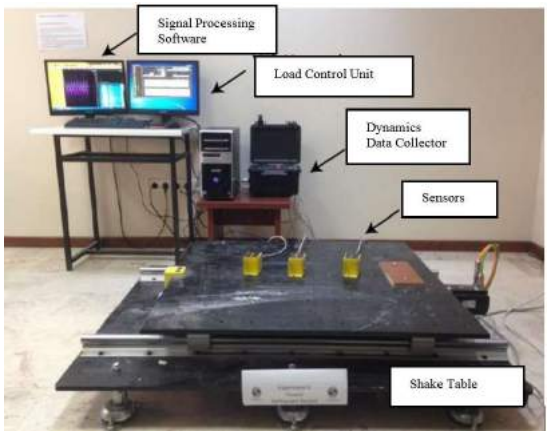

Figure 1.Experiment setup [13]

Experiment setup is comprised of shaking table, smart phone and dynamic data receiver device as well as other units such as laptop computer. Within experiment study, 4 story steel model structure is built on shaking table. Total weights of columns and slabs are 3.76kg and 40.76kg respectively and their geometric features are presented in Table 1.

Table 1. Model structure size

	Number	Top-Length (mm)	Dimensions (mm)
Column	4	1200	50x2
Floor	4	360x360	10

The model structure was parts used in experiment were produced in an industrial factory as shown in Figure 2. All structure elements were brought and assembled on shaking table Figure 3.

Figure 2. Preparation of model structure

In order to provide rigid connection between elements they were connected by bolts and nuts on floor levels where nuts were substantially fastened. In order to extract data from the model, smartphones was placed on top floor (on top of shaking table).

Figure 3. Steel building model, shaking table, computer system, smart phone

3. NUMERICAL ANALYSIS

At present, it is not possible to determine the dynamic behavior of existing structures under forced vibration. That's why many studies start with smaller scaled model in order to determine real-size structure dynamic properties. There are many methods used to determine dynamic behavior of model structures. In this study, model structure is assembled on shaking table, forced by existing earthquake record and goal is to develop structural algorithm using system identification method. Steel structure model dynamic properties are obtained through the established structural algorithm. Thus, by placing sensors it will be

possible to develop algorithm for dynamic characteristic definition of structures with various properties such as suspended bridges, high rise buildings, television towers etc., for structural health monitoring and for detection of damage [14]. In definition techniques, most commonly, it requires an excitation (input) and response (output) measurements to fully determine the dynamic behavior of a model.

In experimental study, the acceleration values is recorded on top of the shaking table (input) and on top of the model (output). These input-output values are created using sensitive receptors within smartphones placed on top of the shaking table (base of the model) and on top of the model.

These unprocessed input-output values are studied using FFT (Fast Fourier Transform) within Seismo program. FFT analyses of smartphone input values are presented in Figure 4.

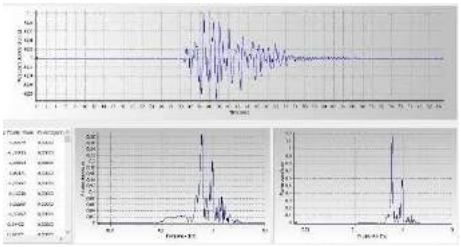

(a)

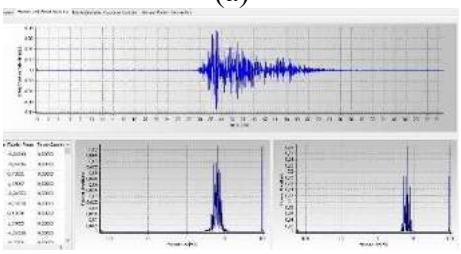

(b)

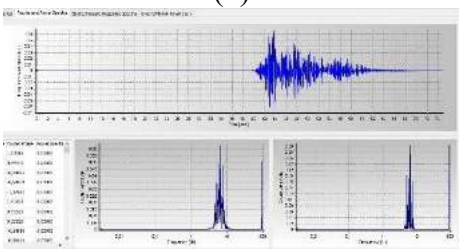

(c)

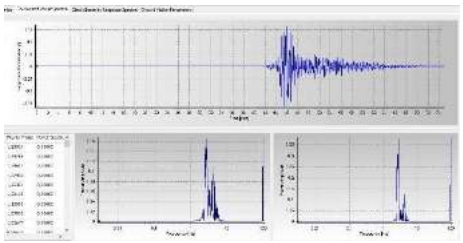

(d)

Figure 4. Fast Fourier Transform of earthquake (a) Kobe, (b) Sakarya, (c) El-Centro, (d)Loma Priate

MATLAB System Identification Toolbox is an application written to establish mathematical models of dynamic systems using measured input-output data. This application allows creation and use of dynamic system models of structures that are complex and not easy to model. It is possible to use input-output data in time or frequency domain in order to define continuous time, incremental time, process models and case space models. Also it contains technics such as algorithms for hidden online parameter prediction, most likeliness and prediction error method and subspace system definition. Toolbox also supports data modeling prediction for time series [15]. It is possible to create mathematical models of smartphone acceleration data whose FFT analyses are performed in Siesmo Signal by choosing proper modeling within system identification method.

3.1. ARX and ARMAX

Engineering structures consist of infinite dimensional parameter systems. Autoregressive ARX and autoregressive moving averages ARMAX models in Matlab System Diagnostics can be expressed as discrete time models. It creates finite dimensional systems in the analysis of discrete time complex systems, thus offering a practical approach to infinite dimensional systems. When creating a model, the determination of modal parameters is expressed as simple eigenvalues. The most important issue here is the selection of the previously unknown model type (ARX, ARMAX…).

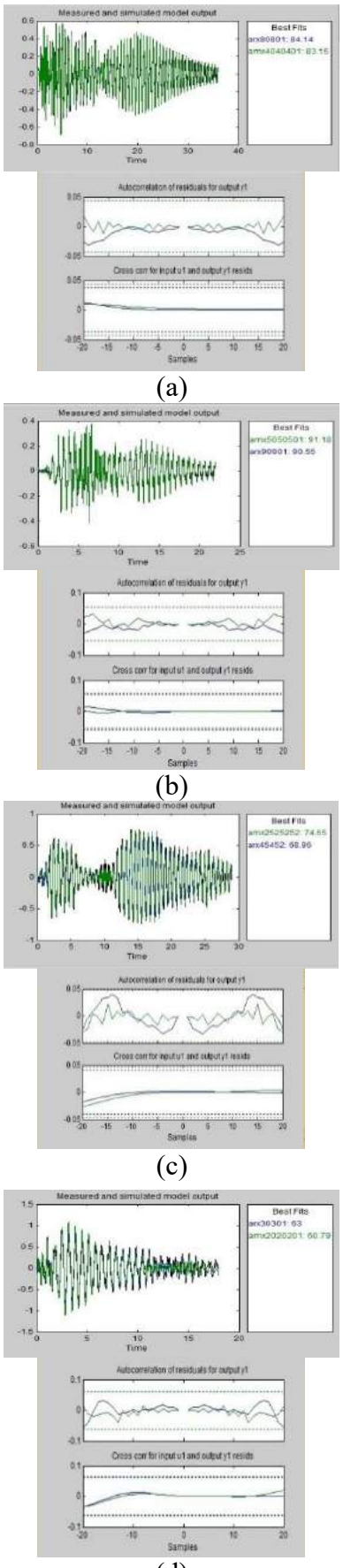

Figure 5. Smartphone input-output recording and compliance ratio (a)Kobe,(b) Sakarya,(c)El-Centro,(d)Loma Priate

The choice of model type often determines the results and the number of modal parameters. In practice, further analysis may be required to determine the model due to noise and discretization errors. In this study, using MATLAB, System Identification, autoregressive ARX and autoregressive moving averages ARMAX models were produced and their advantages and disadvantages in terms of structure recognition technique were investigated

Autoregressive and Autoregressive Moving Averages Models

When a time series (X_t) is given, the ARMA model is used to understand and even predict the values of the series in future periods. The model consists of two parts. One of these is the autoregressive part AR and the other is the moving averages part. ARMA Model is generally shown as ARMA (p,q) model, where p is the degree of autoregressive part and q is the degree of moving average part.

Autoregressive Ar(p), Model Autoregressive Ar(p)

Ar (p) is p. defines an autoregressive model. The Ar (p) model is shown in (1).

$$X_t: c + \sum_{i:1}^{p} \theta_i X_{t-i} + \varepsilon_t \qquad (1)[16]$$

Moving Averages Method, Ma (q) Model

Ma(q), q. A moving averages model of degrees is shown in (2)

$$X_t: \varepsilon_t + \sum_{i:1}^{q} \theta_i \varepsilon_{t-i} \qquad (2)[16]$$

$\theta_1, ..., \theta_q$ are the parameters of the model ε_t, ε_{t-1},... are the error terms of the model. It is understood that in the "moving averages" model, the value of a time series variable at a given time point (value of X_t) q is the predominance of the errors made at each of the previous time points.

Autoregressive Moving Averages, ARMA (p, q), Model

This model is a combination of Ar(p) and Ma(q) models and is shown in (3). An ARMAX model can be seen as an effective model, where all aspects of the AR, ARX and ARMA models are included. ARMAX creates a generalized mathematical description of the nonlinear dynamical system with stochastic noise and integrates the variation of input parameters into the system model [17]. The main advantage of ARMAX model is that, it inherently mitigates for signals with noise from various sources, providing unbiased parameter estimates.

$$X_t: \sum_{i:1}^{p} \theta_i \, x_{t-i} + \sum_{i:1}^{q} \theta_i \, \varepsilon_{t-i} \qquad (3)[14]$$

In the experiment, the input-output of the records that we receive from the smartphone and sensor placed on the building with the shaking table are defined. Baseline correction and filtering procedures were applied to the obtained data. After baseline zero line correction and filtering, the synchronization of the graph was checked by plotting the data in the same graph as input and output. Figure 5 show that the data of the inputs and outputs are synchronized. ARX and ARMAX are a special function of AR and ARMA.

In this study, after checking the input-output matching and synchronization of the data defined on the shaking table, forced vibration intervals obtained from FFT analysis were used. The algorithm has been developed with the help of ARX and ARMAX models in the System Diagnostics section of MATLAB. The input-output values given to the Matlab program are re-created by installing ARX and ARMAX models in the program. Matlab program uses mathematical prediction to generate input-output. Then, it expresses the difference between the predicted data and the experimental data as residues. It was also checked whether there was a cross-correlation between the input-residue and whether the results remained in the safe zone and whether they passed the whiteness and independence tests. Whiteness test; shows that there is no input-residue relationship and the prediction remains within a certain confidence interval. Independence test; checks whether the input-output data is connected to the residue. Figures 5 illustrate that the graph remains within the area indicated by dashed lines; ıt shows that there is no correlation between input-residue. The polynomial coefficients (n) in the mathematical model were increased and maximum fit ratios of the model were tried to be obtained. In addition to increasing coefficient (n) in the formed polynomial, whiteness and independence test remain within the determined limits, this shows the accuracy of the study [17].

4. FINITE ELEMENT MODELLING

In order to obtain the dynamic characteristics of the steel model structure, the finite element program SAP2000 was used. The materials used in the experiment are St 235 steel, yield strength is 235 MPa. Modulus of elasticity 2.1 GPa, slabs arc designed as a rigid diaphragm. The frequency values obtained at the from the finite element model are f_1:1.3204, f_2:3.8039, f_3:5.8332, f_4:7.1601(Figure 6.)

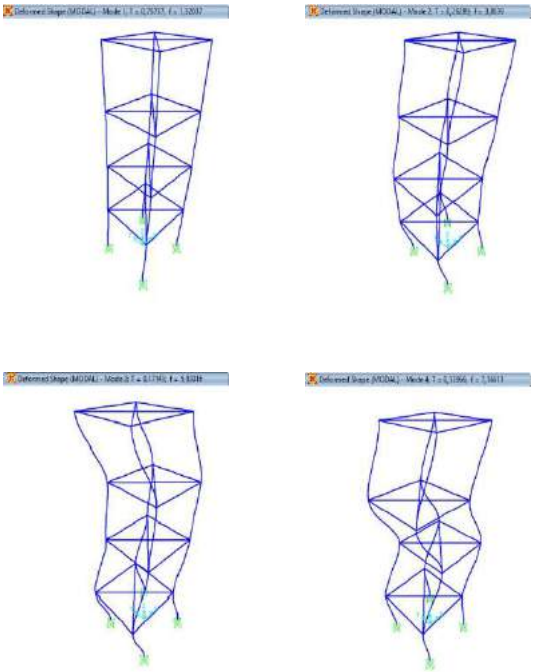

Figure 6. Modal Analysis

5. DISCUSSIONS

In order for the selected model types to give correct results, the input-outputs must be in a certain harmony. In this study, were conducted on the forced vibrations of Kobe, Sakarya, Loma-Priate and El-Centro earthquakes.

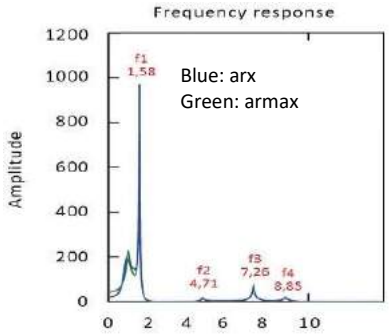

Figure 7. Kobe forced vibration smartphone recording

Table 2. Kobe earthquake data

Kobe earthquake	ARX	ARMAX	Finite Element (Sap 2000)
1th period	1.58	1.58	1.3204
2th period	4.71	4.71	3.8039
3th period	7.26	7.26	5.8332
4th period	8.89	8.89	7.1601
Best Fits (Matlab)	84.14	83.15	-
Difference between (Sap2000)%	19	19	-

When examining the 1st period values, comparison of the results for forced vibration of the Kobe earthquake smartphone recording is show (Figure 7) and (Table 2). The first mode of the finite element module f_1:1.3204. In the ARX model, f_1:1.58. In the ARMAX model, f_1: 1.58. Matlab's input and outputs are compatible with the ARX model defined in Matlab 84%, Matlab's input and outputs are compatible with the ARMAX model defined in Matlab 83%. Considering the Matlab model agreement, it is seen that there is 19% difference when the frequency values obtained in ARX and ARMAX are compared with the finite element frequency values obtained using experimental data.

When examining the 2nd period values, if we compare the results for forced vibration of Kobe earthquake smartphone recording; The second mode of the finite element module f_2: 3.8039. In the ARX model, f_2:4.71. In the ARMAX model, f_2:4.71. Matlab's input and outputs are compatible with the ARX model defined in Matlab 84%, Matlab's input and outputs are compatible with the ARMAX model defined in Matlab 83%. Considering the Matlab model agreement, it is seen that there is 23.82% difference when the frequency value obtained in ARX and ARMAX is compared with the finite element frequency values obtained by using experimental data.

When examining the 3rd period values, if we compare the results for forced vibration of Kobe earthquake smartphone recording; The third mode of the finite element module f_3: 5.8332. In the ARX model, f_3:7.26. In the ARMAX model, f_3:7.26. Matlab's input and outputs are compatible with the ARX model defined in Matlab 84%, Matlab's input and outputs are compatible with the ARMAX model defined in Matlab 83%. Considering the Matlab model agreement, it is seen that there is a 24.46% difference when the frequency values obtained in ARX and ARMAX are compared with the finite element frequency values obtained by using experimental data.

When examining the 4th period values, comparing the results for forced vibration of Kobe earthquake smartphone recording; The thourd mode of the finite element module f_4: 7.1601. In the ARX model, f_4:8.89. In the ARMAX model, f_4: 8.89. Matlab's input and outputs are compatible with the ARX model defined in Matlab 84%, Matlab's input and outputs are compatible with the ARMAX model defined in Matlab 83%. Considering the Matlab model agreement, it is seen that there is a difference of 24.16% when the frequency values obtained in ARX and ARMAX are compared with the finite element frequency values obtained using experimental data.

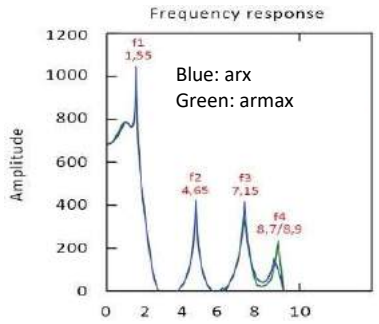

Figure 8. Sakarya forced vibration smartphone recording

Table 3. Sakarya earthquake data

Sakarya earthquake	ARX	ARMAX	Finite Element (Sap 2000)
1th period	1.55	1.55	1.3204
2th period	4.65	4.65	3.8039
3th period	7.15	7.15	5.8332
4th period	8.7	8.9	7.1601
Best Fits (Matlab)	91.18	90.55	-
Difference between (Sap2000)%	17	17	-

When examining the 1st period values, if we compare the results for forced vibration of Sakarya earthquake smartphone recording (Figure 8) and (Table 3). The first mode f_1:1.3204 emerges in the Sap2000 software. In the ARX model, f_1:1.55. In the ARMAX model, f_1:1.55. Matlab's input and outputs are compatible with the ARX model defined in Matlab 91%, Matlab's input and outputs are compatible with the ARMAX model defined in Matlab 90.6%. Considering the Matlab model agreement, it is seen that there is a 17% difference between the frequency values obtained in ARX and ARMAX and finite element frequency values obtained using experimental data.

When examining the 2nd period values, if we compare the results for forced vibration of Sakarya earthquake smartphone recording; The second mode f_2:3.8039 emerges in the Sap2000 software. In the ARX model, f_2:4.65. In the ARMAX model, f_2:4.65. Matlab's input and outputs are compatible with the ARX model defined in Matlab 91%, Matlab's input and outputs are compatible with the ARMAX model defined in Matlab 90.6%. Considering the Matlab model agreement, it is seen that there is a 22% difference between the frequency value obtained from ARX and the finite element frequency values obtained by using experimental data.

When examining the 3rd period values, if we compare the results for forced vibration of Sakarya earthquake smartphone recording; In the Sap2000 software, the third mode is f_3:5.8332. In the ARX model, f_3:7.15. In the ARMAX model, f_3:7.15. Matlab's input and outputs are compatible with the ARX model defined in Matlab 91%, Matlab's input and outputs are compatible with the ARMAX model defined in Matlab 90.6%. Considering the Matlab model agreement, it is seen that there is a 23% difference between the frequency values obtained in ARX and ARMAA and the finite element frequency values obtained using experimental data.

When examining the 4th period values, if we compare the results for forced vibration of Sakarya earthquake smartphone recording; The fourth mode f_4:7.1601 emerges in the Sap2000 software. In the ARX model, f_4:8.7. In the ARMAX model, f_4:8.9. Matlab's input and outputs are compatible with the ARX model defined in Matlab 91%, Matlab's input and outputs are compatible with the ARMAX model defined in Matlab 90.6%. Considering the Matlab model agreement, it is seen that there is a 22% difference between the frequency values obtained in ARX and ARMAX and finite element frequency values obtained using experimental data.

When examining the 1st period values, comparing the results for forced vibration of the El-Centro smartphone recording (Figure 9) and (Table 4). The first mode f_1:1.3204 is displayed in the Sap2000finished software. In the ARX model, f_1:1.56. In the ARMAX model, f_1:1.56. Matlab's input and outputs are compatible with the ARX model defined in Matlab 74.65%, Matlab's input and outputs are compatible with the ARMAX model defined in Matlab 68.96%. Considering the Matlab model agreement, it is seen that there is approximately the same 18% difference between the frequency values obtained in ARX and

ARMAX and finite element frequency values obtained using experimental data.

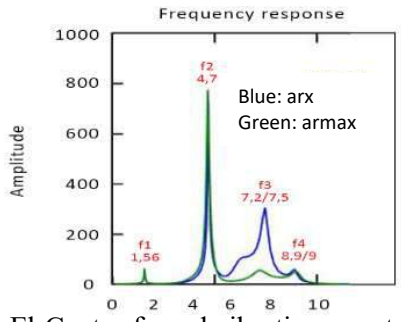

Figure 9. El-Centro forced vibration smartphone recording

Table 4. El-Centro earthquake data

El-Centro earthquake	ARX	ARMAX	Finite Elemant (Sap 2000)
1th period	1.56	1.56	1.3204
2th period	4.7	4.7	3.8039
3th period	7.2	7.15	5.8332
4th period	8.9	9	7.1601
Best Fits (Matlab)	74.65	68.96	-
Difference between (Sap2000)%	18	18	-

When examining the 2nd period values, if we compare the results for forced vibration of El-Centro earthquake smartphone registration; The second mode f_2:3.8039 emerges in the Sap2000 software. In the ARX model, f_2:4.7. In the ARMAX model, f_2:4.7. Matlab's input and outputs are compatible with the ARX model defined in Matlab 74.65%, Matlab's input and outputs are compatible with the ARMAX model defined in Matlab 68.96%. Considering Matlab model agreement, it is seen that there is a 23% difference when the frequency value obtained in ARX and ARMAX is compared with the finite element frequency values obtained using experimental data.

When examining the 3rd period values, compare the results for forced vibration of the El-Centro earthquake smartphone registration; In the Sap2000 software, the third mode is f_3:5.8332. In the ARX model, f_3:7.2. In the ARMAX model, f_3:7.15. Matlab's input and outputs are compatible with the ARX model defined in Matlab 74.65%, Matlab's input and outputs are compatible with the ARMAX model defined in Matlab 68.96%. Considering the Matlab model agreement, when the frequency value obtained from the ARX and the finite element frequency values are compared by using experimental data, it is seen that there is 23% difference in ARMAX and 23% difference in ARMAX.

When examining the 4th period values, if we compare the results for forced vibration of the El-Centro earthquake smartphone registration; The fourth mode f_4:7.1601 emerges in the Sap 2000 software. In the ARX model, f_4:8.9. In the ARMAX model, f_4:9.0 Matlab's input and outputs are compatible with the ARX model defined in Matlab 74.65%, Matlab's input and outputs are compatible with the ARMAX model defined in Matlab 68.96%. Considering Matlab model agreement, it is seen that there is a 24% difference between the frequency values obtained in ARX and ARMAX and finite element frequency values obtained by using experimental data.

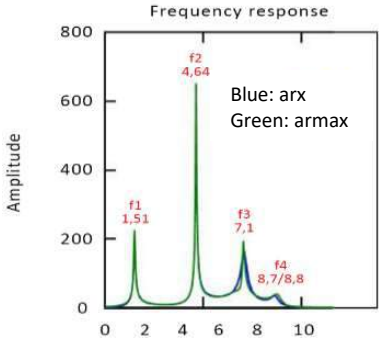

Figure10. Loma-Priate forced vibration smartphone recording

When examining the 1st period values, if we compare the results for forced vibration of Loma-priate smartphone recording (Figure 10) and (Table 5). The first mode f_1:1.3204 emerges in the Sap2000 software. In the ARX model, f_1:1.51. In the ARMAX model, f_1:1.51. The compatibility of the inputs and outputs given to Matlab with the ARX model defined in Matlab is 63%, and the compatibility of the inputs and outputs given to Matlab with the ARMAX model defined in Matlab is 60.79%. Considering Matlab model agreement, it is seen

that there is a 14% difference when the frequency value obtained in ARX and ARMAX is compared with the finite element frequency values obtained by using experimental data.

Table 5. Loma-Priate eartquake

Loma-Priate earthquake	ARX	ARMAX	Finite Elemant (Sap 2000)
1th period	1.51	1.51	1.3204
2th period	4.64	4.64	3.8039
3th period	7.1	7.1	5.8332
4th period	8.7	8.8	7.1601
Best Fits (Matlab)	63	60.79	-
Difference between (Sap2000)%	14	14	-

When examining the 2nd period values, Loma-Priate earthquake smartphone recording forced vibration compared to the results; The second mode f_2:3.8039 emerges in the Sap2000 software. In the ARX model, f_2:4.64. In the ARMAX model, f_2:4.64. The compatibility of the inputs and outputs given to Matlab with the ARX model defined in Matlab is 63%, and the compatibility of the inputs and outputs given to Matlab with the ARMAX model defined in Matlab is 60.79%. Considering the Matlab model agreement, it is seen that there is a 22% difference between the frequency values obtained in ARX and ARMAX and finite element frequency values obtained using experimental data.

When examining the 3rd period values, if we compare the results for forced vibration of Loma-priate earthquake smartphone registration; In the Sap2000 software, the third mode is f_3:5.8332. In the ARX model, f_3:7.1. In the ARMAX model, f_3:7.1. The compatibility of the inputs and outputs given to Matlab with the ARX model defined in Matlab is 63%, and the compatibility of the inputs and outputs given to Matlab with the ARMAX model defined in Matlab is 60.79%. Considering the Matlab model agreement, it is seen that there is a 22% difference between the frequency values obtained in ARX and ARMAX and the finite element frequency values obtained using experimental data.

When examining the 4th period values, Loma-Priate earthquake smartphone recording forced comparison of the results for vibration; The fourth mode f_4:7.1601 emerges in the Sap 2000 software. In the ARX model, f_4:8.7. In the ARMAX model, f_4:8.8. The compatibility of the inputs and outputs given to Matlab with the ARX model defined in Matlab is 63%, and the compatibility of the inputs and outputs given to Matlab with the ARMAX model defined in Matlab is 60.79%. Considering the Matlab model agreement, it is seen that there is a 23% difference between the frequency values obtained in ARX and ARMAX and finite element frequency values obtained using experimental data.

6. CONCLUSIONS

ARX and ARMA's algorithm can be solved in a very short time with Matlab. Although ARMAX and ARX algorithms contain many coefficients, they are preferred in engineering studies because they can be calculated quickly and easily. ARMAX and ARX, one of the mathematical prediction models, have started to be used in structural identification with the developing technology. In this study, 4-storey model structure acceleration data were obtained by using smartphone recorder using 4 different earthquake data. In the determination of the dynamic characteristics of the structure, ARX and ARMAX algorithm is used. The two results were very close. In the four earthquake data used in the study, ARX and ARMAX rigging gave approximately the same values. When the ARX and ARMAX result, were compared with the finite element model result, the best estimation was achieved at Loma Priate with 14% prediction error at the 1st frequency value. The worst estimate was obtained Kobe with a 65% difference. Using only input data, the dynamic characteristics of the structure can be predicted with the help of the algorithm used. Due to noise and other residues, no exact match can be achieved between the data predicted or estimated by Matlab and the results of the experiment.

7. REFERENCES

[1] T. Baran, et al. "Deney ve Eğitim Amaçlı, Mekanik Tek Eksenli Bir Sarsma Tablasının İmalatı ve Performansının Araştırılması" , Altıncı Ulusal Deprem Mühendisliği Konferansı, 605-616, 2007.

[2] Ö. Özçelik, İ.S.Mısır, U. Yücel, "Model bir yapının hasar tanımlaması ve Model-Sarsıcı etkileşiminin azaltılması için kullanılan offline iterasyon tekniği", 2. Türkiye Deprem Mühendisligi ve Sismoloji Konferansı, 2013.

[3] H. Türker, C. Mertayak, H.Çolak, "Peryot hesaplanmasında P-Δ etkisi: Sarsma tablası deneyi", 1. Türkiye Deprem Mühendisligi ve Sismoloji Konferansı, 2011.

[4] E. Aydın, B. Öztürk, M. Gökdemir, H. Çetin, "Sarkaç tipi ayarlı kütle sönümleyicilerin harmonik etkiler altındaki davranışı: Deneysel bir çalışma", 3. Türkiye Deprem Mühendisligi ve Sismoloji Konferansı, 2015.

[5] F. Birdal, F. Altun, A.K. Tanrıkulu, "Sarsma tablası deney sonuçlarına göre dinamik karakteristikleri belirlenmiş ölçekli betonarme bir yapının nonlineer dinamik ve statik analizlerinin karşılaştırılması", 8. Ulusal Deprem Mühendisliği Konferansı, 2015.

[6] J. Goggins, B.M. Broderick, A.Y. Elghazouli, S. Salawdeh, A. Hunt, P. Mongabure, "Shake table testing of concentrically braced steel structures with realistic connection details subjected to earthquakes", In Structures, vol. 13, pp. 102-118, 2018.

[7] Y. Yan, Z. Xuefeng, H. Ruicong, Q. Jiping, "Design and Initial Validation of External Sensors Board of Smart Phones for Mobile Structural Health Monitoring System", In Proceedings of the 7th International Conference on Structural Health Monitoring of Intelligent Infrastructure, 2015.

[8] X. Zhao, K. Ri, R. Han, Y. Yu, M. Li, J. Ou, "Experimental research on quick structural health monitoring technique for bridges using smartphone" , Advances in Materials Science and Engineering, 2016.

[9] E. Mari, D. Shideh, R. Jack, D. B. Jonathan, B. Alexandre, G. Steven, "I-Shake:Mobile Phones as Seismic Sensors User Study Findings", Proceedings of the 10th International Conference on Mobile and Ubiquitous Multimedia, 2011.

[10] K. Qingkai, M. A. Richard, S. Louis, K. Young-Woo, "My Shake: A smartphone seismic network for earthquake early warning and beyond", 2016.

[11] Nasery, Mohammad Manzoor, et al. "Damage effect on experimental modal parameters of haunch strengthened concrete-encased composite column–beam connections", International Journal of Damage Mechanics, 2019.

[12] Hüsem, Metin, et al. "Experimental evaluation of damage effect on dynamic characteristics of concrete encased composite column-beam connections." Engineering Failure Analysis 91, 2018.

[13] H. S. Küyük, Z. D. Yaman, "Eşik Seviyesine Bağlı Protatip bir Deprem Erken Uyari Sistemi Geliştirilmesi", 8. Ulusal Deprem Mühendisliği Konferansı, 2015.

[14] H. S. Ulusoy, Q. Maria, J. F. Paul, "System identification of a building from multiple seismic records", 2010.

[15] https://www.mathworks.com/products/sysid.html Erişim Tarihi: 14.05.2019.

[16] Ü. M. Kahraman, "Çok değişkenli eşiksel otoregresif modeller üzerine bir çalışma," Selçuk Üniversitesi, Fen Bilimleri Enstitüsü, Doktora Tezi, 2012.

[17] M. Ay Ali, Y.Wang, "Structural damage identification based on self-fitting ARMAX

model and multi-sensor data fusion", Struct. Health Monit, vol. 13(4), pp. 445–460, 2014.

JOURNAL OF SCIENCE
SAKARYA UNIVERSITY

Sakarya University Journal of Science

ISSN 1301-4048 | e-ISSN 2147-835X | Period Bimonthly | Founded: 1997 | Publisher Sakarya University | http://www.saujs.sakarya.edu.tr/en/

Title: Effect of Different Heat Treatments on Mechanical Properties of AISI Steels

Authors: Seçil EKŞİ
Recieved: 2019-10-04 12:29:41

Accepted: 2020-02-24 12:10:22

Article Type: Research Article
Volume: 24
Issue: 3
Month: June
Year: 2020
Pages: 472-479

How to cite
Seçil EKŞİ; (2020), Effect of Different Heat Treatments on Mechanical Properties of AISI Steels. Sakarya University Journal of Science, 24(3), 472-479, DOI: https://doi.org/10.16984/saufenbilder.629371
Access link
http://www.saujs.sakarya.edu.tr/en/issue/52472/629371

Sakarya University Journal of Science 24(3), 472-479, 2020

Effect of Different Heat Treatments on Mechanical Properties of AISI Steels

Seçil EKŞİ*[1]

Abstract

Heat treatment has great importance on the mechanical properties of materials. This paper reports experiments on effects of heat treatment on the mechanical and microstructures behavior of AISI 1040 and AISI 1060 steel. To analyze the effect of different heat treatments, AISI 1040 specimens were prepared through quenching, quenching and tempering, normalizing and spheroidizing. To understand effect of tempering time/temperature and annealing time on AISI 1060 steel specimens were prepared through annealing and tempering. Tensile test and hardness test were performed on steel specimens. The mechanical properties of steel specimens were correlated with the microstructure of steels.

Keywords: heat treatment 1, mechanical properties 2, microstructures 3, hardness 4

1. INTRODUCTION

Today, steel materials with the developing technology are used widely from health to space technologies. Heat treatment of steel is becoming more and more important in its widespread use from transportation to communication, from construction to agriculture and consequently improving its mechanical and metallographic properties.

Mechanical properties of steels are depend on different physicochemical applications in steel production. It is a function of the microstructure and chemical structure formed as a result of the processes. In order to obtain a certain condition in terms of internal structure and properties, temperature and the appropriate sequence and time is called heat treatment. In general, heat treatments can be grouped into two main groups: Annealing and hardening: Approach of the internal structure of the stable balance with annealing (cooling is done slowly). In hardening austenitic steel a semi-stable internal structure (martensite) is formed.

Many different heat treatment process can be applied to steels in order to increase tool life and reduce machining costs operations. The aim of these heat treatments is to soften the structure and increase tool life, reduce cutting forces. These

* Corresponding Author: eksi@sakarya.edu.tr
[1] Sakarya University, Mechanical Engineering Department, Sakarya, Turkey. ORCID ID: 0000-0002-1404-718X

treatments generally decrease the mechanical properties of steels.

There are many studies on heat treatment of steels [1-13]. Zhang et al. investigated the effect of tempering temperature on the microstructure properties of stainless steel. They reported that main factors affecting the strength and toughness were austenitization and large-size precipitates when the tempering temperature was above 540 °C [1]. Sanij et al. investigated the effect of double quenching and tempering with conventional quenching and tempering heat treatment processes on microstructure and mechanical behavior of hot rolled AISI 4140 steel. They showed that impact toughness of double quenching and tempering heat treated specimens is much higher than that of the conventional quenching and tempering condition [4]. Saastamoinen et al. studied on effects of chemical composition and mechanical properties on direct-quenched and tempered high-strength structural steel [5]. Jiang et al. studied on heat treatment parameters of quenched and tempered steel. They investigated microstructure and mechanical properties of a heat treated steel. They reported that the tempering temperature is a very effective factor and the quenching temperature the secondary effective factor on mechanical properties of steel [11].

In this study, tensile, hardness and microstructures properties of AISI 1040 and 1060 steels are investigated experimentally. Also, effects of the tempering time/temperature on the hardness of steels were studied.

2. EXPERIMENTAL STUDY

AISI 1040 steel and AISI 1060 steel were used in experiments. Steel specimen were prepared for tensile testing, hardness measurement and microstructure imaging.

2.1. Preparation of Specimen

Tensile specimens were prepared according to the ASTM E-8 standard. View of geometry of tensile test specimen and tensile/hardness/microstructure specimens were given in Figure 1. Three specimens were prepared for each configuration.

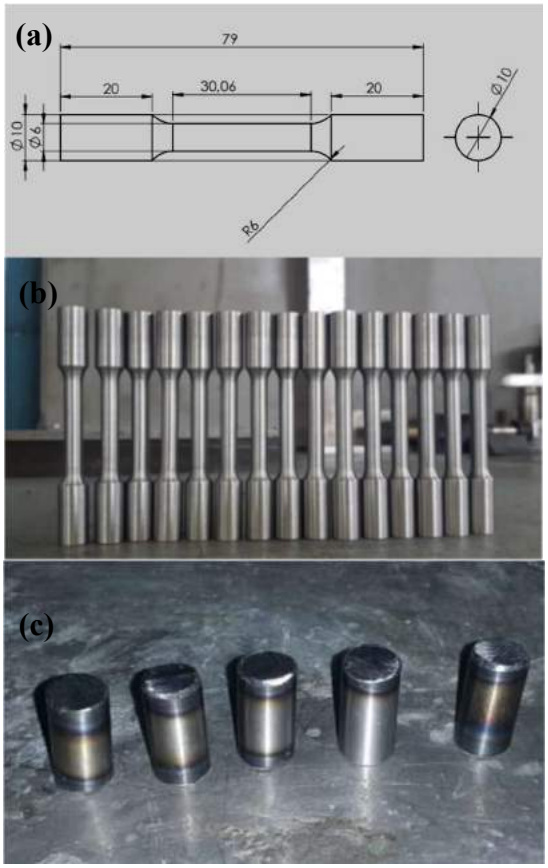

Figure 1. a) Geometric properties of tensile specimen, b) Tensile test specimen, c) Hardness and microstructure test speciemen

2.2. Heat Treatment

Heat treatment process was carried out with Protherm furnace with 1200°C capacity. Heat treatment plan of AISI 1040 steel specimens was given in Table 1.

Table 1. Plan of heat treatment

Heat treatment	Non-treated	Quenching	Quenching+ tempering	Normalizing	Spheroidizing
Process	As received	Annealing at 900°C for 1 hour	Annealing at 900°C for 1 hour	Annealing at 950°C for 1 hour	Annealing at 700°C
		Quenching in water	Quenching in water	Cool in air	Cool in furnace
			Tempering 400°C for 1 hour		

Heat treatment plan of AISI 1060 steel specimens was given in Table 2.

Table 2. Plan of heat treatment

Group no	Annealing temperature [°C]	Annealing time [hour]	Tempering temperature [°C]	Tempering time [hour]
1	-	-	-	-
2	900	1	300	1
		1	400	1
		1	500	1
		1	600	1
3	900	1	500	2
		1	500	4
		1	500	6
4	900	2	500	1
		4	500	1
		6	500	1

2.3. Tensile test

The tensile testing of the steels specimen was carried out by using Zwick universal testing machine with 3000 kg capacity until the specimen broke. Tensile speed was 3 MPa/s. View of tensile test machine was given Figure 2.

Figure 2. Tensile test machine

2.4. Hardness Measurements

Hardness measurement was carried out by LEİCA VMHT MOT micro hardness device.

2.5. Microstructure Analyses

The polished specimens were etched with nital and microstructures were examined respectively. Microstructure analyses were performed with Olympus optical microscope.

3. EXPERIMENTAL RESULTS

3.1. Experimental results of AISI 1040 steel

3.1.1. Microstructures

The microstructures of the non-treated specimen are shown in Figure 3.

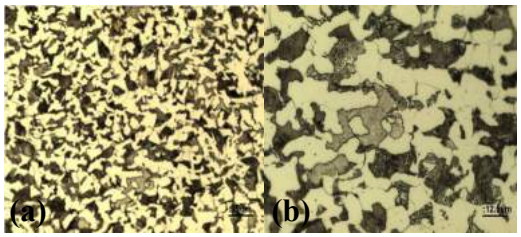

Figure 3. Microstructure of non-treated specimen a) 20X, b) 50X

The structure was consist of ferrite grains and perlite grains (ferrite phase and cementite phase composition).

The microstructures of the quenching specimen under the microscope are given in Figure 4.

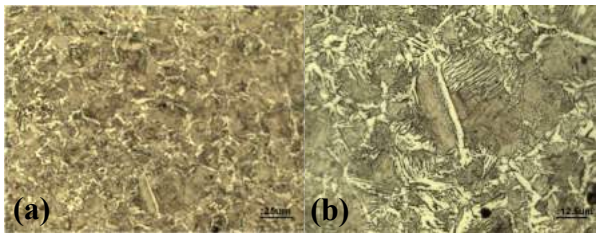

Figure 4. Microstructure of quenching specimen a) 20X, b) 50X

The structure is martensite. White areas show residual austenite. It is very hard and fragile due to high internal stresses. It cannot be used in this way, tempering must be applied.

The microstructures of the quenching + tempering specimen under the microscope are given in Figure 5.

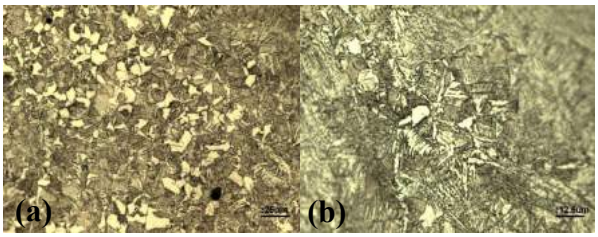

Figure 5. Microstructure of quenching + tempering specimen a) 20X, b) 50X

It is in austenite structure at 900°C and then it is brought to 400°C and the residual austenite is seen besides ferrite and perlite phases.

The microstructures of the spheroidizing specimen under the microscope are given in Figure 6.

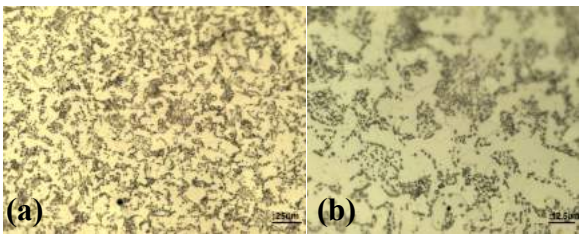

Figure 6. Microstructure of spheroidizing specimen a) 20X, b) 50X

Due to the annealing at 700 degrees, microstructure of steel has a ferrite and cementite phase. Since the steel specimen was cooled in a furnace for a long time, it was seen that the cementite particles turned into a spherical structure after annealing process. The microstructures of the normalization specimen under the microscope are given in Figure 7.

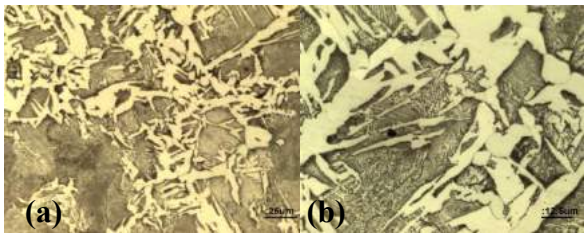

Figure 7. Microstructure of normalizing specimen a) 20X, b) 50X

Microstructure of the normalized specimen is also made up fine grained ferrite and pearlite.

3.1.2. Hardness results

The hardness of each heat treated specimens were measured 3 times in three different area of specimen and average values is given in Table 3.

Table 3. Hardness results

Heat Treatment	Hardness (HV)
Non-treated	224
Quenching	276
Quenching+ Tempering	258
Spheroidizing	163
Normalization	192

According to these results, the specimen with the highest Vickers hardness value is the non-treated specimen with 258 HV value, and the least specimen is the spheroidizing specimen with 163 HV value. The specimen with the highest hardness value from the heat treated specimens is the quenching specimen. The reason for this is that the quenching process is a type of heat treatment performed to make the steel materials more durable. The cooling rate required for this process depends on the specimen size, the tendency to harden and the quenching medium. However, the cooling rate should not be higher than necessary in order to prevent distortion, cracking and even breakage of the part. As mentioned earlier, a higher cooling rate than necessary causes cracks or distortions within the part, resulting in abnormal transformation stresses, and thus deforms by exhibiting lower strength due to internal stresses.

3.1.3. Tensile test results

Stress-strain curves obtained from tension tests are given Figure 8.

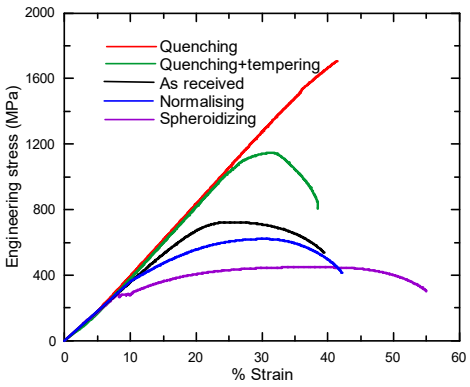

Figure 8. Stress-strain curves of tensile specimens

The highest strength was obtained in the quenched specimen. Although tensile strength is around 1700 MPa, it does not have much ductility due to its brittle fracture. The quenched specimen was brittle fractured. Tensile strength is 1100 MPa in tempered specimen after the quenched. The ductility and toughness values are high. Quenched and tempered specimen showed normal ductile breakage. After the normalization heat treatment of specimen, tensile strength increased up to 600 MPa and ductility values increased further. The specimen subjected to normalization heat treatment showed ductile fracture between spheroidizing and quenching + tempering. Tensile strength decreased and elongation values increased in spheroidizing process specimen greatly. The specimen subjected to spheroidizing heat treatment was broken with high ductility. There are many studies in the literature that support these results [2-5]. The strength of materials decreased after full annealing heat treatment due to a decrease in dislocation density [3]. Double quenching and tempering process provided significant improvement of 23% in impact toughness as compared to the conventional quenching and tempering condition [4].

The damage images of the specimens after the experiment are shown in the Figure 9.

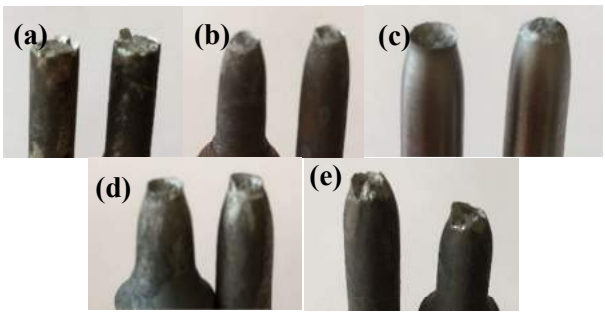

Figure 9. Specimens views after the tension tests a) quenching, b) quenching +tempering, c) as received, d) normalizing, e) spheroidizing

3.2. Experimental results of AISI 1060 steel

The effects of time and temperature parameters on the microstructure and hardness of tempering processes on AISI 1060 were given in this part. Test plan had given in Table 2. 3 different groups of experiments were planned.

Table 4. The hardness values of the specimens which were tempered at 500°C for 1 hour

Annealing time (h) at 900°C	Hardness (HV)
2	**390**
4	**388**
6	**376**

3.2.1. Hardness results

The hardness values of the specimens which were annealed at 900°C for 2, 4, 6 hours and tempered at 500°C for 1 hour are given in Table 4. Views of microstructure was given Figure 10.

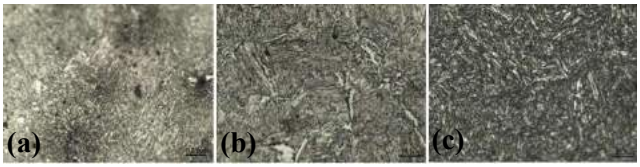

Figure 10. Views of the specimens which were annealed at 900°C for 2 (a), 4 (b), 6 (c) hours and tempered at 500°C for 1 hour

Hardness values decreased slightly with increasing annealing time.

The hardness values of the specimens which were annealed at 900°C for 1 hour and tempered at 500°C for 2, 4, 6 hours are given in Table 5. Views of microstructure was given Figure 11.

Table 5. The hardness values of the specimens which were annealed at 900°C for 1 hour

Tempering time (h) at 500°C	Hardness (HV)
2	354
4	350
6	295

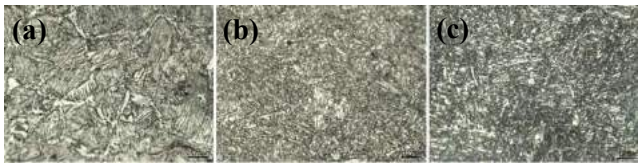

Figure 11. Views of the specimens which were annealed at 900°C for 1 hour and tempered at 500°C for 2 (a), 4 (b), 6 (c) hours

It was observed that hardness values decreased with increasing time of tempering process at same temperature.

The hardness values of the specimens which were annealed at 900°C for 1 hour and tempered at 25°C, 300°C, 400°C, 500°C, 600°C for 1 hour are given in Table 6. Views of microstructure was given Figure 12.

Table 6. The hardness values of the specimens which were annealed at 900°C for 1 hour and tempered for 1 hour

Tempering temperature (°C)	Hardness (HV)
25	728
300	669
400	527
500	480
600	483

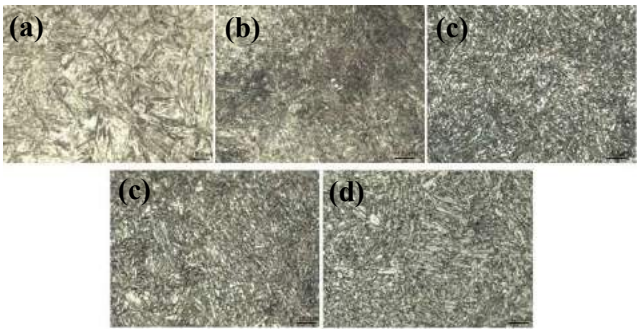

Figure 12. Views of the specimens which were annealed at 900°C for 1 hour and tempered at 25°C, 300°C, 400°C, 500°C, 600°C for 1 hour

When the microstructures were examined, it was observed that the martensitic structures formed during annealing decreased.

After 1 hour annealing at 900 ºC and tempering at 500 ºC for 2, 4 and 6 hours it was observed that hardness decreased with increasing tempering temperatures. Long-tempered steels have been found to have less hardness values than non-treated steels. It has been observed that the martensitic structures in the microstructures are further reduced. After 2, 4, 6 hours annealing at 900 ºC and 1 hour tempering at 500 ºC, hardness was examined and it was seen that there was no effective change with the duration of annealing process. Hardness values were close to each other. A significant decrease in hardness values was observed with increasing tempering temperature. Thereafter, effect of the tempering temperature after quenching process on the hardness value is very important. Similar studies have been conducted in the literature. It supported this in the studies conducted in the literature. Increasing in tempering temperature decrease the mechanical properties of materials [1,6-9]. Tempering time and annealing time have little effect on hardness.

4. CONCLUSION

In this study, effects of heat treatment on the mechanical and microstructures behavior of AISI 1040 and AISI 1060 steel were investigated experimentally. When the above results were

taken into consideration, this study primarily yielded the following conclusions:

- Hardness of 1040 steel specimens was increased only in the quenched specimen according to the non-treated state and a decrease was observed in the others.
- Highest strength and toughness values were achieved in quenched and quenched + tempered samples, respectively.
- The effect of tempering time of 1060 steel on the hardness values was found to be very small. The main important parameter was found to be tempering temperature.
- It has been found that the effect of the annealing time and tempering time in the austenite zone on the hardness is very low.

REFERENCES

[1] Y. Zhang, D. Zhan, X. Qi , Z. Jiang, "Effect of tempering temperature on the microstructure and properties of ultrahigh-strength stainless steel," Journal of Materials Science and Technology, vol.35, pp. 1240–1249, 2019.

[2] S. Ebner, C. Suppan, R. Schnitzer, C. Hofer, "Microstructure and mechanical properties of a low C steel subjected to bainitic or quenching and partitioning heat treatments," Materials Science & Engineering A, vol. 735, pp. 1–9, 2018.

[3] D. Kong, C. Dong, X. Ni, L. Zhang , J. Yao, C. Man, X. Cheng, K. Xiao, X. Li, "Mechanical properties and corrosion behavior of selective laser melted 316L stainless steel after different heat treatment processes," Journal of Materials Science & Technology, vol. 35, pp. 1499–1507, 2019.

[4] M.H. K. Sanij, S.S. G. Banadkouki, A.R. Mashreghi, M. Moshrefifar, "The effect of single and double quenching and tempering heat treatments on the microstructure and mechanical properties of AISI 4140 steel," Materials and Design, vol. 42, pp. 339–346, 2012.

[5] A. Saastamoinen, A. Kaijalainen, T. T. Nyo, P. Suikkanen, D. Porter , J. Kömi, "Direct-quenched and tempered low-C high-strength structural steel: The role of chemical composition on microstructure and mechanical properties," Materials Science & Engineering A, vol. 760, pp. 346–358, 2019.

[6] L. Xu, L. Chen, W. Sun, "Effects of soaking and tempering temperature on microstructure and mechanical properties of 65Si2MnWE spring steel," Vacuum, vol. 154, pp. 322–332, 2018.

[7] K. Chen, Z. Jiang , F. Liu, J. Yu, Y. Li, W. Gong, C. Chen, "Effect of quenching and tempering temperature on microstructure and tensile properties of microalloyed ultra-high strength suspension spring steel," Materials Science and Engineering: A, vol. 766, pp.1–11 2019.

[8] A. Saastamoinen, A. Kaijalainen , J. Heikkal, D. Porter , P. Suikkanen, "The effect of tempering temperature on microstructure, mechanical properties and bendability of direct-quenched low-alloy strip steel," Materials Science and Engineering: A, vol. 730, pp. 284–294, 2018.

[9] F. Liu, X. Lin, M. Song, H. Yang, K. Song, P. Guo, W. Huang, "Effect of tempering temperature on microstructure and mechanical properties of laser solid formed 300M steel," Journal of Alloys and Compounds, vol. 689, pp. 225–232, 2016.

[10] S. Wang, H. Yu, H. Gu, T. Zhou, L. Wang, "Effect of trace ferrite on mechanical properties of a tempered HSLA steel." Materials Science and Engineering: A, vol. 744, pp. 299–304, 2019.

[11] B. Jiang, M. Wu, M. Zhang, F. Zhao, Z. Zhao, Y. Liu, "Microstructural characterization, strengthening and toughening mechanisms of a quenched and tempered steel: Effect of heat treatment parameters," Materials Science and Engineering: A, vol. 707, pp. 306–314, 2017.

Sakarya University Journal of Science

ISSN 1301-4048 | e-ISSN 2147-835X | Period Bimonthly | Founded: 1997 | Publisher Sakarya University | http://www.saujs.sakarya.edu.tr/en/

Title: A New Single Phase Inverter Based on Buck Converter

Authors: Faruk YALÇIN, Uğur ARİFOĞLU, İrfan YAZICI
Recieved: 2020-01-27 22:45:06

Accepted: 2020-03-12 11:49:34

Article Type: Research Article
Volume: 24
Issue: 3
Month: June
Year: 2020
Pages: 480-486

How to cite
Faruk YALÇIN, Uğur ARİFOĞLU, İrfan YAZICI; (2020), A New Single Phase Inverter Based on Buck Converter. Sakarya University Journal of Science, 24(3), 480-486,
DOI: https://doi.org/10.16984/saufenbilder.680718
Access link
http://www.saujs.sakarya.edu.tr/en/issue/52472/680718

Sakarya University Journal of Science 24(3), 480-486, 2020

A New Single Phase Inverter Based on Buck Converter

Faruk YALÇIN*[1], Uğur ARİFOĞLU[2], İrfan YAZICI[3]

Abstract

In this paper, a new single phase inverter is proposed. The proposed inverter topology is obtained through modifying the well-known DC-DC buck converter to produce sine wave alternative voltage at the output. Thus, the peak value of the alternative output voltage can be provided lower than the input direct voltage value. The inverter is designed for producing alternative voltage at the output in the frequency range of 0-50 Hz. PI feedback controller is used for the control of the inverter operation. A simulation study is done for the proposed inverter and its operation in MATLAB-Simulink in order to prove its accuracy on different operation conditions. The results demonstrate that the proposed inverter can accurately produce nearly sine wave alternative voltage in various frequencies with low THD values on different operation conditions.

Keywords: single phase inverter, buck converter, THD, harmonics

1. INTRODUCTION

The inverters are the solid-state power electronics converters that produce alternative voltage from direct voltage and they can find wide application areas in the application such as asynchronous motor control, renewable energy sources, uninterruptible power supplies and power systems [1, 2]. The produced output voltage of the inverter must be as possible as close to sine wave including low total harmonic distortion (THD) to provide voltage quality [3]. According to the international standards, THD values of the alternative voltages have to be less than 5% [4].

The most traditional inverters are pulse width modulation (PWM) inverters and they are widely used in industrial applications [5]. In general, the output voltage wave forms of PWM inverters are far from sine wave because of the natural

* Corresponding Author: farukyalcin@subu.edu.tr / farukyalcin@sakarya.edu.tr
[1] Sakarya University of Applied Sciences, Faculty of Technology, Mechatronics Engineering, Sakarya, Turkey. ORCID ID: 0000-0003-2672-216X
[2] Sakarya University, Faculty of Engineering, Electrical-Electronics Engineering, Sakarya, Turkey. ORCID ID: 0000-0001-8082-5448, e-mail: arifoglu@sakarya.edu.tr
[3] Sakarya University, Faculty of Engineering, Electrical-Electronics Engineering, Sakarya, Turkey. ORCID ID: 0000-0003-3603-7051, e-mail: iyazici@sakarya.edu.tr

technique of PWM technique. However, there are many techniques to reduce the THD levels of the PWM based inverters such as sine-triangle wave comparison method [6] and selective harmonic elimination method (SHEM) [7]. In order to close the output voltage wave form to sine wave, pulse amplitude modulation (PAM) inverters are developed as an alternative instead of PWM inverters [8]. In PAM inverters, various voltage steps are produced through series connected more than one inverters or cascade connected capacitor sets. Although the PAM inverters are better than PWM inverters in terms of producing high quality output voltage, it is clear that the PAM inverters require more components, so, more physical area and cost. The main advantage of the PWM and PAM inverters is the simple controllability because the output voltage wave forms are not dependent of the load.

In recent years, switch mode inverters derived from the DC-DC converters are increasingly researched. There many topologies for boost [9], buck-boost [10] and Ćuk [11] inverters in the literature and they are successfully studied. Switch mode operation structure and naturally consisting low pass filter of these inverters provide producing closely to sine wave output voltage with low THD levels according to the PWM and PAM inverters. On the other hand, the output voltages of these inverters strictly depend on the load. So, difficult feedback control according to the PWM and PAM inverters is required for these switch mode inverters. Buck converter based single phase inverters are also studied well in the literature. Different type topologies and control techniques for the buck inverters are proposed [12-16]. In these studies, the aim of developing various topologies is enhancing the output voltage quality while reducing the number of circuit elements.

In this study, a new type buck converter based single phase inverter is proposed. The proposed inverter topology has reduced number of elements with 8 active switches, 1 inductor and 1 capacitor. The proposed inverter is controlled by a PI feedback controller. The study is tested as simulation for different test cases on MATLAB-Simulink.

2. THE PROPOSED INVERTER

In this section, the proposed single phase buck converter topology, operation procedure, dynamic analysis and control structure are given.

2.1. The Inverter Topology

The general representation of the proposed buck inverter circuit topology can be shown in Fig. 1 [17]. E, $V_i(t)$, $V_s(t)$, $V_o(t)$, L and C define the direct voltage source, inverter input voltage, input voltage of S_5 switch, inverter output voltage, the inductor and the capacitor, respectively in Fig. 1. The direct voltage source can produce a time-variant voltage, but in this paper the direct voltage source is considered as a battery. So, the input voltage of the inverter can be given as,

$$V_i(t) = E \tag{1}$$

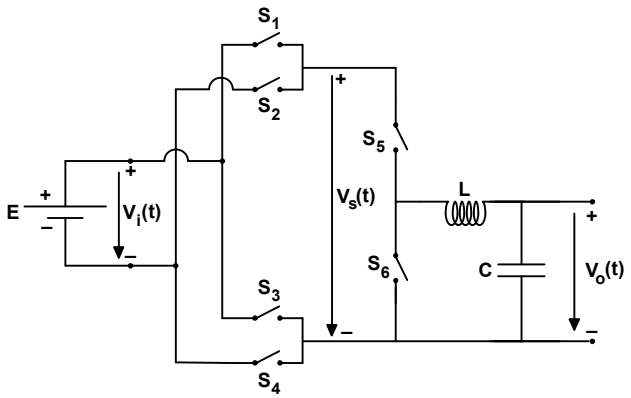

Figure 1. General representation of the inverter circuit topology

In Fig. 1, S_1, S_2, S_3, S_4 switches are unidirectional switches and S_5, S_6 switches are bidirectional active switches. The proposed inverter circuit using MOSFETs for the mentioned switches is shown in Fig. 2.

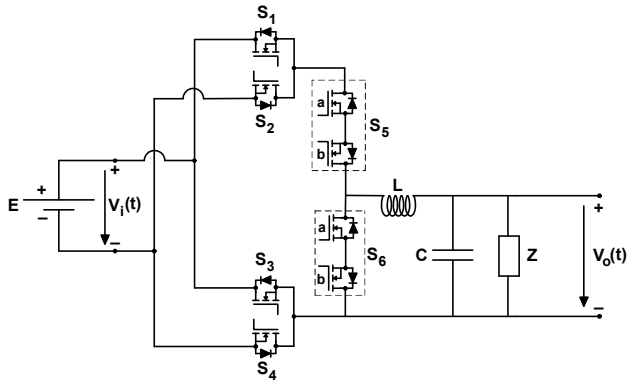

Figure 2. Proposed inverter circuit with MOSFETs

Z defines the load at the output of the inverter in Fig. 2 and it can be ohmic, inductive or capacitive.

2.2. The Procedure of the Inverter Operation

The procedure of the inverter operation can be given by the general topology shown in Fig. 1. The main energy transfer operation is based on the well-known DC-DC buck converter. As similar to the DC-DC buck converter, PWM duty ratio of S_5 switch (d) determines the relationship between the amplitudes of input and output voltages. When S_5 is turned on, S_6 is turned off. During this PWM on stage, $V_s(t)$ supplies the inductor, the capacitor and the load. So, the inductor and the capacitor are energized. S_6 is turned on and S_5 is turned off during PWM off stage. In this stage, the previously energized inductor and capacitor supply the load. Thus, the inverter output voltage is obtained lower than the input voltage depending on the S_5 switch's PWM duty ratio.

S_1, S_2, S_3, S_4 switches determines the polarity of $V_s(t)$ in order to produce alternative voltage at the inverter output. When S_1, S_4 are turned on and S_2, S_3 are turned off, $V_s(t)$ becomes equal to $V_i(t)$ with the same polarity. So, the inverter output voltage $V_o(t)$ can be produced as positive in the determined output polarity in Fig. 1. When S_2, S_3 are turned on and S_1, S_4 are turned off, $V_s(t)$ becomes equal to $V_i(t)$ but with the reverse polarity. So, the inverter output voltage $V_o(t)$ can be produced as negative in the determined output polarity in Fig. 1. Thus, in both positive and negative output voltage producing stages depending on the control of S_1, S_2, S_3, S_4 switches, ideally sine wave can be obtained through determining the PWM duty ratio of S_5 switch continually.

S_5 and S_6 bidirectional switches are built by two back to back MOSFETs as seen in Fig. 2. In positive half-wave output voltage producing stage, S_{5a} is turned on and S_{5b} is turned off to make S_5 turned on. In negative half-wave output voltage producing stage, S_{5b} is turned on and S_{5a} is turned off to make S_5 turned on. In positive half-wave output voltage producing stage, S_{6b} is turned on and S_{6a} is turned off to make S_6 turned on. In negative half-wave output voltage producing stage, S_{6a} is turned on and S_{6b} is turned off to make S_6 turned on. In both positive and negative half-wave output voltage producing stages, both S_{5a} and S_{5b} switches are turned off to make S_5 turned off. Similarly, both S_{6a} and S_{6b} switches are turned off to make S_6 turned off.

2.3. The Dynamic Analysis of the Inverter

In this section, dynamic analysis of the proposed inverter given in Fig. 2 is done in order to obtain small-signal transfer function of the inverter to be used in the feedback controller design. In the dynamic analysis of Fig. 2, all of the elements are considered as ideal and the load is considered as pure ohmic as R.

The dynamic equations of positive half-wave output voltage producing stage can be derived from Fig. 3. Fig. 3(a) represents the equivalent circuit during on stage of S_5 (S_6 is turned off) and Fig. 3(b) represents the equivalent circuit during off stage of S_5 (S_6 is turned on).

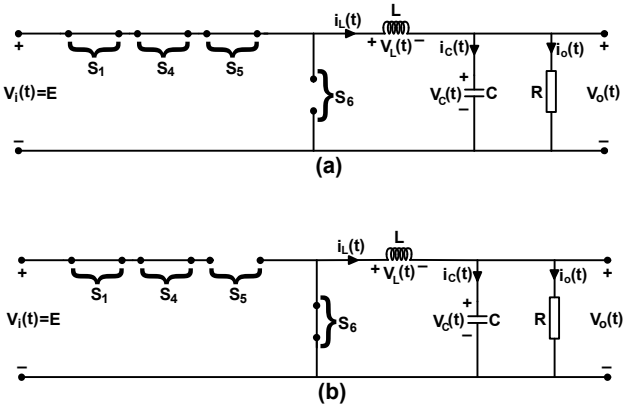

Figure 3. Equivalent circuit of the inverter during producing positive half-wave output voltage (a) On mode – S_5 is on, S_6 is off, (b) Off mode – S_6 is on, S_5 is off

***Stage 1 (on state)*:** From Fig. 3(a), the state equations for the inductor current and the output voltage can be derived as below,

$$\frac{di_L(t)}{dt} = -\frac{1}{L}V_o(t) + \frac{1}{L}V_i(t) \tag{2}$$

$$\frac{dV_o(t)}{dt} = \frac{1}{C}i_L(t) - \frac{1}{RC}V_o(t) \tag{3}$$

***Stage 2 (off state)*:** From Fig. 3(b), the state equations for the inductor current and the output voltage can be derived as below,

$$\frac{di_L(t)}{dt} = -\frac{1}{L}V_o(t) \tag{4}$$

$$\frac{dV_o(t)}{dt} = \frac{1}{C}i_L(t) - \frac{1}{RC}V_o(t) \tag{5}$$

The state-space equation for on state (stage 1) can be derived from Eq. (2) and (3) as,

$$\begin{bmatrix} \dot{i}_L(t) \\ V_o(t) \end{bmatrix} = \begin{bmatrix} 0 & -\frac{1}{L} \\ \frac{1}{C} & -\frac{1}{RC} \end{bmatrix} \begin{bmatrix} i_L(t) \\ V_o(t) \end{bmatrix} + \begin{bmatrix} \frac{1}{L} \\ 0 \end{bmatrix} V_i(t) \tag{6}$$

The state-space equation for off state (stage 2) can be derived from Eq. (4) and (5) as,

$$\begin{bmatrix} \dot{i}_L(t) \\ V_o(t) \end{bmatrix} = \begin{bmatrix} 0 & -\frac{1}{L} \\ \frac{1}{C} & -\frac{1}{RC} \end{bmatrix} \begin{bmatrix} i_L(t) \\ V_o(t) \end{bmatrix} + \begin{bmatrix} 0 \\ 0 \end{bmatrix} V_i(t) \tag{7}$$

During negative half-wave producing operation of the inverter, just only, S_2 and S_3 replaces instead of S_1 and S_4 switches in Fig. 3. And so, $V_i(t)$ and the other voltage/current representations change their polarities/directions. In this case, the state-space equations are the same as obtained in Eq. (6) and (7).

By using the state-space equations derived by Eq. (6) and (7), linearized small-signal transfer function between the PWM duty ratio of S_5 switch d and the inverter output voltage $V_o(t)$ can be derived as,

$$G_S(s) = \frac{\hat{V_o}(s)}{d(s)} = \frac{\bar{V_i}}{LC} \frac{1}{s^2 + \frac{s}{RC} + \frac{1}{LC}} \tag{8}$$

In Eq. (8), $\bar{V_i}$ defines the input voltage value at the operation point.

2.4. The Control Structure of the Inverter

The control structure of the inverter can be represented by Fig. 4.

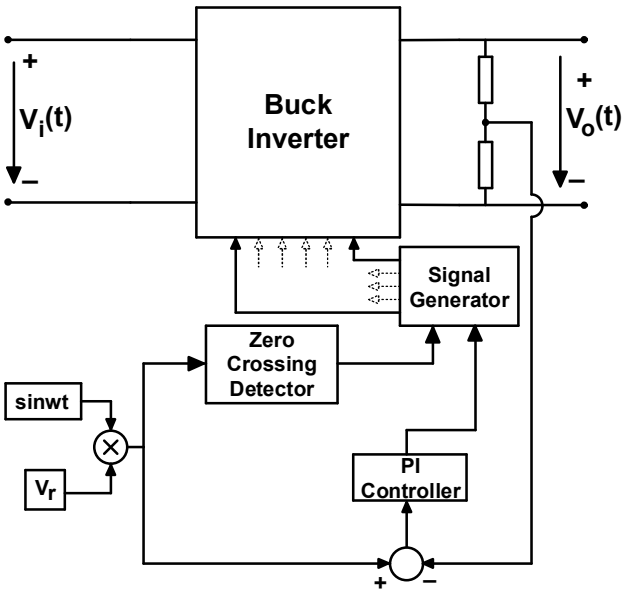

Figure 4. General inverter control structure

V_r represents the peak value of the reference output voltage that is lower than the inverter input voltage $V_i(t)$ in Fig. 4. From the figure, reference output voltage can be defined as below,

$$V_{ref}(wt) = V_r \sin wt \tag{9}$$

In Eq. (9), w represents the angular frequency. So, the desired output voltage frequency is determined by w. Thus, Eq. (9) determines both the desired frequency and amplitude of the inverter output voltage together. The signal generator generates the control signal of all of the active switches. The zero crossing detector detects the zero crossing points of the reference output voltage and determines the alternation of it. When the zero crossing detector determines the reference output voltage in positive half-wave, signal generator generates on signal for S_1, S_4 switches and generates off signal for S_2, S_3 switches. When the zero crossing detector determines the reference output voltage in negative half-wave, signal generator generates off signal for S_1, S_4 switches and generates on signal for S_2, S_3 switches.

The PI feedback controller compensates the error between reference and actual output voltages and eliminates the error. Thus, it provides to obtain desired duty ratio of S_5 switch (d) to produce the reference voltage at the output of the inverter. The control block diagram of the closed loop inverter operation system can be given in Fig. 5.

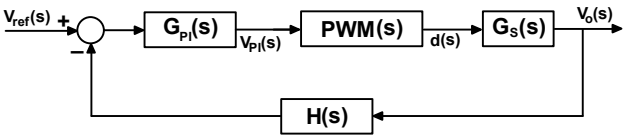

Figure 5. Control block diagram of the inverter

In Fig. 5, $G_{PI}(s)$, $PWM(s)$ and $H(s)$ define the transfer functions of PI controller, measurement stage and PWM stage of duty, respectively. $G_{PI}(s)$ is described as,

$$G_{PI}(s) = K_P + K_I / s\,. \tag{10}$$

3. THE SIMULATION RESULTS

In order to prove the accuracy of the proposed inverter and its control, a simulation study is done in MATLAB-Simulink. Switching frequency of S_5 switch is selected as $f_s = 20kHz$. The study is tested on three different cases.

Test case 1: In case 1, inverter input voltage is selected as 75V. The amplitude and the frequency of the desired sine wave inverter output voltage are determined as 30V and 50Hz, respectively. A pure ohmic load with the value of 3Ω is connected to the inverter output. The obtained voltage and current wave forms of the inverter output for case 1 are given in Fig. 6.

As seen from Fig. 6, the desired output voltage is obtained at the output of the inverter closely to sine wave with the determined amplitude and frequency. THD value of the output voltage is measured as THD_V=1.547. As the load is pure ohmic, THD value of the output current is measured identical to THD_V as THD_I=THD_V=1.547.

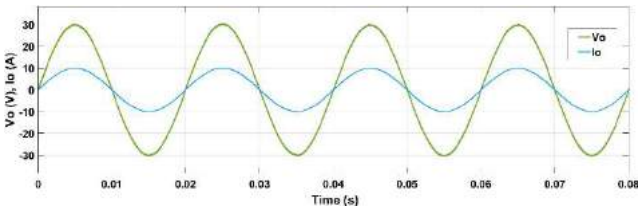

Figure 6. Inverter output wave forms for case 1

Test case 2: In case 2, inverter input voltage is selected as 90V. The amplitude and the frequency of the desired sine wave inverter output voltage are determined as 50V and 30Hz, respectively. An inductive load with the resistor value of 7Ω and the inductor value of 4.7mH is connected to the inverter output. The obtained voltage and current wave forms of the inverter output for case 2 are given in Fig. 7.

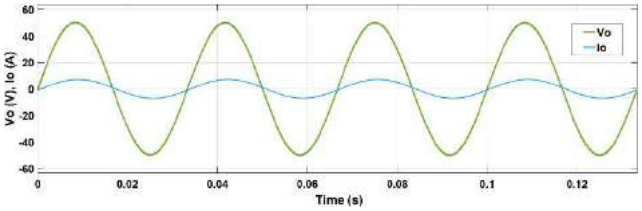

Figure 7. Inverter output wave forms for case 2

As seen from Fig. 7, the desired output voltage is obtained at the output of the inverter closely to sine wave with the determined amplitude and frequency. THD value of the output voltage is measured as THD_V=1.763. THD value of the output current is measured as THD_I= 0.459. It is clear that the inductive characteristic of the load reduces the high order harmonics of the output current.

Test case 3: In case 3, inverter input voltage is selected as 110V. The amplitude and the frequency of the desired sine wave inverter output voltage are determined as 90V and 10Hz, respectively. A capacitive load with the resistor value of 5Ω and the capacitor value of 10mF is connected to the inverter output. The obtained voltage and current wave forms of the inverter output for case 3 are given in Fig. 8.

As seen from Fig. 8, the desired output voltage is obtained at the output of the inverter closely to sine wave with the determined amplitude and frequency. THD value of the output voltage is measured as THD_V=1.665. THD value of the output current is measured as THD_I= 3.452. It is clear that the capacitive characteristic of the load increases the high order harmonics of the output current.

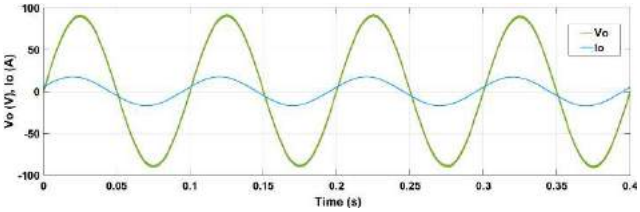

Figure 8. Inverter output wave forms for case 3

The simulation results show that the proposed inverter can produce close to sine wave output voltage with low THD values in various frequencies on different input and output operation conditions.

4. CONCLUSION

This study presents a novel single phase inverter based on buck converter. The inverter can produce alternative voltage at the output in the frequency range of 0-50 Hz close to sine wave. The simulation results on MATLAB-Simulink prove that the proposed inverter can successfully produce close to sine wave inverter output voltage in various frequencies with low THD values less than 5% on different operation conditions. The comprehensive experimental design study of the proposed inverter is still being proceeded on a supported research project given in the acknowledgements.

ACKNOWLEDGMENTS

This study is supported by Sakarya University of Applied Sciences Scientific Research Projects Coordination Unit. Project Number: 2018-09-18-001.

REFERENCES

[1] S. G. Song, S. J. Park, Y. H. Joung, and F. S. Kang, “Multilevel inverter using cascaded 3-

phase transformers with common-arm configuration," Electric Power System Research, vol. 81, no. 8, pp. 1672–1680, 2011.

[2] L. K. Haw, M. S. A. Dahidah, and H. A. F. Almurib, "SHE-PWM cascaded multilevel inverter with adjustable DC voltage levels control for STATCOM applications," IEEE Transactions on Power Electronics, vol. 29, no. 12, pp. 6433–6444, 2014.

[3] M. Malarvizhi and I. Gnanambal, "An integrated technique for eliminating harmonics of multilevel inverter with unequal DC sources," International Journal of Electronics, vol. 102, no. 2, pp. 293–311, 2015.

[4] 'Harmonics and IEEE 519', http://energylogix.ca/harmonics_and_ieee.pdf, accessed 24 January 2020.

[5] P. C. Sen, "Power Electronics," New Delhi: McGraw-Hill, 2008.

[6] N. Mohan, T. M. Undeland, and W. P. Robbins, "Power Electronics: Converters, Applications, and Design," USA: John Wiley & Sons Inc., 2003.

[7] M. Narimani and G. Mochopoulos, "Selective harmonic elimination in three-phase multi-module voltage source inverters," 27th Annual IEEE Applied Power Electronics Conference and Exposition, pp 1562–1567, 2012.

[8] K. Taniguchi and A. Okumura, "A PAM inverter system for vector control of induction motor," Power Conversion Conference, pp. 478–483, 1993.

[9] F. Flores-Bahamonde, H. Valderrama-Blavi, J. Maria Bosque-Moncusi, G. Garcia, and L. Martinez-Salamero, "Using the sliding-mode control approach for analysis and design of the boost inverter," IET Power Electronics, vol. 9, no. 8, pp. 1625–1634, 2016.

[10] M. Lee, J. W. Kim, and J. S. Lai, "Single inductor dual buck-boost inverter based on half-cycle PWM scheme with active clamping devices," IET Power Electronics, vol. 12, no. 5, pp. 1011–1020, 2019.

[11] S. Mehrnami and S. K. Mazumder, "Discontinuous modulation scheme for a differential-mode Cuk inverter," IEEE Transactions on Power Electronics, vol. 30, no. 3, pp. 1242–1254, 2015.

[12] L. Zhang, T. Zhang, Y. Hao, and B. Wang, "Two-stage dual-buck grid-tied inverters with efficiency enhancement," IEEE Applied Power Electronics Conference and Exposition, pp. 3251–3256, 2019.

[13] B. L. H. Nguyen, H. Cha, and H. G. Kim, "Single-phase six-switch dual-output inverter using dual-buck structure," IEEE Transactions on Power Electronics, vol. 33, no. 9, pp. 7894–7903, 2018.

[14] Y. Dai, Z. Guan, R. Zhang, S. Zhuang, and Y. Wang, "Research on common-mode leakage current for a novel non-isolated dual-buck photovoltaic grid-connected inverter," IEICE Electronics Express, vol. 15, no. 12, pp. 1–10, 2018.

[15] F. Hong, Y. Wu, Z. Ye, B. Ji, and Y. Zhou, "A passive lossless soft-switching single inductor dual buck full-bridge inverter," Journal of Power Electronics, vol. 18, no. 2, pp. 364–374, 2018.

[16] J. Singh, R. Dahiya, and L. M. Saini, "Buck converter–based cascaded asymmetrical multilevel inverter with reduced components," International Transactions on Electrical Energy Systems, vol. 28, no. 3, e2501, pp. 1–17, 2018.

[17] F. Yalcin, "Single phase inverter based on buck converter," Turkish Patent Institute, TR 2015 01818 B, filed 16.02.2015, applied 21.02.2018.

JOURNAL OF SCIENCE
SAKARYA UNIVERSITY

Sakarya University Journal of Science

ISSN 1301-4048 | e-ISSN 2147-835X | Period Bimonthly | Founded: 1997 | Publisher Sakarya University | http://www.saujs.sakarya.edu.tr/en/

Title: Left-sided Hermite-Hadamard Type Inequalities for Trigonometrically P-functions

Authors: Kerim BEKAR
Recieved: 2020-01-09 16:51:27

Accepted: 2020-03-17 20:48:12

Article Type: Research Article
Volume: 24
Issue: 3
Month: June
Year: 2020
Pages: 487-493

How to cite
Kerim BEKAR; (2020), Left-sided Hermite-Hadamard Type Inequalities for Trigonometrically P-functions. Sakarya University Journal of Science, 24(3), 487-493, DOI: https://doi.org/10.16984/saufenbilder.672838
Access link
http://www.saujs.sakarya.edu.tr/en/issue/52472/672838

Sakarya University Journal of Science 24(3), 487-493, 2020

Left-sided Hermite-Hadamard Type Inequalities for Trigonometrically P-Functions

Kerim BEKAR[*1]

Abstract

In this paper, we obtain refinements of the left-sided Hermite-Hadamard inequality for functions whose first derivatives in absolute value are trigonometrically P-function.

Keywords: Convex function, trigonometrically convex function, trigonometrically P-functions, Hermite-Hadamard inequality

1. INTRODUCTION

Convexity theory provides powerful principles and techniques to study a wide class of problems in both pure and applied mathematics. See articles [2, 4, 7, 9, 11, 12] and the references therein.

Throughout the paper I is a non-empty interval in $\mathbb{R}$. Let $f:I\to\mathbb{R}$ be a convex function. Then the following inequality hold

$$f\left(\frac{a+b}{2}\right)\leq\frac{1}{b-a}\int_a^b f(x)dx\leq\frac{f(a)+f(b)}{2}$$

for all $a,b\in I$ with $a<b$. This double inequality is well known as the Hermite-Hadamard inequality (for more information, see [5]). Since then, some refinements of the Hermite-Hadamard inequality for convex functions have been obtained [3, 14].

Definition 1. [4] *A non-negative function $f:I\to\mathbb{R}$ is said to be a P-function if the inequality*

$$f(tx+(1-t)y)\leq f(x)+f(y)$$

holds for all $x,y\in I$ and $t\in[0,1]$. The set of P-functions on the interval I is denoted by $P(I)$.

Definition 2. [13] *Let $h:J\to\mathbb{R}$ be a non-negative function, $h\neq 0$. We say that $f:I\to\mathbb{R}$ is an h-convex function, or that f belongs to the class $SX(h,I)$, if f is non-negative and for all $x,y\in I$, $\alpha\in(0,1)$ we have*

$$f(\alpha x+(1-\alpha)y)\leq h(\alpha)f(x)+h(1-\alpha)f(y).$$

If this inequality is reversed, then f is said to be h-concave, i.e. $f\in SV(h,I)$.

[*]Corresponding Author: kebekar@gmail.com
[1] Department of Mathematics, Faculty of Arts and Sciences, Giresun University, 28200, Giresun-Turkey
ORCID ID: 0000-0002-7531-9345

In [8], Kadakal gave the concept of trigonometrically convex function as follows:

Definition 3. [8] *A non-negative function* $f: I \to \mathbb{R}$ *is called trigonometrically convex if for every* $x, y \in I$ *and* $t \in [0,1]$,

$$f(tx + (1-t)y) \leq \left(sin\frac{\pi t}{2}\right) f(x) + \left(cos\frac{\pi t}{2}\right) f(y).$$

The class of all trigonometrically convex functions is denoted by $TC(I)$ on interval I.

In [1], Bekar gave the concept of trigonometrically P-function as follows:

Definition 4. [1] *A non-negative function* $f: I \to \mathbb{R}$ *is called trigonometrically P-functions if for every* $x, y \in I$ *and* $t \in [0,1]$,

$$f(tx + (1-t)y) \leq \left(\sin\frac{\pi t}{2} + \cos\frac{\pi t}{2}\right)[f(x) + f(y)].$$

We will denote by $TP(I)$ the class of all trigonometrically P-functions on interval I. The range of the trigonometrically P-functions is greater than or equal to 0. Every non-negative trigonometrically convex function is trigonometrically P-functions. We note that, every trigonometrically convex function is a h-convex function for $h(t) = \sin\frac{\pi t}{2}$. Morever, if $f(x)$ is a nonnegative function, then every trigonometric convex function is a P-function.

We will denote by $L[a,b]$ the space of (Lebesgue) integrable functions on the interval $[a,b]$.

In [1], Bekar also obtained the following Hermite-Hadamard type inequalities for the trigonometrically P-function as follows:

Theorem 1. *Let the function* $f: [a,b] \to \mathbb{R}$ *be a trigonometrically P-function. If* $a < b$ *and* $f \in L[a,b]$, *then the following inequality holds:*

$$\frac{1}{2\sqrt{2}} f\left(\frac{a+b}{2}\right) \leq \frac{1}{b-a}\int_a^b f(x)dx \leq \frac{4}{\pi}[f(a) + f(b)].$$

In [6], İşcan gave a refinement of the Hölder integral inequality as follows:

Theorem 2. [6] *Let* $p > 1$ *and* $\frac{1}{p} + \frac{1}{q} = 1$. *If* f *and* g *are real functions defined on interval* $[a,b]$ *and if* $|f|^p$, $|g|^q$ *are integrable functions on* $[a,b]$ *then*

$$\int_a^b |f(x)g(x)|dx \leq \frac{1}{b-a}\left\{\left(\int_a^b (b-x)|f(x)|^p dx\right)^{\frac{1}{p}} \times \left(\int_a^b (b-x)|g(x)|^q dx\right)^{\frac{1}{q}} + \left(\int_a^b (x-a)|f(x)|^p dx\right)^{\frac{1}{p}} \times \left(\int_a^b (x-a)|g(x)|^q dx\right)^{\frac{1}{q}}\right\}.$$

2. SOME NEW INEQUALITIES FOR TRIGONOMETRICALLY *P*-FUNCTION

The main purpose of this section is to establish new estimates that refine left-sided Hermite-Hadamard inequality for functions whose first derivative in absolute value, raised to a certain power which is greater than one, respectively at least one, is trigonometrically P-function. Kırmacı [10] used the following lemma:

Lemma 1. *Let* $f: I^* \subset \mathbb{R} \to \mathbb{R}$ *be differentiable mapping on* I^*, $a, b \in I^\circ$ *(*I^* *is the interior of I) with* $a < b$. *If* $f' \in L[a,b]$, *then we have*

$$\frac{1}{b-a}\int_a^b f(x)dx - f\left(\frac{a+b}{2}\right) = (b-a)\left[\begin{array}{c}\int_0^{\frac{1}{2}} tf'(ta + (1-t)b)dt \\ + \int_{\frac{1}{2}}^1 (t-1)f'(ta + (1-t)b)dt\end{array}\right]$$

for $t \in [0,1]$.

Theorem 3. *Let* $f: I \to \mathbb{R}$ *be a continuously differentiable function, let* $a < b$ *in I and assume that* $f' \in L[a,b]$. *If* $|f'|$ *is trigonometrically P-function on interval* $[a,b]$, *then the following inequality*

$$\left|\frac{1}{b-a}\int_a^b f(x)dx - f\left(\frac{a+b}{2}\right)\right| \leq 16(b-a)\left(\frac{\sqrt{2}-1}{\pi^2}\right) A(|f'(a)|, |f'(b)|)$$

holds for $t \in [0,1]$, where A is the arithmetic mean.

Proof. Using Lemma 1 and the inequality

$$|f'(ta+(1-t)b)|$$

$$\leq \left(sin\frac{\pi t}{2}+cos\frac{\pi t}{2}\right)[|f'(a)|+|f'(b)|],$$

we get

$$\left|\frac{1}{b-a}\int_a^b f(x)dx - f\left(\frac{a+b}{2}\right)\right|$$

$$\leq (b-a)\left[\begin{matrix}\int_0^{\frac{1}{2}} |t||f'(ta+(1-t)b)|dt \\ +\int_{\frac{1}{2}}^1 |t-1||f'(ta+(1-t)b)|dt\end{matrix}\right]$$

$$\leq (b-a)\left[\int_0^{\frac{1}{2}} |t|\left(\sin\frac{\pi t}{2}+\cos\frac{\pi t}{2}\right)[|f'(a)|+|f'(b)|]dt\right.$$

$$\left.+\int_{\frac{1}{2}}^1 |t-1|\left(\sin\frac{\pi t}{2}+\cos\frac{\pi t}{2}\right)[|f'(a)|+|f'(b)|]dt\right]$$

$$=(b-a)[|f'(a)|+|f'(b)|]$$

$$\times\left[\int_0^{\frac{1}{2}} |t|\left(\sin\frac{\pi t}{2}+\cos\frac{\pi t}{2}\right)dt\right.$$

$$\left.+\int_{\frac{1}{2}}^1 |t-1|\left(\sin\frac{\pi t}{2}+\cos\frac{\pi t}{2}\right)dt\right]$$

$$=2(b-a)[|f'(a)|+|f'(b)|]\left(\frac{4(\sqrt{2}-1)}{\pi^2}\right)$$

$$=16(b-a)\left(\frac{\sqrt{2}-1}{\pi^2}\right)A(|f'(a)|,|f'(b)|),$$

where

$$\int_0^{\frac{1}{2}} |t|\left(\sin\frac{\pi t}{2}+\cos\frac{\pi t}{2}\right)dt=\frac{4(\sqrt{2}-1)}{\pi^2}$$

$$\int_{\frac{1}{2}}^1 |t-1|\left(\sin\frac{\pi t}{2}+\cos\frac{\pi t}{2}\right)dt=\frac{4(\sqrt{2}-1)}{\pi^2}.$$

This completes the proof of the theorem.

Theorem 4. *Let $f:I\to\mathbb{R}$ be a continuously differentiable function, let $a<b$ in I and assume that $q>1$. If $|f'|^q$ is a trigonometrically P-function on interval $[a,b]$, then the following inequality*

$$\left|\frac{1}{b-a}\int_a^b f(x)dx - f\left(\frac{a+b}{2}\right)\right|$$

$$\leq 2^{\frac{3}{q}-1}\left(\frac{1}{\pi}\right)^{\frac{1}{q}}\left(\frac{1}{p+1}\right)^{\frac{1}{p}}(b-a)A^{\frac{1}{q}}(|f'(a)|^q,|f'(b)|^q)$$

holds for $t\in[0,1]$, where $\frac{1}{p}+\frac{1}{q}=1$ and A is the arithmetic mean.

Proof. Using Lemma 1, Hölder's integral inequality and the following inequality

$$|f'(ta+(1-t)b)|^q$$

$$\leq \left(sin\frac{\pi t}{2}+cos\frac{\pi t}{2}\right)[|f'(a)|^q+|f'(b)|^q]$$

which comes from the definition of trigonometrically P-function for $|f'|^q$, we get

$$\left|\frac{1}{b-a}\int_a^b f(x)dx - f\left(\frac{a+b}{2}\right)\right|$$

$$\leq \left|(b-a)\left[\begin{matrix}\int_0^{\frac{1}{2}} tf'(ta+(1-t)b)dt \\ +\int_{\frac{1}{2}}^1 (t-1)f'(ta+(1-t)b)dt\end{matrix}\right]\right|$$

$$\leq (b-a)\left(\int_0^{\frac{1}{2}} |t|^p dt\right)^{\frac{1}{p}}$$

$$\times\left(\int_0^{\frac{1}{2}} |f'(ta+(1-t)b)|^q dt\right)^{\frac{1}{q}}$$

$$+(b-a)\left(\int_{\frac{1}{2}}^1 |t-1|^p dt\right)^{\frac{1}{p}}\left(\int_{\frac{1}{2}}^1 |f'(ta+(1-t)b)|^q dt\right)^{\frac{1}{q}}$$

$$\leq (b-a)\left(\int_0^{\frac{1}{2}} |t|^p dt\right)^{\frac{1}{p}}$$

$$\times\left(\int_0^{\frac{1}{2}}\left(\ sin\frac{\pi t}{2}+cos\frac{\pi t}{2}\right)[|f'(a)|^q+|f'(b)|^q]dt\right)^{\frac{1}{q}}$$

$$+(b-a)\left(\int_{\frac{1}{2}}^1 |t-1|^p dt\right)^{\frac{1}{p}}$$

$$\times\left(\int_{\frac{1}{2}}^{1}\left(\sin\frac{\pi t}{2}+\cos\frac{\pi t}{2}\right)[|f'(a)|^q+|f'(b)|^q]dt\right)^{\frac{1}{q}}$$

$$=(b-a)2^{\frac{1}{q}}A^{\frac{1}{q}}(|f'(a)|^q,|f'(b)|^q)$$

$$\times\left(\frac{1}{(p+1)2^{p+1}}\right)^{\frac{1}{p}}\left[\int_0^1\left(\sin\frac{\pi t}{2}+\cos\frac{\pi t}{2}\right)dt\right]^{\frac{1}{q}}$$

$$+(b-a)2^{\frac{1}{q}}A^{\frac{1}{q}}(|f'(a)|^q,|f'(b)|^q)$$

$$\times\left(\frac{1}{(p+1)2^{p+1}}\right)^{\frac{1}{p}}\left[\int_{\frac{1}{2}}^{1}\left(\sin\frac{\pi t}{2}+\cos\frac{\pi t}{2}\right)dt\right]^{\frac{1}{q}}$$

$$=2^{\frac{3}{q}-1}\left(\frac{1}{\pi}\right)^{\frac{1}{q}}\left(\frac{1}{p+1}\right)^{\frac{1}{p}}(b-a)A^{\frac{1}{q}}(|f'(a)|^q,|f'(b)|^q),$$

where

$$\int_0^{\frac{1}{2}}|t|^p dt=\int_{\frac{1}{2}}^{1}|t-1|^p dt=\frac{1}{(p+1)2^{p+1}}$$

$$\int_0^{\frac{1}{2}}\left(\sin\frac{\pi t}{2}+\cos\frac{\pi t}{2}\right)dt=\frac{2}{\pi}$$

$$\int_{\frac{1}{2}}^{1}\left(\sin\frac{\pi t}{2}+\cos\frac{\pi t}{2}\right)dt=\frac{2}{\pi}.$$

This completes the proof of the theorem.

Theorem 5. *Let $f:I\subseteq\mathbb{R}\to\mathbb{R}$ be a continuously differentiable function, let $a<b$ in I and assume that $q\geq 1$. If $|f'|^q$ is a trigonometrically P-function on the interval $[a,b]$, then the following inequality holds for $t\in[0,1]$*

$$\left|\frac{1}{b-a}\int_a^b f(x)dx-f\left(\frac{a+b}{2}\right)\right|$$

$$\leq(b-a)2^{\frac{6}{q}-2}A^{\frac{1}{q}}(|f'(a)|^q,|f'(b)|^q)\left(\frac{\sqrt{2}-1}{\pi^2}\right)^{\frac{1}{q}},$$

where *A* is the arithmetic mean.

Proof. Assume first that $q>1$. From Lemma 1, Hölder integral inequality and the property of $|f'|^q$ which is trigonometrically *P*-function, we obtain

$$\left|\frac{1}{b-a}\int_a^b f(x)dx-f\left(\frac{a+b}{2}\right)\right|\leq(b-a)\left(\int_0^{\frac{1}{2}}|t|dt\right)^{1-\frac{1}{q}}$$

$$\times\left(\int_0^{\frac{1}{2}}|t||f'(ta+(1-t)b)|^q dt\right)^{\frac{1}{q}}$$

$$+(b-a)\left(\int_{\frac{1}{2}}^{1}|t-1|dt\right)^{1-\frac{1}{q}}$$

$$\times\left(\int_{\frac{1}{2}}^{1}|t-1||f'(ta+(1-t)b)|^q dt\right)^{\frac{1}{q}}$$

$$\leq(b-a)\left(\int_0^{\frac{1}{2}}|t|dt\right)^{1-\frac{1}{q}}$$

$$\times\left(\int_0^{\frac{1}{2}}|t|\left(\sin\frac{\pi t}{2}+\cos\frac{\pi t}{2}\right)[|f'(a)|^q+|f'(b)|^q]dt\right)^{\frac{1}{q}}$$

$$+(b-a)\left(\int_{\frac{1}{2}}^{1}|t-1|dt\right)^{1-\frac{1}{q}}$$

$$\times\left(\int_{\frac{1}{2}}^{1}|t-1|\left(\sin\frac{\pi t}{2}+\cos\frac{\pi t}{2}\right)[|f'(a)|^q+|f'(b)|^q]dt\right)^{\frac{1}{q}}$$

$$=2(b-a)\left(\frac{1}{8}\right)^{1-\frac{1}{q}}8^{\frac{1}{q}}A^{\frac{1}{q}}(|f'(a)|^q,|f'(b)|^q)\left(\frac{4(\sqrt{2}-1)}{\pi^2}\right)^{\frac{1}{q}}$$

$$=(b-a)2^{\frac{6}{q}-2}A^{\frac{1}{q}}(|f'(a)|^q,|f'(b)|^q)\left(\frac{\sqrt{2}-1}{\pi^2}\right)^{\frac{1}{q}}.$$

It can be seen that

$$\int_0^{\frac{1}{2}}|t|dt=\int_{\frac{1}{2}}^{1}|t-1|dt=\frac{1}{8}$$

$$\int_0^{\frac{1}{2}}|t|\left(\sin\frac{\pi t}{2}+\cos\frac{\pi t}{2}\right)dt=\frac{4(\sqrt{2}-1)}{\pi^2}$$

$$\int_{\frac{1}{2}}^{1}|t-1|\left(\sin\frac{\pi t}{2}+\cos\frac{\pi t}{2}\right)dt=\frac{4(\sqrt{2}-1)}{\pi^2}.$$

Therefore, the desired result is obtained.

For $q=1$ we use the estimates from the proof of the Theorem 3, which also follow step by step the above estimates.

This completes the proof of the theorem.

Corollary 1. *Under the assumption of the Theorem 5 with $q = 1$, we get the conclusion of the Theorem 3.*

Theorem 6. *Let $f: I \to \mathbb{R}$ be a continuously differentiable function, let $a < b$ in I and assume that $q > 1$. If $|f'|^q$ is a trigonometrically P-function on interval $[a, b]$, then the following inequality*

$$\left|\frac{1}{b-a}\int_a^b f(x)dx - f\left(\frac{a+b}{2}\right)\right|$$

$$\leq 2^{\frac{1}{q}+2}(b-a)A^{\frac{1}{q}}(|f'(a)|^q, |f'(b)|^q)\left(\frac{1}{p+2}\right)^{\frac{1}{p}}$$

$$\times\left[\left(\frac{1}{p+1}\right)^{\frac{1}{p}}\left(\frac{\pi-4\sqrt{2}+4}{\pi^2}\right)^{\frac{1}{q}} + \left(\frac{4\sqrt{2}-4}{\pi^2}\right)^{\frac{1}{q}}\right]$$

holds for $t \in [0,1]$, where $\frac{1}{p}+\frac{1}{q}=1$ and A is the arithmetic mean.

Proof. Using Lemma 1, Hölder-İşcan integral inequality and the following inequality

$$|f'(ta+(1-t)b)|^q$$

$$\leq \left(sin\frac{\pi t}{2} + cos\frac{\pi t}{2}\right)[|f'(a)|^q + |f'(b)|^q]$$

which comes from the definition of trigonometrically P-function for $|f'|^q$, we get

$$\left|\frac{1}{b-a}\int_a^b f(x)dx - f\left(\frac{a+b}{2}\right)\right|$$

$$\leq (b-a)\begin{bmatrix}\int_0^{\frac{1}{2}} |t||f'(ta+(1-t)b)|dt \\ +\int_{\frac{1}{2}}^1 |t-1||f'(ta+(1-t)b)|dt\end{bmatrix}$$

$$\leq 2(b-a)\left[\left(\int_0^{\frac{1}{2}}\left|\frac{1}{2}-t\right||t|^p dt\right)^{\frac{1}{p}}\right.$$

$$\times\left(\int_0^{\frac{1}{2}}\left|\frac{1}{2}-t\right||f'(ta+(1-t)b)|^q dt\right)^{\frac{1}{q}}$$

$$+\left(\int_0^{\frac{1}{2}}|t||t|^p dt\right)^{\frac{1}{p}}\left(\int_0^{\frac{1}{2}}|t||f'(ta+(1-t)b)|^q dt\right)^{\frac{1}{q}}$$

$$+\left(\int_{\frac{1}{2}}^1 |1-t||t-1|^p dt\right)^{\frac{1}{p}}$$

$$\times\left(\int_{\frac{1}{2}}^1 |1-t||f'(ta+(1-t)b)|^q dt\right)^{\frac{1}{q}}$$

$$+\left(\int_{\frac{1}{2}}^1\left|t-\frac{1}{2}\right||t-1|^p dt\right)^{\frac{1}{p}}$$

$$\left.\left(\int_{\frac{1}{2}}^1\left|t-\frac{1}{2}\right||f'(ta+(1-t)b)|^q dt\right)^{\frac{1}{q}}\right]$$

$$\leq 2(b-a)\left[\left(\int_0^{\frac{1}{2}}\left|\frac{1}{2}-t\right||t|^p dt\right)^{\frac{1}{p}}\right.$$

$$\times\left(\int_0^{\frac{1}{2}}\left|\frac{1}{2}-t\right|\left(\sin\frac{\pi t}{2}+\cos\frac{\pi t}{2}\right)[|f'(a)|^q+|f'(b)|^q]dt\right)^{\frac{1}{q}}$$

$$+\left(\int_0^{\frac{1}{2}}|t||t|^p dt\right)^{\frac{1}{p}}$$

$$\times\left(\int_0^{\frac{1}{2}}|t|\left(\sin\frac{\pi t}{2}+\cos\frac{\pi t}{2}\right)[|f'(a)|^q+|f'(b)|^q]dt\right)^{\frac{1}{q}}$$

$$+\left(\int_{\frac{1}{2}}^1 |1-t||t-1|^p dt\right)^{\frac{1}{p}}$$

$$\times\left(\int_{\frac{1}{2}}^1 |1-t|\left(\sin\frac{\pi t}{2}+\cos\frac{\pi t}{2}\right)[|f'(a)|^q+|f'(b)|^q]dt\right)^{\frac{1}{q}}$$

$$+\left(\int_{\frac{1}{2}}^1\left|t-\frac{1}{2}\right||t-1|^p dt\right)^{\frac{1}{p}}$$

$$\times\left(\int_{\frac{1}{2}}^1\left|t-\frac{1}{2}\right|\left(\sin\frac{\pi t}{2}+\cos\frac{\pi t}{2}\right)[|f'(a)|^q+\right.$$

$$\left.|f'(b)|^q]dt\right)^{\frac{1}{q}}\Bigg]$$

$$= 2^{1+\frac{1}{q}}(b-a)A^{\frac{1}{q}}(|f'(a)|^q, |f'(b)|^q)$$

$$\times\left[\left(\frac{2^{-(p+2)}}{(p+1)(p+2)}\right)^{\frac{1}{p}}\left(\frac{\pi-4\sqrt{2}+4}{\pi^2}\right)^{\frac{1}{q}}\right.$$

$$+\left(\frac{2^{-(p+2)}}{p+2}\right)^{\frac{1}{p}}\left(\frac{4\sqrt{2}-4}{\pi^2}\right)^{\frac{1}{q}}+\left(\frac{2^{-(p+2)}}{p+2}\right)^{\frac{1}{p}}\left(\frac{4\sqrt{2}-4}{\pi^2}\right)^{\frac{1}{q}}$$

$$+\left(\frac{2^{-(p+2)}}{(p+1)(p+2)}\right)^{\frac{1}{p}}\left(\frac{\pi-4\sqrt{2}+4}{\pi^2}\right)^{\frac{1}{q}}\Bigg]$$

$$=2^{\frac{1}{q}+2}(b-a)A^{\frac{1}{q}}(|f'(a)|^q,|f'(b)|^q)\left(\frac{1}{p+2}\right)^{\frac{1}{p}}$$

$$\times\left[\left(\frac{1}{p+1}\right)^{\frac{1}{p}}\left(\frac{\pi-4\sqrt{2}+4}{\pi^2}\right)^{\frac{1}{q}}+\left(\frac{4\sqrt{2}-4}{\pi^2}\right)^{\frac{1}{q}}\right]$$

where

$$\int_0^{\frac{1}{2}}\left|\frac{1}{2}-t\right||t|^p dt=\frac{2^{-(p+2)}}{(p+1)(p+2)}$$

$$\int_{\frac{1}{2}}^1\left|t-\frac{1}{2}\right||t-1|^p dt=\frac{2^{-(p+2)}}{(p+1)(p+2)}$$

$$\int_0^{\frac{1}{2}}|t||t|^p dt=\int_{\frac{1}{2}}^1|1-t||t-1|^p dt=\frac{2^{-(p+2)}}{p+2}$$

$$\int_0^{\frac{1}{2}}\left|\frac{1}{2}-t\right|\left(\sin\frac{\pi t}{2}+\cos\frac{\pi t}{2}\right)dt=\frac{\pi-4\sqrt{2}+4}{\pi^2}$$

$$\int_{\frac{1}{2}}^1\left|t-\frac{1}{2}\right|\left(\sin\frac{\pi t}{2}+\cos\frac{\pi t}{2}\right)dt=\frac{\pi-4\sqrt{2}+4}{\pi^2}$$

$$\int_0^{\frac{1}{2}}|t|\left(\sin\frac{\pi t}{2}+\cos\frac{\pi t}{2}\right)dt=\frac{4\sqrt{2}-4}{\pi^2}$$

$$\int_{\frac{1}{2}}^1|1-t|\left(\sin\frac{\pi t}{2}+\cos\frac{\pi t}{2}\right)=\frac{4\sqrt{2}-4}{\pi^2}.$$

This completes the proof of the theorem.

REFERENCES

[1] K. Bekar, "Hermite-Hadamard type inequalities for trigonometrically P-functions", C. R. Acad. Bulgare Sci., 72(11), 2019.

[2] S.S. Dragomir and R.P. "Agarwal, Two inequalities for differentiable mappings and applications to special means of real numbers and to trapezoidal formula", Appl. Math. Lett. 11 (1998), 91-95.

[3] S.S. Dragomir and C.E.M. Pearce, "Selected Topics on Hermite-Hadamard Inequalities and Its Applications", RGMIA Monograph 2002.

[4] S.S. Dragomir, J. Pečarić and LE.Persson, "Some inequalities of Hadamard Type", Soochow J. Math., 21 (3)(2001), pp. 335-341.

[5] J. Hadamard, "Étude sur les propriétés des fonctions entières en particulier d'une fonction considérée par Riemann", J. Math. Pures Appl. 58(1893), 171-215.

[6] İ. İşcan, "New refinements for integral and sum forms of Hölder inequality", J. Inequal. Appl., (2019) 2019:304, 11 pages.

[7] İ. İşcan and M. Kunt, "Hermite-Hadamard-Fejer type inequalities for quasi geometrically convex functions via fractional integrals", J. Math., Volume 2016, Article ID 6523041, 7 pages.

[8] H. Kadakal, "Hermite-Hadamard type inequalities for trigonometrically convex functions", Sci. Stud. Res. Ser. Math. Inform., Vol. 28(2018), No. 2, 19-28.

[9] M. Kadakal, H. Kadakal and İ. İşcan, "Some new integral inequalities for n-times differentiable s-convex functions in the first sense", TJANT, Vol. 5, No. 2 (2017), 63-68.

[10] U.S., Kırmacı, "Inequalities for differentiable mappings and applications to special means of real numbers and to midpoint formula", Appl. Math. Comput. 147 (1) (2004), 137-146.

[11] S. Maden, H. Kadakal, M. Kadakal and İ, İşcan, "Some new integral inequalities for n-times differentiable convex and concave functions", J. Nonlinear Sci. Appl., 10, 12(2017), 6141-6148.

[12] S. Özcan, and İ. İşcan, "Some new Hermite-Hadamard type inequalities for s-convex functions and their applications", J. Inequal. Appl., Article number: 2019:201 (2019).

[13] S. Varošanec, "On h-convexity", J. Math. Anal. Appl. 326 (2007) 303-311.

[14] G. Zabandan, "A new refinement of the Hermite-Hadamard inequality for convex functions", J. Inequal. Pure Appl. Math. 10 2(2009), Article ID 45.

JOURNAL OF SCIENCE
SAKARYA UNIVERSITY

Sakarya University Journal of Science

ISSN 1301-4048 | e-ISSN 2147-835X | Period Bimonthly | Founded: 1997 | Publisher Sakarya University | http://www.saujs.sakarya.edu.tr/en/

Title: Spectral Analysis of Non-selfadjoint Second Order Difference Equation with Operator Coefficient

Authors: Gökhan MUTLU, Esra KIR ARPAT
Recieved: 2019-10-01 12:41:15

Accepted: 2020-03-20 12:52:18

Article Type: Research Article
Volume: 24
Issue: 3
Month: June
Year: 2020
Pages: 494-500

How to cite
Gökhan MUTLU, Esra KIR ARPAT; (2020), Spectral Analysis of Non-selfadjoint Second Order Difference Equation with Operator Coefficient. Sakarya University Journal of Science, 24(3), 494-500, DOI: https://doi.org/10.16984/saufenbilder.627496
Access link
http://www.saujs.sakarya.edu.tr/en/issue/52472/627496

Sakarya University Journal of Science 24(3), 494-500, 2020

Spectral Analysis of Non-selfadjoint Second Order Difference Equation with Operator Coefficient

Gökhan MUTLU*[1], Esra KIR ARPAT[2]

Abstract

In this paper, we consider the discrete Sturm-Liouville operator generated by second order difference equation with non-selfadjoint operator coefficient. This operator is the discrete analogue of the Sturm-Liouville differential operator generated by Sturm-Liouville operator equation which has been studied in detail. We find the Jost solution of this operator and examine its asymptotic and analytical properties. Then, we find the continuous spectrum, the point spectrum and the set of spectral singularities of this discrete operator. We finally prove that this operator has a finite number of eigenvalues and spectral singularities under a specific condition.

Keywords: Sturm-Liouville's operator equation, Non-selfadjoint operators, Discrete operators, Continuous spectrum, Operator coefficients.

1. INTRODUCTION

Difference equations are very important for modelling certain problems in physics, biology, economics, engineering, control theory etc. Spectral analysis of certain difference equations gives us useful information about these problems.

Let us give some literature on the spectral analysis of non-selfadjoint operators and the concept of spectral singularities. Spectral analysis of non-selfadjoint Sturm-Liouville operator has begun and the spectral singularities was discovered by Naimark [1-2]. Spectral singularities of differential operators [3-4] and certain classes of abstract operators [5] are studied.

Recently, non-Hermitian Hamiltonians and complex extension of quantum mechanics have been studied extensively (see review papers [6-7]). Moreover, the spectral singularities are identified for some concrete complex scattering potentials and some physical interpretations are suggested [8-9]. In [9], the authors identify the spectral singularities of complex scattering potentials with the real energies at which the reflection and transmission coefficients tend to

*Corresponding Author
[1]Gazi University, Faculty of Science, Department of Mathematics, Ankara-Turkey. gmutlu@gazi.edu.tr ORCID: 0000-0002-0674- 2908
[2]Gazi University, Faculty of Science, Department of Mathematics, Ankara-Turkey. esrakir@gazi.edu.tr ORCID: 0000-0002-6322-5130

infinity, i.e., they correspond to resonances having a zero width.

Spectral analysis of selfadjoint difference equations has been studied by many authors (see [10-11] for review and references). Further, spectral analysis of the selfadjoint differential and difference equations with matrix coefficients has been investigated [12-16]. In [17-19], the authors investigated the difference equation

$$a_{n-1}y_{n-1} + b_n y_n + a_n y_{n+1} = \lambda y_n,\ n \in \mathbb{N}, \quad (1)$$

where $(a_n)_{n\in\mathbb{N}}$ and $(b_n)_{n\in\mathbb{N}}$ are complex sequences such that an $a_n \neq 0$ for all $n \in \mathbb{N}$ and the condition

$$\sum_{n=1}^{\infty} n(|1-a_n| + |b_n|) < \infty \quad (2)$$

holds. We can refer to Equation (1) as the Sturm-Liouville difference equation since it can be rewritten

$$\Delta(a_{n-1}\Delta y_{n-1}) + q_n y_n = \lambda y_n,\ n \in \mathbb{N},$$

where $q_n = a_{n-1} + a_n + b_n$ and Δ denotes the forward difference operator.

In [20-21], the authors considered the case $n \in \mathbb{Z}$ with the analogous condition to (2). Further, the spectral analysis of the Sturm-Liouville difference equation with finite dimensional non-Hermitian matrix coefficients has been done [22].

Although there are many studies on spectral properties of the Sturm-Liouville difference equation with scalar or finite dimensional matrix coefficients, there isn't any study when the coefficients are infinite dimensional operators. In scalar or matrix coefficient cases, the discrete spectrum and spectral singularities are obtained as zeros of Jost function by using the results about analytic scalar functions. The infinite dimensional case requires a different treatment and new methods since the Jost function is an operator function on the contrary to finite dimensional case. The new method is due to Keldysh [23] which gives the fundamental tools to examine the singular points of analytic operator functions.

We consider the following difference operator defined in the Hilbert space $H_1 := l_2(\mathbb{N}, H)$ of vector sequences $y = (y_n)_{n\in\mathbb{N}}$ $(y_n \epsilon H)$ such that

$$\sum_{n=1}^{\infty} \|y_n\|_H^2 < \infty,$$

where H is a separable Hilbert space $(dim H \leq \infty)$.

Let us denote the difference operator L defined in H_1;

$$l(y)_n := A_{n-1}y_{n-1} + B_n y_n + A_n y_{n+1},\ n \in \mathbb{N}, \quad (3)$$

$$y_0 = 0, \quad (4)$$

where A_n $(n \in \mathbb{N} \cup \{0\})$ and B_n $(n \in \mathbb{N})$ are non-selfadjoint, $A_n - I$ $(n \in \mathbb{N} \cup \{0\})$ and B_n $(n \in \mathbb{N})$ are completely continuous operators in H such that A_n is invertible for $n \in \mathbb{N} \cup \{0\}$.

In this paper, we investigate the spectral properties of the non-selfadjoint difference operator L which is generated by the Sturm-Liouville difference equation with non-selfadjoint operator coefficients. In particular, we find the Jost solution, continuous spectrum, discrete spectrum and spectral singularities of L. Finally, we prove the finiteness of eigenvalues and spectral singularities.

2. THE JOST SOLUTION AND CONTINUOUS SPECTRUM OF *L*

Let us consider the eigenvalue equation of L

$$A_{n-1}y_{n-1} + B_n y_n + A_n y_{n+1} = \lambda y_n,\ n \in \mathbb{N}, \quad (5)$$

where λ is the spectral parameter. Equivalently, we might consider the corresponding operator equation

$$A_{n-1}Y_{n-1} + B_n Y_n + A_n Y_{n+1} = \lambda Y_n,\ n \in \mathbb{N},$$

where (Y_n) is an operator sequence i.e. Y_n is an operator in H for each $n \in \mathbb{N}$.

Assumption 1. We assume that the coefficients of Equation (5) satisfy
$\sum_{n=1}^{\infty}(\|I - A_n\| + \|B_n\|) < \infty$.

Definition 1. Let $E(z) \coloneqq E_n(z)$ $(n \in \mathbb{N} \cup \{0\})$ denote the operator solution of the equation

$$A_{n-1}Y_{n-1} + B_nY_n + A_nY_{n+1} = (z + z^{-1})Y_n, \quad n \in \mathbb{N},$$

satisfying the condition

$$\lim_{n\to\infty} Y_n(z)\, z^{-n} = I,$$

for $z \in D_0 := \{z \in \mathbb{C}: |z| = 1\}$. $E(z)$ is called the Jost solution of Equation (5).

Remark 1. The remaining results of this section will be given without proofs since they are similar to the matrix coefficient case which have been obtained in [12].

Assumption 2. Let us assume

$$\sum_{n=1}^{\infty} n(\|I - A_n\| + \|B_n\|) < \infty.$$

Theorem 1. The Jost solution can be represented

$$E_n(z) = T_n z^n \left[I + \sum_{m=1}^{\infty} K_{n,m} z^m\right], n \in \mathbb{N} \cup \{0\}, \quad (6)$$

where

$$T_n = \prod_{p=n}^{\infty} A_p^{-1},$$

$$K_{n,1} = -\sum_{p=n+1}^{\infty} T_p^{-1} B_p T_p,$$

$$K_{n,2} = -\sum_{p=n+1}^{\infty} T_p^{-1} B_p T_p K_{p,1} + \sum_{p=n+1}^{\infty} T_p^{-1} \left(I - A_p^2\right) T_p,$$

$$K_{n,m+2} = \sum_{p=n+1}^{\infty} T_p^{-1} \left(I - A_p^2\right) T_p K_{p+1,m} - \sum_{p=n+1}^{\infty} T_p^{-1} B_p T_p K_{p,m+1} + K_{n+1,m},$$

where $n \in \mathbb{N} \cup \{0\}$, $m \in \mathbb{N}$. Further,

$$\left\|K_{n,m}\right\| \le c \sum_{p=n+\left[\left[\frac{m}{2}\right]\right]}^{\infty} \left(\left\|I - A_p\right\| + \left\|B_p\right\|\right)$$

holds where $c > 0$ is a constant. Moreover, $E_n(z)$ $(n \in \mathbb{N} \cup \{0\})$ has an analytic continuation from D_0 to $D_1 := \{z \in \mathbb{C}: |z| < 1\} \backslash \{0\}$.

Theorem 2. The Jost solution satisfies the asymptotic relation

$$E_n(z) = z^n[I + o(1)], \quad n \to \infty,$$

for $z \in D := \{z \in \mathbb{C}: |z| \le 1\} \backslash \{0\}$.

Theorem 3. The continuous spectrum of L is $\sigma_c(L) = [-2, 2]$.

Proof. Let L_0 and L_1 denote the operators defined in H_1

$$L_0(y)_n = y_{n-1} + y_{n+1}, n \in \mathbb{N},$$

$$L_1(y)_n = (A_{n-1} - I)y_{n-1} + B_n y_n + (A_n - I)y_{n+1}, n \in \mathbb{N},$$

with the boundary condition

$$y_0 = 0,$$

respectively. It easily follows $L_0 = L_0^*$ and also $\sigma_c(L_0) = [-2, 2]$ (see [24]).

It is well known that L_1 is a compact operator iff L_1 is bounded and the set

$$R = \{L_1 y: \ \|y\|_1 \le 1\}$$

is compact in H_1. It is obvious that L_1 is bounded. Moreover, if we use the compactness criteria in l_p spaces (see [25], p. 167), we obtain the compactness of R. Indeed, let $y \in H_1$ such that $\|y\|_1 \le 1$. Then, Assumption 2 implies that for $\varepsilon > 0$, there exists $n_0 \in \mathbb{N}$ such that for $n \ge n_0$

$$\sum_{i=n+1}^{\infty} (\|A_i - I\| + \|B_i\|) < \frac{\varepsilon}{C}$$

holds and also

$$\sum_{i=n+1}^{\infty} \|(L_1 y)_i\|_H^2 = \sum_{i=n+1}^{\infty} \|(A_{i-1} - I)y_{i-1} + B_i y_i + (A_i - I)y_{i+1}\|_H^2$$

$$\le \sum_{i=n+1}^{\infty} \|A_{i-1} - I\|^2 \|y_{i-1}\|_H^2 + \|B_i\|^2 \|y_i\|_H^2 + \|A_i - I\|^2 \|y_{i+1}\|_H^2$$

$$\le \|y\|_1^2 (\sum_{i=n+1}^{\infty} \|A_{i-1} - I\|^2 + \|B_i\|^2 + \|A_i - I\|^2)$$

$$\le \sum_{i=n+1}^{\infty} 2\|A_i - I\|^2 + \|B_i\|^2$$

$$\le \sum_{i=n+1}^{\infty} C_1 \|A_i - I\| + C_2 \|B_i\|$$

$$\le \sum_{i=n+1}^{\infty} C(\|A_i - I\| + \|B_i\|) < \varepsilon ,$$

where

$C_1 = \frac{1}{2} sup_{i\in\mathbb{N}} \|A_i - I\|,\ C_2 = sup_{i\in\mathbb{N}} \|B_i\|,\ C = C_1 + C_2.$

Therefore, we proved that L_1 is a compact operator in H_1. Weyl's theorem of compact perturbation [26] implies

$$\sigma_c(L) = \sigma_c(L_0) = [-2, 2].$$

3. EIGENVALUES AND SPECTRAL SINGULARITIES OF L

It is easy to show that the discrete spectrum and the set of spectral singularities of L are

$\sigma_d(L) = \{\lambda: \lambda = z + z^{-1}, z\epsilon D_1, E_0(z) \text{ is not invertible}\},$

$\sigma_{ss}(L) = \{\lambda: \lambda = z + z^{-1}, z\epsilon D_0, E_0(z) \text{ is not invertible}\},$

respectively. $E_0(z)$ is called the Jost function of L. Note that, this function is an operator function on the contrary to finite dimensional case. Hence, the methods need to be changed in our case. We will use Keldysh [23] in order to analyze the singular points of $E_0(z)$. Let us define the sets

$M_1 = \{z\epsilon D_1: E_0(z) \text{ is not invertible}\},$

$M_2 = \{z\epsilon D_0: E_0(z) \text{ is not invertible}\}.$

Then,

$\sigma_d(L) = \{\lambda: \lambda = z + z^{-1}, z\epsilon M_1\},$

$\sigma_{ss}(L) = \{\lambda: \lambda = z + z^{-1}, z\epsilon M_2\}.$

From the representation (6) we have

$E_0(z) = T_0\left[I + \sum_{m=1}^{\infty} K_{0,m} z^m\right],$

where

$T_0 = \prod_{p=0}^{\infty} A_p^{-1}$

is invertible. This implies $E_0(z)$ is invertible iff

$F(z) := I + \sum_{m=1}^{\infty} K_{0,m} z^m$

is invertible. Hence

$M_1 = \{z\epsilon D_1: F(z) \text{ is not invertible}\}.$

From Theorem 1 we have

$K_{0,1} = -\sum_{p=1}^{\infty} T_p^{-1} B_p T_p,$

$K_{0,2} = -\sum_{p=1}^{\infty} T_p^{-1} B_p T_p K_{p,1} + \sum_{p=1}^{\infty} T_p^{-1} \left(I - A_p^2\right) T_p,$

$K_{0,m+2} = \sum_{p=1}^{\infty} T_p^{-1} \left(I - A_p^2\right) T_p K_{p+1,m} - \sum_{p=1}^{\infty} T_p^{-1} B_p T_p K_{p,m+1} + K_{1,m},$

where $m \in \mathbb{N}$. These equations together with the conditions that $A_n - I$ $(n \in \mathbb{N} \cup \{0\})$ and B_n $(n \in \mathbb{N})$ are completely continuous operators imply that $K_{0,m}$ is completely continuous for every $m \in \mathbb{N}$. As a result,

$K(z) := \sum_{m=1}^{\infty} K_{0,m} z^m$

is a completely continuous operator for every $z \in D_1$. Moreover, since $E_0(z)$ is analytic on D_1 (see Theorem 1) $F(z)$ is also analytic on D_1. Hence, we can use [23] to find the singular points of the operator valued function $F(z)$ on D_1 and these singular points give us the eigenvalues.

Definition 2. [23] Let A and R be operators such that

$$(I + R)(I - A) = I$$

holds. Then, R is called the resolvent of A.

Theorem 4. Let $R(z)$ denote the resolvent of $-K(z)$. Then,

$M_1 = \{z\epsilon D_1: z \text{ is a pole of } I + R(z)\}.$

Proof. Since $R(z)$ is the resolvent of $-K(z)$, we have

$$I + R(z) = (I + K(z))^{-1} = (F(z))^{-1}.$$

Since $M_1 \neq D_1$ there exists $z\epsilon D_1$ such that $I + R(z)$ exists. Therefore, $I + R(z)$ exists on D_1 except for a set of isolated points and $I + R(z)$ is

a meromorphic function of z on D_1 [23]. These isolated points are clearly the eigenvalues of L. Hence we have

$$(F(z))^{-1} = \frac{U(z)}{v(z)},\ z\epsilon D_1, \tag{7}$$

where $U(z)$ is an operator function and $v(z)$ is a scalar function which are both analytic on D_1. Since

$M_1 = \{z\epsilon D_1 : F(z) \text{ is not invertible}\}$,

it follows from (7) that

$M_1 = \{z\epsilon D_1 : z\ is\ a\ pole\ of\ I + R(z)\} = \{z\epsilon D_1 : v(z) = 0\}$.

Corollary 1. $\sigma_d(L) = \{\lambda : \lambda = z + z^{-1}, z\epsilon D_1, v(z) = 0\}$.

Proof. The proof is obvious from Theorem 4 since $\sigma_d(L) = \{\lambda : \lambda = z + z^{-1}, z\epsilon M_1\}$.

Theorem 5. $\sigma_d(L)$ is bounded and countable. Moreover, its limit points can only lie in the circle $|z| \leq 2$.

Proof. From (6) it follows

$E_0(z) = T_0\left[I + \sum_{m=1}^{\infty} K_{0,m} z^m\right]$

and also

$E_0(z) = T_0 I + o(1),\ |z| \to 0,$

which implies $E_0(z)$ is invertible for sufficiently small z and hence $\lambda = z + z^{-1}$ is not an eigenvalue for $|z| \to 0$. Thus, $\sigma_d(L)$ is bounded. Since $v(z)$ is analytic on D_1, its zeros are isolated. From Corollary 5, it follows $\sigma_d(L)$ is countable. Further, the limit points (if exist) of the zeros of $v(z)$ lie on the boundary of D_1 i.e. on D_0 [27].

If z is a limit point of the set

$M_1 = \{z\epsilon D_1 : v(z) = 0\}$,

then $|z| = 1$ and $|\lambda| = |z + z^{-1}| \leq 2$. Hence, the limit points (if exist) lie in the circle $|z| \leq 2$.

Theorem 6. Let $R(z)$ denote the resolvent of $-K(z)$. Then,

$$M_2 = \{z\epsilon D_0 : z\ is\ a\ pole\ of\ I + R(z)\} = \{z\epsilon D_0 : v(z) = 0\}.$$

Proof. From (7) it follows

$F(z)U(z) = v(z)I,$

which implies $U(z)$ is invertible whenever $v(z) \neq 0$. Moreover, if $z\epsilon D_1$ such that $v(z) \neq 0$ then

$F(z) = v(z)(U(z))^{-1}.$

Since $F(z)$ is continuous on D, we can extend this representation continuously to D;

$$(F(z))^{-1} = \frac{U(z)}{v(z)},\ z\epsilon D. \tag{8}$$

Recall that

$M_2 = \{z\epsilon D_0 : F(z) \text{ is not invertible}\}$.

The representation (8) implies that

$M_2 = \{z\epsilon D_0 : z\ is\ a\ pole\ of\ I + R(z)\} = \{z\epsilon D_0 : v(z) = 0\}$.

Theorem 7. The set of spectral singularities $\sigma_{ss}(L)$ of L is compact and has zero Lebesgue measure.

Proof. It is well known that $\sigma_{ss}(L) \subset \sigma_c(L) = [-2,2]$. This gives us the boundedness of $\sigma_{ss}(L)$. We only have to show $\sigma_{ss}(L)$ or equivalently M_2 is closed for the compactness. Let $(\lambda_n) \subset M_2$ such that $\lambda_n \to \lambda$. $(\lambda_n) \subset M_2$ implies $\lambda_n \in D_0$ and $v(\lambda_n) = 0$ for every $n \in \mathbb{N}$. Since D_0 is closed $\lambda_n \to \lambda$ implies $\lambda \in D_0$. Moreover, since $v(z)$ is continuous on D, $\lambda_n \to \lambda$ implies $v(\lambda_n) \to v(\lambda)$ and hence $v(\lambda) = 0, \lambda \in M_2$ as required. Finally, since

$M_2 = \{z\epsilon D_0 : v(z) = 0\}$,

it follows from Privalov's Theorem [27] that M_2 has zero Lebesgue measure.

Assumption 3. Let us assume

$\sum_{n=0}^{\infty} e^{\varepsilon n}(\|I - A_n\| + \|B_n\|) < \infty,\ \varepsilon > 0.$

Theorem 8. L has a finite number of eigenvalues and spectral singularities.

Proof. Recall that

$\|K_{n,m}\| \leq c \sum_{p=n+\left[\left[\frac{m}{2}\right]\right]}^{\infty} (\|I - A_p\| + \|B_p\|),$

where c is a constant. This implies together with the Assumption 3 that

$\|K_{0,m}\| \leq C e^{\frac{-\varepsilon}{6}m}, m \epsilon \mathbb{N},$

where $C > 0$. The series

$\sum_{m=0}^{\infty} K_{0,m} z^m, \sum_{m=0}^{\infty} m K_{0,m} z^{m-1}$

are uniformly convergent iff $ln|z| < \frac{\varepsilon}{6}$. Hence, $E_n(z)$ $(n \in \mathbb{N} \cup \{0\})$ has an analytic continuation to $D_2 := \left\{z \in \mathbb{C}: |z| < e^{\frac{\varepsilon}{6}}\right\}$. Thus, we can write

$(F(z))^{-1} = \frac{U(z)}{v(z)},\ z \epsilon D_2.$

Let us suppose that M_1 and M_2 are not finite. Since M_1 and M_2 are bounded (see Theorem 5 and 7), they have limit points by Bolzano-Weierstrass Theorem. Since $v(z)$ is analytic on D_2, the limit points of its zeros must lie on the boundary of the domain D_2 [27]. This gives a contradiction since $e^{\frac{\varepsilon}{6}} > 1$. Therefore, M_1 and M_2 must be finite.

REFERENCES

[1] M.A. Naimark, "Investigation of the spectrum and the expansion in eigenfunctions of a non-selfadjoint operator of second order on a semi-axis," AMS Transl. 2 (16), pp. 103-193, 1960.

[2] M.A. Naimark, "Linear Differential Operators, II," Ungar, New York, 1968.

[3] V.E. Lyance, "A differential operator with spectral singularities, I-II," AMS Transl. 2 (60), pp. 185-225, 227-283, 1967.

[4] B.S. Pavlov, "The non-selfadjoint Schrödinger operator in Spectral Theory and Wave Processes, Topics in Mathematical Physics, Vol.1, Birman M.S. (eds), Springer, Boston, MA, pp. 87-114, 1967.

[5] J.T. Schwartz, "Some non-selfadjoint operators," Comm. Pure Appl. Math., 13, pp. 609-639, 1960.

[6] C.M. Bender, "Making sense of non-Hermitian Hamiltonians," Rep. Prog. Phys., 70, pp. 947-1018, 2007.

[7] A. Mostafazadeh, "Pseudo-Hermitian representation of quantum mechanics," arXiv:0810.5643, 2008.

[8] B.F. Samsonov, "SUSY transformations between digonalizable and non-diagonalizable Hamiltonians," arXiv:quant-ph/0503075, 2005.

[9] A. Mostafazadeh, "Spectral singularities of complex scattering potentials and infinite reaction and transmission coefficients at real energies," arXiv:0901.4472, 2009.

[10] R.P. Agarwal, "Difference Equations and Inequalities: Theory, Methods and Applications," Marcel Dekker, New York, 2000.

[11] R.P. Agarwal and P.J.Y. Wong, "Advanced Topics in Difference Equations," Kluwer, Dordrecht, 1997.

[12] Y. Aygar and E. Bairamov, "Jost solution and the spectral properties of the matrix-valued difference operators," Appl. Math. Comput., 218, pp. 9676-9681, 2012.

[13] E. Bairamov, Y. Aygar and S. Cebesoy, "Spectral analysis of a selfadjoint matrix

valued discrete operator on the whole axis," J. Nonlinear Sci. Appl., 9, pp. 4257-4262, 2016.

[14] R. Carlson, "An inverse problem for the matrix Schrödinger equation," J. Math. Anal. Appl., 267, pp. 564-575, 2002.

[15] S. Clark, F. Gesztesy and W. Renger, "Trace formulas and Borg-type theorems for matrix valued Jacobi and Dirac finite difference operators," J. Differential Equations, 219, pp. 144-182, 2005.

[16] F. Gesztesy, A. Kiselev and K.A. Makarov, "Uniqueness results for matrix-valued Schrödinger, Jacobi and Dirac-type operators," Math. Nachr., 239, pp. 103-145, 2002.

[17] E. Bairamov, Ö. Çakar and A.M. Krall, "Non-selfadjoint difference operators and Jacobi matrices with spectral singularities," Math. Nachr., 229, pp. 5-14, 2001.

[18] A.M. Krall, E.Bairamov and Ö. Çakar, "Spectral analysis of a non-selfadjoint discrete Schrödinger operators with spectral singularities," Math. Nachr., 231, pp. 89-104, 2001.

[19] T. Koprubasi and R.N. Mohapatra, "Spectral properties of generalized eigenparameter dependent discrete Sturm-Liouville type equation," Quaestiones Mathematicae, 40 (4), pp. 491-505, 2017.

[20] M. Adivar and E. Bairamov, "Spectral properties of non-selfadjoint difference operators," J. Math. Anal. Appl., 261, pp. 461-478, 2001.

[21] M. Adivar and E. Bairamov, "Difference equations of second order with spectral singularities," J. Math. Anal. Appl., 277, pp. 714-721, 2003.

[22] S. Cebesoy, Y. Aygar and E. Bairamov, "Matrix valued difference equations with spectral singularities," International Journal of Mathematical, Computational, Physical, Electrical and Computer Engineering, 9 (11), pp. 579-582, 2015.

[23] M.V. Keldysh, "On the completeness of the eigenfunctions of some classes of nonselfadjoint linear operators," Russ. Math. Surv., 26 (4), pp. 15-44, 1971.

[24] V.P. Serebrjakov, "An inverse problem of the scattering theory for difference equations with matrix coeffcients," Dokl. Akad. Nauk SSSR, 250 (3), pp. 562-565, 1980 (in Russian).

[25] L.A. Lusternik and V.I. Sobolev, "Elements of Functional Analysis," Halsted Press, New York, 1974.

[26] I.M. Glazman, "Direct Methods of Qualitative Spectral Analysis of Singular Differential Operators," Israel Program for Scientific Translations, Jerusalem, 1965.

[27] E.P. Dolzhenko, "Boundary value uniqueness theorems for analytic functions," Math. Notes, 26 (6), pp. 437-442, 1979.

JOURNAL OF SCIENCE
SAKARYA UNIVERSITY

Sakarya University Journal of Science

ISSN 1301-4048 | e-ISSN 2147-835X | Period Bimonthly | Founded: 1997 | Publisher Sakarya University | http://www.saujs.sakarya.edu.tr/en/

Title: Alloying Effect on the Local Atomic Pressures of Nanoclusters

Authors: Songül TARAN
Recieved: 2020-02-06 12:03:15

Accepted: 2020-03-23 14:25:19

Article Type: Research Article
Volume: 24
Issue: 3
Month: June
Year: 2020
Pages: 501-510

How to cite
Songül TARAN; (2020), Alloying Effect on the Local Atomic Pressures of Nanoclusters. Sakarya University Journal of Science, 24(3), 501-510, DOI: https://doi.org/10.16984/saufenbilder.685370
Access link
http://www.saujs.sakarya.edu.tr/en/issue/52472/685370

Sakarya University Journal of Science 24(3), 501-510, 2020

Alloying Effect on the Local Atomic Pressures of Nanoclusters

Songül TARAN*[1]

Abstract

In this study, simulations were performed to investigate local atomic pressures of icosahedral nanoclusters with 55 atoms. Before analyzing the local atomic pressures, the best chemical ordering structures were obtained using Monte Carlo Basin-Hopping algorithm within Gupta potential. Binary and ternary alloying effect on the local atomic pressures of mono, binary and ternary nanoclusters formed by Cu, Ag and Pt atoms was investigated in detail. It was obtained that adding one atom of second alloying metal in pure nanoclusters and also third alloying metal in binary nanoalloys can change the local atomic pressure due to locating tendency in the icosahedral structure. Also, it was observed that adding a smaller atom at the central site of the icosahedral structure exhibits decreasing of core stress.

Keywords: nanocluster, alloying, simulation, atomic pressure

1. INTRODUCTION

Nanoclusters occupy a very important place, since they are the building blocks of nanosicence [1]. Nanoclusters are aggregates of ~10 to 10^6 atoms or molecules within a size range of 1-100 nm [2]. Nanoclusters may consist of identical atoms, molecules and two or more different type of atoms [3]. Nanoclusters are well suited for several applications ranging from catalysis to optoelectronics, magnetism, optics and biomedicine [4]. Therefore, understanding of structural properties of nanoclusters is very important issue to fabricate and control nano materials.

Nanocluster structures can be classified due to geometric shape and chemical ordering [5]. Nanoclusters can present both crystalline and noncrystalline geometric structures with several chemical ordering [6]. Noncrystalline structures exist at nanosize with icosahedra and decahedra [7]. Since the addition of different type atom of alloying metal to nanoclusters can lead to structural variations, alloying of icosahedral nanoclusters organized in concentric atomic layers are gaining increasing attention especially

* Corresponding Author:songultaran@duzce.edu.tr
[1] Düzce University, Department of Physics, Düzce, Turkey, ORCID ID:0000-0001-8115-2169

for catalysis. Also, it is well known that catalytic activity is related to surface area, so icosahedral core-shell nanoalloys can be used effectively for catalytic applications due to their large surface-volume ratio.

In icosahedral nanoparticles, interatomic distances are non-optimal. With alloying of icosahedral nanoclusters, strain effects become more important due to size mismatch of the different type atoms [8]. It is still unclear how the alloying or introduction different type atom to nanocluster effects the preferential chemical ordering [9]. In this study, alloying effect on the local atomic pressures was investigated by substitution of only one different type atom of the second alloying metal in the pure monometallic clusters and also by substitution of one different type atom of the third alloying metal in the binary clusters. Local atomic pressure is quite important when analyzing the chemical ordering in binary and multimetallic nanoalloys where size mismatch occurs between the metal atoms. As it is well known that the element with larger atomic size prefers to locate on nanoalloy surface while small elements prefer to locate in core. Thus, with alloying of icosahedral nanoclusters, the stability of icosahedral structures can be explained through the strain induced by the size difference between the atoms.

Interest in nanoalloys formed with group 10 and group 11 transition metals arises as they can vary the structure and also catalytic activity. Thus, in this study 55-atom nanoclusters formed by Cu, Ag and Pt atoms were analyzed. The choice reason of this size is that 55 is a geometric magic number for icosahedral structures which have quasi-spherical shape and close-packed surface at small sizes. Also, icosahedral geometric structure with high symmetry is especially interesting for core-shell segregated behaviour of nanoalloys.

In literature, melting properties of Cu_{55} and Ag_{55} monometallic nanoclusters were studied in some studies [10], [11]. Moreover, structures of $Ag_{54}Cu_1$ [11], [12] and $Cu_{13}Ag_{42}$ [13] bimetallic nanoclusters were examined. Since there is not sufficient data about structural properties of mono, binary and ternary compositions formed by Cu, Ag and Pt atoms, alloying effect on the structural properties nanoclusters were detailed investigated by analyzing the local atomic pressures of the systems. The best chemical ordering structures were obtained using Monte Carlo Basin-Hopping algorithm within Gupta potential.

2. SIMULATION METHODS

The interatomic interactions of the nanoclusters were modeled by using Gupta many body potential energy function [14], [15]. Gupta potential has been widely used in several studies [16]–[23]. Gupta potential energy of nanoclusters is obtained by summing over all N atoms of the repulsive pair term (V_i^r) and the attractive many body (V_i^m):

$$V = \sum_i^N (V_i^r - V_i^m) \quad (1)$$

$$V_i^r = \sum_{j\neq i}^N A(a,b) exp\left[-p(a,b)\left(\frac{r_{ij}-r_o(a,b)}{r_o(a,b)}\right)\right] \quad (2)$$

$$V_i^m = \left(\sum_{j\neq i}^N \xi^2(a,b) exp\left[-2q(a,b)\left(\frac{r_{ij}-r_o(a,b)}{r_o(a,b)}\right)\right]\right)^{\frac{1}{2}} \quad (3)$$

The Gupta potential parameters used in this study were taken from the studies [24], [25] and were given in Table 1. Also, chemical ordering searches were performed by using Monte Carlo-Basin-Hopping algorithm [26]. Local relaxations were carried out for the chemical ordering optimization. For each nanocluster, searches of 2.0×10^6 Monte Carlo steps were made and the atomic labels were permuted randomly in the Basin-Hopping steps.

Table 1. The Gupta potential parameters for nanoclusters

	A (eV)	ξ (eV)	p	q	r_0 (Å)
Cu-Cu	0.0855	1.224	10.96	2.278	2.556
Ag-Ag	0.1031	1.1895	10.85	3.18	2.89
Pt-Pt	0.2975	2.695	10.612	4.004	2.7747
Cu-Ag	0.098	1.2274	10.700	2.805	2.7224
Cu-Pt	0.16	1.82	10.786	3.141	2.666
Ag-Pt	0.175	1.79	10.73	3.59	2.833

3. RESULTS AND DISCUSSION

In this study, local atomic pressures of 55-atom monometallic Cu, Ag and Pt nanoclusters were investigated. Besides, binary and ternary alloying effect on the local atomic pressures was investigated.

The local pressure P_i acting on atom i is proportional to the trace of the tensor given as follows [6], [8], [27]:

$$P_i = -\frac{1}{3}Tr(\boldsymbol{\sigma_i}) \quad (4)$$

where $\boldsymbol{\sigma_i}$ is atomic stres tensor. P_i can assume positive and negative values. $P_i > 0$ indicates compressive stress on atom i and $P_i < 0$ indicates tensile stress on atom i. If $P_i = 0$, it indicates the absence of stres [8].

Fig.1 shows the local atomic pressure for 55-atom icosahedral Cu-Ag-Pt nanoclusters. In the figure, the best chemical ordering structure, side view, cross-section view and pressure scale are given for each nanocluster.

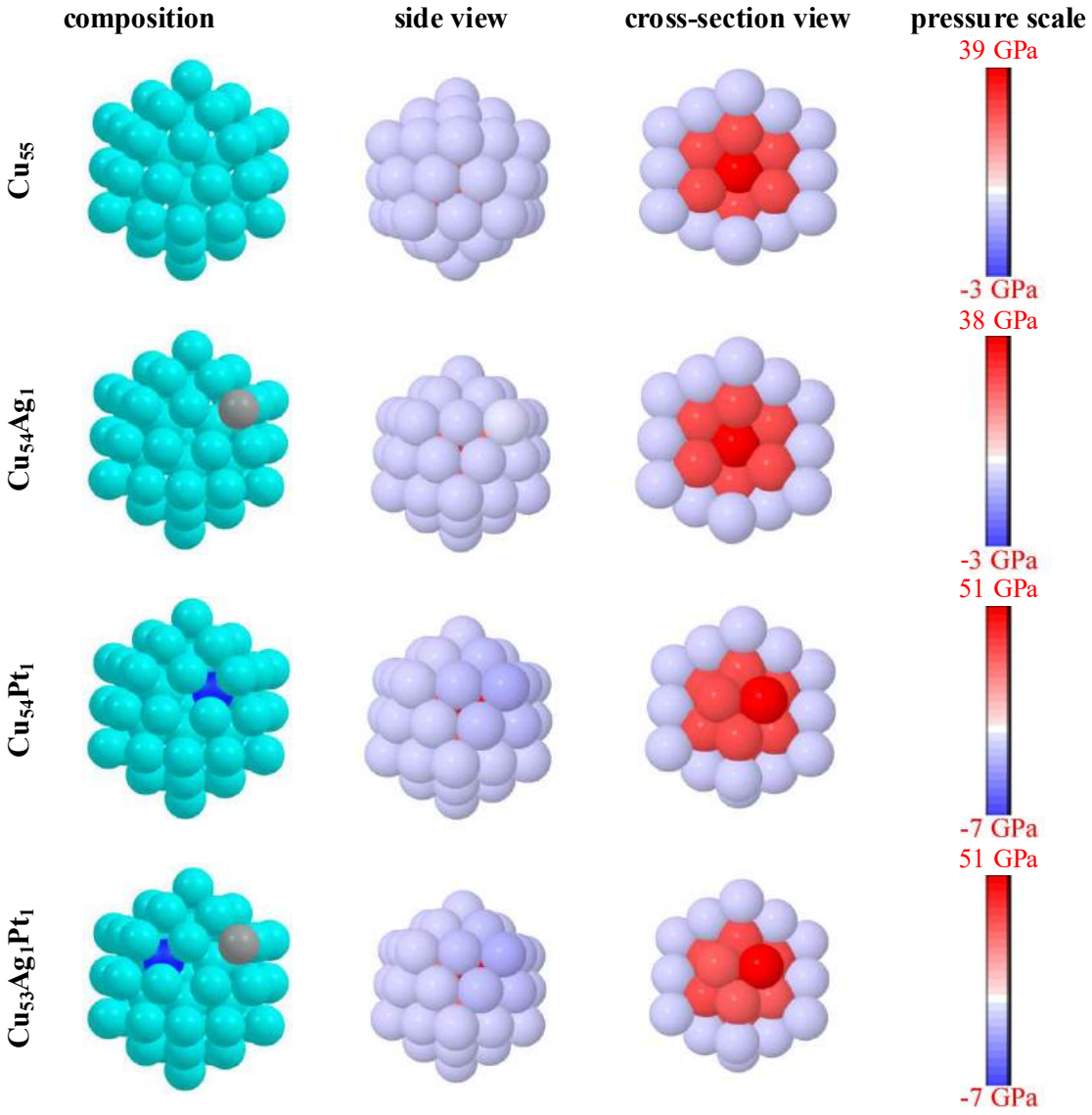

Figure 1. Local atomic pressure for icosahedral Cu-based nanoclusters

The central site is heavily compressed in pure Cu icosahedral nanocluster, so the pressure is strongly positive. The subshell atoms of the icosahedral structure have also positive pressure values lower than the central site. The shell atoms of the structure present negative local pressure values.

With the addition of one Ag atom, Ag atom prefers to locate on surface in $Cu_{54}Ag_1$ binary nanoalloy due to lower surface and cohesive energy of Ag atom. The vertex Ag atom presents negative pressure and the pressure color of Ag atom is a bit lighter than surface Cu atoms. However, with the addition of one Pt atom in pure Cu cluster, single Pt atom prefers to locate at subshell of the $Cu_{54}Pt_1$ binary nanoalloy structure due to higher surface and cohesive energy. With the locating in subshell, the pressure of the central Cu atom shows a bit decrease. Besides, the shell Cu atoms exhibit higher negative pressure values. Single Pt atom also has strongly positive pressure.

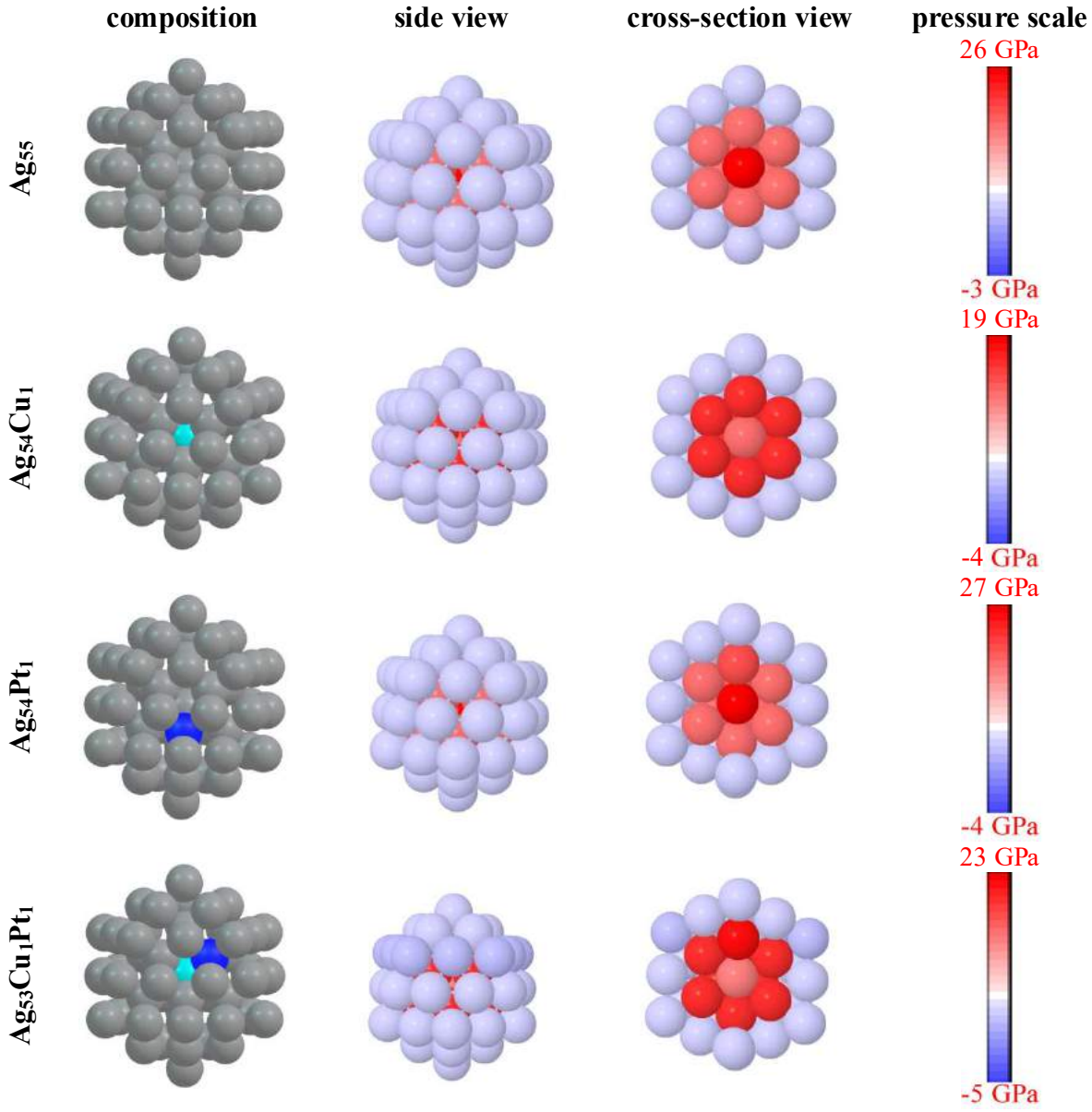

Figure.2. Local atomic pressure for icosahedral Ag-based nanoclusters

For $Cu_{53}Ag_1Pt_1$ ternary nanoalloy, single Ag and Pt atoms prefer to locate on shell and subshell of the icosahedral structure, respectively. The pressure scale shows similarity with $Cu_{54}Pt_1$, although it was observed that some increase and decrease of the pressure values of shell and subshell Cu atoms.

Fig.2 shows the local atomic pressure for 55-atom icosahedral pure Ag nanocluster and binary and ternary nanoalloys formed by doping one atom. For pure Ag nanocluster, local pressure values of core and shell atoms are positive and negative, respectively. With the addition of Cu atom, Cu atom preferentially placed at the central site in $Ag_{54}Cu_1$ nanoalloy. Pressure value of central site decreases and also, the largest positive pressure value of the structure considerably decreases. Besides, subshell Ag atoms have higher positive value, as can be seen in cross-section view of $Ag_{54}Cu_1$ and shell Ag atoms present a bit lower negative pressure. However, with the doping of one Pt atom, single Pt atom prefers to locate on subshell of $Ag_{54}Pt_1$ and central Ag atom has more positive pressure value than single Pt atom.

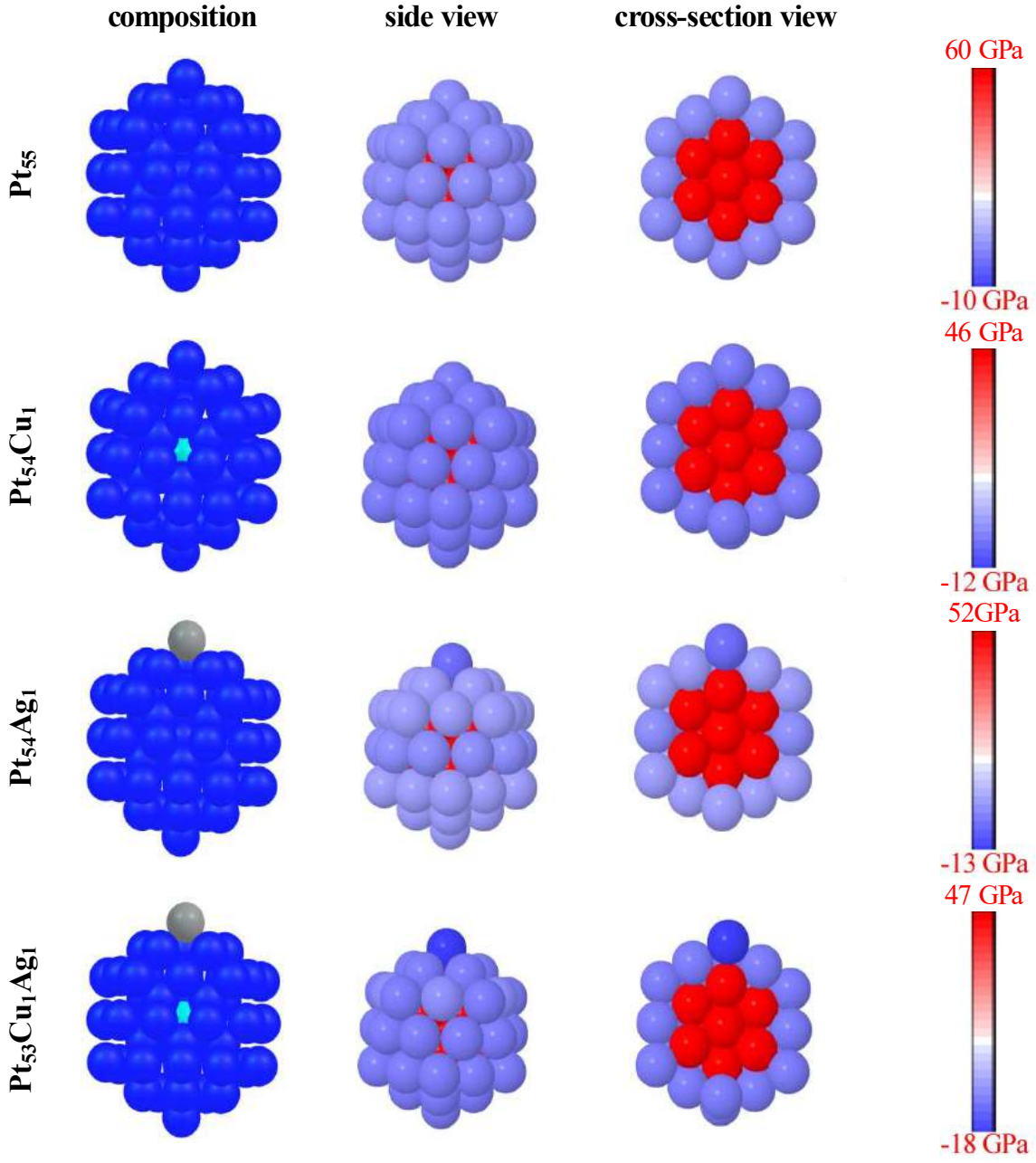

Figure.3. Local atomic pressure for icosahedral Pt-based nanoclusters

For $Ag_{53}Cu_1Pt_1$ ternary nanoalloy, central site presents again lower positive pressure value due to central Cu atom and shell Ag atoms present more negative pressure values.

Fig.3 shows the local atomic pressure for 55-atom icosahedral Pt-based nanoclusters. Pure Pt nanocluster has a central site atom which is heavily compressed. The pressure value of central site is strongly positive. With the substitution of one Cu atom, single Cu atom locates on central site and for $Pt_{54}Cu_1$ binary nanoalloy the most positive pressure value of core atoms decreases and the most negative pressure value of shell atoms increases. In the case of adding one Ag atom to pure cluster, single Ag atom prefers to locate on surface of the structure and it can be seen from the figure that vertex single Ag atom presents more negative pressure value. For $Pt_{53}Cu_1Ag_1$ ternary nanoalloy, single Cu atom is central atom and single Ag atom is vertex atom of surface. When compared to pure and binary nanoclusters, ternary nanoalloy presents much higher negative pressure value.

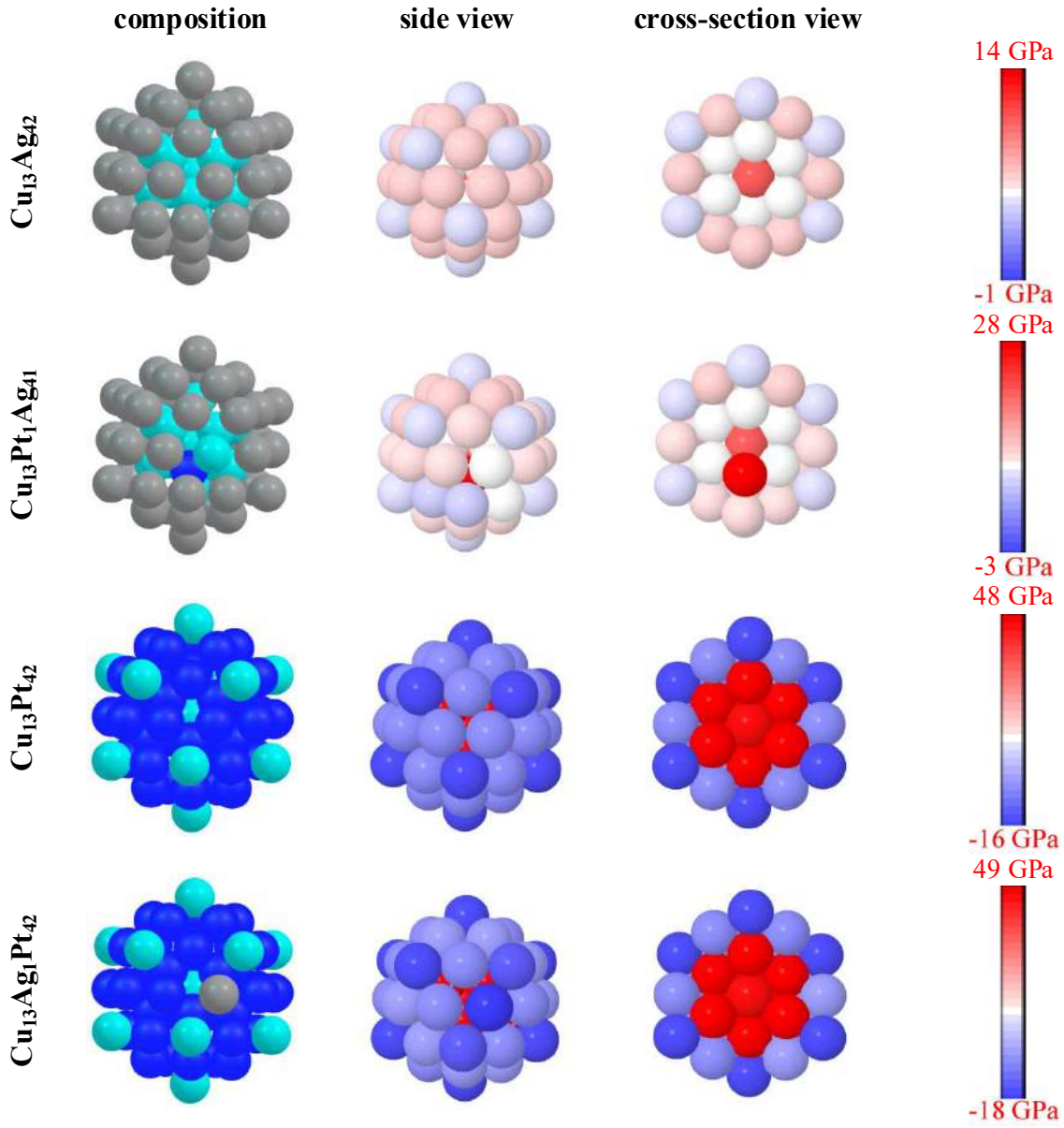

Figure 4. Local atomic pressure for $Cu_{13}Ag_{42}$, $Cu_{13}Pt_1Ag_{41}$, $Cu_{13}Pt_{42}$ and $Cu_{13}Ag_1Pt_{42}$ nanoalloys

Fig.4 shows the local atomic pressure for some chosen binary nanoalloys and ternary nanoalloys formed by doping one atom to chosen binary nanoalloys. $Cu_{13}Ag_{42}$ binary core-shell nanoalloy has 13 Cu core atoms and 42 Ag surface atoms. The local pressure of central Cu atom is positive, however other 12 Cu subshell atoms exhibit negative pressure which are closer to zero. While pressure values of 12 Ag vertex atoms are negative, other 30 Ag shell atoms present positive pressure values. In order to analyze the ternary alloying effect on local pressure values, one Pt atom was introduced to $Cu_{13}Ag_{42}$ binary nanoalloy and it was obtained that central Cu atom becomes more compressive by locating of Pt atom on subshell and reposition of one Cu atom on shell. As for $Cu_{13}Ag_{42}$ all subshell atoms are negative, single Pt atom and one Cu atom in subshell present positive pressure values for $Cu_{13}Pt_1Ag_{41}$ ternary nanoalloy. Also, Pt atom presents the more positive value. In shell of ternary nanoalloy, two Ag atoms exhibit pressure values which are close to 0 shown by white color. The negative pressure values of the shell atoms become more negative.

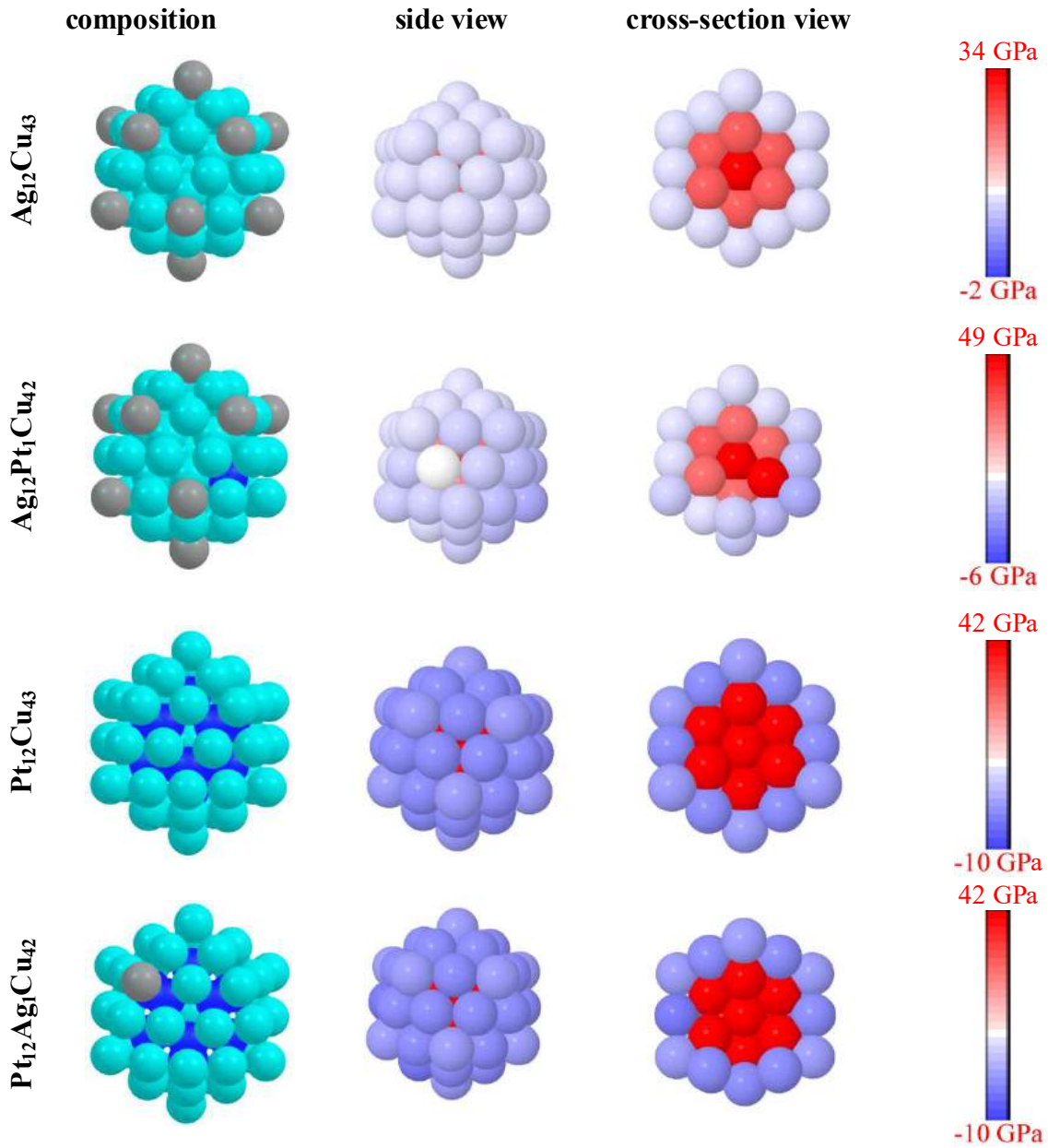

Figure 5. Local atomic pressure for $Ag_{12}Cu_{43}$, $Ag_{12}Pt_1Cu_{42}$, $Pt_{12}Cu_{43}$ and $Pt_{12}Ag_1Cu_{42}$ nanoalloys

In $Cu_{13}Pt_{42}$ binary nanoalloy, one Cu atom occupies the central site and remaining 12 Cu atoms occupy the vertex atoms of the shell. Central Cu atom has a positive pressure value however, 12 vertex Cu atoms have negative pressure. Besides, 12 Pt atoms occupy the subshell and remaining 30 Pt atoms locate on shell. 12 subshell Pt atoms have positive pressure values however, shell Pt atoms have negative values. It can be said that positive local pressure increases with the distance in the core region. In shell region the pressure of vertex atoms is more negative than others. With the introduction of one Ag atom, single Ag atom locates on surface in ternary $Cu_{13}Ag_1Pt_{42}$ nanoalloy and has the more negative pressure value of the shell. Also, with the introduction of one Ag atom more negative and positive pressures appear.

Fig.5 shows the local atomic pressure for $Ag_{12}Cu_{43}$, $Ag_{12}Pt_1Cu_{42}$, $Pt_{12}Cu_{43}$ and $Pt_{12}Ag_1Cu_{42}$ nanoalloys. For binary $Ag_{12}Cu_{43}$ nanoalloy, 12 Ag atoms prefer to locate on surface vertex and local pressures of vertex atoms are negative. The pressure of the Cu atom at central site is also positive and on average decreases with the distance from the center. However, for $Ag_{12}Pt_1Cu_{42}$ nanoalloy all of the Ag atoms are not at vertex of the surface and pressure value of one Ag atom is much closer to 0. The pressure of the Cu atoms at surface is between -2 GPa and -6 GPa. The pressure of the single Pt atom is higher than the central site. It can be concluded that positive and negative local pressure values increase with the addition of one Pt atom to binary $Ag_{12}Cu_{43}$ nanoalloy.

$Pt_{12}Cu_{43}$ binary nanoalloy exhibits a classical three-shell onion-like structure. There is a Cu atom located in the central site of the icosahedral structure with the 12 Pt atoms occupying the whole subshell and the remaining 42 Cu atoms occupy the third shell. The pressure of the central site is more positive than subshell Pt atoms. All surface Cu atoms have negative pressure. For $Pt_{12}Ag_1Cu_{42}$, the doped Ag atom locates on surface and has a negative pressure value. The pressure scale shows similarity with $Pt_{12}Cu_{43}$, although it was observed that some increase and decrease of the local atomic pressure values of the structure.

As a result, if an atom feels a negative pressure, it means it is suffering tensile strain and if an atom feels a positive pressure, the strain is compressive. It can be concluded that doping one atom of second alloying metal in pure nanoclusters and also third alloying metal in binary nanoalloys can change the local atomic pressure due to elemental properties of the doped atom.

4. CONCLUSIONS

In this study, simulations were performed to analyze alloying effect on chemical ordering and structural properties of nanoclusters. 55-atom nanoclusters consist of Cu, Ag and Pt atoms were chosen to study. The best chemical ordering structures were obtained and Cu, Ag and Pt atoms preferred to locate in accordance with their elemental properties such as surface, cohesive and atomic radius. Our results show that doping one atom of second alloying metal in pure nanoclusters and also third alloying metal in binary nanoalloys can change the local atomic pressure due to elemental properties of the doped atom. It can be concluded that doping a smaller atom at the central site of the icosahedral structure exhibits decreasing of core stress and also relaxation of the strained icosahedral structure.

Acknowledgments

The author thanks to Dr. Haydar Arslan for providing the atomic pressure code.

REFERENCES

[1] F. Baletto and R. Ferrando, “Structural properties of nanoclusters: Energetic, thermodynamic, and kinetic effects,” *Rev. Mod. Phys.*, vol. 77, no. 1, pp. 371–423, 2005.

[2] R. Ismail, “Theoretical studies of free and supported nanoalloy clusters,” 2013.

[3] R. Johnson, *Atomic and Molecular Clusters*. 2014.

[4] R. Ferrando, J. Jellinek, and R. L. Johnston, "Nanoalloys: From Theory to Applications of Alloy Clusters and Nanoparticles," *Chem. Rev.*, vol. 108, no. 3, pp. 845–910, 2008.

[5] R. Ferrando, "Determining the equilibrium structures of nanoalloys by computational methods," *J. Nanoparticle Res.*, vol. 20, p. 179, 2018.

[6] R. Ferrando, *Structure and properties of nanoalloys*. Elsevier, 2016.

[7] T. P. Martin, "Shells of atoms," *Phys. Rep.*, vol. 273, pp. 199–241, 1996.

[8] R. Ferrando, "Symmetry breaking and morphological instabilities in core-shell metallic nanoparticles," *J. Phys. Condens. Matter*, vol. 27, p. 013003, 2015.

[9] D. Bochicchio and R. Ferrando, "Morphological instability of core-shell metallic nanoparticles," *Phys. Rev. B - Condens. Matter Mater. Phys.*, vol. 87, no. 16, p. 165435, 2013.

[10] T. X. Li, Y. L. Ji, S. W. Yu, and G. H. Wang, "Melting properties of noble metal clusters," *Solid State Commun.*, vol. 116, no. 10, pp. 547–550, 2000.

[11] C. Mottet, G. Rossi, F. Baletto, and R. Ferrando, "Single impurity effect on the melting of nanoclusters," *Phys. Rev. Lett.*, vol. 95, no. 3, p. 035501, 2005.

[12] D. Cheng and D. Cao, "Ternary alloying effect on the melting of metal clusters," *Eur. Phys. J. B*, vol. 66, no. 1, pp. 17–23, 2008.

[13] M. Zhang and R. Fournier, "Structure of 55-atom bimetallic clusters," *J. Mol. Struct. THEOCHEM*, vol. 762, no. 1–3, pp. 49–56, 2006.

[14] R. P. Gupta, "Lattice relaxation at a metal surface," *Phys. Rev. B*, vol. 23, no. 12, p. 626, 1981.

[15] V. Rosato, M. Guillope, and B. Legrand, "Thermodynamical and structural properties of f.c.c. transition metals using a simple tight-binding model," *Philos. Mag. A*, vol. 59, no. 2, pp. 321–336, 1989.

[16] S. Taran, A. K. Garip, and H. Arslan, "Theoretical study of the structures and chemical ordering of CoPd nanoalloys supported on MgO(001)," *Int. J. Mod. Phys. C*, vol. 27, no. 12, p. 1650146, 2016.

[17] H. Arslan, A. K. Garip, and S. Taran, "A molecular dynamics study: structural and thermal evolution of 147 atom ComAun nanoalloys," *J. Nanoparticle Res.*, vol. 21, no. 6, p. 130, 2019.

[18] H. Arslan, A. K. Garip, and R. L. Johnston, "Theoretical study of the structures and chemical ordering of cobalt–palladium nanoclusters," *Phys. Chem. Chem. Phys.*, vol. 17, no. 42, pp. 28311–28321, 2015.

[19] S. Taran, "Composition effect on melting behaviors of Cu-Au-Pt trimetallic nanoalloys," *Comput. Theor. Chem.*, vol. 1166, p. 112576, 2019.

[20] H. Akbarzadeh, M. Abbaspour, and E. Mehrjouei, "Effect of systematic addition of the third component on the melting characteristics and structural evolution of binary alloy nanoclusters," *J. Mol. Liq.*, vol. 249, pp. 412–419, 2018.

[21] G. Rossi and R. Ferrando, "Combining shape-changing with exchange moves in the optimization of nanoalloys," *Comput. Theor. Chem.*, vol. 1107, pp. 66–73, 2017.

[22] X. Wu, G. Wu, Y. Chen, and Y. Qiao, "Structural optimization of Cu - Ag - Au trimetallic clusters by adaptive immune optimization algorithm," *J. Phys. Chem. A*, vol. 115, no. 46, pp. 13316–13323, 2011.

[23] Z. Zhao, M. Li, D. Cheng, and J. Zhu, "Understanding the structural properties and thermal stabilities of Au-Pd-Pt trimetallic clusters," *Chem. Phys.*, vol. 441,

pp. 152–158, 2014.

[24] D. J. Borbón-González, A. Fortunelli, G. Barcaro, L. Sementa, R. L. Johnston, and A. Posada-Amarillas, "Global minimum Pt13M20 (M = Ag, Au, Cu, Pd) dodecahedral core-shell clusters," *J. Phys. Chem. A*, vol. 117, no. 51, pp. 14261–14266, 2013.

[25] D. Cheng, X. Liu, D. Cao, W. Wang, and S. Huang, "Surface segregation of Ag-Cu-Au trimetallic clusters," *Nanotechnology*, vol. 18, no. 47, p. 475702, 2007.

[26] D. J. Wales and J. P. K. Doye, "Global Optimization by Basin-Hopping and the Lowest Energy Structures of Lennard-Jones Clusters Containing up to 110 Atoms," *J. Phys. Chem. A*, vol. 101, no. 28, pp. 5111–5116, 1997.

[27] R. Ferrando, "Stress-driven structural transitions in bimetallic nanoparticles," *Front. Nanosci.*, vol. 12, pp. 189–204, 2018.

JOURNAL OF SCIENCE
SAKARYA UNIVERSITY

Sakarya University Journal of Science

ISSN 1301-4048 | e-ISSN 2147-835X | Period Bimonthly | Founded: 1997 | Publisher Sakarya University | http://www.saujs.sakarya.edu.tr/en/

Title: Modeling Active Learning in a Robot Collective

Authors: Mehmet Dinçer ERBAŞ
Recieved: 2020-01-28 16:52:06

Accepted: 2020-03-25 13:16:18

Article Type: Research Article
Volume: 24
Issue: 3
Month: June
Year: 2020
Pages: 511-520

How to cite
Mehmet Dinçer ERBAŞ; (2020), Modeling Active Learning in a Robot Collective. Sakarya University Journal of Science, 24(3), 511-520, DOI: https://doi.org/10.16984/saufenbilder.681272
Access link
http://www.saujs.sakarya.edu.tr/en/issue/52472/681272

Sakarya University Journal of Science 24(3), 511-520, 2020

Modeling Active Learning in a Robot Collective

Mehmet Dinçer ERBAŞ*[1]

Abstract

In this research, we model an active learning method on real robots that can visually learn from each other. For this purpose, we initially design an experiment scenario in which a teacher robot presents a simple classification task to a learner robot through which the learner robot can discriminate different colors based on a predefined lexicon. It is shown that, with passive learning, the learner robot is able to partially achieve the given task. Afterwards, we design an active learning procedure in which the learner robot can manifest what it understand from the presented information. Based on this manifestation, the teacher robot determines which parts of the classification system are misunderstood and it rephrases those parts. It is shown that, with the help of active learning procedure, the robots achieve a higher success rate in learning the simple classification task. In this way, we qualitatively analyze how active learning works and why it enhances learning.

Keywords: Active Learning, Learning by Demonstration, Multi-Robot Group, Robot Learning.

1. INTRODUCTION

Active learning is a well-known teaching method that is widely accepted to enhance the learning activities of students. The basic idea behind active learning is that the students are able to understand and later recall the information that is presented to them if they, instead of passively listen, get involved in the learning process [1]. As the students actively participate in the learning process, their experiences support the grounding of the perceived information. Therefore, it is seen as a key mechanism that can transform students from passive listeners to active information gatherers. It is generally compared with traditional lectures in which students passively listen and possibly get notes about the newly presented information. According to Kyriacou [2], when active learning is utilized, the students should be given a degree of control over the learning activities such that they can have a sense of ownership on what is learned and how it is learned. In addition, he claimed that through active learning, the learning experience should be open-ended instead of predetermined so that the

* Corresponding Author: dincer.erbas@ibu.edu.tr
[1] Bolu Abant Izzet Baysal University, Engineering Faculty, Computer Engineering Department, 14030, Bolu, TURKEY, ORCID ID: 0000-0003-1762-0428

active participation of the students can shape the learning process.

A number of basic student activities, including reading, writing, discussing, asking, explaining, form the basis of any active learning method. In particular, the students are expected to engage in high-level cognitive tasks, such as analysis, synthesis and evaluation so that they can think, understand and finally learn the information that is presented to them [3]. Although these activities can be included in traditional homework practices, active learning is generally implemented during lectures in a classroom. In an active learning environment, the main objective is to draw the students' attention as high as possible while keeping them engaged [4]. For this purpose, students are encouraged to think critically, communicate their opinions with classmates or teachers, express their understandings through writing and most importantly provide feedback about their ongoing learning process [4].

It may be beneficial to list some other well-known teaching techniques that can be used in accordance with active learning. For instance, collaborative or cooperative learning is a method in which students work in small groups in order to achieve a common goal [5]. The students are encouraged to form small groups and cooperate with others to solve some specific problems that can be partitioned into a set of distinct issues for which each member of the group can contribute. Another well-known teaching method, problem-based learning (PBL) [5] aims to present a set of relevant problems that shape the learning process at the beginning of every learning activity. Both collaborative and PBL methods increase student engagement and cooperation; therefore they are widely used as a part of active learning methods.

As active learning methods can be designed with a variety of different approaches, there have been some efforts for formalizing the main principles of active learning. For instance, Barnes [6] defined seven principles of active learning as:

- Purposive: The content of the learned task should be relevant to the learner's concerns. In effect, the learner should intentionally participate in the learning process.
- Reflective: The student should be allowed to reflect his/her own opinion about what is learned. Instead of passively listening, the student should be allowed to openly express what he/she understands from the presented information.
- Negotiated: The teacher and the student should negotiate the objective and methods of learning.
- Critical: The students should possess ways of appreciating different methods of learning.
- Complex: The students should be able to compare what is learned with the complexities encountered in the real life.
- Situation-driven: The task that is learned should be a part of a specific situation.
- Engaged: The task that is learned should correspond to a real life activity.

Barnes claimed that the first four principles encourage the participation of the students while the last three enhance the realism of the learning process. Kyriacou [2] identified five key concepts for active learning:

- Concrete materials should be used as a part of direct experience.
- Problem-oriented techniques should be utilized.
- Students should work in small groups.
- Students should own the learning process.
- Learning process or task should be relevant and personally focused.

He stated that the application of at least one of these concepts to a learning activity implements an active learning process. Felder and Brent [7] designed distinct steps which they claimed that an active learning process should include. These steps had detailed timings and objectives that are implemented to increase the level of participation of students in a classroom.

Active learning methods are designed and tested on some student communities in a number of researches. Some of these researches reported an enhanced level of success. For instance, Laws et

al. [8] examined the effects of active learning methods on students in a course in physics. They reported that the students managed to get a better learning rate when they had interactive engagements during the lectures. The number of students that could understand the basic concepts of physics, such as force and acceleration was two to three times higher with the help of active learning methods. Freeman et al. [9] examined the learning performance of students in primary and secondary level students with active learning methods. They reported that the students had a higher mean score of success compared to their performance with traditional passive learning methods. Marcondes et al. [10] attempted to utilize active learning methods for undergraduate psychology classes. They stated that simple puzzles can be utilized to explain cardiac cycle to students.

Although many teachers have become interested in active learning in recent years and some reports claimed high success rate of certain active learning methods, there are still some issues that makes its implementation hard for new practitioners. For instance, Borrego [11] stated that there is a lack of consensus about the exact definition of active learning. As a result, its implementations in different disciplines possess many uncertainties. Konopka et al. [4] claimed that many teachers who are interested in active learning have no clear understanding about what active learning means and how it is different from the traditional teaching methods. Furthermore, many teachers do not know the meaning and use of different active learning techniques and so cannot use them effectively based on the students' needs. Additionally, Prince [5] claims that there is a significant problem in the assessment of the outcomes of active learning methods. For instance, some researchers declared improvement in the learning performance with active learning; however they did not mention the improvement was in fact small. Konopka et al. [4] claimed that the effectiveness of any active learning method is difficult to measure because many different methods were compared on different metrics. As a result of these difficulties, although many teachers feel that the current educational methods should be improved, they avoid trying active learning methods and pursue the traditional teaching activities.

The issues that make the implementation and evaluation of active learning methods are partly due to the fact that these methods have never been mathematically modeled and examined on any platform. A number of adaptive learning algorithms, including reinforcement learning [12], supervised learning [13], learning by demonstration [14] or deep learning [15], have been implemented, tested and examined on simulations or robotics platforms. There is continuing effort in modeling some of the well-known human cognitive processes, such as language acquisition on simulation or real robot experiments [16]. These models explain the mechanisms that allow humans to gradually develop a shared and complex communication system in noisy social learning environments. The systems that model noisy social learning environments are particularly significant for active learning research because active learning attempts to improve the quality of learning in noisy learning environments that may cause misconception or partial retention of the information that is presented with the traditional teaching methods. If we can model an environment in which robots or simulated agents learn from each other, though imperfectly due to their limited perceptual abilities and noisy interactions, we can examine and then explain how and why active learning methods enhances learning.

In this research we attempt to model an active learning method on real robots that can visually learn from each other. For this purpose, we design an experiment scenario in which a teacher robot presents a simple classification system to a learner robot through which the learner robot can discriminate different colors based on a predefined lexicon. It is shown that, with passive learning, the learner robot is able to partially comprehend the presented classification system. Afterwards, we design an active learning procedure in which the learner robot can manifest what it understand form the presented information. Based on this manifestation, the teacher robot determines which parts of the

classification system is misunderstood and it rephrases those parts to make them more suitable to the perceptual abilities of the learner robot. As a result of this active learning procedure, it is shown that the presented classification system can be fully comprehended by the learner robot. We qualitatively analyze how the procedure works and why it enhances learning.

The article proceeds as follows: section 2 presents the robots and the visual learning algorithm that are used to model active learning. Section 3 presents our method of passive and active. Finally, section 4 discusses the experiment results and concludes the article.

2. ROBOTS AND VISUAL LEARNING ALGORITHM

To model learning between robots, we use two e-puck miniature robots that are shown in figure 1 [17]. The robots are programmed to visually learn from each other by using their on-board image sensors. One of the robots is declared as the teacher and it can follow predefined movement patterns that can be learned by the learner robot. The learner robot can learn a demonstrated movement pattern by using a movement imitation algorithm [18]. The algorithm works as follows:

- As the teacher robot moves on a predefined movement trajectory, the learner robot captures multiple frames from its image sensor.
- The robots wear a colorful hat to enhance on-board image processing. On each frame, the learner robot determines the relative position of the hat of the teacher robot and saves this information in a list of relative positions.
- When the movement pattern is completed, the learner robot processes the relative position list in order to reproduce the demonstrated movement pattern of the teacher robot.
- The learner robot saves the reproduced movement pattern in its memory so that it can be executed at a later time.

In this way, the learner robot is able to observe and learn the movement patterns that are demonstrated by the teacher robot. Further details about the movement imitation algorithm and an analysis on the type of copying errors can be seen in [18].

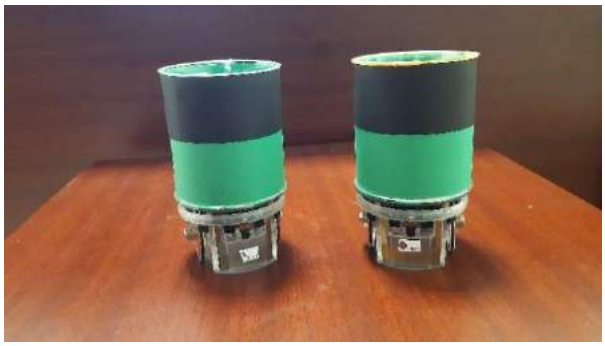

Figure 1. Two E-puck robots that are used in the experiments. As can be seen in the figure, the robots are fitted with a colorful hat to make it easier for them to detect each other.

The learner robot watches a demonstrated movement pattern from a single point of view; hence it has monoscopic vision. Furthermore, it can capture relatively low resolution image frames (320 x 240 pixels). As a result of these facts, the learner robot may have perceptual errors due to imperfect sensor system, therefore we have noisy social learning among the robots. For instance, figure 2 shows a movement pattern that is followed by the teacher robot and its reproduced copy by the learner robot. When we compare two movement trajectories, it can be seen that the reproduced copy has some discrepancies. For instance, in comparison with the original movement pattern, the first straight line segment is partitioned into two parts, the second straight line segment becomes slightly longer, third turn has a wider angle, fourth straight line segment is slightly longer and the last straight line segment is shorter in the copy.

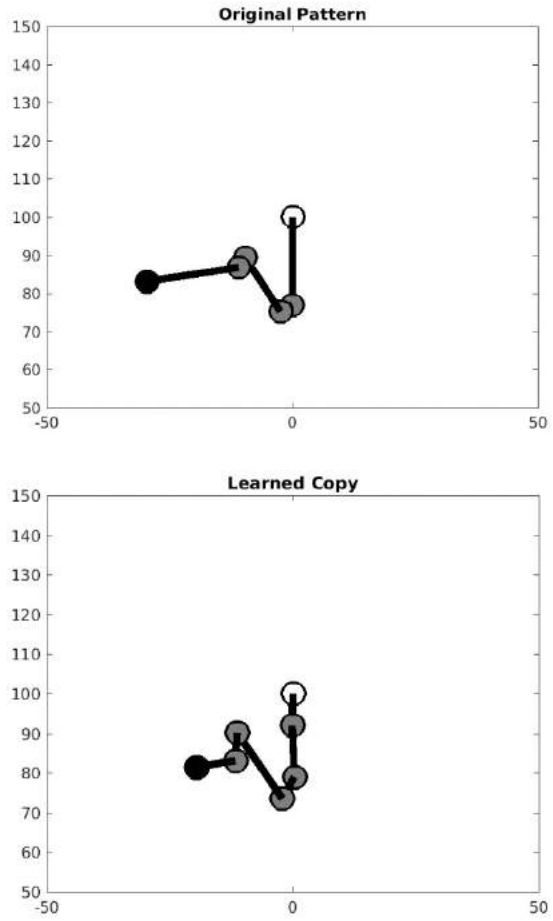

Figure 2. An original movement pattern that is followed by the teacher robot and its reproduced copy. The original pattern consists of 23 cm straight move, 54° clockwise turn, 3 cm move, 99° clockwise turn, 16 cm move, 128° counter-clockwise turn, 3 cm move, 54° clockwise turn and 19 cm move. Its copy consists of 8 cm move, 3° counter-clockwise turn, 13 cm move, 26° clockwise turn, 6 cm move, 127° clockwise turn, 19 cm move, 148° counter-clockwise turn, 7 cm move, 75° clockwise turn, 8 cm move. The trajectories are shown in cm.

In order to qualitatively determine how accurately a demonstrated movement pattern is learned by the learner robot, we need a quality of learning metric that compares two distinct movement patterns. For this purpose, we devise Edit Distance with Penalty metric (ERP) that is widely used as a trajectory similarity measure [19]. Based on ERP metric, the difference between an original pattern O which consist of a list of vectors ($o_1, o_2, o_3, \ldots, o_m$) and its copy C, which consist of a list of vectors ($c_1, c_2, c_3, \ldots, c_n$) is calculated as follows:

$$ERP(O,C) = \begin{cases} \sum_{i=1}^{m} dist(o_i, g) & if\ n = 0 \\ \sum_{i=1}^{n} dist(c_i, g) & if\ m = 0 \\ min \begin{cases} ERP(Rest(O), Rest(C)) + dist(o_i, c_i) \\ ERP(Rest(O), C) + dist(o_i, g) \\ ERP(O, Rest(C)) + dist(c_i, g) \end{cases} & oth. \end{cases} \quad (1)$$

in which *Rest(O)* and *Rest(C)* are the O and C with the first element removed, $dist(r_i,s_i) = |r_i - s_i|$, the Euclidean distance between the vectors r_i and s_i, $dist(s_i,g) = |s_i - g|$ and $dist(r_i,g) = |r_i - g|$ where g is the gap constant which is set to 0 vector. Based on this metric, the distance between the movement patterns that are shown in figure 2 is equal to 0.3225. An ERP value that is less than 0.5 is accepted as a high quality copy.

At this point, it should be noted that the robots are not allowed to communicate in any other way except visual learning. For instance, they cannot send any message or executed motor commands to other robots. Therefore, they can only interact through a noisy channel by using their on-board image sensors.

3. MODELING LEARNING METHODS

3.1. Modeling Passive Learning

To model passive learning, we designed experiments in which the learner robot attempts to learn and then tested on a lexicon. The lexicon consists of 5 different randomly generated movement patterns and each movement pattern is matched with a specific color. Figure 3 shows the randomly generated movement patterns and their corresponding colors. The passive learning experiment starts with teaching procedure during which the teacher robot teaches the learner robot each of the movement patterns and their corresponding colors. This is done by the following steps:

- At the start of each teaching procedure, as shown in figure 4, the teacher robot and a block with the specific color are placed 1 m away from the learner robot on a 120 x 120 cm robot arena.
- The learner robot captures a frame and determines the color of the presented block.

- The teacher robot then turns its LEDs on for two seconds to signal movement pattern start. The learner gets ready for the demonstration.
- The teacher turns its light off and follows the movement pattern that is matched with the presented color, while the learner robot learns the movement pattern by using the movement imitation algorithm presented in the previous section.
- When the execution of the movement pattern is completed, the teacher robot turns its lights on for two seconds to signal movement pattern completed.
- The learner robot saves the reproduced movement pattern as the meaning of the presented color in its memory.

The above steps are repeated for all of the 5 colors so that the learner robot learns the pattern of each color.

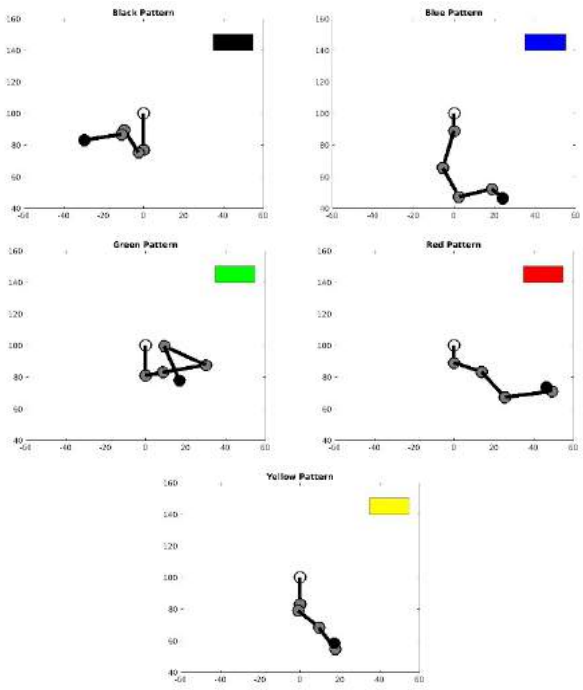

Figure 3. The randomly generated movement patterns of colors.

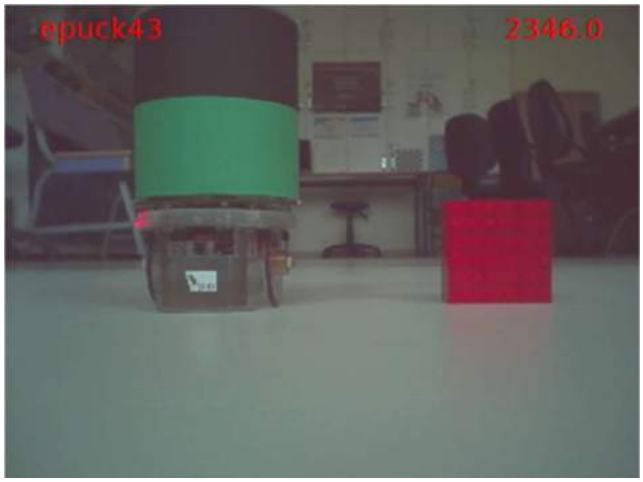

Figure 4. A captured image from the image sensor of the learner robot. In the figure, the teacher robot and the red block can be seen.

At this point, it should be noted that so far, with the passive learning method during which the learner solely observes the presented information through noisy learning channel, the teacher has no clue about how accurately the presented information is comprehended by the learner. In order to test the learning success of the learner, the teaching procedure is followed by an examination procedure. For this purpose, the following steps are applied:

- The teacher robot selects one of the colors and follows its matched movement pattern.
- The learner robot copies the pattern. Then it compares the newly reproduced pattern with the movement patterns of each color that it saved in its memory during the teaching procedure, by using the ERP function.
- The learner robot determines the pattern that is most similar pattern (lowest ERP value) to the newly reproduced pattern and declares its corresponding color as its answer.
- The teacher compares the answer of the learner to the actual color that it previously choose. If it is the same color, the learner is given 1 point.

During the examination procedure, the teacher robot selects and executes the patterns of each color 10 times. In this way, we are able to check

if the learning activity in the teaching procedure is successful.

Figure 5 shows the results of the examination procedure. As can be seen, the learner robot can detect the patterns of the black, blue, green and yellow; however it has a low performance when it needs to detect the pattern of red.

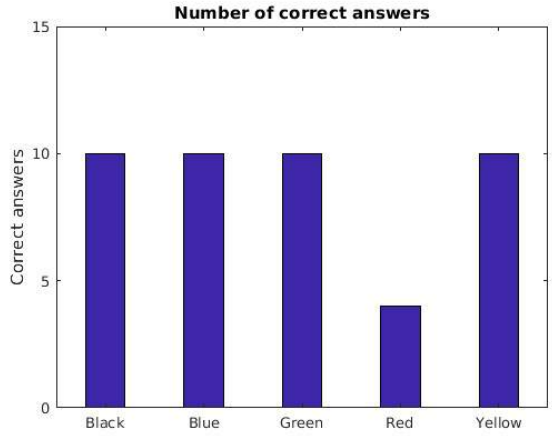

Figure 5. The results of examination procedure with passive learning.

In order to observe the reasons of the results shown above, we examine how accurately the presented patterns are learned by the learner robot. Figure 6 shows the learned patterns of the learner robot after the teaching procedure. When we apply the ERP function to compare the original and learned movement patterns, it reveals that four of the patterns, namely patterns of black, blue, green and yellow, are learned with relatively low error (ERP value 0.3225, 0.2425, 0.3415, 0.2343, respectively), while the pattern of red can be learned with a much higher error (ERP value 1.0564). This fact explains why the learner robot has a low performance when it needs to detect the pattern of red. As it is learned with high error, the robot cannot detect it in the examination procedure. A visual inspection of the learned patterns also reveals that the learned version of the pattern of red is highly dissimilar to its original. In fact, some geometrical properties of the pattern of red make it harder to learn. For instance, its first straight line segment is shorter compared to other patterns which make it harder to detect. Furthermore, the teacher robot seems to move on the same direction while it executes pattern of red as there is only one distinct change of direction in this pattern. Other patterns that are learned have sharper turns which are much easier to detect. As a result of these unique geometrical properties, overall shape of the copy of the pattern of red is highly dissimilar to its original demonstration.

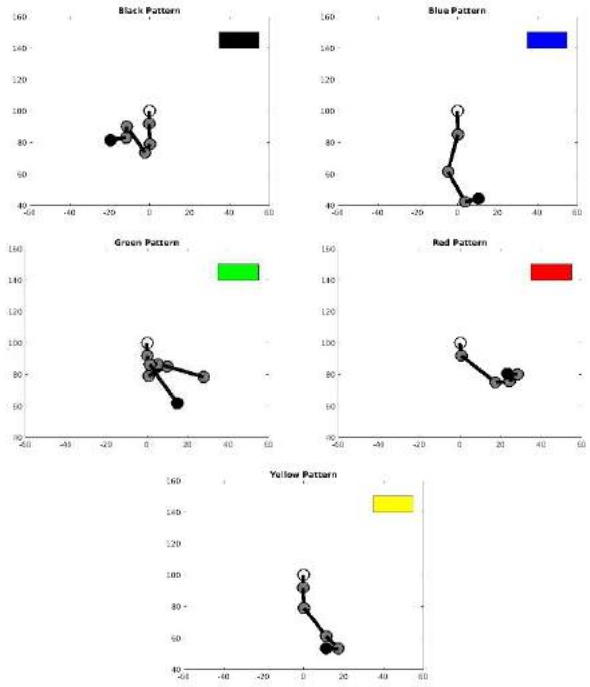

Figure 6. Reproduced patterns of the learner robot.

As stated above, with traditional passive learning methods, as the learner robot just observes and does not actively participate in the learning process, there is no way for teacher robot to detect the fact that four of the presented patterns are learned accurately while one of the patterns is not. The noisy learning channel may have different effects on the learning process of different subjects and it may cause principal differences between how a subject is explained by the teacher and how it is understood by the learner. Unfortunately, there is no way that an excessive error in learning can be detected and corrected.

3.2. Modeling Active Learning

As stated above, the main issue about the passive learning is that for the teacher, there is no feedback mechanism from the learner. The learner may misunderstand some parts of the information that is presented; however, as it only

passively listen, they cannot declare the issue to the teacher. Actually, the learner may not be aware that it misunderstands something. Therefore, as a part of the active learning, there needs to be a procedure that allows learner to actively declare what it understands. To model this, we present a feedback procedure after the teaching procedure. During the feedback procedure, the learner robot declares what it has understood from the presented patterns of each color by executing all patterns that it previously saved. In effect, the robots change roles and the teacher robot watches the demonstrations of the learner robot. When the teacher robot gets the feedback by copying the demonstrated patterns of the learner robot, it compares the copied patterns with what it previously presented, by using the ERP function. This comparison immediately reveals that the patterns of the four colors, namely black, blue, green and yellow, are learned accurately (ERP value 0.4545, 0.2953, 0.4747, 0.2723, relatively) while there is a high error in the learned version of the pattern of red (ERP value 1.2137). As a result of the feedback procedure, the teacher robot now can determine which part of the presented information is misunderstood by the learner robot.

Obviously, as the pattern of red cannot be accurately learned by the learner robot, this pattern should be reconfigured and re-thought. The ERP value reveals that there is a high error in the copies of the pattern of red; however, it does not indicate the specific parts of the pattern in which the errors occur. For the reconfigured version of the pattern of red, we program the teacher robot to utilize the pattern that it copied during the feedback procedure. As this pattern was previously reproduced by the learner robot, we assume that it is a pattern that can be accurately learned by the learner. In this way, we are able to model an active learning procedure in which the feedbacks received from the learners are utilized to achieve enhanced learning. The teacher robot presents the new version of the pattern of red, which is shown in figure 7, along with the patterns of other colors to the learner. After this modification, when we check how accurately the 5 patterns are learned by the learner robot, it can be seen that now all the patterns are learned with high fidelity (ERP value for black, blue, green, red and yellow are 0.2757, 0.1152, 0.3706, 0.3495, 0.1196, respectively). Finally, we repeat the examination procedure to check if the learner robot can discriminate all colors based on the learned patterns. Figure 8 shows the results for the second examination procedure. As can be seen, with updated learned patterns, the learner robot has the correct answer for all colors.

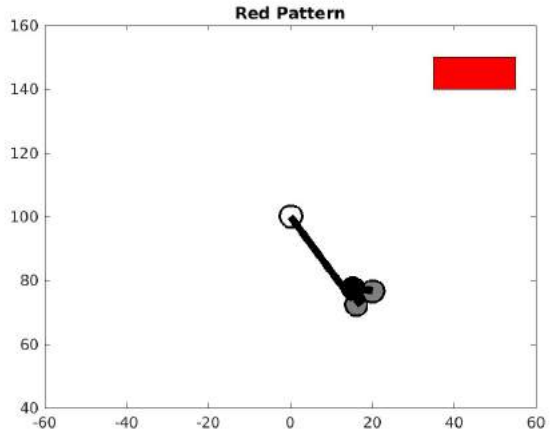

Figure 7. Reconfigured pattern of red.

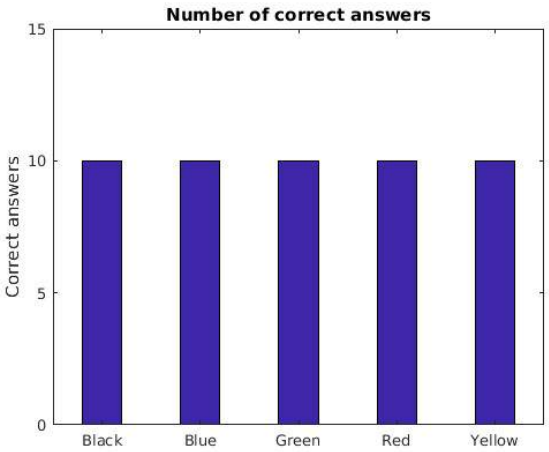

Figure 8. Results of examination procedure with active learning.

4. CONCLUSION

In this research, we aimed to utilize robotic experiments to model a well-known learning method, namely active learning. For this purpose, we initially designed a noisy social environment where mobile robots can visually learn from each other, albeit imperfectly due to uncertainties in

their perceptual system. It is shown that, as the robots learned from each other, the movement trajectories contained some copying errors. In this noisy learning environment, we designed a passive learning procedure in which a teacher robot presented a lexicon that can be used to categorize multiple colors. Based on this method, the learner robot passively observed the movement patterns and then it was tested to determine if the presented information was accurately learned. The experiments revealed that due to copying errors, the learner robot had low performance in detecting the movement pattern of one of the colors. With passive learning method, the learner passively observed, therefore there was no way to overcome this issue. Later, we designed an active learning method that includes an extra feedback procedure during which the learner robot declared what it understood from the presented information. Based on the feedback that it received from the learner robot, the teacher robot was able to determine which part of the presented information was misunderstood by the learner robot. As the teacher robot reconfigured the misunderstood parts, an increase in the learning performance was observed. In this way, we were able to model an active learning method in which the learner actively participated in the learning process. Based on our model, we were able to qualitatively show how and why active learning approach enhances learning.

The active learning method that is modeled in this research involves two of the principles that were presented by Barnes [6]. First, the method is reflective as the learner robot was allowed to express what it understood during the feedback procedure. Second, the method is negotiated as the final reconfigured version of the pattern of red was determined based on the feedback from the learner robot. Therefore, in effect, the teacher and the learner negotiated the objectives and the methods of learning. It should be possible and testable to model and examine other active learning principles on robotic platforms that involve noisy social learning between robots.

In our experiments, robots learned a simple categorization task. The robots were able to achieve a high performance with the help of one feedback procedure. However, with a more complex learning task, we may need to run multiple feedback procedures to achieve an enhancement in learning. In this respect, the feedback procedure should be designed as a feedback loop so that it can be repeated until an agreement on the content of the presented information can be achieved.

Our analysis reveals some important deductions about active learning methods. As other researches strongly suggested, the participation of the learners in the learning process is a crucial factor for enhancing learning. The learners should definitely possess ways of expressing themselves and they should be able to clearly explain what they understand. For this purpose, students should be encouraged to write, talk and discuss from an early age so that they can effectively be a part of an active learning environment.

REFERENCES

[1] C. C. Bonwell, and J. A. Eison. “Active Learning: Creating Excitement in the Classroom,” 1991 ASHE-ERIC Higher Education Reports. ERIC Clearinghouse on Higher Education, The George Washington University, 1991.

[2] C. Kyriacou, “Active learning in secondary school mathematics,” British Educational Research Journal, vol. 18, no. 3, pp. 309-318, 1992.

[3] A. Renkl, R. K. Atkinson, U. H. Maier, and R. Staley, “From example study to problem solving: Smooth transitions help learning,” The Journal of Experimental Education, vol. 70, no. 4, pp.293-315, 2002.

[4] C. L. Konopka, M. B. Adaime, and P. H. Mosele, “Active teaching and learning methodologies: some considerations,” Creative Education, vol. 6, no. 14, p.1536-1545, 2015.

[5] M. Prince, “Does active learning work? A review of the research,” Journal of

engineering education, vol. 93, no. 3, pp.223-231, 2004.

[6] D. R. Barnes, "Active learning," Leeds University TVEI Support Project, 1989.

[7] R. M. Felder, and R. Brent, "Active learning: An introduction," ASQ higher education brief, vol. 2, no. 4, pp.1-5, 2009.

[8] P. Laws, D. Sokoloff, and R. Thornton, "Promoting active learning using the results of physics education research," UniServe Science News, 13, pp.14-19, 1999.

[9] S. Freeman, S. L. Eddy, M. McDonough, M. K. Smith, N. Okoroafor, H. Jordt, and M. P. Wenderoth, "Active learning increases student performance in science, engineering, and mathematics," Proceedings of the National Academy of Sciences, vol. 111, no. 23, pp.8410-8415 2014.

[10] F. K. Marcondes, M. J. Moura, A. Sanches, R. Costa, P. O. de Lima, F. C. Groppo, M. E. Amaral, P. Zeni, K. C. Gaviao, and L. H. Montrezor, "A puzzle used to teach the cardiac cycle," Advances in Physiology Education, vol. 39, no. 1, pp.27-31, 2015.

[11] M. Borrego, S. Cutler, M. Prince, C. Henderson, and J. E. Froyd, "Fidelity of implementation of research-based instructional strategies (RBIS) in engineering science courses," Journal of Engineering Education, vol. 102, no. 3, pp.394-425, 2013.

[12] R. S. Sutton, and A. G. Barto, "Introduction to reinforcement learning," Cambridge: MIT press, 1998.

[13] R. Caruana, and A. Niculescu-Mizil, "An empirical comparison of supervised learning algorithms," In Proceedings of the 23rd international conference on Machine learning, pp. 161-168, 2006.

[14] C. G. Atkeson, and S. Schaal, "Robot learning from demonstration," In ICML vol. 97, pp. 12-20, 1997.

[15] Y. LeCun, Y. Bengio, and G. Hinton, G., "Deep learning," Nature, vol. 521, no: 7553, pp.436-444, 2015.

[16] S. Kirby, "Spontaneous evolution of linguistic structure-an iterated learning model of the emergence of regularity and irregularity," IEEE Transactions on Evolutionary Computation, vol. 5, no. 2, pp.102-110, 2001.

[17] F. Mondada, M. Bonani, X. Raemy, J. Pugh, C. Cianci, A. Klaptocz, S. Magnenat, J. C. Zufferey, D. Floreano, and A. Martinoli, "The e-puck, a robot designed for education in engineering," In Proceedings of the 9th conference on autonomous robot systems and competitions, pp. 59-65. IPCB: Instituto Politécnico de Castelo Branco.

[18] M. D. Erbas, "The development of a robust symbolic communication system for robots via embodied iterated imitation," Adaptive Behavior, vol. 27, no. 2, pp.137-156, 2019.

[19] L. Chen, and R. Ng, "On the marriage of lp-norms and edit distance," In Proceedings of the Thirtieth international conference on Very large data bases, pp. 792-803, 2004.

JOURNAL OF SCIENCE
SAKARYA UNIVERSITY

Sakarya University Journal of Science

ISSN 1301-4048 | e-ISSN 2147-835X | Period Bimonthly | Founded: 1997 | Publisher Sakarya University | http://www.saujs.sakarya.edu.tr/en/

Title: Examination of Wear and Rockwell-C Adhesion Properties of Nitronic 50 Steel Coated with Pack Boriding Method

Authors: Ersan MERTGENÇ
Recieved: 2019-12-16 09:09:25

Accepted: 2020-03-25 21:29:34

Article Type: Research Article
Volume: 24
Issue: 3
Month: June
Year: 2020
Pages: 521-530

How to cite
Ersan MERTGENÇ; (2020), Examination of Wear and Rockwell-C Adhesion Properties of Nitronic 50 Steel Coated with Pack Boriding Method. Sakarya University Journal of Science, 24(3), 521-530, DOI: https://doi.org/10.16984/saufenbilder.659782
Access link
http://www.saujs.sakarya.edu.tr/en/issue/52472/659782

Sakarya University Journal of Science 24(3), 521-530, 2020

Examination of Wear and Rockwell-C adhesion Properties of Nitronic 50 Steel Coated with Pack Boriding Method

Ersan MERTGENÇ*[1]

Abstract

The Nitronic 50 steel is a nitrogen containing stainless steel, which has a high corrosion resistance, and high strength but its surface resistance against wear is low, making it extremely limited to use in areas subject to wear. In this study, in order to improve the material surface and to investigate its effect on tribological properties, boronizing process was carried out by used pack boriding method at 850 ° C, 900 ° C and 950 ° C for 4 hours. As a result of coating process, the boride layer has a smooth and flat structure in SEM investigations, the coating thickness varies between 9 µm and 36 µm and the boride layer thickness increases with increasing temperature. While the hardness of the uncoated material was around 250 $HV_{0.05}$, the surface hardness of the material reached up to 1.712 $HV_{0.05}$ with the coating process and increased about 7 times. According to XRD analysis, the surface of the coating layer consisted of phases FeB, CrB, Ni_3B, Fe_2B, Cr_2B and MnB. Wear behavior was performed by ball-on-disk wear test in dry environment. The friction coefficient and wear rate decreases with increasing temperature, while the wear resistance is increased by 20 times compared to unboronized sample. When the wear tracks were examined, the uncoated Nitronic 50 had an adhesive wear mechanism, on the other hand the boronized samples had an adhesive and abrasive wear mechanism together. The Rockwell-C adhesion test was carried out under a load of 1.471 N and the resulting surface damages were evaluated according to the quality map. Boronized steel at 850 °C is defined as HF3 type, at 900 °C and 950 °C at boronized steel it is defined as HF4 type and adhesion is acceptable.

Keywords: Nitronic 50, pack boriding, Rocwell-C adhesion, wear

1. INTRODUCTION

Nitronic steels are seen as an erosion resistant alternative to 13/4 martensitic stainless steel currently used [1]. Nitronic steels are mainly austenitic stainless steels containing nitrogen as an alloying element in the matrix [2]. By adding nitrogen to the content of stainless steels; strength, ductility, toughness, work hardening capacity, erosion and corrosion resistance increases [3-5].

Nitronic 50 is a high nitrogen, weldable stainless steel and superior to SAE 304 and 316 and 316L in strength and corrosion resistance [6] and is also known as 22-13-5 stainless steel [7]. They have almost two times higher yield strength and good corrosion resistance than standard 316 L stainless steel [8], which is due to the high content of

* Corresponding Author: ersanmertgenc@hotmail.com
[1] Department of Railway Systems, Afyon Vocational High School, Afyon Kocatepe University, Afyonkarahisar, Turkey. ORCID: 0000-0001-8247-2922

chromium and molybdenum in the content, thus rivaling nickel alloys in seawater. Unlike most austenitic stainless steels, they are not magnetic when working in cold or sub-zero temperatures [7]. Nitronic 50 exhibits good mechanical properties at low and high temperatures where corrosion resistance and strength are required to be combined and is used extensively in a variety of applications such as naval construction, pumps, fittings, cables and heat exchangers [9].

Although stainless steels exhibit high corrosion resistance, low surface hardness is a major disadvantage, especially when exposed to wear, and it is important to improve the tribological and mechanical properties of their surfaces. In recent years, researchers have been working extensively on various coating techniques such as Pysical Vapor Deposition (PVD) [10-12], Diamond-like Carbon (DLC) [13-17], Plasma Nitriding [18-20], Boronizing [21-23] to increase surface hardness through surface modification.

Fundamentally boronizing is a thermo-chemical process [24] diffusing the boron atoms from the surface of materials by means of solid, liquid and gas [25]. Boronizing can be carried out in solid, liquid and gas environments. Boron method is widely used because of its low cost and simple. [26]. Pack boronizing is carried out in the temperature range of 700 °C - 1000 °C for 0,5 to 10 hours [27].

When the studies on Nitronic 50 stainless steel are examined; It has been observed that mainly the corrosion properties of the material have been studied. It is noteworthy that different methods have been used for coating, but the effects of pack boring on the material have not been investigated.

In this study, by using pack boriding method, Nitronic 50 steel was treated at 850 °C, 900 °C and 950 °C temperatures for 4 hours, the acceptability of the coating was evaluated by Rockwell-C adhesion test and the effect of coating on the wear behavior was investigated.

2. MATERIALS AND METHODS

Nitronic 50 stainless steel was used in this study. The chemical composition is given in Table 1.

Table 1. Chemical composition of Nitronic 50 steel (wt. %)

C	Si	Mn	P	S	N	Cr	Mo	Ni	V
0.032	0.6	5.04	0.027	0.0005	0.30	21.49	2.17	12.06	0.16

The test samples were cut into Ø16 × 8 mm dimensions and ground up to 1200 grid and polished using diamond solution. Samples were placed in a stainless-steel box with Ekabor-II commercial powder. Then, they were boronized in a temperature controlled chamber type furnace under atmospheric pressure for 4 hours 850 °C, 900 °C and 950 °C. After the completion of boriding process, test specimens removed from the sealed box were eventually allowed to cool down in still air.

For microstructure analysis, samples were cut along longitudinal section, sanded with SiC abrasive paper up to 120 - 1200 grit, polished with 1 μm alumina suspension and etched with stainless steel etch (HCl: HNO_3: H_2O to 1: 1: 1). Coating layer, matrix microstructure, wear tracks and boride thickness measurements were examined by using a Leo 1430VP scanning electron microscope (SEM). The presence of boride in the coating layer was confirmed by x-ray diffraction (Shimadzu XRD-6000) using CuKα (λ = 1.5406 Å) radiation at 20˚ - 90˚.

Shimadzu HMV-2 micro-hardness tester was used for hardness measurements. The measurements were made under conditions of 50 g load for 10 seconds from the cross-sectional surfaces of the coated samples to the matrix.

The wear tests of Nitronic 50 stainless steel coated by pack boring method were carried out in the ball disk system ball-on-disc system, dry conditions at room temperature, under 5 N load, 0.3 m / s wear rate and 500 m distance. 8 mm diameter WC-Co balls were used in the wear tests. The surface of

each sample was cleaned with alcohol before and after the abrasion wear tests. After the tests, the wear volumes of the samples were quantified by multiplying cross-sectional area by the width of wear track obtained from a Tribotechnic Rugosimeter. The wear rate was calculated with the following formula.

Wear rate = Wear volume / (Applied load × Sliding distance), mm^3 / Nm.

The Rockwell-C adhesion test was developed in Germany and standardized in VDI 3198. The Rockwell-C adhesion test, also known as the quality test for coated compounds, is applied at a load of up to 1471 N. It is mapped between HF1 and HF6 according to the condition of damage to the coating in figure 1 [28]. According to this test, which is easy to apply and evaluated especially during quality control processes during production; HF1-HF4 describes adequate adhesion, ie the acceptability of the coating, whereas HF5 and HF6 represent insufficient adhesion [29,30].

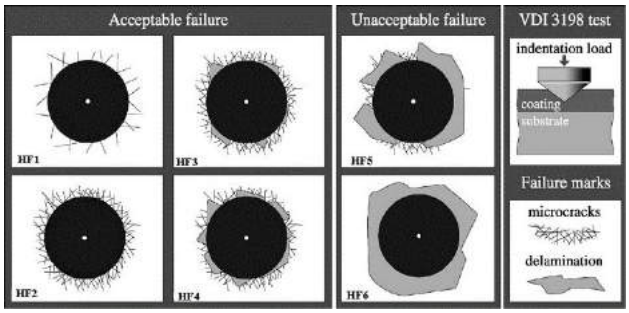

Figure 1. Principle of the VDI 3198 indentation test [28]

3. RESULTS AND DISCUSSIONS

3.1. Characterization of Coating Layer and Thickness

The microstructures of Nitronic 50 steel from the cross section of 850 °C, 900 °C and 950 °C for 4 hours are shown in figure 2.

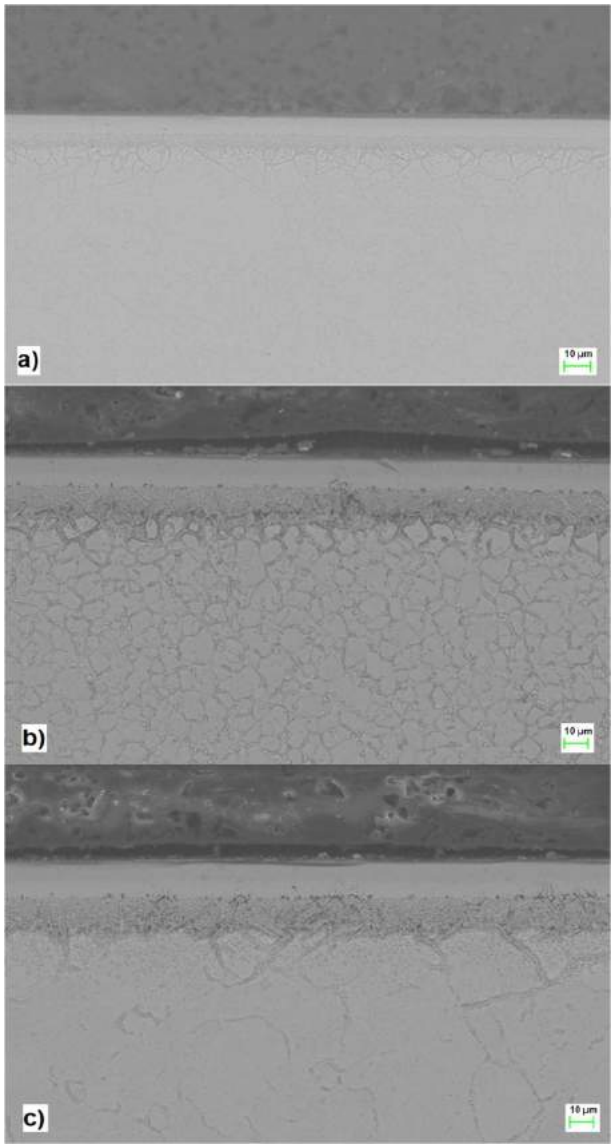

Figure 2. SEM cross-sectional views of boronized Nitronic 50 steel for 4 hours at a) 850 °C, b) 900 °C c) 950 °C

Boride layer has a flat and smooth structure and increase in boride layer thickness with increasing temperature [31, 32].

In steels, the thickness of the boride layer is strongly influenced by the alloying elements as a chorium, nickel and carbon in the substrate material [33]. Especially the presence of chromium makes it difficult to diffuse boron atoms due to its lower solubility compared to iron and prevents the growth of iron borides [34, 35]. The presence of as high as about 21 % chromium in Nitronic 50 steel results in a reduced boride layer thickness compared to steels. boride layer thickness was given table 2 and measured at

850 °C 13 µm, 900 °C 29 µm and 950 °C 36 µm. It is observed that an increase in the boride layer thickness is caused by the change in the process temperature for a treatment time of 4 h. This is due to the fact that the substrate material has high alloying elements, especially chromium and nickel.

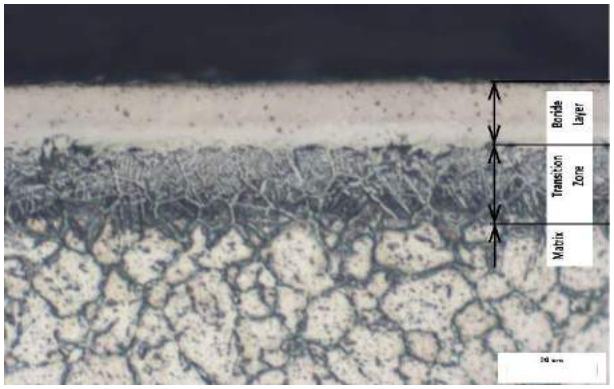

Figure 3. Zones of the coating layer of boronized Nitronic-50 steel for 950 ° C and 4 hours

When the figure 3 is examined, it is seen that there are 3 zones in coated Nitronic 50 steel; zone 1: coating layer FeB/CrB and composed of rich Fe, B, Cr, Ni alloys, zone 2: diffusion zone with higher hardness than matrix but lower hardness than boride layer, zone 3: steel matrix free of boron [36, 37].

3.2. X-Ray Diffraction Analysis

Figure 4 shows the x-ray diffraction analysis of boronized Nitronic 50 steel at 850 °C, 900 °C and 950 °C for 4 hours.

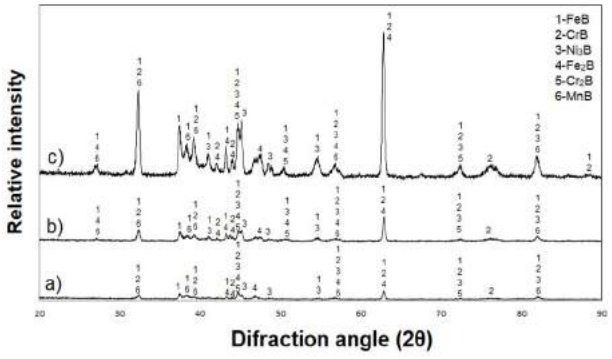

Figure 4. X-ray diffraction patterns of boronized Nitronic 50 steel for 4 hours at a) 850 °C, b) 900 °C c) 950 °C.

According to xrd analysis, FeB, CrB, Ni_3B, Fe_2B, Cr_2B and MnB phases were formed on the surface of the material depending on the process temperature. FeB and CrB phases increase with increasing temperature in boronizing treatment. The reason for this is that the diffusion process is accelerated with increasing temperature and the layer thickness increases. Due to the high amount of alloying elements such as Mn, Mo, Cr and Ni in Nitronic 50 steel, different phases were obtained due to these elements. The microstructure and the mechanical properties of the boronized material depend largely on the chemical composition of the material, the boriding temperature and the boriding time [38]. It is the reason why chromium based phases settle in dominant peaks due to the chemical composition of the material. On the other hand, the presence of FeB phase as the dominant peak in iron-based peaks is close to the surface, while Fe2B phase settles between FeB phase and matrix [35, 39, 40]. The coexistence of the CrB and FeB peaks is due to the fact that these phases are very difficult to distinguish due to their similar structure [41].

3.3. Hardness of Boride Layer

Micro-hardness measurements were performed from cross-sectional area from surface to matrix (figure 5).

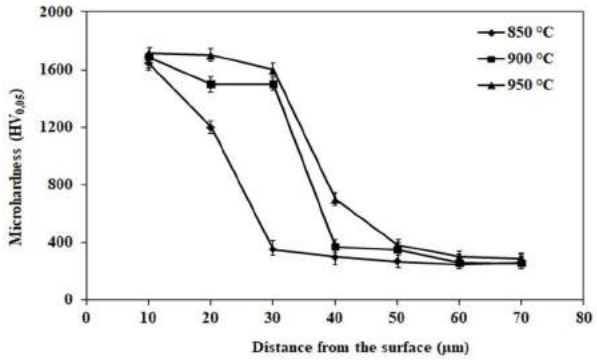

Figure 5. Micro-hardness profiles of boronized samples at 850 °C, 900 °C and 950 °C for 4 h.

The hardness of boronized Nitronic 50 steel was between 1080 $HV_{0.05}$ and 1.712 $HV_{0.05}$, while the hardness of untreated steel was found to be (<) 247 HV0.05. Hardness of boronized Nitronic 50

steel increased by seven times compared to the hardness of non-treated Nitronic 50 steel.

3.4. Wear Properties

In Table 2, coating thickness, friction coefficient and wear rate values of non-boronized and boronized samples are given.

Table 2. Friction coefficient and wear rates of boronized Nitronic 50 steel.

	Conditions			
	Uncoated	850 °C – 4 h	900 °C – 4 h	950 °C – 4 h
Coating layer	-	13	29	36
Friction coefficient	0.71	0.64	0.63	0.61
Wear rate x 10^{-8} (mm^3 / Nm)	81.15	10,85	5.42	3,43

When the wear test results of Nitronic 50 steel were examined, it was found that the friction coefficient was 0.71 in the non-boronized sample, whereas the friction coefficient in the boronized samples at different temperatures for 4 hours ranged from 0.64 to 0.61. Wear rate was 81.15 mm^3 / Nm in non-boronized sample and lower values were obtained in boronized samples. The lowest wear rate was measured as 3.43 mm^3 / Nm in boron-treated sample at 950 °C for 4 hours.

When the wear tests of steels are examined in the literature, the coefficient of friction changes between 0.5 – 0.7 [42, 43, 44] and this shows that this study is consistent with the literature. On the other hand, surface investigators such as Kovaci et al. [16], Cuao-Moreu et al. [45], Teng et al. [46] and He et al. [47] have studied the tribological properties of metal specimens by coating different metal surfaces with different materials, temperature, time and method. The reason for the serious decrease in wear rate is the wear resistance of the hard coating layer on the surface of the material [48-50]. As seen from the XRD analysis, the amount of high hardness phases such as FeB and CrB increased.

The SEM images of the wear marks on the ball on disk system, against WC-Co balls, at 5 N load, 0.3m / s wear rate and 500 m distance are given in figure 6.

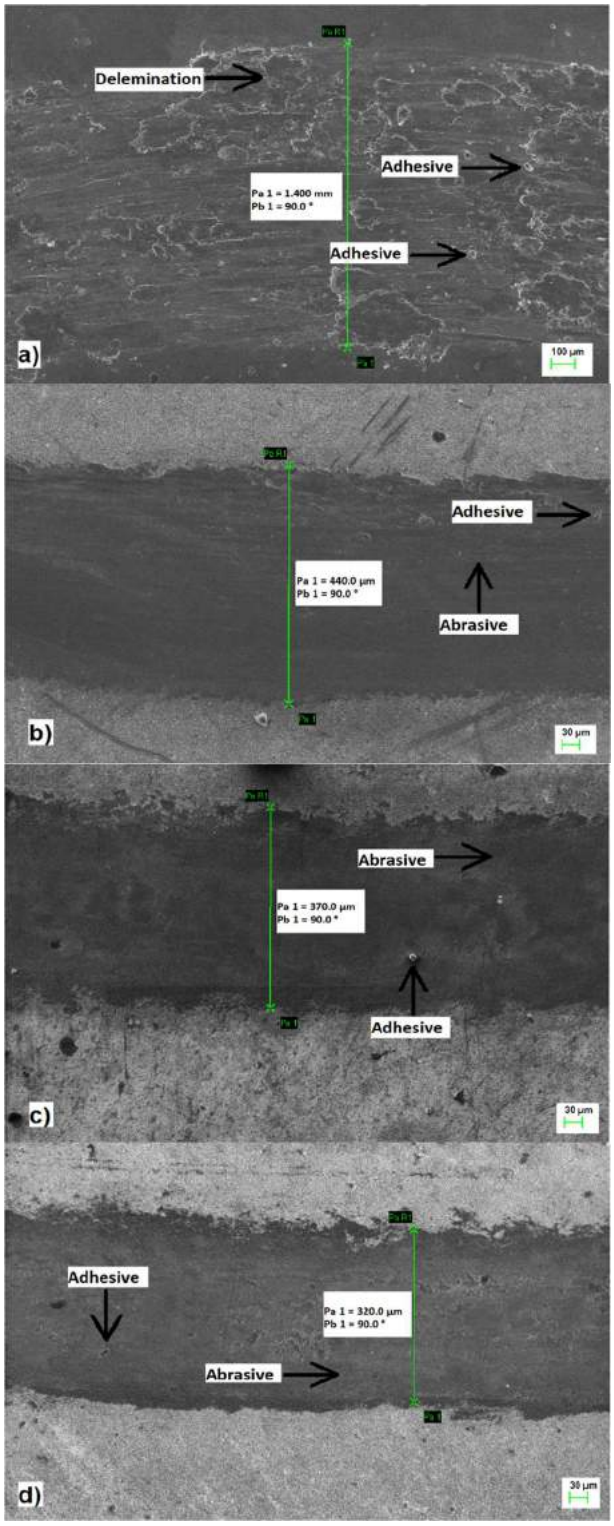

Figure 6. Wear traces of boronized Nitronic 50 steel a) non-boronized, b) 850 °C – 4 h, c) 900 °C – 4 h, d) 950 °C – 4 h

Wear traces vary according to boride layer thickness [33, 51, 52]. When the surface morphology of the wear marks is examined, adhesive wear is seen in the non-boronized

sample, while abrasive wear is seen in both the adhesive and abrasive wear by boring samples repeatedly cutting the coating surface by friction pairs. The width of the wear tracks ranges from 1.400 µm to 320 µm and when the tracks are examined, it is seen that the largest wear tracks and damages such as smearing (plastic deformation) in the wear direction are non-boronized specimen (figure 6 (a)) and the narrowest wear tracks are boronized at 950 °C (figure 6 (d)), the highest temperature used for 4 hours in the experiment. With the reduction of boride layer thickness, wear marks become more deeper [53].

3.5. Rockwell-C Adhesion

SEM images obtained from the adhesion test using a standard Rockwell-C hardness tester are shown in figure 7. Damage to the boride layer and adhesion strength are defined according to quality maps. According to the quality map, HF1-HF6 is grouped between HF1-HF4 and HF5 and HF6 are defined as inadequate adhesion [28].

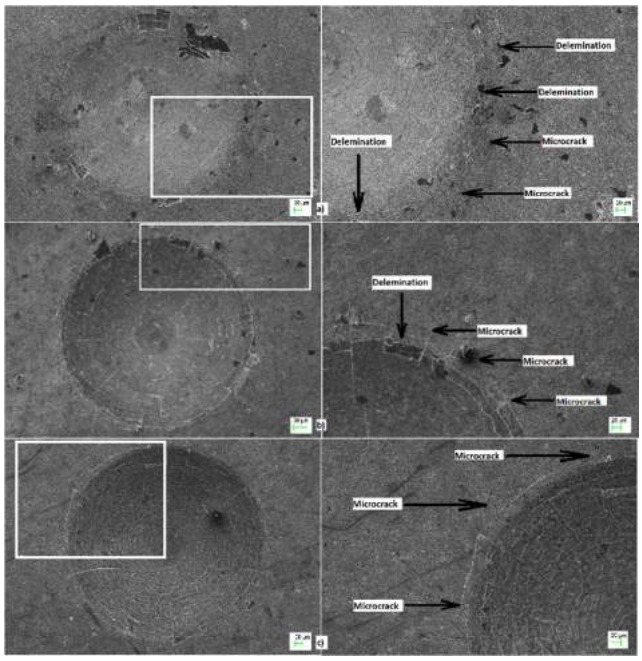

Figure 7. SEM micrographs and radial cracks of VDI adhesion test on boronized Nitronic 50 steel for 4 hours at a) 850 °C, b) 900 °C c) 950 °C.

When the damage images of boronized Nitronic 50 steel are examined for 4 hours, it is observed that radial cracks occur around the craters in the boring at 850 °C (figure 7 (a)) and it is compatible with HF3 according to the quality map. In samples boronized at 900 °C (figure 7 (b)) and 950 °C (figure 7 (c)), delamination occurs along with radial cracks around the indentation craters and the amount of delemination increases with increasing boronizing temperature. This is due to the increase at the process temperature and the depth of the hard and brittle structure FeB phase. However, the images of samples according to the quality test were identified as HF4 and represent sufficient adhesion.

4. CONCLUSIONS

The results obtained from the investigation of tribological properties by coating the Nitronic 50 steel with pack boriding method at 850 °C, 900 °C and 950 °C for 4 hours are given below;

- The coating and the matrix interface exhibit a flat structure, which can be clearly seen the SEM observations. Boride layer thickness increased with temperature increase and reached 13 µm, 29 µm and 35 µm respectively.

- FeB, CrB, Ni_3B, Fe_2B, Cr_2B and MnB phases were formed in all boriding conditions and FeB, CrB phases increased with increasing temperature.

- The matrix hardness is around 250 $HV_{0.05}$, while the hardness of the boride layer ranges from 1080 $HV_{0.05}$ to 1712 $HV_{0.05}$, and the surface hardness of the Nitronic 50 steel has increased about 7 times.

- The friction coefficient and wear rate of Nitronic 50 steel boronized by pack boring method decreased with increasing boriding temperature. While wear rate was 81.15 mm^3 / Nm for unborided sample, with boriding treatment decreased to 3.43 mm^3 / Nm and the wear resistance of the material surface increased about 20 times.

- As a result of the wear tests, non-boron steel has been exposed to intensive adhesive wear along with deleminations. In boronized samples,

adhesive and abrasive wear types are seen together.

• In the Rockwell-C adhesion test, the boronized sample at 850 °C represents HF3 according to the quality map, while the 900 °C and 950 °C samples were damaged in the HF4 type. Adhesion for coating is acceptable.

Acknowledgments

Author would like to thank Assoc. Prof. Yusuf KAYALI who assisted in carrying out the wear tests in this study, and the Department of Metallurgy and Materials Engineering, Faculty of Technology, Afyon Kocatepe University.

REFERENCES

[1] A. K. Chauhan, D. B. Goel and S. Prakash, "Solid particle erosion behaviour of 13Cr–4Ni and 21Cr–4Ni–N steels," Journal of Alloys and Compounds, vol. 467, no. 1-2, pp. 459–464, 2009.

[2] A. Kumar, A. Sharma and S. K. Goel, "Effect of heat treatment on microstructure, mechanical properties and erosion resistance of cast 23-8-N Nitronic steel," Materials Science and Engineering: A, vol. 637, pp. 56-62, 2015.

[3] Y. Qiao, J. Chen, H. Zhou, Y. Wang, Q. Song, H. Li and Z. Zheng, "Effect of solution treatment on cavitation erosion behavior of high-nitrogen austenitic stainless steel," Wear, vol. 424-425, pp. 70-77, 2019.

[4] C. M. Hong, J. Shi, L. Y. Sheng, W. C. Cao, W. J. Hui and H. Dong, "Effects of hot-working parameters on microstructural evolution of high nitrogen austenitic stainless steel," Materials and Design, vol. 32, pp. 3711-3717, 2011.

[5] D. H. M. Grajales, C. M. G. Ospina and A. P. Tschiptschina, "Mesoscale plasticity anisotropy at the earliest stages of cavitation-erosion damage of a high nitrogen austenitic stainless steel," Wear, vol. 267, pp. 99-103, 2009.

[6] A. M. Ritter and M. F. Henry, "Phase transformations during aging of a nitrogen-strengthened austenitic stainless steel," Metallurgical Transactions A, vol. 16, pp.1759–1771, 1985.

[7] W-G. Guo and S. Nemat-Nasser, "Flow stress of Nitronic-50 stainless steel over a wide range of strain rates and temperatures," Mechanics of Materials, vol. 38, pp. 1090–1103, 2006.

[8] A. S. Pokrovsky and S. A. Fabritsiev, "Effect of neutron irradiation on tensile properties of austenitic steel XM-19 for the ITER application," Journal of Nuclear Materials, vol 417, pp874-877, 2011.

[9] F. H. Abed, S. I. Ranganathan, "Constitutive modeling of nitrogen-alloyed austenitic stainless steel at low and high strain rates and temperatures," Mechanics of Materials, vol. 77, pp. 142-157, 2014.

[10] A. I. Fernández-Abia, J. Barreiro, J. Fernández-Larrinoa, L. N. López de Lacalle, A. Fernández-Valdivielso and O. M. C. Pereira, "Behaviour of PVD coatings in the turning of austenitic stainless steels," Procedia Engineering, vol. 63, pp. 133 – 141, 2013.

[11] E. D. L. Heras, D. A. Egidi, P. Corengia, D. González-Santamaría, A. García-Luis, M. Brizuela, G. A. López and M. F. Martinez, "Duplex surface treatment of an AISI 316L stainless steel; microstructure and tribological behavior," Surface & Coatings Technology, vol. 202, pp. 2945–2954, 2008.

[12] H. P. Feng, C. H. Hsu, J. K. Lu and Y. H. K. Shy, "Effects of PVD sputtered coatings on the corrosion resistance of AISI 304 stainless steel," Materials Science and Engineering A, vol. 347, pp. 123-129, 2003.

[13] R. Lan, Z. Ma, C. Wang, G. Lu, Y. Yuan and C. Shi, "Microstructural and tribological

characterization of DLC coating by in-situ duplex plasma nitriding and arc ion plating," Diamond & Related Materials, vol. 98, pp. 107473, 2019.

[14] E. Marin, A. Lanzutti, M. Nakamura, M. Zanocco, W. Zhu, G. Pezzotti and F. Andreatta, "Corrosion and scratch resistance of DLC coatings applied on chromium molybdenum steel," Surface and Coatings Technology, vol. 378, pp. 124944, 2019.

[15] H. Cicek, "Wear behaviors of TiN/TiCN/DLC composite coatings in different environments," Ceramics International, vol. 44, pp. 4853–4858, 2018.

[16] H. Kovacı, O. Baran, A. F. Yetim, Y. B. Bozkurt, L. Kara and A. Çelik, "The friction and wear performance of DLC coatings deposited on plasma nitrided AISI 4140 steel by magnetron sputtering under air and vacuum conditions," Surface & Coatings Technology, vol. 349, pp. 969–979, 2018.

[17] C. Jaoul, C. Dublanche-Tixier, O, Jarry, P. Tristant, J. P. Lavoute, L. Kilman, M. Colas, E. Laborde and H. Ageorges, "Tribological properties of hard a-C:H:F coatings," Surface & Coatings Technology, vol. 237, pp. 328–332, 2013.

[18] G. S. Savonov, M. G. G. Camarinha, L. O. Rocha, M. J. R. Barboza, G. V. Martins and D. A. B. Reis, "Study of the influence of the RRA thermal treatment and plasma nitriding on corrosion behavior of 7075-T6 aluminum alloy," Surface & Coatings Technology, vol. 374, pp. 736–744, 2019.

[19] S. Li, S. Hu, A. C. Hee and Y. Zhao, "Surface modification of a Ti2AlC soft ceramic by plasma nitriding treatment," Surface and Coatings Technology, vol. 281, pp. 164–168, 2015.

[20] M. Tsujikawa, N. Yamauchi, N. Ueda, T. Sone and Y. Hirose, "Behavior of carbon in low temperature plasma nitriding layer of austenitic stainless steel," Surface & Coatings Technology, vol. 193, pp. 309– 313, 2015.

[21] E. Mertgenc, O. F. Kesici and Y. Kayali, "Investigation of wear properties of borided austenitic stainless-steel different temperatures and times," Materials Research Express, vol. 6, pp. 076420, 2019.

[22] İ. Türkmen, E. Yalamaç and M. Keddam, "Investigation of tribological behaviour and diffusion model of Fe2B layer formed by pack-boriding on SAE 1020 steel," Surface and Coatings Technology, vol. 377, pp. 124888, 2019.

[23] J. Ballinger, S. A. Catledge, "Metal-boride interlayers for chemical vapor deposited nanostructured NSD films on 316 and 440C stainless steel," Surface & Coatings Technology, vol. 261, pp. 244–252, 2015.

[24] A. Bartkowska, A. Pertek, M. Kulka and L. Klimek, "Laser surface modification of boronickelized medium carbon steel," Optics & Laser Technology, vol. 74, pp. 145–157, 2015.

[25] O. Torun, "Boriding of nickel aluminide," Surface & Coatings Technology, vol. 202, pp. 3549–3554, 2008.

[26] O. A. Gómez-Vargas, J. Solis-Romero, U. Figueroa-López, M. Ortiz-Domínguez, J. Oseguera-Peña and A. Neville, "Boro-nitriding coating on pure iron by powder-pack boriding and nitriding processes," Materials Letters, vol. 176, pp. 261–264, 2016.

[27] O. Ozdemir, M. A. Omar, M. Usta, S. Zeytin, C. Bindal and A. H. Ucisik, "An investigation on boriding kinetics of AISI 316 stainless steel," Vacuum, vol. 83, pp. 175–179, 2009.

[28] N. Vidakis, A. Antoniadis and N. Bilalis, "The VDI 3198 indentation test evaluation of a reliable qualitative control for layered compounds," Journal of Materials Processing Technology, vol. 143–144, pp. 481–485, 2003.

[29] E. Heinke, A. Leyland, A. Matthews, G. Berg, C. Friedrich and E Broszeit, "Evaluation of PVD nitride coatings, using impact, scratch and Rockwell-C adhesion tests" Thin Solid Films, vol. 270, pp. 431-438, 1995.

[30] Y. Kayali and S. Taktak, "Characterization and Rockwell-C adhesion properties of chromium-based borided steels," Journal of Adhesion Science and Technology, vol. 19, pp. 2065-2075, 2015.

[31] O. Ozdemir, M. Usta, C. Bindal and A. H. Ucisik, "Hard iron boride (Fe_2B) on 99.97wt% pure iron," Vacuum, vol. 80, pp. 1391–1395, 2006.

[32] I. Ozbek and C. Bindal, "Mechanical properties of boronized AISI W4 steel," Surface and Coatings Technology, vol. 154, pp. 14–20, 2002.

[33] T. Balusamy, T. S. N. S. Narayanan, K. Ravichandran, II. P. Song and M. H. Lee, "Effect of surface mechanical attrition treatment (SMAT) on pack boronizing of AISI 304 stainless steel," Surface & Coatings Technology, vol. 232, pp. 60–67, 2013.

[34] Y. Kayali, I. Günes and S. Ulu, "Diffusion kinetics of borided AISI 52100 and AISI 440C steels," Vacuum, vol. 86, pp. 1428-1434, 2012.

[35] S. Taktak, "Some mechanical properties of borided AISI H13 and 304 steels," Materials and Design, vol. 28, pp. 1836–1843, 2007.

[36] M. Usta, I. Ozbek, M. Ipek, C. Bindal and A. H. Ucisik, "A comparison of mechanical properties of borides formed on pure Nb and W," Materials Forum, Vol. 29, pp. 65-70, 2005.

[37] A. Tabur, M. Izciler, F. Gul and I. Karacan, "Abrasive wear behavior of boronized AISI 8620 steel," Wear, vol. 266, pp. 1106–1112, 2009.

[38] Y. Kayali, A. Büyüksağiş and Y. Yalçin, "Corrosion and wear behaviors of boronized AISI 316L stainless steel," Metals and Materials International, vol. 19 1053-1061, 2013.

[39] G. Ç. Efe, M. İpek, İ. Özbek and C. Bindal, "Kinetics of borided 31CrMoV9 and 34CrAlNi7 steels," Materials Characterization, vol. 59, pp. 23–31, 2008.

[40] L. G. Yu, X. J. Chen, K. A. Khor and G. Sundararajan, "FeB/Fe_2B phase transformation during SPS pack-boriding: Boride layer growth kinetics," Acta Materialia, vol. 53, pp. 2361–2368, 2005.

[41] V. I. Dybkov, W. Lengauer and P. Gas, "Formation of boride layers at the Fe–25% Cr alloy–boron interface," Journal of Materials Science, vol 4, pp. 4948-4960, 2006.

[42] H. B. Abdelali, C. Claudin, J. Rech, W. B. Salem, PH. Kapsa and A. Dogui, "Experimental characterization of friction coefficient at the tool–chip–workpiece interface during dry cutting of AISI 1045," Wear, vol. 286-287, pp. 108-115, 2012.

[43] C. Jessop and J. Ahlström, "Friction between pearlitic steel surfaces," Wear, vol. 432-433, pp. 102910, 2019.

[44] L. R. R. Silva, R. S. Ruzzi, V. C. Teles, W. F. Sales, W. L. Guesser and A. R. Machado, "Analysis of the coefficient of friction at the workpiece-tool interface in milling of high strength compacted graphite cast irons," Wear, vol. 426-427(b), pp. 1646-1657, 2019.

[45] C. A. Cuao-Moreu, E. Hernández-Sanchéz, M. Alvarez-Vera, E. O. Garcia-Sanchez, A. Perez-Unzueta and M. A. L. Hernandez-Rodrigueza, "Tribological behavior of borided surface on CoCrMo cast alloy," Wear, vol. 426–427, pp. 204–211, 2019.

[46] Y. Teng, Y. Y. Guo, M. Zhang, Y. J. Yang, Z. Huang, Y. W. Zhou, F. Y. Wu and Y. S. Liang, "Effect of Cr/CrN_x transition layer on mechanical properties of CrN coatings

deposited on plasma nitrided austenitic stainless steel," Surface & Coatings Technology, vol. 367, pp. 100–107, 2019.

[47] X. M. He, X. B. Liu, M. D. Wang, M. S. Yang, S. H. Shi, G. Y. Fu and S. F. Chen, "Elevated temperature dry sliding wear behavior of nickel-based composite coating on austenitic stainless steel deposited by a novel central hollow laser cladding," Applied Surface Science, vol. 258, pp. 535–541, 2011.

[48] A. A. Joshi and S. S. Hosmani, "Pack-boronizing of AISI 4140 steel: boronizing mechanism and the role of container design," Materials and Manufacturing Processes, vol. 29, pp. 1062–1072, 2014.

[49] S. Y. Lee, G. S. Kim and B. S. Kim, "Mechanical properties of duplex layer formed on AISI 403 stainless steel by chromizing and boronizing treatment," Surface and Coatings Technology, vol. 177 – 178, pp. 178–184, 2004.

[50] D. Mu, B. L. Shen and X. Zhao, "Effects of boronizing on mechanical and dry-sliding wear properties of CoCrMo alloy" Materials and Design, vol. 31, pp. 3933–3936, 2010.

[51] I. Campos-Silva, A. D. Contla-Pacheco, A. Ruiz-Rios, J. Martínez-Trinidad, G. Rodríguez-Castro, A. Meneses-Amador and W. D. Wong-Angel, "Effects of scratch tests on the adhesive and cohesive properties of borided Inconel 718 superalloy," Surface & Coatings Technology, vol. 349, pp. 917-927, 2018.

[52] A. M. M. El-Bahloul, "Surface capacity of gears of circular-arc tooth-profile," Wear, vol. 93, pp. 146–154, 1996.

[53] I. Gunes, Y. Kayali and S. Ulu, "Investigation of surface properties and wear resistance of borided steels with different B_4C mixtures," Indian Journal of Engineering & Materials Sciences, vol.19, pp. 397-402, 2012.

Sakarya University Journal of Science

ISSN 1301-4048 | e-ISSN 2147-835X | Period Bimonthly | Founded: 1997 | Publisher Sakarya University | http://www.saujs.sakarya.edu.tr/en/

Title: Degree Distance of Zero-Divisor Graph Γ[Z_n]

Authors: N. Feyza YALÇIN
Recieved: 2019-04-04 22:02:46

Accepted: 2020-03-30 14:31:37

Article Type: Research Article
Volume: 24
Issue: 3
Month: June
Year: 2020
Pages: 531-535

How to cite
N. Feyza YALÇIN; (2020), Degree Distance of Zero-Divisor Graph Γ[Z_n]. Sakarya University Journal of Science, 24(3), 531-535, DOI: https://doi.org/10.16984/saufenbilder.549532
Access link
http://www.saujs.sakarya.edu.tr/en/issue/52472/549532

Sakarya University Journal of Science 24(3), 531-535, 2020

Degree Distance of Zero-Divisor Graph $\Gamma[\mathbb{Z}_n]$

N. Feyza YALÇIN*[1]

Abstract

In this article, degree distance of zero-divisor graph $\Gamma[\mathbb{Z}_n]$ is computed for $n = p^2$, $n = pq$ and $n = p^3$, where p, q are distinct prime numbers.

Keywords: zero-divisor graph, degree distance, topological index, graph

1. INTRODUCTION

Let $G = (V(G), E(G))$ be a simple graph with $V(G)$, set of all vertices and $E(G)$, the set of all edges that join the vertices. If there is an edge joining a pair of vertices, those vertices are said to be adjacent. An edge is incident to a vertex if the edge is joined to the vertex. If $e = uv$ be an edge of the graph G, e is incident to the vertices u and v. Degree of a vertex u in a graph G is the number of edges incident to u and is denoted by $deg_G(u)$. If there is a path between any two distinct vertices of a graph, then the graph is called connected. Length of the shortest path connecting the vertices u and v in a graph G is called distance between u and v, denoted by $d_G(u, v)$. If any two vertices of a graph is adjacent then the graph is called complete. A complete graph has n vertices is denoted by K_n. Complement graph of the complete graph K_n is $\overline{K}_n$, which has n vertices and no edges, namely null graph of order n. A complete bipartite graph is a graph that the set of vertices $V(G)$ can be decomposed into two disjoint subsets such that none of two vertices in the same set is not adjacent and every pair of vertices in the two sets. If these two sets have n and m vertices, then the complete bipartite graph is denoted by $K_{n,m}$.

$Top(G)$, topological index of a graph G is a real number which is invariant under isomorphism of graphs. In other words, let $\mathcal{G}$ be the class of all finite graphs and if $G, H \in \mathcal{G}$ are isomorphic, then $Top(G) = Top(H)$. Topological indices are basically related to connectivity and distance in a graph. Let $G = (V(G), E(G))$ be a simple finite connected graph. In [4] degree distance of a graph G is defined as

$$D'(G) = \sum_{v \in V(G)} deg_G(v)\, D_G(v),$$

where $D_G(v) = \sum_{u \in V(G)} d_G(u, v)$, which is the distance of a vertex v in G. "Schultz index" name was proposed by Gutman in [5] for degree distance of a graph which can also be expressed as

*Corresponding Author: fyalcin@harran.edu.tr
[1] Department of Mathematics, Harran University, 63050, Şanlıurfa, Turkey. ORCID: 0000-0001-5705-8658

$D'(G) =$

$$\sum_{\{u,v\}\subseteq V(G)} [deg_G(u) + deg_G(v)]d_G(u,v).$$

Wiener index which is equal to the sum of distances between all pairs of vertices and introduced in [10] as

$$W(G) = \sum_{\{u,v\}\subseteq V(G)} d_G(u,v).$$

Degree distance of a graph can be also considered as a weighted version of the Wiener index.

Anderson and Livingston [2] introduced the zero-divisor graph of a commutative ring R (with 1) denoted by $\Gamma[R]$ with the vertex set $Z^*(R) = Z(R)\backslash\{0\}$ via this adjacency: for distinct $x, y \in Z^*(R)$, the vertices x and y are adjacent if and only if $xy = 0$. Actually, zero-divisor graph of a commutative ring is due to Beck [3] who considered the set of all elements of the ring as vertices and two distinct x, y elements of the ring are adjacent iff $xy = 0$. Beck is mainly dealt with colourings in [3].

Let $\mathbb{Z}_n$ be the commutative ring of all residue classes of integers modulo n. Ahmadi and Jahani-Nezhad [1] computed energy and Wiener index of $\Gamma[\mathbb{Z}_n]$ for $n = pq$ and $n = p^2$, where p, q are prime numbers. Mohammad and Authman [8] determined Hosoya polynomial of $\Gamma[\mathbb{Z}_n]$ and computed the Wiener index of $\Gamma[\mathbb{Z}_n]$ for $n = p^m$ and $n = p^m q$, where p, q are distinct prime numbers and $m \geq 2$ is an integer. Reddey et al. [9] consider $\Gamma[\mathbb{Z}_n]$ for $n = p^2q$ and $n = p^3$, where p, q are prime numbers and studied adjacency matrix of $\Gamma[\mathbb{Z}_n]$, its eigenvalues and computed the Wiener index of $\Gamma[\mathbb{Z}_n]$.

In this article $\Gamma[\mathbb{Z}_n]$, the zero-divisor graph of $\mathbb{Z}_n$ is considered for $n = p^2$, $n = pq$ and $n = p^3$, where p, q are distinct prime numbers and degree distance of $\Gamma[\mathbb{Z}_n]$ is computed which is a weighted version of the Wiener index.

2. PRELIMINARIES

In this section we give some definitions and lemmas which are required for proofs of the results will be presented.

Definition 2.1. A sum (join) of graphs G and H with disjoint vertex sets $V(G)$ and $V(H)$ is a graph has vertex set $V(G) \cup V(H)$ and the edge set $E(G) \cup E(H) \cup \{uv: u \in V(G) \text{ and } v \in V(H)\}$. The sum of the graphs G and H is denoted by $G + H$.

Lemma 2.1. Let $G = (V(G), E(G))$ and $H = (V(H), E(H))$ be graphs. Then the following assertions are hold.

i. $|E(G + H)| = |E(G)| + |E(H)| + |V(G)||V(H)|$,

ii. $d_{G+H}(u,v) =$
$$\begin{cases} 0, & u = v \\ 1, & uv \in E(G) \text{ or } uv \in E(H) \text{ or } \\ & (u \in V(G) \,\&\, v \in V(H)) \\ 2, & otherwise \end{cases},$$

iii. $deg_{G+H}(u) =$
$$\begin{cases} deg_G(u) + |V(H)|, & u \in V(G) \\ deg_H(u) + |V(G)|, & u \in V(H) \end{cases}.$$

Proof. The proof of the parts (i)-(ii) and (iii) can be seen from [6] and [7], respectively.

Lemma 2.2. ([1]) Let $G = \Gamma[\mathbb{Z}_n]$ and let $n = p^2$, where p is a prime number. Then $Z^*(\mathbb{Z}_{p^2}) = \{p, 2p, \dots, (p-1)p^2\}$. Thus for every $x, y \in Z^*(\mathbb{Z}_{p^2})$, $xy = 0$ and $\Gamma[\mathbb{Z}_{p^2}] = K_{p-1}$. If $n = pq$ such that p, q are distinct prime numbers, then

$$Z^*(\mathbb{Z}_{pq}) = A \cup B,$$

where $A = \{pk: k = 1,2, \dots, q-1\}$ and $B = \{qk: k = 1,2, \dots, p-1\}$. For any $x, y \in Z^*(\mathbb{Z}_{pq})$, $xy = 0$ if and only if $x \in A, y \in B$ or $x \in B$, $y \in A$. So, $\Gamma[\mathbb{Z}_{pq}] = K_{p-1,q-1}$.

Theorem 2.1. ([8]) $\Gamma[\mathbb{Z}_{p^3}] \cong K_{p-1} + \overline{K}_{p^2-p}$, where $\overline{K}_{p^2-p}$ is complement graph of complete graph K_{p^2-p}.

The zero-divisor graph of the ring $\mathbb{Z}_{27}$ is illustrated in Figure 1.

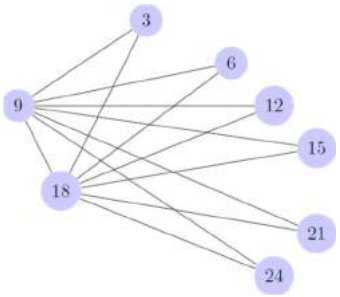

Figure 1. $\Gamma[\mathbb{Z}_{27}]$

3. MAIN RESULTS

In this section we compute the degree distance of the zero-divisor graph $\Gamma[\mathbb{Z}_n]$ for $n = p^2$, $n = pq$ and $n = p^3$, where p, q are distinct prime numbers.

Theorem 3.1. The degree distance of $G = \Gamma[\mathbb{Z}_{p^2}]$ is

$$D'(G) = (p-1)(p-2)^2.$$

Proof. From Lemma 2.2, we have $\Gamma[\mathbb{Z}_{p^2}] = K_{p-1}$. Since for any $x, y \in V(K_{p-1})$, $deg(x) = p-2$ and $d_G(x,y) = 1$, we obtain

$$\begin{aligned} D'(G) &= \sum_{\{u,v\}\subseteq V(G)} [deg_G(u) + deg_G(v)] d_G(u,v) \\ &= \sum_{u\neq v} (p-2+p-2)\,.\,1 \\ &= |E(K_{p-1})|.(2p-4) \\ &= \frac{(p-1)(p-2)}{2}.(2p-4) \\ &= (p-1)(p-2)^2, \end{aligned}$$

which completes proof.

Theorem 3.2. The degree distance of $G = \Gamma[\mathbb{Z}_{pq}]$ is

$$D'(G) = 5(p^2q + pq^2 - (p^2+q^2)) - 28pq + 23(p+q) - 18.$$

Proof. From Lemma 2.2, we have $Z^*(\mathbb{Z}_{pq}) = A \cup B$, where $A = \{pk:\ k = 1,2,\dots,q-1\}$ and $B = \{qk:\ k = 1,2,\dots,p-1\}$ and $\Gamma[\mathbb{Z}_{pq}] = K_{p-1,q-1}$. For $u \in A, v \in B$, we have $deg_G(u) = p-1$, $deg_G(v) = q-1$. The number of paths of length 2 for $u, v \in A$ is $(q-1)(q-2)$ and for $u, v \in B$ is $(p-1)(p-2)$. Thus we get

$$\begin{aligned} D'(G) &= \\ &\sum_{\{u,v\}\subseteq V(G)} [deg_G(u) + deg_G(v)] d_G(u,v) \\ &= \sum_{u\in A, v\in B} [deg_G(u) + deg_G(v)].1 \\ &+ \sum_{u,v\in A, u\neq v} [deg_G(u) + deg_G(v)].2 \\ &+ \sum_{u,v\in B, u\neq v} [deg_G(u) + deg_G(v)].2 \\ &= (p+q-2)(p-1)(q-1) \\ &\quad +2(2p-2)(q-1)(q-2) \\ &\quad +2(2q-2)(p-1)(p-2) \\ &= 5(p^2q + pq^2 - (p^2+q^2)) - 28pq \\ &\quad +23(p+q) - 18. \end{aligned}$$

Thus proof is complete.

Theorem 3.3. The degree distance of $G = \Gamma[\mathbb{Z}_{p^3}]$ is

$$D'(G) = 3p^5 - 6p^4 - 3p^3 + 9p^2 + p - 4.$$

Proof. From proof of the Theorem 2.1 in [8], we have

$$Z^*(\mathbb{Z}_{p^3}) = A \cup B,$$

where $A = \{p^2k:\ k = 1,2,\dots,p-1\}$ and $B = \{pk:\ k = 1,2,\dots,p^2-1;\ p \nmid k\}$. From the features of these sets and adjacency relation of zero-divisor graph, three cases occur:

If $u, v \in A$, then u is adjacent to v; if $u \in A, v \in B$, then u is adjacent to v; if $u, v \in B$, then u is not adjacent to v, thus $d_G(u,v) = 2$. Since by Theorem 2.1 we have $\Gamma[\mathbb{Z}_{p^3}] \cong K_{p-1} + \overline{K}_{p^2-p}$,

we will consider the graph G as $K_{p-1} + \overline{K}_{p^2-p}$ with $|V(G)| = |V(\Gamma[\mathbb{Z}_{p^3}])| = p^2 - 1$ vertices. From Lemma 2.1, we have

$$deg_G(a) = \begin{cases} p^2 - 2, & a \in V(K_{p-1}) \\ p - 1, & a \in V(\overline{K}_{p^2-p}) \end{cases} \quad (1)$$

and

$$|E(G)| = |E(\Gamma[\mathbb{Z}_{p^3}])|$$

$$= |E(K_{p-1})| + |E(\overline{K}_{p^2-p})| + |V(K_{p-1})|.|V(\overline{K}_{p^2-p})|$$

$$= \frac{(p-1)(p-2)}{2} + (p-1)(p^2-p)$$

$$= \frac{(p-1)(2p^2-p-2)}{2}. \quad (2)$$

We can also write

$$D'(G) = \sum_{\{u,v\} \subseteq V(G)} [deg_G(u) + deg_G(v)] d_G(u,v)$$

$$= \sum_{u \in A, v \in B} [deg_G(u) + deg_G(v)].1 + \sum_{u,v \in A, u \neq v} [deg_G(u) + deg_G(v)].1 + \sum_{u,v \in B, u \neq v} [deg_G(u) + deg_G(v)].2. \quad (3)$$

If we consider the distance matrix of the zero-divisor graph $\Gamma[\mathbb{Z}_{p^3}]$ with $p^2 - 1$ vertices, the number of entries above the main diagonal is $\frac{(p^2-1)(p^2-2)}{2}$. The total number of paths of length 1 is the number of the edges, that is $\frac{(p-1)(2p^2-p-2)}{2}$. Therefore the number of paths of length 2 is

$$\frac{(p^2-1)(p^2-2)}{2} - \frac{(p-1)(2p^2-p-2)}{2} = \frac{p^4 - 2p^3 + p}{2}. \quad (4)$$

By using (1), (2), (4) in (3), we obtain

$$D'(G) = (p-1)(p^2-p)(p^2+p-3) + \frac{(p-1)(p-2)}{2}.2(p^2-2) + 2\left(\frac{p^4-2p^3+p}{2}\right).2(p-1)$$

$$= 3p^5 - 6p^4 - 3p^3 + 9p^2 + p - 4.$$

So, proof is complete.

Acknowledgment

The author declare that there is no conflict of interests regarding the publication of this work and thank the referees for his/her valuable contributions.

REFERENCES

[1] M.R., Ahmadi and R., Jahani-Nezhad, "Energy and Wiener index of zero divisor graphs", Iranian Journal of Mathematical Chemistry, vol. 2, pp. 45-51, 2011.

[2] D.F., Anderson and P.S., Livingston, "The zero-divisor graph of a commutative ring", Journal of Algebra, vol. 217, pp. 434-447, 1999.

[3] I., Beck, "Coloring of commutative rings", Journal of Algebra, vol. 116, no.1, pp. 208-226, 1988.

[4] A.A., Dobrynin and A.A., Kochetova, "Degree Distance of a Graph: A Degree analogue of the Wiener Index", Journal of Chemical Information and Computer Sciences, vol. 34, pp. 1082-1086, 1994.

[5] I., Gutman, "Selected properties of the Schultz molecular topological index",

Journal of Chemical Information and Computer Sciences, vol. 34, pp. 1087-1089, 1994.

[6] W., Imrich and S., Klavzar, "Product Graphs: Structure and Recognition", John Wiley&Sons, New York, USA, 2000.

[7] M.H., Khalifeh, H., Yousefi-Azari and A.R., Ashrafi, "The Hyper-Wiener index of graph operations", Comput. Math. Appl., vol. 56, pp. 1402-1407, 2008.

[8] H.Q., Mohammad and M.N., Authman, "Hosoya polynomial and Wiener index of zero-divisor graph of $\mathbb{Z}_n$", Raf. J. Comp.&Math's., vol. 12, no. 1, pp. 47-59, 2018.

[9] B.S., Reddy, R.S., Jain, N., Laxmikanth, "Eigenvalues and Wiener index of the zero divisor graph $\Gamma[\mathbb{Z}_n]$", https://arxiv.org/pdf/1707. 05083, 2017.

[10] H., Wiener, "Structural determination of paraffin boiling points", Journal of the American Chemical Society, vol. 69, pp. 17-20, 1947.

JOURNAL OF SCIENCE
SAKARYA UNIVERSITY

Sakarya University Journal of Science

ISSN 1301-4048 | e-ISSN 2147-835X | Period Bimonthly | Founded: 1997 | Publisher Sakarya University | http://www.saujs.sakarya.edu.tr/en/

Title: Developing a Model for Measuring Project Performance with Software Life Cycle Process Metrics and Calculating Project Success Score

Authors: Özgür GÜN, Pınar YILDIZ KUMRU, Zerrin ALADAĞ
Recieved: 2019-11-21 16:10:20

Accepted: 2020-04-03 17:10:47

Article Type: Research Article
Volume: 24
Issue: 3
Month: June
Year: 2020
Pages: 536-554

How to cite
Özgür GÜN, Pınar YILDIZ KUMRU, Zerrin ALADAĞ; (2020), Developing a Model for Measuring Project Performance with Software Life Cycle Process Metrics and Calculating Project Success Score. Sakarya University Journal of Science, 24(3), 536-554, DOI: https://doi.org/10.16984/saufenbilder.649588
Access link
http://www.saujs.sakarya.edu.tr/en/issue/52472/649588

Sakarya University Journal of Science 24(3), 536-554, 2020

Developing a Model for Measuring Project Performance with Software Life Cycle Process Metrics and Calculating Project Success Score

Özgür GÜN*[1], Pınar YILDIZ KUMRU[1], Zerrin ALADAĞ[1]

Abstract

Despite the developments in the process and tool infrastructure in the software world, project success has not significantly improved. In software projects, the definition of project success means to produce products that the customer desires in the planned effort, time and budget. To achieve this goal, planning, analysis, design, coding, integration, testing and delivery processes are operated interactively from the beginning to the end of a software project. Metrics of these processes are used to measure the performance of software projects. Since the literature review shows that project management process metrics such as budget, effort, schedule, customer satisfaction, product quality are used in measuring project performance, more comprehensive and effective criteria are needed to be defined and applied in measuring project performances. Due to the importance of the project performance evaluation, a general evaluation model was created in this study. The proposed model is designed for use in the software industry. In terms of project performance, a model has been developed that focuses on management of project, requirement, risk, quality and configuration, development, verification and validation processes. The purpose of this article is to present a model that evaluates the performance of software projects and expresses project success with a numerical value. Analytical hierarchy process (AHP) was used to calculate the relative importance of each process metric criterion and sub-criteria that provide input to the performance evaluation. Statistical process control method was used in the evaluation of project performance and calculation of the project success score. It was operated in an R&D organization to verify the proposed model and the performance of a project in delivery phase to the customer was measured. It is thought that the model presented in this study will help the managers, who monitor the project status, to evaluate project performance, as well as provide the numerical comparison of performance between projects.

Keywords: Project Performance Evaluation, Project Success Score, Analytical Hierarchy Process, Statistical Process Control

*Corresponding Author: ozgur.gun@tubitak.gov.tr
[1]Kocaeli University, Faculty of Engineering, Department of Industrial Engineering, Turkey, ORCID: 0000-0002-4987-2980; ORCID: 0000-0002-6729-7721; ORCID: 0000-0002-5986-7210

1. INTRODUCTION

Policies in Turkey have been established to support technological product investments and clustering efforts in priority sectors such as energy, health, aviation, space, automotive, rail systems, IT, defense, information security and public digital transformation [1-3]. There is a huge increase in the number of software projects launched in these areas. Successful completion of these projects is of great importance.

The beginning of modern project management dates back to 1950. In the last 50 years, processes, methodologies, standards, good practices and many tools and techniques have contributed to the field of project management [4]. Despite the developments in the process and tool infrastructure in the software world, the number of projects that have failed is high [5]. One of the biggest causes of project failures is that software life cycle processes are not fully and correctly operated. Software life cycle processes are an interactive management system that defines activities and instructions for the procurement, planning, requirement analysis, design, coding, integration, review, testing, delivery and disposal stages of software projects [6]. These processes define process steps and responsibilities for analysts, software developers, integrators, operators, maintainers, managers, quality assurance managers and end users who will use the software in a software project. The software lifecycle first begins with the planning phase. At this stage, all processes that a software project should operate are planned. In the second stage of analysis, the functions and requirements expected from the software to be developed are defined. In the design phase, the first and basic version of the software that will be the solution to the needs determined in the analysis phase is created. At this stage, coding activity is not performed. Implementation stage can be detailed as coding, unit testing, code review and integration. Reviews on project documents and software components are made in verification phase. Software requirements are tested during validation. During the testing phase, errors in the software are corrected. The software defined in project contract is delivered to the customer and the maintenance phase is started. During the maintenance phase, operations such as troubleshooting and updating are performed in the software installed in the customer environment [6].

The metrics used in this study were used to measure the performance of software lifecycle processes. Project time, budget and effort metrics were used in the project management process. In the requirements management process, metric related to the volatility of the requirements is used. During the development process, defects, improvements, requirements changes and average open times and rates of these metrics were used. The verification and validation process is divided into two sub processes, review and test. Metrics related to the effectiveness, efficiency and error intensity of the reviews, on the other hand, the percentage of capture and detection of defects found in the test process were used as metrics. Although the objectives of the quality and configuration processes are different, their metrics are similar. In both processes, deviation from the audit plan and the average open time and rate of the nonconformities found in the audits were used as metrics. In the risk management process, the risk review rate was determined as metric.

The aim of this study is to present a new model for performance evaluation of software projects. As a result of the performance evaluation, the success of the project is shown with a numerical value. Structured interviews with experts were used to identify process criteria that affect project success. Analytical Hierarchy Process (AHP) was used to find the relative importance of the criteria in order to find the contribution of the determined criteria to the project success. The Statistical Process Control (SPC) method was used to analyze the metric measurement results collected from the projects.

In order to have sufficient decision making capacity, it is necessary to determine the relative importance of the criteria that affect the success of the project [7]. In this study, the judgements are taken from expert project managers and researchers working in an R&D organization. It is rule that weights have reflected the relative

importance of the individual criteria. Therefore the AHP method is chosen to calculate the relative importance of criteria and the sub-criteria in consistent with the judgments of experts.

It is considered that this proposed model that evaluates the performance of software projects and calculates project success points will help project managers and senior executives to take decisions on projects success.

The paper is organized as follows. The next section provides literature review on project performance evaluation and project success factor. Section 3 describes the methods used in modeling. Section 4 presents project performance evaluation and project success score model, explains hierarchy of project metrics criteria, data collecting environment and finalizes the model. Section 5 explains the implementation of the model. Finally, conclusions are presented in Section 6.

2. RELATED STUDIES

In the literature, there are studies on the determination of project success criteria and project performance evaluation by using these criteria. In this section, these studies will be briefly mentioned. Table 1 summarizes most commonly used methods with references. On the other hand, Table 2 gives the set of process success criteria already employed.

Akyol [8] stated the parameters affecting the project success in software organizations with different scales and features. Number of employees in the project, experience and graduated university of the project manager, resource rate allocated to the requirements and test process, ratio of employees leaving the job, number of words in requirements, and number of lines of code are stated to affect the success of the project. Ayyıldız [9] identified software complexity, function point, reusability, project budget, technology used, employee competence, working environment characteristics, productivity status and product features as metrics. Radujković et al. [4] introduced Work Breakdown Structure for process factors. The factors were divided into three groups: project management competence, organization and methodology. In WBS project management competence consists of project manager competence, project team competence and coordination factors. Again, organizational factor consist of structure, culture, atmosphere and competence of the organization as a sub-factor. The methodology factor consist of the methods used, project management software, project management tools, decision-making techniques, risk assessment tools and information communication support tools. Sanchez et al. [10] discussed the key aspects of project success from a multi-level perspective with using correlation and regression analysis. Project size, duration, postponement, project team size, involvement of the team and formal strength of the project manager were determined as success factors. Mir et al. [11] conducted a research testing the relationship between project management performance and project success by using regression analysis. Todorović et al. [12] presented a framework of project success analysis based on critical success factors and performance indicators by using correlation and regression analysis. Verner et al. [13] conducted a study to identification of factors that affect project success and failure. Customer, requirements, estimation and scheduling, development process/team, project manager factor were analyzed with correlation and logistic regression methods.

Garousi et al. [14] investigated the correlation between software project success and critical success factors. According to the results of the analysis, the factors affecting the project success the most are the experience of the project team in the project development methodologies, the field expertise of the project team and the project monitoring control. Wadugodapitiya et al. [15] proposed a multidimensional performance measurement model for projects in the construction industry. In the study, project performance indicators were weighted by AHP. AHP results showed that customer satisfaction and project efficiency were the most important indicators on project success. Ilbeigi et al. [16]

developed a model that evaluates project management performance and calculates a numerical performance value. Cost Performance Index, Billing Performance Index, Schedule Performance Index, Safety Performance Index, Quality Performance Index, and Environment Performance Index parameters are used for success criteria to calculate project management performance. AHP method was used for relative importance of success factors. Koelmans [17] has grouped the factors by using WBS method in terms of customer, project team and society. Project scope, quality, schedule, cost, project team morale and customer satisfaction were determined as project success factors. Sen Leu at al. [18] improved the performance of traditional Earn Value Management (EVM) by the introduction of statistical control chart techniques. Bauch at al. [19] presented SPC tool includes charts that monitor time, cost, and technical performance-related project parameters. Bower at al. [20] used EVM as a project performance evaluation technique. Shahzad at al. [21] identified cost, time, team size, requirement change, reusable code, quality and risk management as success factor in large scale projects and implemented correlation and reliability analysis on the factors. Viglioni at al. [22] proposed a performance evaluation model for software industry based on a multi-criteria approach by using measuring attractiveness by a categorical based evaluation technique. Doskočil at al. [23] presented a new expert decision-making fuzzy model for the evaluation of project success. EVM metrics, total value of project risk and quality were identified as success factors. Shashi at al. [24] conducted impact analysis of resources such as cost, time, and number of developers towards the successful completion of the project as allocated by the project manager during the developmental process.

Table 1. Most Commonly Used Methods with References

Techniques	Reference	Author Name and Year	Key Topics
Statistical Process Control (SPC), Earn Value management (EVM)	[16] [18] [19]	Ilbeigi at al. (2009), Sen Leu at al. (2008), Bauch at al. (2001)	Critical and effective indices were defined develop a model, by which the project management performance can be evaluated.
Earn Value management (EVM)	[20]	Bower at al. (2009)	Use of EVM criteria in project performance evaluation
Analytical Hierarchy Process (AHP), Balanced Scorecard (BSC)	[15] [16]	Wadugodapitiya at al. (2010), Ilbeigi at al. (2009),	Multidimensional performance measurement model for project performance evaluation by integrating BSC and AHP tools.
Work breakdown structure (WBS) evaluation	[4] [17]	Radujković at al. (2017), Koelmans (2004)	Indicators are developed into a work breakdown structure (WBS)-like chart to demonstrate success indicators
Correlation, Logistic Regression Analysis	[13] [14]	Garousi at al. (2019), Verner at al. (2007)	Correlation study of project variables and project outcome and logistic models to predict failure
Correlation, Regression Analysis	[8] [10] [11] [12]	Sanchez, at al. (2017), Todorović (2015), Mir at al. (2014), Akyol (2014)	Multi-dimensional frameworks are used to measure PM performance and project success
Empirical study, Data analysis	[24] [28]	Shashi at al. (2014), Bryde at al. (2005)	Impact analysis of resources such as cost, time, and number of developers towards the successful completion of the project
Correlation analysis and reliability analysis	[21] [27]	Gomes at al. (2016), Shahzad at al. (2014)	Statistical analysis of defining project success criteria
MACBETH Multi-criteria decision making method	[22]	Viglioni at al. (2016)	Performance evaluation model by measuring attractiveness by a categorical based evaluation technique
Fuzzy modeling	[23]	Doskočil at al. (2016)	Use of fuzzy logic in the evaluation of project success

Table 2. A Set of Process Success Criteria Already Employed

Criteria	Reference	Author Name and Published Year
cost	[10, 14, 17, 22, 23, 25, 26, 27, 28, 29, 30]	Garousi (2019), Sanchez (2017), Badewi (2016), Mossalam (2016), Gomes (2016), Viglioni (2016), Doskočil (2016), Bryde (2005), Jugdev (2005), Koelmans (2004), Baccarini (1999)
time	[10,14, 17, 22, 25, 27, 28, 29, 30]	Garousi (2019), Sanchez (2017), Badewi (2016), Gomes (2016), Viglioni (2016), Bryde (2005), Jugdev (2005), Koelmans (2004), Baccarini (1999)
quality	[10, 14, 17, 22, 25, 28, 29, 30]	Garousi (2019), Sanchez (2017), Badewi (2016), Viglioni (2016), Bryde (2005), Jugdev (2005), Koelmans (2004), Baccarini (1999)
scope	[10, 17, 22, 23, 26, 27, 29, 31, 32]	Sanchez (2017), Gomes (2016), Mossalam (2016), Viglioni (2016), Doskočil (2016), Besner (2006), [Koelmans (2004), Jugdev (2005), Lim (1999)
human resources	[4, 11, 14, 22, 29, 32, 33, 34]	Garousi (2019), Radujković (2017), Viglioni (2016), Radujković (2014), Mir (2014), Jugdev (2005), Cooke-Davies (2002), Lim (1999)
satisfaction of stakeholders	[14, 15, 17, 22, 23, 27, 35, 36]	Garousi (2019), Gomes (2016), Viglioni (2016), Doskočil (2016), Wadugodapitiya (2010), Müller (2012), Koelmans (2004), Bryde (2003)
organizational benefits	[32, 37]	Chou (2013), Lim (1999)
technical, financial, educational, social, professional elements	[27, 38]	Gomes (2016), Ellatar (2009)
project management tools and techniques	[4, 14, 37, 39]	Garousi (2019), Radujković (2017), Chou (2014), PricewaterCuppers (2012)
organizational structure	[4, 14, 33, 40]	Garousi (2019), Radujković (2017), Radujković (2014), Feger (2012)
risk assessment	[4, 27]	Radujković (2017), Gomes (2016)
requirements	[13, 23, 27, 41, 42]	Gomes (2016), Doskočil (2016), Keil (2012), Verner (2007), Taylor (2006),
leadership, personnel, politics and strategy, partnership and resources	[27, 36]	Gomes (2016), Bryde (2003)
project life cycle management process	[36, 45]	Bryde (2008), Bryde (2003)
return and profit, market share, repute	[27, 43, 44]	Gomes (2016), Al-Tmeemy (2011), Blindenbach-Driessen (2006)
competitive edge	[43, 44]	Al-Tmeemy (2011), Blindenbach-Driessen (2006)
project management standards	[4, 37, 46]	Radujković (2017), Nahod (2013), Chou (2013)
total competencies of project manager	[4, 13, 33, 40, 47, 48, 49, 50]	Radujković (2017),Radujković (2014), Ramazani (2015), Feger (2011), Turner (2009), Ika (2009), Verner (2007), Radujković (2000)
organizational culture	[4, 14, 51, 52]	Garousi (2019), Radujković (2017), Westerveld (2003), Skulmoski (2001)
project managers' emotional intelligence	[46, 53]	Nahod (2013), Yang (2011)
purpose	[23, 26]	Mossalam (2016), Doskočil (2016)
project team factors	[4, 11, 13, 14, 17, 22, 27, 33]	Garousi (2019), Radujković (2017), Gomes (2016), Viglioni (2016), Mir (2014), Radujković (2014), Verner (2007), Koelmans (2004)
earned value management key performance indicators	[12, 16, 22, 23]	Viglioni (2016), Doskočil (2016), Todorović (2015), Ilbeigi (2009)
estimates	[13]	Verner (2007)
customer factors	[13, 14, 22]	Garousi (2019), Viglioni (2016), Verner (2007)

In the literature, studies related to the determination of the criteria affecting the success of the project and the project performance evaluation models in which these criteria are entered have been seen. When the literature is analyzed, it has been observed that configuration management, quality management, verification and validation and development process metrics are not evaluated as project success criteria. It is thought that using software life cycle process metrics as the project success factor in this study and using it in the project performance evaluation model will contribute to the literature by innovating.

3. THE METHODOLOGY

3.1. Analytical Hierarchy Process

Analytical Hierarchy Process (AHP) is a multi-criteria decision making method developed by

Thomas L. Saaty in 1970s. AHP allows the decision maker to correctly and logically apply data, experience, understanding and intuition by modeling a complex problem in a hierarchical structure by showing the relationship between goals, objectives (criteria), sub-goals and alternatives [54]. It needs a hierarchical structure to modeling the decision problem and pairwise comparisons to determine relations between objectives [55].

There are different AHP implementations in literature regarding with prioritizing process success criteria sets [15]. This study uses AHP to solve two decision problems: 1) creating hierarchical structure that assess project success criteria; 2) determining relative importance of each criterion in the hierarchical structure.

AHP consists of three main stages: Separating the problem or establishing the hierarchy, comparative judgments and synthesis [55]. The first stage of AHP implementation is to develop a hierarchy by taking the complex problem into sub-problems. Goals, objectives, and alternatives are three basic levels of the hierarchy [56]. Starting from the top, the goal of the decision, the objectives, the intermediate levels and the alternatives at the lowest levels should be structured hierarchically [57]. Saaty, taking into account the limits of human cognitive abilities, recommends the number of elements in the each hierarchy level as 7 ± 2 [58].

The comparative judgments help decision makers to do pairwise comparisons of the relative importance of criteria in the hierarchies. In this study, judgments are gathered from the project managers, department managers and quality assurance managers who have worked in the R&D organization. After creating the hierarchy, the decision makers separately evaluates the importance of each decision criterion in the hierarchies and make pairwise comparisons at each level to calculate how many times the criteria (relative importance) are important to each other by using the scale given in Table 3.

Finally, the AHP synthesis the judgments obtained from the experts to provide a set of overall priorities for the hierarchy structures. The synthesis step includes calculation and normalization of the largest eigenvalue and the corresponding eigenvector. Although there are various methods of normalizing, the elements of each column are divided into column sums and the resulting row totals are divided into number of elements in this row. This method is widely preferred [59]. The consistency of judgments is calculated with using the following formula [60].

$$A\ x\ W = \lambda_{max}\ x\ W \quad (1)$$

A shows the pairwise comparisons matrix, W is the normalized weight vector and λmax is the maximum eigenvalue of matrix A. The maximum eigenvalue is used to estimate consistency in a matrix. Formula 2 gives the consistency index (CI) measured for the inconsistency.

$$Consistency\ Index\ (CI) = (\lambda_{max} - n)/(n-1) \quad (2)$$

The corresponding ratio (CR) is calculated by dividing the CI value by Random Consistency Index (RCI). In this calculation depending on the number of n alternatives random index (RCI) numbers are used [60]. Pairwise comparisons are considered to be consisted if the corresponding ratio (CR) is less than 10%. The AHP study in this article aimed to calculate the relative importance of the process metrics to be input in the project performance evaluation model. Because of there are no alternatives, sensitivity analysis in classical AHP method was not performed in this study.

Table 3. The Fundamental Scale [55]

Value	Definition	Explanation
1	Equal importance	Two activities contribute equally to the objective
3	Moderate importance of one over another	Experience and judgment strongly favor one activity over another
5	Essential or strong importance	Experience and judgment strongly favor over activity over another
7	Very strong importance	An activity is strongly favored and its dominance demonstrated in practice
9	Extreme importance	The evidence favoring one activity over another is of

Value	Definition	Explanation
		the highest possible order of affirmation
2,4,6,8	Intermediate values between the two adjacent judgments	When compromise is needed

3.2. Statistical Process Control (SPC)

SPC is a tool that applies statistics to the control process. There are different kinds of methods for SPC: scatter diagrams, run charts, cause and effect diagram, histograms, bar charts, Pareto charts, and control charts [18]. SPC control charts can be a successful tool for manufacturing and software process improvement [61]. In this study, control chart has been used to determine the lower and upper control limits of the process metrics.

The variation in a process may be due to common causes or assignable causes. The common cause variation is the normal variation related to the result of normal interactions of people, machines, environment and methods. Assignable cause change results from events that are not part of the normal process. Those causes occur sometimes and can be prevented [62]. If all process data are plotted within the control limits and without any particular tendency, the process is regarded as being in the controlled state [62].

In SPC, control charts are widely used for monitoring and controlling the process. There are different types of control charts in statistics [63-65]. In software processes, the data points are not generally as frequent as in manufacturing processes [66]. Each data point is plotted and evaluated individually. Therefore, the most used control chart in the software engineering area is Individual (I) and Moving Range (MR) control charts.

I-MR control charts consist of two basic features; centerline and sigma value. Centerline is the average value of data points, and sigma is the standard deviation of these data points. In I charts, data points are separate values in the charts, while in MR graphs, the data is obtained by calculating the absolute difference between two successive values. In these control charts, upper and lower control limits are calculated generally with three sigma values from the centerline [61], which covers 99% of all data.

4. MODEL DESIGN

In this study, literature research, determination of criteria, suggesting the model and application of the model have been done within the framework of scientific principles. In this section, the whole activities are specified in Figure 1 according to the workflow.

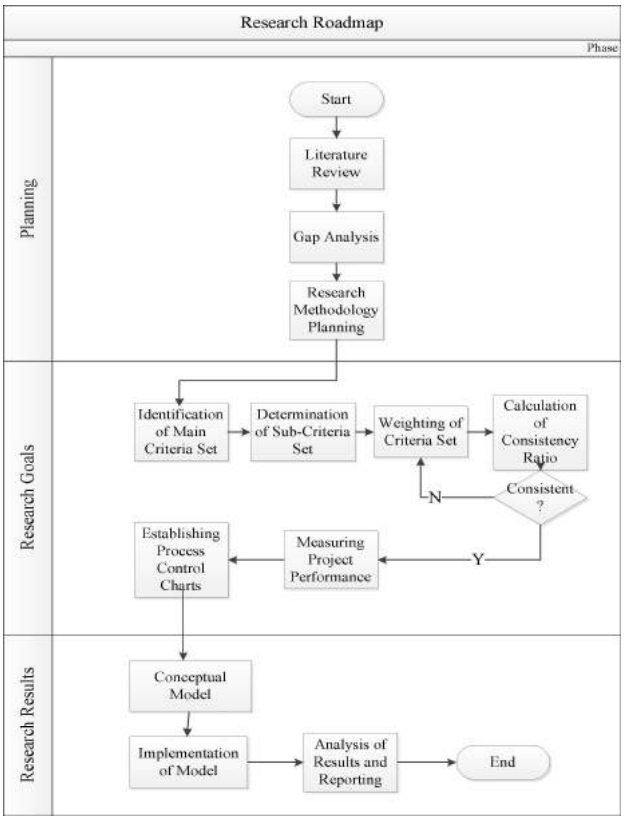

Figure 1. Research Flow Chart

4.1. Hierarchy of Process Metric Criteria

The software life cycle process metrics were determined as a result of interviews with the process improvement team and project managers in an R&D organization and the analysis of the current processes of the organization. The identified metrics are considered as process success criteria in this study. Process metrics are

organized as main criteria and sub-criteria for AHP study. The hierarchy of criteria is shown in Figure 2.

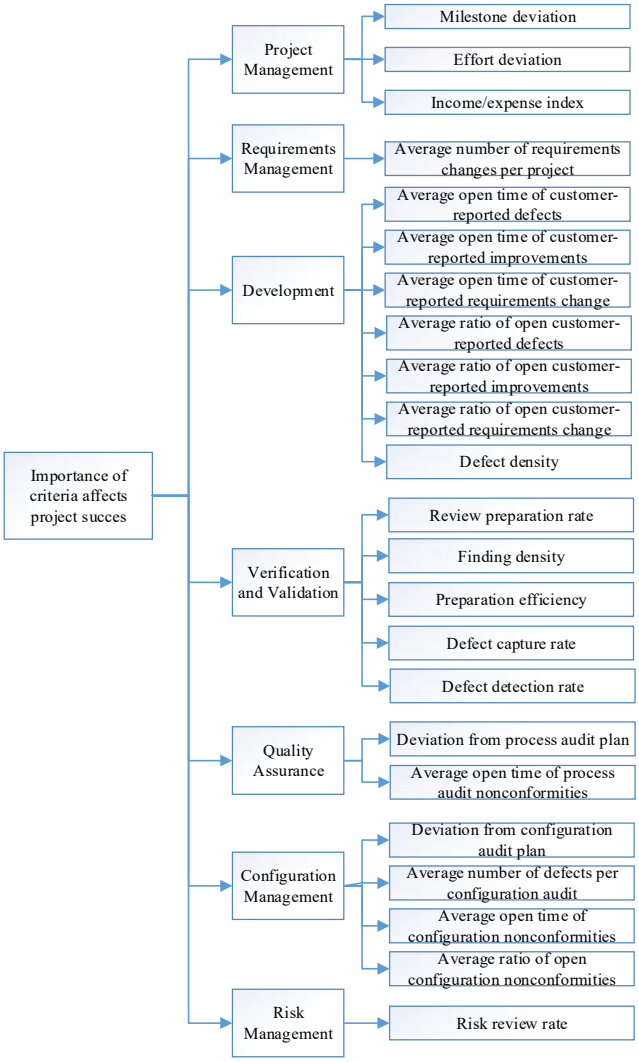

Figure 2. Hierarchy of Process Metric Criteria

As a result of the literature review, it has been observed that there is not enough study on the process metrics in the software life cycle in determining the factors affecting the project success. In the metric determination study conducted with expert project managers and quality managers in the R&D institution, it has been evaluated that measuring and analyzing the critical activities of the processes operated in the project life cycle will affect project success. In this context, an application has been made to verify the proposed model by deciding the weighted contribution of the criteria specified in Figure 2 to the success of the project.

4.2. Data Collection

A questionnaire including process metric criteria was designed to determine relative importance of criteria given in Figure 2. The process metric criteria consisted of 7 criteria at level 2 and 23 sub-criteria al level 3 was assessed according to the level of importance to the organization.

Project performance is measured through collecting and analysis of process metrics results. The data as a result of implementing processes were collected from a total of 25 projects in an R&D organization which develops software and system projects in the defense and civilian sectors. The R&D organization has more than 400 engineers. Process metric measurements are taken from the development tools used in projects. The project development tools that applied in the R&D organization are given in Table 4.

Table 4. Project Development Tools

Process Name	Tool Name
Project Planning and Task Management	Atlassian JIRA
	Atlassian Confluence
	IBM Rational Team Concert
	SAP and MS Project
Requirements Management	IBM DOORS
	IBM DOORS Next Generation
	Atlassian JIRA
Analysis and Design	Enterprise Architect
	IBM Rational Rhapsody
	IBM Rational Software Architect
	Altium Designer
Coding	Eclipse, Visual Studio
Unit Test	Junit
	Google Code Pro
	Quick Test Professional
Build and Integration	Atlassian Bamboo
	Jenkins
	Ant
	IBM Rational Team Concert
Test Management	Rational Quality Manager
Configuration Management	IBM Rational Team Concert
	SVN (Subversion)
	GIT
Task Management	Atlassian JIRA
	IBM Rational Team Concert
Review	SmartBear Collaborator
Software Quality Evaluation	Understand
	Sonar Source

Process metric values are generated as a result of operating the workflows in the project development tools. The relationship between metrics and tools related to workflows is given in Table 5.

Table 5. Project Process Workflows and Related Tool

Workflow Name	Related Tool	Related Process Metric
Task activities	IBM Rational Team Concert, Atlassian JIRA	Milestone and effort deviation Income/expense index Defect capture and detection rate
Change requests	IBM Rational Team Concert, Atlassian JIRA	Open ratio and time of customer reported defects, changes and improvements Number of requirements changes
Defects/ bugs	IBM Rational Team Concert, Atlassian JIRA	Defect density
Risk forms	IBM Rational Team Concert, Atlassian JIRA	Risk review rate
Process audits	IBM Rational Team Concert, Atlassian JIRA	Deviation from process audit plan
Work product conf. audits	IBM Rational Team Concert, Atlassian JIRA	Deviation from configuration audit plan
Reviews	SmartBear Collaborator	Preparation efficiency and rate Finding density
Corrective actions	IBM Rational Team Concert, Atlassian JIRA	Open ratio and time of process and configuration nonconformities

4.3. The Model

Figure 3 shows the project performance evaluation model with using process metric criteria. The project phases indicated in Figure 3 may vary from organization to organization. The process metrics measured at each project stage may also vary according to the business objectives of the organizations and the product and process performance objectives.

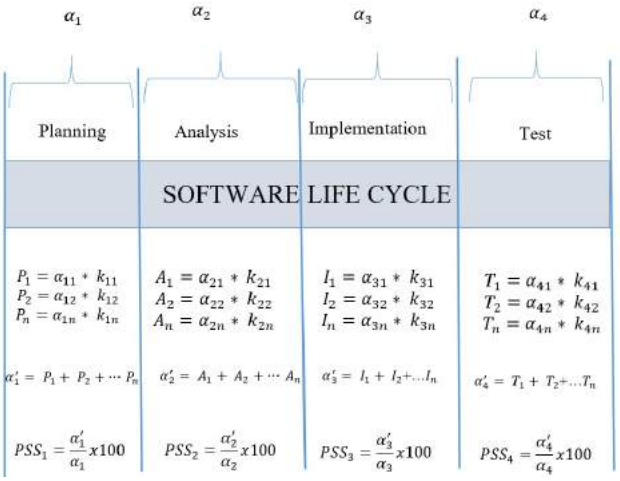

Figure 3. Project Success Score Calculation Model

k_{ij} is a metric weight coefficient calculated by AHP method.

$\alpha_1, \alpha_2, \alpha_3, \alpha_4$ are expected success scores. The expected success points are determined by the weight totals of the process metrics operated at the relevant project stage.

$\alpha_{1n}, \alpha_{2n}, \alpha_{3n}, \alpha_{4n}$ are measured process metric values.

P_n, A_n, I_n, T_n are measured metric success score value of the project relevant stage.

PSS_n are project success scores at the relevant project stage.

The metrics that will be input to the model during the planning, analysis, implementation and testing stages of the project are given in Table 6. The metric codes are defined in Figure 4.

Table 6. Metric Criteria Entering the Model

Project phase	Metric criteria entering the model
Planning	PM1.1,PM1.2, PM1.3,QA1.1, QA1.2, VV1.1, VV1.2, VV1.3, RM1.1
Analysis	PM1.1,PM1.2, PM1.3,RM1.1,DEV 1.3, DEV1.6, QA1.1, QA1.2, VV1.1, VV1.2, VV1.3
Implementation	All process metric criteria
Test	All process metric criteria

Project performance success score is calculated by summing the metric values and metric weight coefficient multiplication results. The process metric criterion which is out of control does not contribute to the project success score. In order to calculate the success score, the metric measurement values were compared with the related process control charts. The process metrics within the upper and lower control limit values contribute to the project success score by their own metric weight.

5. IMPLEMENTATION OF THE MODEL

5.1. AHP Results

AHP methodology was carried out in an R&D organization to weight process metrics in terms of their impact on project success. A series of meetings were held with experienced Project Managers, Department Managers and Quality Assurance Managers in the organization. For this purpose, a structured survey was given to the experts. The experts were asked to evaluate the importance of process metrics on the project success. They have made pairwise comparisons at each hierarchy level by using scale given in Table 3. Geometric mean method is used to aggregate these individual judgments for the final group decision. The results of the pairwise comparison surveys from the participants were evaluated and in cases where the inconsistency rate was greater than 10%, re-interviews were conducted with the relevant participants for reviewing their individual opinions and making corrections. The corrected values from the experts were analyzed. The analysis results and inconsistency rates of the main criteria are given in Table 7. The fact that CR is close to zero means that judgments from experts are more consistent and acceptable.

As can be seen in Table 7, the requirement management process is the criterion that has the most important impact on project success with 21.7%. The development process with 21.5%, the project management process and configuration management with 11.9%, and the verification and validation criteria with 15.1%, respectively follow this. The risk management process with 9.5% and the quality assurance process with 8.4% take the last places. The consistency between the pairwise comparisons has been checked at level 3 for sub-criteria. According to Figure 4, all CR values are close to zero. Sub-criteria weights are given in Figure 4.

Table 7. Main Criteria Weight Results

Process metrics (success criteria)	Weights
Project management	0.119
Requirements management	0.217
Development	0.215
Verification and Validation	0.151
Quality assurance	0.084
Configuration management	0.119
Risk management	0.095
CI = 0.00963	CR = 0.00730

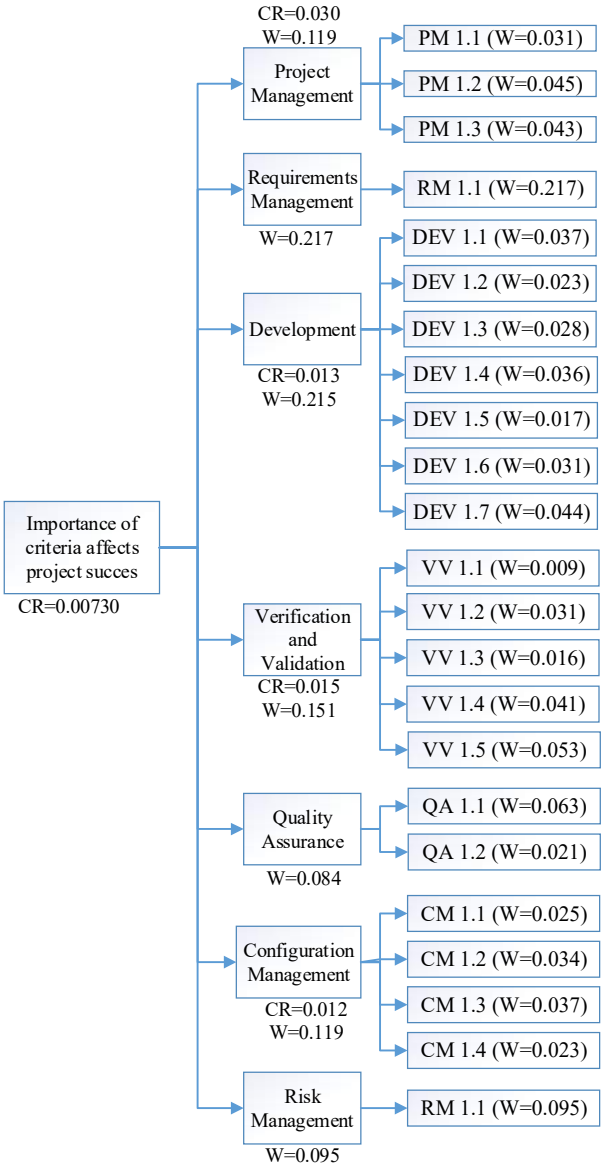

Figure 4. Weights of the Process Metric Criteria

The ordering of the process metric sub-criteria according to their importance is given in Table 8. According to Figure 4 and Table 8, the most important criterion affecting project success is average number of requirements changes per project. This result emphasizes that the high number of requirement changes while the project is continuing prevents the success of the project.

The risk review rate is the second most important criterion in terms of impact on project success. This criterion shows the degree of management of the risks in the project from the beginning to the end of the project. The higher the risk review rate, the higher the chances of project success.

Average open time of process audit nonconformities criterion is the third most important criterion. The experts emphasized that the prolonged closing times of nonconformities found in products and processes as a result of quality audits have a negative effect on project success.

Again, the percentage of defect detection is the fourth most important criterion. The fewer defects that detected by customers, the more successful the project will be.

The effort deviation is fifth in importance. If the planned effort is exceeded, it will have a negative impact on project success, as the total cost will increase. Defect intensity ranks sixth in terms of impact on project success. Since the defect intensity is high, correcting the errors will require additional labor and time, so it will have a negative impact on the project budget and schedule.

The fact that the income expense index, which is in the seventh place, is greater than 1 indicates that it has a positive effect on the success of the project. The defect capture rate that is in the eight place, gives the ratio of the number of defects captured before the software product is delivered to the customer, in the total number of defects. The higher rate means that the product is delivered to customer with fewer defects. This situation has a positive effect on project success. The average open time criterion of configuration non-conformities is important in ninth place. The prolongation of this period decreases the success of the project.

The tenth and eleventh rank metrics are related. The fact that the average open time and rate of defects reported by the customer is high has a negative effect on the success of the project. Similarly, experts emphasized that the high values of all metrics between twelve and twenty one have an adverse effect on project success.

The twenty-second and twenty-third metrics are metrics related to software and documentation reviews. Experts thought these metrics were least important.

Table 8. Ranking Table of Process Metric Criteria

Rank	Criteria	Weight
1	Average number of requirements changes per project	0.2166
2	Risk review rate	0.0953
3	Average open time of process audit nonconformities	0.0633
4	Defect detection rate	0.0531
5	Effort deviation	0.0447
6	Defect density	0.0435
7	Income/expense index	0.0428
8	Defect capture rate	0.0414
9	Average open time of configuration nonconformities	0.0371
10	Average open time of customer-reported defects	0.0370
11	Average ratio of open customer-reported defects	0.0362
12	Average number of defects per configuration audit	0.0335
13	Finding density	0.0314
14	Milestone deviation	0.0313
15	Average ratio of open customer-reported requirements change	0.0307
16	Average open time of customer-reported requirements change	0.0275
17	Deviation from configuration audit plan	0.0253
18	Average ratio of open configuration nonconformities	0.0230
19	Average open time of customer-reported improvements	0.0229
20	Deviation from process audit plan	0.0211
21	Average ratio of open customer-reported improvements	0.0172
22	Preparation efficiency	0.0165
23	Review preparation rate	0.0087

5.2. Using Process Performance Control Charts in the Model

Process performance control charts is established for each process metric indicated in Figure 2. In this section, the process control chart for the review preparation rate criteria, which is related to the review process, is explained. Review preparation rate results have been collected from a total of 25 software projects in the organization in order to create a review preparation rate process control chart.

Review preparation rate measurement aims to determine the central tendency of the time allocated for review activities. Preparation rate equals size of material per preparation hour. If the reviewed material is a document then size is number of pages. If reviewed material is source code the size is logical lines of code. Logical line of code means the code size without comment lines. The data for 24 months collected from the projects in the R&D organization are shown in Table 9. The value for each month is the median average of the review preparation rate for all projects in the relevant month. In the software world, U chart or I-MR control charts are used as control chart type [67]. If the distribution of the data is suitable for the poisson or binomial distribution, the U control chart can be used. If there is no clear idea about the distribution of data, I-MR chart is used [67]. In this study, I-MR control chart graph has been used to create control chart in Minitab tool.

Table 9. Review Preparation Rate Measurements

Months	Review Prep. Rate	Months	Review Prep. Rate
2017-January	21	2018-January	485
2017-February	24	2018-February	33
2017-March	80	2018-March	7
2017-April	90	2018-April	1507
2017-May	26	2018-May	86
2017-June	24	2018-June	28
2017-July	19	2018-July	41
2017-Augost	97	2018-Augost	40
2017-September	19	2018-September	89
2017-October	18	2018-October	76
2017-November	13	2018-November	103
2017-December	158	2018-December	25

After the first iteration the points outside of the control limits have been deleted and the control chart was re-established with the remaining data. Continuing in this way, the data remaining as a result of the third iteration has created a stable process control chart. The control chart generated is shown in Figure 5.

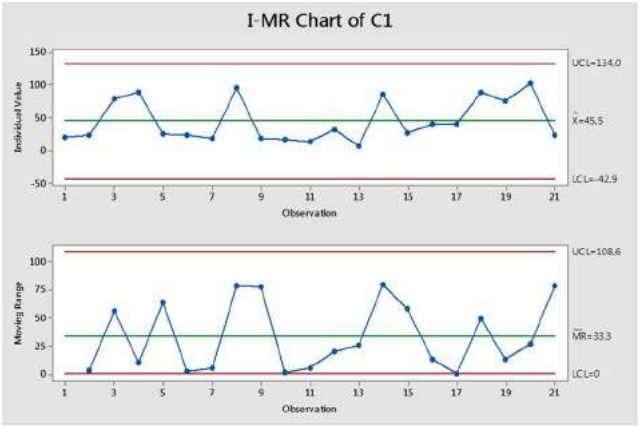

Figure 5. Review Preparation Rate Control Chart - Third Iteration Result

As shown in Figure 5, the process has become stable by eliminating all points that are out of control. In this study, process control charts have been created for all process metric criteria in the software life cycle. The upper and lower control limits of the control charts created for the process metric criteria specified in Figure 2 are given in Table 10. The value of the lower control limit, which is calculated as negative value, is shifted to zero; since it is logically impossible to have a negative value for review preparation rate metric [68].

Table 10. Process Metric Criteria Lower-Upper Control Limit Values

Metric Name	Lower Control Limit Values	Upper Control Limit Values
Milestone deviation (day)	0	30
Effort deviation (%)	0	10%
Income / expense index*	>1	
Average open time of process audit nonconformities (day)	0	15
Deviation from process audit plan (day)	0	15

Metric Name	Lower Control Limit Values	Upper Control Limit Values
Average open time of customer-reported defects (day)	0	30
Average open time of customer-reported improvements (day)	0	30
Average open time of customer-reported requirements change (day)	0	30
Average ratio of open customer-reported defects (%)	0	10%
Average ratio of open customer-reported improvements (%)	0	10%
Average ratio of open customer-reported requirements change (%)	0	10%
Defect density (#/KLOC)	0	1.40
Deviation from configuration audit plan (day)	0	15
Average defect per configuration audit (number)	0	5
Average open time of configuration nonconformities (day)	0	30
Average ratio of open configuration nonconformities (%)	0	10%
Risk review rate (%)	90%	100%
Average Number of Requirements Changes per Project (number)	0	15
Review preparation rate (size/hour)	0	134
Finding density (#/size)	0	0,19
Preparation Efficiency (#/hour)	0	0,08
Defect capture rate (%)	57%	100%
Defect detection rate (%)	60%	100%

*Note: Analysis has been made according to the case of being larger or smaller than 1.

5.3. Results of the Model Implementation

The model has been applied with a real project data in an R&D organization. In project planning, analysis, implementation and test stages, which are the software lifecycle stages, project performance evaluation has been performed. As a result of each evaluation, a numerical project success score has been created.

Process metric measurement results collected from the project in the acceptance test phase are given in Table 11.

Table 11. Real Project Measurements

Metric Name	Metric value
Milestone deviation (day)	47
Effort deviation (%)	15
Income / expense index*	0.83
Average open time of process audit nonconformities (day)	11
Deviation from process audit plan (day)	0
Average open time of customer-reported defects (day)	24
Average open time of customer-reported improvements (day)	22
Average open time of customer-reported requirements change (day)	18
Average ratio of open customer-reported defects (%)	8
Average ratio of open customer-reported improvements (%)	7
Average ratio of open customer-reported requirements change (%)	8
Defect density (#/KLOC)	1.1
Deviation from configuration audit plan (day)	7
Average defect per configuration audit (number)	2
Average open time of configuration nonconformities (day)	15
Average ratio of open configuration nonconformities (%)	6
Risk review rate (%)	100
Average Number of Requirements Changes per Project (number)	14
Review preparation rate (size/hour)	80
Finding density (#/size)	0,12
Preparation Efficiency (#/hour)	0,05
Defect capture rate (%)	61
Defect detection rate (%)	70

The metrics to enter the model during the planning phase are given in Table 12. If the related process metrics measured in the project planning stage are within the upper and lower control limits, the total weight of the metrics is 0.355. The weight value of the process metrics that are out of control is assumed to be zero. The analysis phase total weight of the metrics is 0.630. While performing the performance evaluation during the project's implementation

and testing phase, all of the software life cycle process metrics are inputs to the model. So both total metric weights equals to 1.

In the real project measurement results, milestone deviation, effort deviation and income / expense index values of the project have been found to be outside the limits of the relevant control charts. Other process metric values have been found within the control limits. In this case, the total weight values of the metrics within the control limits have been calculated as 0.236. The total expected metric weight of the project is 0.355. The ratio of these two values to each other and multiplied by 100 gives the success score for the planning phase of the project.

$$\text{Planning phase project success score} = \frac{0,236}{0,355} x100 = 66 \quad (3)$$

As of the planning phase, the project meets 66% of the expected success.

The reasons for the deviation of the process metric values from the targeted limits in this project were analyzed by Ishikawa diagram and root causes have been found. As a result of the analysis, it has been concluded that due to technical difficulties in the project, the milestone of the project is extended and in this case the effort value increases. As an applied corrective activity, an experienced employee has been assigned to the project. Again, the results of the evaluation made at other stages of the project are given in Table 12.

Table 12. Results of Model Implementation

Project phase	Metric criteria entering the model	Calculated project success score
Planning	PM1.1,PM1.2, PM1.3,QA1.1, QA1.2, VV1.1, VV1.2, VV1.3, RM1.1	66
Analysis	PM1.1,PM1.2, PM1.3,RM1.1,DEV 1.3, DEV1.6, QA1.1, QA1.2, VV1.1, VV1.2, VV1.3	81
Implementation	All process metric criteria	88
Test	All process metric criteria	88

6. CONCLUSION

The project management philosophy has been supported by international standards and turned into a methodology. With the principle of common understanding, which is one of the most important results of this standardization, minimum requirements for project management activity steps are determined. In line with the researches, it is observed that these activities are intended to form a common understanding about measurement, analysis, evaluation, improvement, but some gaps in this matter have been observed and discussed in this study. As a result of the literature research, it has been concluded that the project success factors are determined in general terms, but when these are discussed on a sector basis, these general lines should be further customized. In other words, when the literature is analyzed, models for measurement, analysis and evaluation have been created predominantly in the production and service sectors, but it has been observed that there are no models and application examples for the software R&D sector.

The purpose of this paper is to develop a model to evaluate project performance with software life cycle process metrics and calculate project success score. The project success factors, which are seen as deficiencies in the literature, were discussed with experts, who have advanced experience and competence in R&D organization, the project success criteria, which were felt deficient, were determined, and these measurements have been proposed in the study.

In order to create a project performance evaluation model from these criteria, judgements were collected from experienced researchers and project managers in an R&D organization. The relative importance of the process metrics was determined by AHP method. As a result of the calculations made with the judgements of the experts, the weighting of each criterion was found and its effect on the model was revealed. As a result of the main criteria weighting, it has been observed that the requirement management process will have 21.7% impact on the project success. The development process with 21.5%,

the project management process and configuration management with 11.9%, and the verification and validation criteria with 15.1%, risk management process with 9.5% and the quality assurance process with 8.4%, respectively, follow this. As a result of the sub-criteria weighting, the effect of each process metric on project success was revealed.

AHP was used because of the ability to 1) establishment of a hierarchical decision structure for the solution of the problem, 2) enables the assessment of multiple expert opinions, 3) pairwise comparison advantage, 4) no need for decision-making groups to engage in lengthy discussions, 5) ability to address inconsistency in expert judgements. On the other hand, the process takes a lot of time when new criteria are added.

A case study was conducted from an R&D organization to observe the proposed model applicability and the effects of obtaining the results. As a result of this application example, process control charts were created and process performances were evaluated. In case the process metric measurements exceed the upper and lower control limits on the control charts, project managers can investigate the cause of that situation with root cause analysis and aim to increase the project performance by initiating corrective action if needed.

This study has important implications for project managers and senior managers. First, this study created a list of project success factors to be used in project performance evaluation. This list will help project managers understand the key process success criteria that are important to project success. Secondly, this study provides project managers with a model to measure the success of their projects. The model can serve as a tool for project managers to improve the process performance of projects.

This study is limited to the context of the R&D organization and therefore the results may only be considered valid in this particular context. Other organizations can collect data from their own software lifecycle processes metrics and set up their own project success score calculation model.

REFERENCES

[1] Presidency of the Republic of Turkey Strategy And Budget Department (in 681 article).

[2] Presidency of the Republic of Turkey Strategy and Budget Department Medium Term Program 2016-2018 (in 180 article).

[3] Republic of Turkey Ministry of Industry and Technology, Turkey Software Sector Strategy and Action Plan 2017-2019.

[4] M. Radujković and M. Sjekavica, “Project Management Success Factors,” in Creative Construction Conference 2017, Procedia Engineering 196, Croatia, pp. 607-615, 2017.

[5] Merrow, E.: Independent Project Analysis Report, IPA, 2011.

[6] 12207-2017 ISO/IEC/IEEE International Standard Systems and software engineering - Software life cycle processes. DOI:10.1109/IEEESTD.2017.8100771

[7] R. Santhanam and M. J. Schniederjans, “A model formulation system for information system project selection,” Computers & operations research, vol. 20, no. 7, pp. 755-767, 1993.

[8] M. M. Akyol, “Yazılım Süreçlerini Etkileyen Faktörlerin Belirlenmesine İlişkin Bir Ölçüm Ve İyileştirme Modeli Ve Uygulaması,” Ph.D. dissertation, Istanbul University, Istanbul, Turkey, 2013.

[9] M. Ayyıldız, O. Kalıpsız, and S. Yavuz, “YEEM: Yazılım Projeleri Maliyet Tahminleme Ölçev Seti ve Modeli,” ELECO, Bursa, Turkey, pp. 1-4, 2006.

[10] O. P. Sanchez, M. A. Terlizzi, and H. Moraes, "Cost and time project management success factors for information systems development projects," International Journal of Project Management, vol. 35, pp. 1608–1626, 2017.

[11] F. A. Mir and A. H. Pinnington, "Exploring the value of project management: linking project management performance and project success," International Journal of Project Management, vol. 32, pp. 202–217, 2014.

[12] M. J. Todorović, D. Č. Petrović, M. M. Mihić, V. L. Obradović, and S. D. Bushuyev, "Project success analysis framework: a knowledge-based approach in project management," International Journal of Project Management, vol. 33, pp. 772–783, 2015.

[13] J. Verner, B. Kitchenham, and N. Cerpa, "Estimating Project Outcomes," ICSSEA Conference, 2007-11, 2007.

[14] V. Garousi, A. Tarhan, D. Pfahl, A. Coşkunçay, and O. Demirörs, "Correlation of critical success factors with success of software projects: an empirical investigation," Software Quality Journal, vol. 27, pp. 429–493, 2019.

[15] R. R. M. M. K. Wadugodapitiya, Y. G. Sandanayake, and N. Thurairajah, "Building project performance evaluation model," Proc. CIB World Congress, Salford, UK, 2010.

[16] M. Ilbeigi and G. Heravi, "Developing a model to evaluate project performance: contractor company's viewpoint," in Joint Int. Symp. CIB, Rotterdam, Netherlands, pp. 130–139, 2009.

[17] R.G. Koelmans, "Project success and performance evaluation," Int. Platinum Conf. The South African Institute of Mining and Metallurgy, Sun City, South Africa, Oct. 3-7, pp. 229–236, 2004.

[18] S. S. Leu and Y. C. Lin, "Project performance evaluation based on statistical process control techniques," Journal of Construction Engineering and Management, vol. 134, no. 10, pp. 813-819, 2008.

[19] G. T. Bauch and C. A. Chung, "A statistical project control tool for engineering managers," Project Management Journal, vol. 32, no. 2, pp. 37-44, 2001.

[20] D. C. Bower and A. D. Finegan, "New approaches in project performance evaluation techniques," International Journal of Managing Projects in Business, vol. 2, no. 3, pp. 435-444, 2009.

[21] B. Shahzad and A. M. Said, "Identification and quantitative analysis of project success factors for large scale projects," International Journal of Knowledge Society Research (IJKSR), vol. 5, no. 1, pp. 83-95, 2014.

[22] T. G. Viglioni, J. A. O. Cunha, and H. P. Moura, "A performance evaluation model for project management office based on a multicriteria approach," Procedia Computer Science, vol.100, pp. 955-962, 2016.

[23] R. Doskočil, S. Škapa, and P. Olšová, "Success evaluation model for project management," Economics and Management, 2016.

[24] K. N. Shashi, T. G. Nair, and V. Suma, "SLI, a new metric to determine success of a software project," 2014 International Conference on Electronics and Communication Systems (ICECS), pp. 1-5, 2014.

[25] A. Badewi, "The impact of project management (PM) and benefits management (BM) practices on project success: Towards developing a project benefits governance framework," International Journal of Project

Management, vol. 34, no. 4, pp. 761-778, 2016.

[26] A. Mossalam and M. Arafa, "The role of project manager in benefits realization management as a project constraint/driver," HBRC Journal, vol. 12, no. 3, pp. 305-315, 2016.

[27] J. Gomes and M. Romão, "Improving project success: A case study using benefits and project management," Procedia Computer Science, vol. 100, pp. 489-497, 2016.

[28] D. J. Bryde and L. Robinson, "Client versus contractor perspectives on project success criteria," International Journal Of Project Management, vol. 23, no. 8, pp. 622-629, 2005.

[29] K. Jugdev and R. Müller, "A retrospective look at our evolving understanding of project success," Project Management Journal, vol. 36, no. 4, pp. 19-31, 2005.

[30] D. Baccarini, "The logical framework method for defining project success," Project Management Journal, vol. 30, no. 4, pp. 25-32, 1999.

[31] C. Besner and B. Hobbs, "The project management tools and techniques: The portrait of current professional practice," Project Management Journal, vol. 37, no. 3, pp. 37-48, 2006.

[32] C. S. Lim and M. Z. Mohamed, "Criteria of project success: an exploratory re-examination, International Journal of Project Management," vol. 17, no. 4, pp. 243-248, 1999.

[33] M. Radujković, "The Role of Project Management in Construction Industry Modernization," 13th China International Construction Project Management Summit, Hangzhou, Zhejiang, pp. 10-28, 2014.

[34] T. Cooke-Davies, "The "real" success factors on projects," International Journal of Project Management, vol. 20, no. 3, pp. 337-342, 2002.

[35] R. Müller and K. Jugdev, "Critical success factors in projects: Pinto, Slevin, and Prescott - the elucidation of project success," International Journal of Managing Projects in Business, vol. 5, no. 4, pp.757-775, 2012.

[36] D. J. Bryde, "Project management concepts, methods and application," International Journal of Operations & Production Management, vol. 23, no. 7, pp. 775 – 793, 2003.

[37] J. S. Chou, N. Irawan, and A. D. Pham, "Project management knowledge of construction professionals: Cross-country study of effects on project success," Journal of Construction Engineering and Management, vol. 139, no. 11, 04013015, 2013.

[38] S. M. S. Ellatar, "Towards developing an improved methodology for evaluating performance and achieving success in construction projects," Scientific Research and Essay, vol. 4, no. 6, pp. 549-554, 2009.

[39] PricewaterCuppers (PWC) Insights and Trends: Current Portfolio, Programme and Project Management Practices, 3rd Global survey on the current state of project management, PWC, 2012.

[40] A. L. R. Feger and G. A. Thomas, "A framework for exploring the relationship between project manager leadership style and project success," International Journal of Management, vol. 1, no. 1, pp. 1-19, 2012.

[41] M. Keil, A. Rai, and S. Liu, "How user risk and requirements risk moderate the effects of formal and informal control on the process performance of IT projects," European Journal of Information Systems, vol. 22, no. 6, pp. 650-672, 2013.

[42] H. Taylor, "Critical risks in outsourced IT projects: the intractable and the unforeseen," Communications of the ACM, vol. 49, no. 11, pp. 74-79, 2006.

[43] S. M. H. M. Al-Tmeemy, H. Abdul-Rahman, and Z. Harun, "Future criteria for success of building projects in Malaysia," International Journal of Project Management, vol. 29, no. 3, pp. 337-348, 2011.

[44] F. Blindenbach-Driessen, J. Van Den Ende, "Innovation in project-based firms: The context dependency of success factors," Research Policy, vol. 35, no. 4, pp. 545-561, 2006.

[45] D. J. Bryde, "Perceptions of the impact of project sponsorship practices on project success," International Journal of Project Management, vol. 26, no. 8, pp. 800–809, 2008.

[46] M. M. Nahod and M. V. M. Radujković, "The impact of ICB 3.0 competences on project management success," Procedia-Social and Behavioral Sciences, vol. 74(0), pp. 244-254, 2013.

[47] J. Ramazani and G. Jergeas, "Project managers and the journey from good to great: The benefits of investment in project management training and education," International Journal of Project Management, vol. 33, no. 1, pp. 41-52, 2015.

[48] J. R. Turner, R. Müller, and V. Dulewicz, "Comparing the leadership styles of functional and project managers," International Journal of Managing Projects in Business, vol. 2, no. 2, pp. 198-216, 2009.

[49] L.A. Ika, "Project success as a topic in project management journals," Project Management Journal, vol. 40, no. 4, pp. 6-19, 2009.

[50] M. Radujković, "Voditelj projekta," Građevinar, vol. 52, no. 03, pp. 143-151, 2000.

[51] E. Westerveld, "The Project Excellence Model®: linking success criteria and critical success factors," International Journal of Project Management, vol. 21, no. 6, pp. 411-418, 2003.

[52] G. Skulmoski, "Project maturity and competence interface," Cost Engineering - Ann Arbor Then Morgantown, vol. 43, no. 6, pp. 11-24, 2001.

[53] L. R. Yang, C. F. Huang, and K. S. Wu, "The association among project manager's leadership style, teamwork and project success," International Journal of Project Management, vol. 29, no. 3, pp. 258–267, 2011.

[54] M. S. Ozdemir and T. L. Saaty, "The unknown in decision making: What to do about it," European Journal of Operational Research, vol. 174, no. 1, pp. 349-359, 2006.

[55] R. W. Saaty, "The Analytic Hierarchy Process-what it is and how it is used," Mathematical Modelling, vol. 9, no. 3-5, pp. 161-176, 1987.

[56] E. H. Forman and M. A. Selly, "Decision By Objectives (How To Convince Others That You Are Right)," World Scientific Pub. Co., Petersburg, USA, 2001.

[57] T. L. Saaty, "Decision Making with the Analytic Hierarchy Process," International Journal of Services Sciences, vol. 1, no. 1, pp. 83–98, 2008.

[58] T. L. Saaty and S.M. Ozdemir, "Why the Magic Number Seven Plus or Minus Two," Mathematical and Computer Modelling, vol. 38, no. 3-4, pp. 233-244, 2003.

[59] P. T. Garker and L. G. Vargas, "The Theory of Ratio Scale Estimation: Saaty's Analytic Hierarchy Process," Management

Science, vol. 33, no. 11, pp. 1383-1403, 1987.

[60] T. L. Saaty, The Analytic Hierarchy Process. McGraw-Hill, New York, 1980.

[61] W. A. Florac and A. D. Carleton, “Measuring the Software Process,” SEI Series in Software Engineering, 1999.

[62] A. L. Jacob and S. K. Pillai, “Statistical process control to improve coding and code review,” IEEE software, vol. 20, no. 3, pp. 50-55, 2003.

[63] W. A. Florac and A. D. Carleton, J. R. Barnard, “Statistical process control: analyzing space shuttle onboard software process,” IEEE Software, vol. 17, no. 4, pp. 97-106, 2000.

[64] P. Jalote and A. Saxena, “Optimum control limits for employing statistical process control in software process,” IEEE Transactions on Software Engineering, vol. 28, no. 12, pp. 1126-1134, 2002.

[65] Q. Wang, N. Jiang, L. Gou, X. Liu, M. Li, and Y. Wang, “BSR : A Statistic-based Approach for Establishing and Refining Software Process Performance Baseline,” pp. 585–594, 2006.

[66] D. Card, “Statistical process control for software?,” IEEE Software, vol. 11, no. 3, pp. 95–97, 1994.

[67] W. A. Florac, R. E. Park, and A. D. Carleton, “Practical software measurement: measuring for Process Management and Improvement,” Guidebook, CMU/SEI-97-HB-003, 1997.

[68] B. D. Günel, O. Erdoğan and A. Dikici, "Learner Control Charts: A Structured Way for Finding Common Causes with Decision Trees." Euro SPI, Dundalk, Ireland, 2013.

JOURNAL OF SCIENCE
SAKARYA UNIVERSITY

Sakarya University Journal of Science

ISSN 1301-4048 | e-ISSN 2147-835X | Period Bimonthly | Founded: 1997 | Publisher Sakarya University | http://www.saujs.sakarya.edu.tr/en/

Title: Mechanical and Electrical Response of Structural Capacitor for Various Dielectric Materials

Authors: Aysun EĞRİSÖĞÜT TİRYAKİ, Oğuzhan Bartuğ KURUKAYA
Recieved: 2019-11-12 11:36:28

Accepted: 2020-04-08 15:16:22

Article Type: Research Article
Volume: 24
Issue: 3
Month: June
Year: 2020
Pages: 555-563

How to cite
Aysun EĞRİSÖĞÜT TİRYAKİ, Oğuzhan Bartuğ KURUKAYA; (2020), Mechanical and Electrical Response of Structural Capacitor for Various Dielectric Materials. Sakarya University Journal of Science, 24(3), 555-563, DOI: https://doi.org/10.16984/saufenbilder.645408
Access link
http://www.saujs.sakarya.edu.tr/en/issue/52472/645408

Sakarya University Journal of Science 24(3), 555-563, 2020

Mechanical and Electrical Response of Structural Capacitor for Various Dielectric Materials

Aysun EĞRİSÖĞÜT TİRYAKİ*[1], Oğuzhan Bartuğ KURUKAYA[1]

Abstract

Due to the run out of the fossil energy sources and environmental issues, new energy storage systems are developed in conjunction with renewable energy technologies. The machines that supplied energy from the batteries consume extra energy because they carry both the weight of the batteries and the structural weight. Recently, the idea of storing energy in structural elements has been studied. In this study, the multifunctionality of structural capacitors made by placed of varied dielectric layers between the carbon fiber plates has been investigated. The effects on the mechanical and electrical properties of different dielectric material combinations has been investigated by the simulation, experimentally and by the calculations based on Hook's law. Thus, the results of structural dielectric capacitors in these combinations have been compared and discussed.

Keywords: Structural capacitor, energy storage, multifunctional composites, dielectric materials.

1. INTRODUCTION

The materials that can give a functional response to environmental changes or stimulating external influences are called Smart Materials. These materials are affected by electromagnetic field, light, pressure, humidity, temperature, power. Smart materials can perform more than two tasks at the same time. This is called multifunctionality. The composite materials used in energy storage mechanism are also multifunctional materials just like them. Multifunctional energy storage composites represent a novel form of multifunctional structural battery materials that can carry mechanical loads while simultaneously providing energy-storage capabilities [1]. By placing dielectric film between these materials, structural capacitors are obtained that function as energy storage capacitors. O'Brien at all [2] calculated to multifunctionality and built structural capacitor. In his work, he found specific mechanical properties such as specific stiffness etc. Also, O'Brien et al. [3] showed that electrode materials and processing method have a significant effect on performance. Tony Carlson and al. [4,5] used three different surface weights

*Corresponding Author: aysune@sakarya.edu.tr ; ORCID: https://orcid.org/0000-0001-6440-8396.
[1]Sakarya University, Department of Mechanical Engineering, Sakarya, Turkey.

of paper and three different polymer films (Polyamide-PA, Polyethylene Terephthalate-PET and Polycarbonate-PC) as a dielectric layers in his work and characterized multifunctional performance of the structural capacitor by measuring capacitance, dielectric strength and interlaminar shear strength. Shen and Zhou [6] studied the effects of delamination and interlaminar damage on the mechanical and electrical performance of carbon-fiber structural capacitor (CFSC) materials. Chan and al. [7,8] developed the multifunctional structural dielectric capacitor by using carbon fiber reinforced composites and graphene oxide paper and showed that the electrical and mechanical properties of the this new structural dielectric capacitors were significantly enhanced. Chan and al. [9] added gold nanoparticles into the epoxy matrix of carbon fibre reinforced polymer based electrodes used in graphene oxide-bearing structural dielectric capacitors in his later work and provided improving both the electrical and mechanical properties of the capacitor. Ladpli and al. proposed and analyzed the multifunctional energy storage composite structures that encapsulated lithium-ion battery materials inside high-strength carbon-fiber composites [1].

In this study, the structural dielectric capacitors have been manufactured by using of paper, Polyvinyl Chloride (PVC) and Polytetrafluoroethylene (PTFE) film as dielectric material between reinforced carbon fiber plates. Mechanical and electrical properties of these capacitors have been studied experimentally, by simulation and calculation and obtained results are compared.

2. THEORETICAL MODEL

2.1. Mechanical Properties of Carbon Fiber Reinforced Polymer (CFRP) Matrix

Carbon fiber reinforced polymer matrix materials are consist of a combination of one or more carbon fiber layer to make a heterogeneous material with polymer matrix. The layer formed by the polymer matrix with single layer carbon fiber is called lamina. The structure that many layers come together is called laminate. Lamina and laminate are shown in Figure 1.

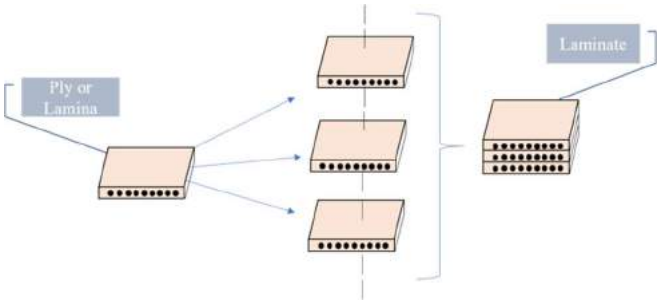

Figure 1. Lamina and laminate

CFRP is generally anisotropic, i.e. it exhibits different mechanical properties in different directions. The calculation of the mechanical properties of the laminate [10] is shown in equation (1).

$$\begin{bmatrix} N_x \\ N_y \\ N_{xy} \\ M_x \\ M_y \\ M_{xy} \end{bmatrix} = \begin{bmatrix} A_{11} & A_{22} & A_{16} & B_{11} & B_{12} & B_{16} \\ A_{12} & A_{22} & A_{26} & B_{12} & B_{22} & B_{26} \\ A_{16} & A_{26} & A_{66} & B_{16} & B_{26} & B_{66} \\ B_{11} & B_{12} & B_{16} & D_{11} & D_{12} & D_{26} \\ B_{12} & B_{22} & B_{26} & D_{12} & D_{22} & D_{26} \\ B_{16} & B_{26} & B_{66} & D_{16} & D_{26} & D_{66} \end{bmatrix} \begin{bmatrix} \varepsilon_x^0 \\ \varepsilon_y^0 \\ \gamma_{xy}^0 \\ \kappa_x \\ \kappa_y \\ \kappa_{xy} \end{bmatrix} \quad (1)$$

$$A_{ij} = \sum_{k=1}^{n} [(\bar{Q}_{ij})]_k (h_k - h_{k-1}), i = 1,2,6; j = 1,2,6 \quad (2)$$

$$B_{ij} = \frac{1}{2} \sum_{k=1}^{n} [(\bar{Q}_{ij})]_k (h^2{}_k - h^2{}_{k-1}), i = 1,2,6; j = 1,2,6 \quad (3)$$

$$D_{ij} = \frac{1}{3} \sum_{k=1}^{n} [(\bar{Q}_{ij})]_k (h^3{}_k - h^3{}_{k-1}), i = 1,2,6; j = 1,2,6 \quad (4)$$

2.2. Carbon Fiber Composite Capacitor

The capacitor is a device for storing electrical charge or electrical energy in an electrical field. In its simplest form a capacitor consist of two metal plates separated by a dielectric layer, as shown in Figure 2 [11].

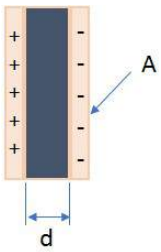

Figure 2. Parallel plate capacitor

The ability of a capacitor to store a charge on its conductive plates gives it its Capacitance value and is calculated as:

$$C = \frac{\varepsilon_r \times \varepsilon_0 \times A}{d} \tag{5}$$

where C is capacitance, A is plate area, d is separation distance of the plates, ε_0 is permittivity of space and ε_r is the relative permittivity of the dielectric material.

A composite capacitor is formed by placing a dielectric separator between two carbon fiber laminae. As can be seen in Figure 3, two carbon fiber laminae numbered 2 are placed in front of and behind a dielectric separator.

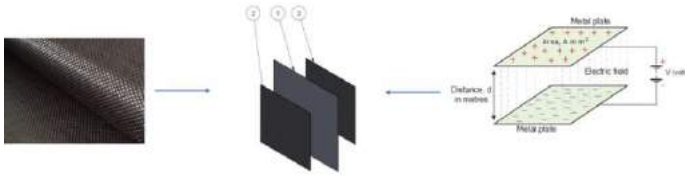

Figure 3. Structure of carbon fiber capacitor

To investigate mechanical and electrical performance of dielectric materials in the structural capacitor, the representative properties should be selected. While tensile testing for mechanical properties the capacitance and hence electrical energy density were measured for electrical performance.

2.3. Energy Density

The energy density is the amount of energy stored per mass. The maximum energy storage is calculated based on the dielectric strength voltage. The energy density [4] is calculated as follows eq. (6).

$$\bar{\Gamma} = \frac{\frac{1}{2}CV^2}{m_{sc}} \tag{6}$$

In this formula $\bar{\Gamma}$ is energy density, C is capacitance, V is dielectric strength voltage of dielectric material and m_{SC} is mass of the structural capacitor.

3. MANUFACTURING OF ENERGY STORAGE STRUCTURE

3.1. Vacuum Bagging Method

In this study is used vacuum bagging method for molding. Figure 4 shows Vacuum Bagging Method. The sample is prepared on a metal mold. Dielectric material is placed between the wet carbon fiber plate pair. There is a separating cloth and glass wool layer on top of this structure, respectively. Finally, vacuum is applied by covering the vacuum bag.

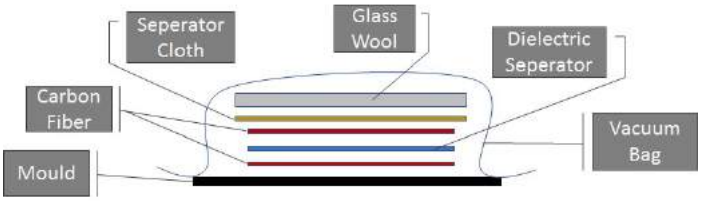

Figure 4. Vacuum Bagging Method

The materials used in the vacuum bag method are illustrated in Figure 5 and Figure 6 shows the vacuum application.

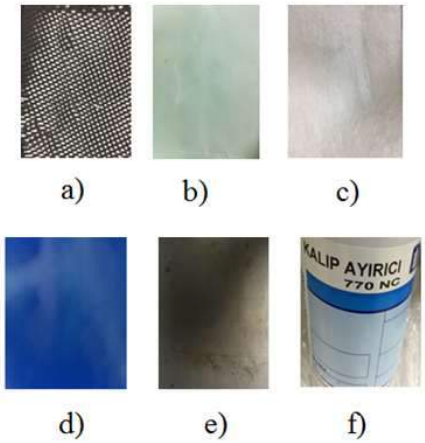

Figure 5. Vacuum bagging materials (a-Carbon fiber, b-Separator cloth, c-Glass wool, d-Vacuum bag, e-Metal mold, f-770 NC mold separator)

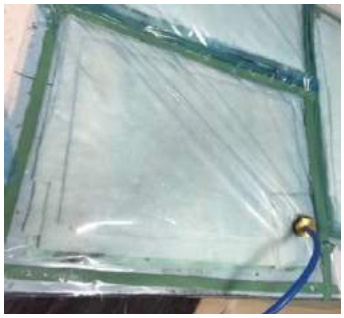

Figure 6. Vacuum bag application

3.2. Product and Features

Five samples containing various dielectric materials were produced by vacuum bag method for electrical test. These test samples are shown in Figure 7, respectively 80 microns PVC (ETS1), 120 micron PVC (ETS2), 80 micron PTFE (ETS3), 120 micron PTFE (ETS4) and 100 micron paper (ETS5). The electrical test specimens were formed by inserting 100 x 100 mm carbon fiber laminate in the center of the 130 x 130 mm dielectric material.

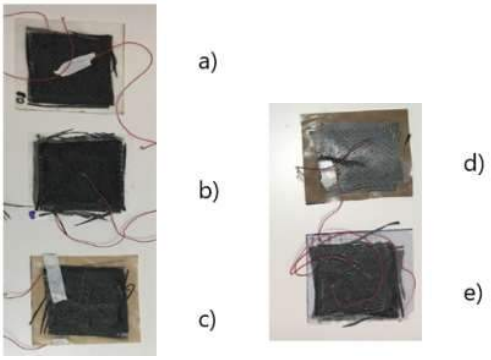

Figure7. Electrical Test Specimens (a-ETS1, b-ETS2, c-ETS3, d-ETS4, e-ETS5)

In addition, each dielectric-carbon fiber pair was produced in accordance with ASTM D3039 standards to perform mechanical tests. These mechanical test specimens were produced with 80 micron PVC (MTS1), 120 micron PVC (MTS2), 80 micron PTFE (MTS3), 120 micron PTFE (MTS4), paper (MTS5) and only carbon fiber (MTS6). Mechanical test specimens produced according to ASTM D3039 standards are shown in Figure 8. However, as seen in Figure 8 e-f, the mechanical test specimens made with PTFE test specimens were separated into pieces when cut.

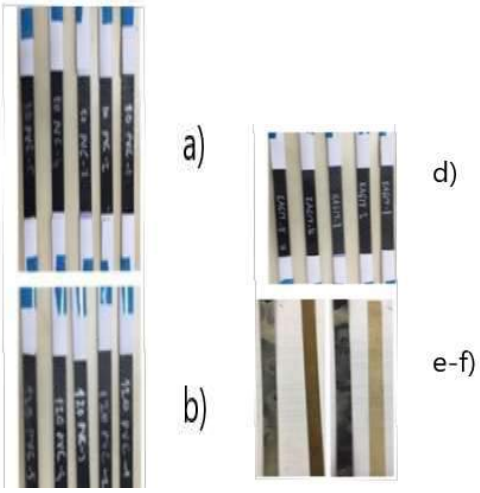

Figure 8. Mechanical Test Specimens (a-MTS1, b-MTS2, c-MTS6, d-MTS5, e-f-MTS3-MTS4)

4. MODELING AND SIMULATIONS

4.1. 3D Plain Model

The 3D plain model (Figure 9) was created using TexGen geometric modelling scheme developed by the University of Nottingham. 3x3 yarn, 1.75mm yarn spacing, 1.5mm yarn width and 0.25mm fabric thickness were used in model.

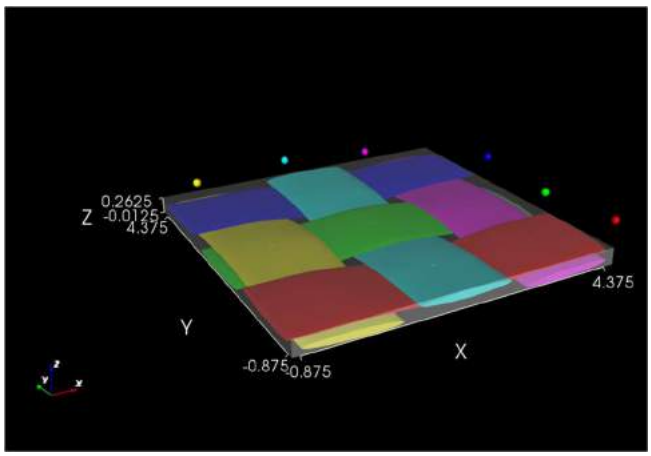

Figure 9. Geometric model of 3x3 unit cell

4.2. Electrostatic Simulation

The electric field and capacitance are solved under electrostatic conditions. Electrostatic

simulations were performed for models obtained using different dielectric materials in this study. In simulation, 90% of the dielectric strength voltage of each insulator material was applied. The dielectric strength voltages of the materials and applied voltages in the simulation are shown on the Table 1.

Table 1. Applied voltages in electrostatic simulation

	Applied Voltage[V]	Dielectric Strength Voltage [kV/mm]
ETS1(80pvc)	3528	3920
ETS2(120pvc)	8794,8	9772
ETS3(80ptfe)	2304	2560
ETS4(120ptfe)	3456	3840
ETS5(paper)	1440	1600

Figure 10 shows electric potentials applied to ETS1, ETS2, ETS3, ETS4 and ETS5 test specimens. In these simulations, the effects of matrix material are neglected. The electric field results obtained from the simulations are shown in Figure 11.

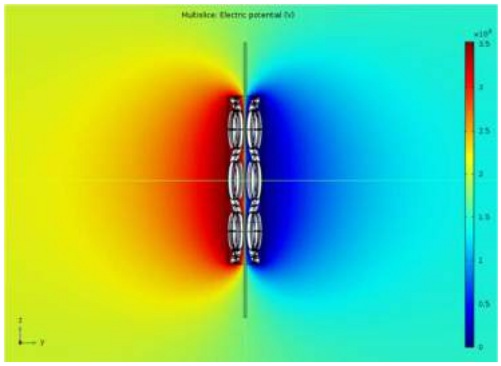

(a)

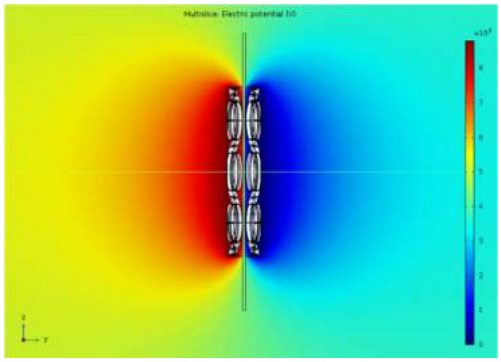

(b)

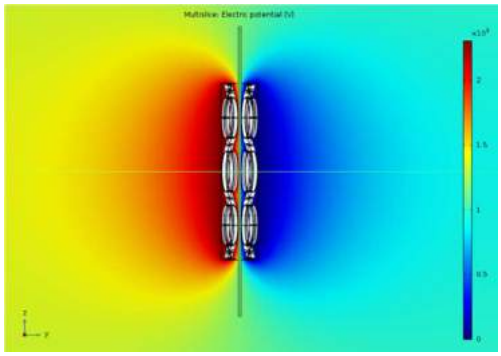

(c)

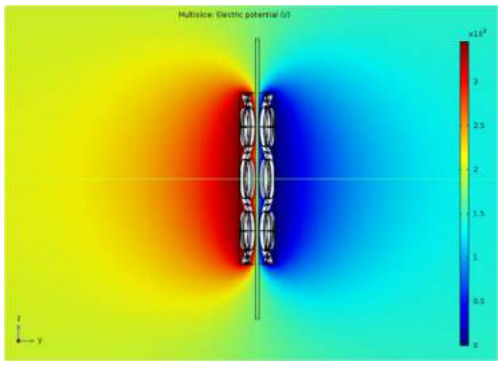

(d)

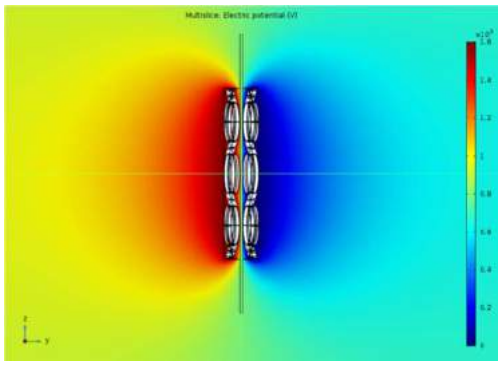

(e)

Figure 10. Electric potentials applied in electrostatic simulations (a-ETS1, b-ETS2, c-ETS3, d-ETS4 and e-ETS5)

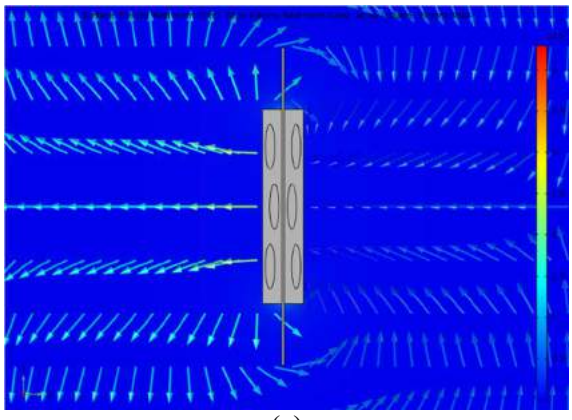

(a)

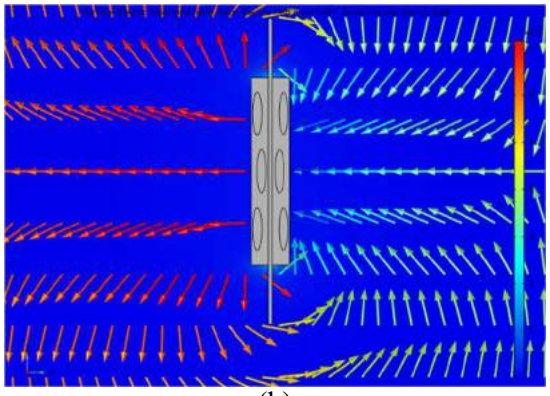

(b)

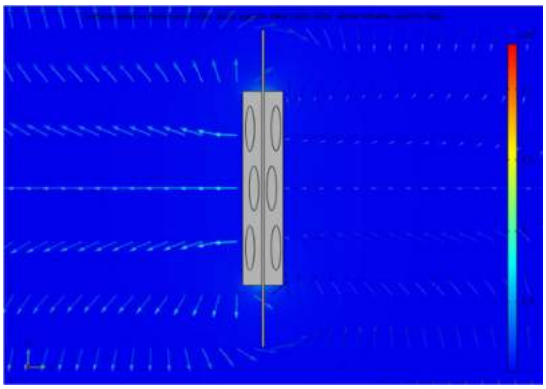

(c)

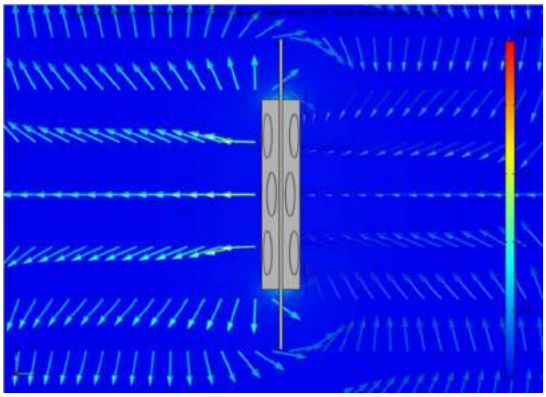

(d)

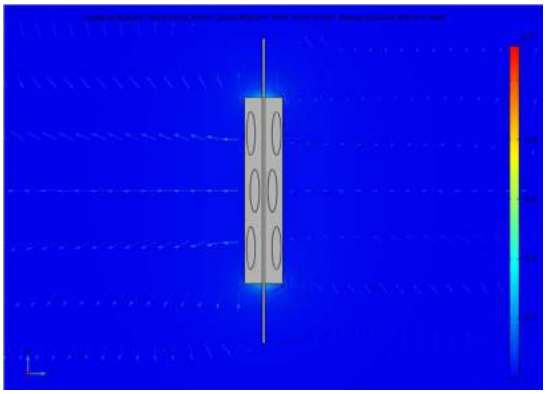

(e)

Figure 11. Electric fields obtained from simulations (a-ETS1, b-ETS2, c-ETS3, d-ETS4 and e-ETS5)

The highest value of electric field is obtained with voltage of applied 8794,8 V to PVC material. In addition to being the strongest electric field in PVC material, there is increase in the electric field with increase in the loading.

Electric Potential, as seen in the graphs, the carbon fiber surface has not spread properly due to its wavy structure. Due to the fluctuating nature of the surfaces, the distance d varies. Therefore, the carbon fiber plate capacitor stored less energy than a normal flat surface capacitor.

5. RESULTS AND CONCLUSION

Each specimen was tested five times under the same conditions for the sake of repeatability. Table 2 shows the mean test results and calculated mechanical properties. The mean tensile strength and stiffness test values were calculated by using ordinary least squares method. In addition, Hook's Law was used to calculate the mechanical properties.

Table 2. Mechanical Test Results and Calculated Mechanical Properties (E is Stiffness, v is Poisson Ratio, S is Tensile Strength)

	Calculated		**Test Results**		
	E[GPa]	**v**	**E[GPa]**	**v**	**S[MPa]**
MTS1	64.50	0.42	47.20	0.45	419
MTS2	65.77	0.41	61.40	0.41	528
MTS5	64.53	0.40	63.10	0.30	605
MTS6	-	-	62.97	0.43	514

TABLE 3 shows the dielectric strength of the specimens, measured capacitance values and capacitance results obtained from the simulations.

Table 3. Dielectric Strength Simulation's Capacitance Results and Measured Capacitances of Electrical Test Specimens

Specimen	**Dielectric Strength[kV/mm]**	**Measured C[nF/m2]**	**Simulation C[nF/m2]**
ETS1	3920	130	129,19
ETS2	9772	118	100,82
ETS3	2560	67	97,53
ETS4	3840	85	78,95
ETS5	1600	460,59	241,4

The difference between the electrostatic simulation results and the measurements is caused by the epoxy layer formed between the fibers. The accumulation of epoxy between the thin film and the carbon fiber surface increases the insulating strength of the structural capacitor and provide it to be charged with more electricity. Furthermore, the epoxy that is irregularly cured forms different insulation coefficients in different regions. Especially paper, because it absorbs epoxies, a new hybrid dielectric material is formed.

Electric fields show irregularities as shown in Figure 11. This is because a carbon fiber fabric surface has a wavy structure. If there was a flat plate, there would be a more regular electric field and a higher capacity electric storage feature. This surface ripple affects the capacity feature negatively.

The strain-stress graphs of the mechanical test specimens are shown in Figure 12. When the strain-stress graphs are examined, it is clearly evident that the mechanical test sample containing paper dielectric material shows high mechanical performance.

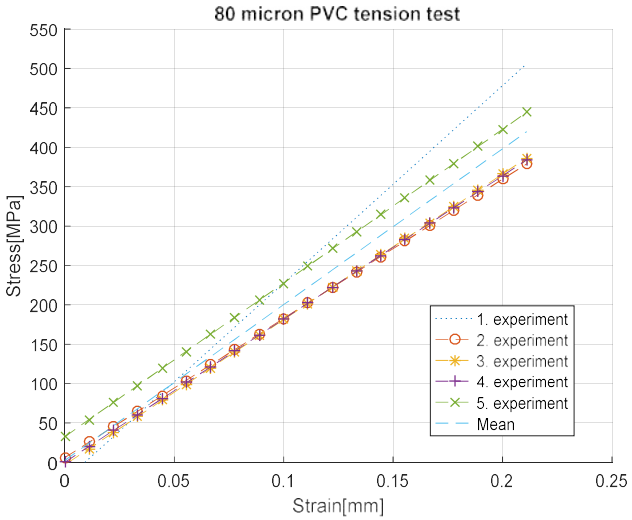

(a)

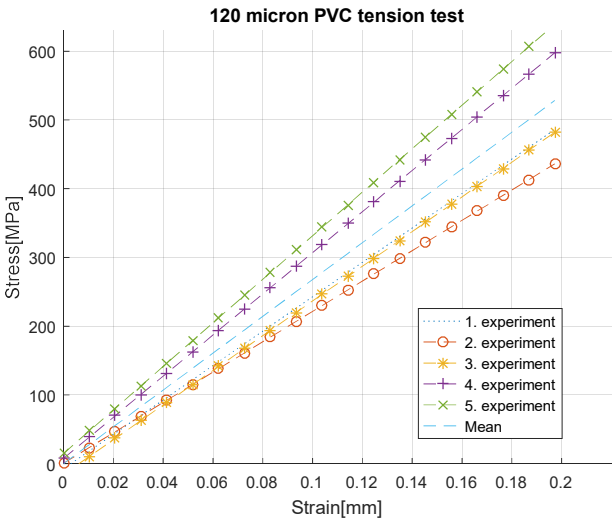

(b)

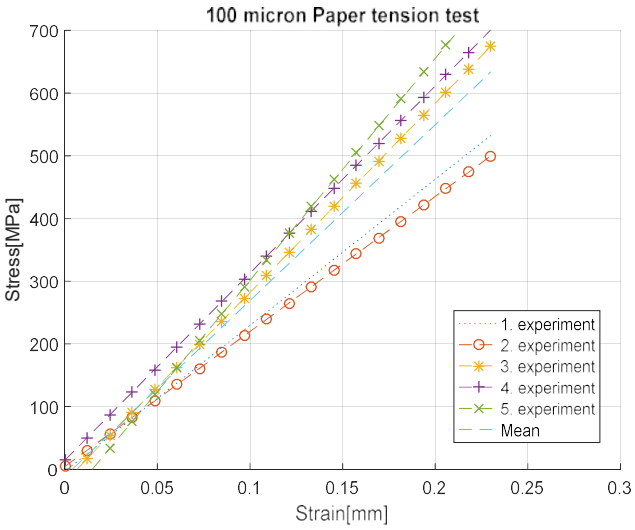

(c)

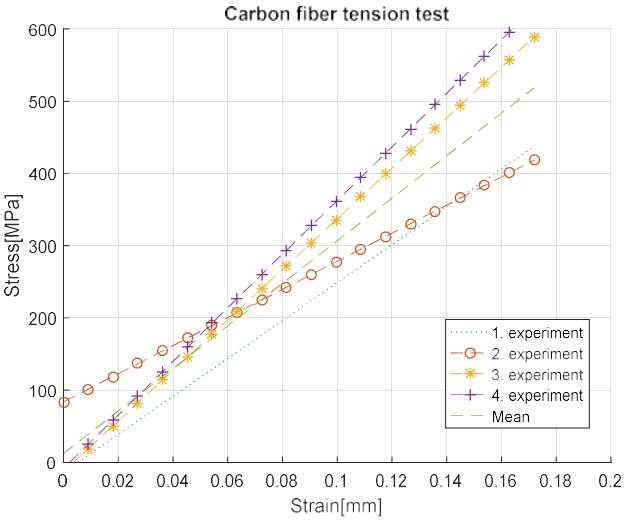

(d)

Figure 12. Tensile Test Results (a-MTS1, b-MTS2, c-MTS5 and d-MTS6)

The multifunctionality of structural capacitors made by placed of varied dielectric layers between the carbon fiber plates were compared in Figure 13. It is seen in Figure 13.a that the capacitor that stores the most energy is ETS2. Figures 13.b and c show that the capacitor that stores the most energy density with high stiffness and strength is also ETS2.

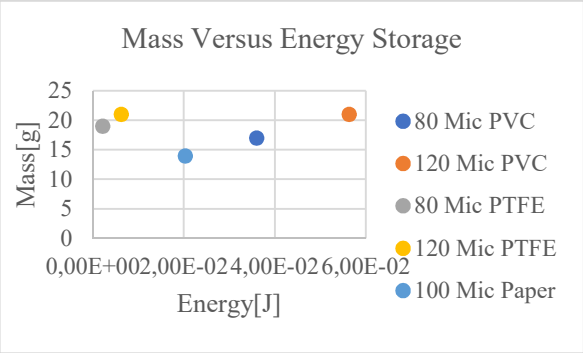

(a)

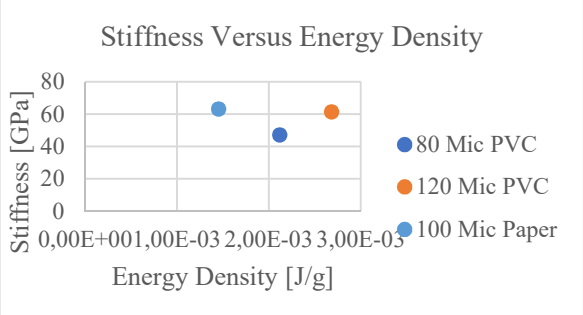

(b)

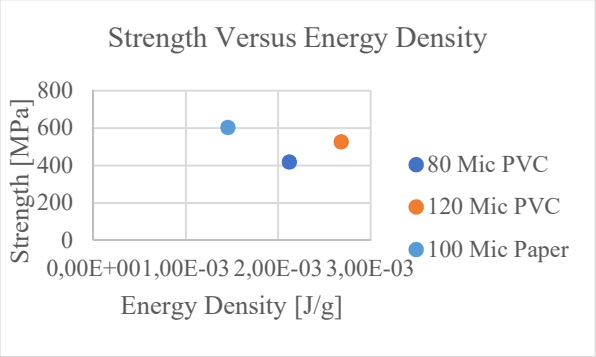

(c)

Figure 13. For the structural capacitors with various dielectric materials: a-Mass Versus Energy Storage, b-Stiffness Versus Energy Density, c-Strength Versus Energy Density

In the study, the capacitor made of PTFE has been found to have very low mechanical properties despite the energy storage. As previously predicted and as can be also seen in the tests carried out the layer formed between the PTFE separator layer and the carbon fiber did not adhere to each other. That's why, using of this pair in structural capacitors is not recommended because it tends to break apart.

The paper made capacitor showed both higher energy storage and higher mechanical properties than the others. Paper-containing carbon fiber capacitor has a better adhesion surface with epoxy than other dielectric materials. This has affected the electrical and mechanical properties positively. But due to its low dielectric strength, it has less energy storage capability than PVC.

Better mechanical and capacitive properties of the 120 micron PVC-made capacitor may be associated with better adhesion to carbon fiber. In terms of energy density, 120 micron PVC provides higher capacity. The main reason for this is that the insulation strength is higher than other thin films, and combinations with this film can be loaded at higher voltages.

As a result manufacturing defects and the failure to adhere well to the dielectric materials of carbon fiber affect mechanical and electrical properties of the capacitor. Thin films with low adhesion energy have a negative effect on the system in terms of both mechanical properties and capacity.

In addition, another factor that increases the capacity, and accordingly, the energy density of the structural capacitor is the accumulation of epoxy between the thin film and the carbon fiber surface. This accumulation will increase the insulating resistance of the structural capacitor and it will provide that loaded it with more electricity. However, this accumulation is very difficult to measure. If epoxy accumulation is measured, its effect on mechanical properties and energy density can be discussed.

Acknowledgments

This study is supported by Sakarya University Scientific Research Projects Coordination Unit. Project Number: 2018-50-01-006.

REFERENCES

[1] P. Ladpli, R. Nardari, F. Kopsaftopoulos, F.K. Chang, "Multifunctional energy storage composite structures with embedded lithium-ion batteries," Journal of Power Sources, vol.414, pp.517-529, February 2019.

[2] D.J. O'Brien, D.M. Baechle, E.D. Wetzel, "Multifunctional structural composite capacitors for U.S. army applications," Proceedings of SAMPLE 2006, Dallas, Texas, USA, 2006.

[3] D.J. O'Brien, D.M. Baechle, O.B. Yurchak, E.D. Wetzel, "Effect of Processing Conditions and electrode characteristics on the electrical properties of structural composite capacitors," Composites Part A: Applied Science and Manufacturing, vol.68, pp.47-55, January 2015.

[4] T. Carlson, D. Ordeus, M. Wysocki, L.E. Asp, "Structural capacitor materials made from carbon fiber epoxy composites," Composite Science Technology, vol.70, no.7, pp. 1135-1140, July 2010.

[5] T. Carlson, L.E. Asp, "Structural carbon fibre composite/PET capacitors – Effects of dielectric separator thickness" Composites Part B: Engineering, vol.49, pp. 16-21, June 2013.

[6] Z. Shen and H. Zhou, "Mechanical and electrical behavior of carbon fiber structural capacitors: Effects of delamination and interlaminar damage," Composite Structures, vol.166, pp. 38-48, 2017.

[7] K.Y.Chan, B. Jia, H. Lin, B. Zhu, K.T.Lau, "Design of a structural power composite using graphene oxide as a dielectric material layer," Mater. Lett., vol.216, pp. 162-165, 2018.

[8] K.Y. Chan, H. Lin, K. Qiao, B. Jia, K.T.Lau, "Multifunctional graphene oxide paper embodied structural dielectric capacitor based on carbon fibre reinforced composites," Composite Science and Technology, vol.163, pp. 180-190, 2018.

[9] K.Y. Chan, D. Yang, B. Demir, A.P. Mouritz, H. Lin, B. Jia, K.T.Lau, "Boosting the electrical and mechanical properties of structural dielectric capacitor composites via gold nanoparticle doping," Composites Part B, vol.178, 107480, 2019.

[10] Autar K. Kaw, Mechanics of Composite Materials, Second Edition. Published in 2006 by CRC Press. International Standard Book Number-10: 0-8493-1343-0 (Hardcover).

[11] P. Jain, E.J. Rymaszewski, Rensselaer Polytechnic Institute Troy, NY, 2004. Thin-Film Capacitors for Packaged Electronics. ISBN 978-1-4419-9144-7 (eBook), DOI 10.1007/978-1-4419-9144-7.